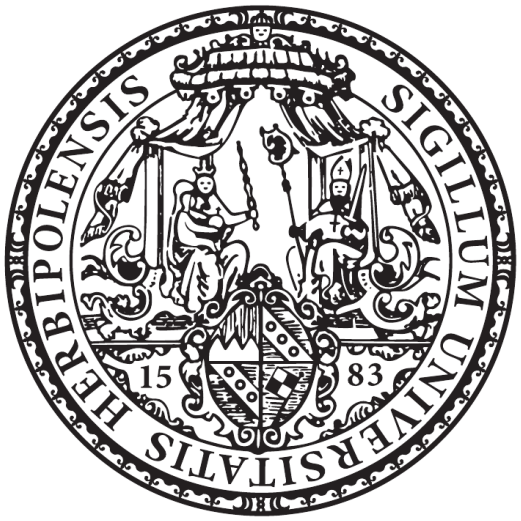

Model System for Correlation Phenomena in Reduced Dimensions - Gold-induced Atomic Chains on Germanium

Dissertation zur Erlangung des
naturwissenschaftlichen Doktorgrades der
Julius-Maximilians-Universität Würzburg

vorgelegt von
Sebastian Meyer
geboren in Paderborn

Würzburg 2013

Eingereicht am: 04.10.2012

bei der Fakultät für Physik und Astronomie

Gutachter der Dissertation:

1. Gutachter & Betreuer: Priv.-Doz. Dr. Jörg Schäfer

2. Gutachter: Prof. Dr. Jean Geurts

3. Gutachter:

Prüfer im Promotionskolloquium:

1. Prüfer: Priv.-Doz. Dr. Jörg Schäfer

2. Prüfer: Prof. Dr. Jean Geurts

3. Prüfer: Prof. Dr. Giorgio Sangiovanni

Tag des Promotionskolloquiums: 01.03.2013

Abstract

Atomic chains, often called nanowires, form in a self-organized process after the adsorption of metal atoms. These wires are spatially well confined representing a close approach of a true one-dimensional structure. The low-dimensional architecture thereby often leads to anisotropic electronic states with vanishing interchain interaction. In the presence of weak coupling to the substrate a one-dimensional metal can experience a phase transition according to Peierls into an insulating ground state upon temperature, which is accompanied by a periodic lattice distortion. Without any coupling a strict one-dimensional regime is reached, where the common Fermi liquid description breaks down with the quasi-particles being replaced by collective excitations of spin and charge. This state is referred to as a Tomonaga-Luttinger liquid (TLL), which has been observed so far only in anisotropic bulk materials. An experimental fingerprint for both phenomena can be obtained from the electronic states close to the chemical potential, i.e. the Fermi energy. Using a semiconducting substrate provides the best observation conditions since any bulk projection onto the interesting bands is avoided.

In case of Au/Ge(001) the growth of gold-induced chains is guided by the dimerized bare Ge (2×1) reconstruction yielding two different domains of wires rotated by 90° going from one terrace to the next by a single height step. The superior wetting capabilities of gold on germanium enables a complete coverage of the Ge(001) surface with long-range ordered wires. Their length scale and defect density is limited by the underlying substrate, for which a cleaning procedure is introduced based on wet-chemical etching followed by thermal dry oxidation.

The band structure of Au/Ge(001) is investigated by angle-resolved photoelectron spectroscopy as a function of temperature. Two states are observed: a two-dimensional metallic state with hole-like dispersion and a one-dimensional electron pocket, whose band-integrated spectral function does not show the typical Fermi distribution at the chemical potential. Instead, a decrease of spectral weight applies following a power-law. This behavior can be well explained within the Tomonaga-Luttinger liquid theory which replaces the Fermi-Landau formalism in strictly one-dimensional systems.

To enable theoretical modeling, a structural analysis was performed on the basis of surface x-ray diffraction (SXRD). From the in-plane scattering data a Patterson-map could be extracted leading to in-plane distances between gold atoms in the unit cell. This provides the first step towards a complete structural model and therefore towards a band structure calculation. First successful attempts have been made to manipulate the system by controlled adsorption of potassium. Here, an n-type doping effect is

observed for submonolayer coverage whereas slightly increased coverages in combination with thermal energy lead to a new surface reconstruction.

Zusammenfassung

Atomare Ketten, sogenannte Nano-Drähte, entstehen durch Selbstorganisation adsorbierter Metallatome auf einer Halbleiteroberfläche. Aufgrund der starken räumlichen Einschränkung der Ladungsträger innerhalb dieser Ketten entsteht dabei oftmals eine metallische Bandstruktur mit starker Anisotropie. Im Falle phononischer Ankopplung an das Substrat kann so ein eindimensionales (1D) Metall instabil gegen eine periodische Gitterverzerrung werden, bei der es zu einer Ausbildung einer Energielücke kommt. Dieser Metall-Isolator-Übergang wird dabei als Peierls Übergang bezeichnet. Für verschwindend geringe Kopplung der Ketten untereinander bzw. an das Substrat, d.h. im strikt eindimensionalen Fall, bricht das Fermi Flüssigkeitsmodell für dreidimensionale (3D) Metalle zusammen. Dessen Quasiteilchen werden durch kollektive Anregungen von Spin und Ladung ersetzt. Diesen Zustand bezeichnet man als Tomonaga-Luttinger Flüssigkeit. Beide Phänomene, Peierlsübergang und Tomonaga-Luttinger Flüssigkeit lassen sich anhand der elektronischen Bandstruktur experimentell nachweisen.

Bei dem hier untersuchten Probensystem handelt es sich um Gold-induzierte Nandrähte auf der Germanium (001)-Oberfläche, kurz Au/Ge(001). Deren Wachstum erfolgt epitaktisch entlang der durch das Substrat vorgegebenen Dimer-Reihen, welche die freie Germaniumoberfläche in Form einer (2×1)-Symmetrie einnimmt. Die abwechselnde Stapelfolge ABAB des Substrates führt dabei zu zwei unterschiedlichen Drahtrichtungen, die jeweils um 90° zueinander gedreht sind, wenn man eine Einfachstufe von 1.4 Å von einer A-Terrasse auf eine B-Terrasse oder umgekehrt geht. Die vorherrschende Kinetik während der Gold-Deposition bzw. das Benetzungsverhalten ermöglicht dabei eine vollständige Bedeckung der vormals freien Oberfläche mit Nanodrähten, deren Abmessungen einzig und allein durch Defekte bzw. die Größe der darunterliegenden Ge-Terrasse begrenzt sind.

Um die Längenskala der Subtrat-Terrassen zu optimieren, wurde eine Reinigungsprozedur für Ge (001) entwickelt, bei der nass-chemisches Ätzen mit anschliessender Trocken-Oxidation zum Einsatz kommt. Die darauf aufbauenden Nanodrähte wurden im Anschluss mittels winkelaufgelöster Photoelektronenspektroskopie auf ihre elektronische Bandstruktur untersucht. Dabei wurden zwei neuartige Zustände beobachtet: ein metallischer, zweidimensionaler Loch-Zustand, der seinen Ursprung höchstwahrscheinlich in tieferen Schichten des Germaniums hat; und ein eindimensionaler Oberflächenzustand mit elektronenartiger Dispersion, dessen bandintegrierte Spektralfunktion von der einer Fermiflüssigkeit abweicht. Stattdessen wird ein exponentieller Abfall des spektralen Gewichtes als Funktion der Energie zum Ferminiveau hin beobachtet. Dieses Verhalten

kann über einen weiten Temperaturbereich beobachtet werden und lässt sich mit der Tomonaga-Luttinger Flüssigkeit für strikt eindimensionale Systeme erklären.

Zum weiteren theoretischen Verständnis dieses Phänomes, beispielsweise durch Bandstrukuturrechnungen mittels Dichte-Funktional-Theorie, bedarf es der genauen Kenntnis der atomaren Struktur dieser Ketten. Selbige wurde mittels Oberflächenröntgenbeugung (engl. surface x-ray diffraction, SXRD) untersucht. Auf Basis der gewonnenen Patterson-Karte lassen sich Rückschlüsse auf die interatomaren Abstände der Goldatome untereinander in der Einheitszelle ziehen. Dies stellt einen ersten wichtigen Schritt auf dem Weg zu einem vollständigen Strukturmodell dar. Darüber hinaus wurden erste vielversprechende Schritte unternommen, das Nanodrahtsystem kontrolliert zu manipulieren. Durch geringfügige, zusätzliche Deposition von Kalium konnte dabei eine schrittweise Erhöhung der Bandfüllung erzielt werden. Für weitergehende Kaliumanlagerungen im (Sub-)Monolagenbereich konnte sogar eine neue Rekonstruktion erzielt werden.

Contents

List of figures

List of acronyms

1D	one-dimensional
2D	two-dimensional
3D	three-dimensional
AFM	atomic force microscopy
ARPES	angle-resolved photoelectron spectroscopy
CDW	charge density wave
CTR	crystal truncation rod
DFT	density functional theory
DOS	density of states
EDC	energy distribution curve
HH	heavy-hole
IMFP	inelastic mean free path
LEED	low-energy electron diffraction
LH	light-hole
MBE	molecular beam epitaxy
MDC	momentum distribution curve
MIT	metal-insulator transition
PES	photoelectron spectroscopy
PM	Patterson map
PT	phase transition
PLD	periodic lattice distrortion
quasi-1D	quasi one-dimensional
RT	room temperature
SBZ	surface Brillouin zone
SO	split-off
SOI	spin-orbit interaction
STM	scanning tunneling microscopy
STR	surface truncation rod
STS	scanning tunneling spectroscopy
SWNT	single-walled carbon nanotube
SXRD	surface x-ray diffraction
TB	tight-binding
TLL	Tomonaga-Luttinger liquid
UHV	ultra-high vacuum
XPS	x-ray photoelectron spectroscopy

1. Introduction

The physics of strongly correlated electron systems is mostly driven by coupling of microscopic degrees of freedom in solids, as well as the interplay between competing interactions (electron-electron, electron-phonon, spin-orbit type) that arises from the underlying architecture, i.e. the *structural confinement in reduced dimensions*. Emerging phenomena are often accompanied by a transition involving ground states of *superconductivity* [15], *Mott-Hubbard insulators* [16] or a *Peierls instability* [17]. Their description goes beyond conventional independent electron theory thereby requiring many-body treatments both in experiment and theory. Real-life model systems to probe these physics are rare and mainly comprise anisotropic and thus quasi-one-dimensional (quasi-1D) crystals like Bechgaard salts - crystals that are mostly based on van-der-Waals bound layers which cause the anisotropic crystalline structure and electronic states [18–20].

Realizing such phenomena on a surface is advantageous because it allows access by a lot of powerful surface science techniques including scanning tunneling microscopy (STM), low-energy electron diffraction (LEED) or angle-resolved photoelectron spectroscopy (ARPES). In addition, these systems exhibit certain degrees of tunability. The symmetry of the substrate determines whether two-dimensional (2D) or one-dimensional (1D) structures can from. The adatom species contributing different in size and valence electrons affects the lattice and the electronic, e.g. by spin-orbit interaction (SOI). A large variety of different reconstructions is already known for gold on silicon substrates where the examples comprise triangular lattices and 1D atomic chains (often denoted as nanowires) as a function of adatom coverage. Detailed phase diagrams for planar and vicinal substrates are given in Ref. [21, 22]. In case of nanowires a limited but discrete set of wire distances is provided by specific substrate miscut angles. A similar diversity of structures forming on silicon (111) is also observed for indium adsorption [23]. A comprehensive review on these two examples is given by Snijders and Weitering in Ref. [24]. These well-ordered reconstructions offer the possibility for structural modifications, e.g. chains ends that have been accidentally terminated by defects, which might act as scattering barriers within the chains. In terms of intentional defects one can imagine manipulation with a STM by pulling and dropping of single atoms [25], insufficient or excessive adsorbate material or additional adatoms [26, 27], e.g. alkali metals which can also dope the system by releasing their outer valence electron [28, 29].

Depending on the degree of structural confinement and its influence on the electronic states, e.g. on the contour of the Fermi surface, two fundamental ground state scenarios can apply: a *Peierls instability* and the *Tomonaga-Luttinger liquid (TLL)*. A Peierls instability requires a former metallic system - ideally a half-filled band. If the system is

cooled below a certain critical temperature it opens up an energy gap and gets insulating [30, 31]. These lowering of occupied states below and unoccupied above the Fermi level provides free energy which is used to modulate the charge density (*charge density wave, CDW*). Simultaneously, the underlying lattice is periodically distorted [17]. The so-called *periodic lattice distortion (PLD)*, i.e. a new real space periodicity, is the second fingerprint for this phenomenon beside the *metal-insulator transition (MIT)*. As the lattice plays an essential role, at least weak coupling to the substrate or between the nanowires has to apply. Previously reported metal-insulator transitions in atomic wire systems are mostly related to a Peierls instability, see for instance [32–34], although alternative explanations like structural origins are discussed [35, 36].

The alternative TLL scenario holds for a complete absence of coupling [37–39]. In this strict 1D case the common Fermi liquid picture is no longer valid. The quasi-particle picture is replaced by new, *collective excitations* of spin and charge called *spinon* and *holon*. Due to their different propagation velocity they form two separated dispersion branches which merge at the Fermi level (*spin-charge separation*). This effect can be observed on a relatively high energy scale (∼eV), while for the low energy excitation a *power-law suppression* of spectral weight towards the chemical potential μ (more common 'Fermi energy' E_F, i.e. $\mu(T = 0K)$) occurs. Current examples of nanowires exhibiting such an exotic electronic ground state are missing, which must be attributed to the non-vanishing coupling to higher dimensions, i.e. interactions with the lattice (phonons), present in all previously reported nanowire systems.

Another aspect which has recently attracted interest in the surface science community is the *Rashba-type splitting* of bands for adsorbate-induced reconstructions [40]. The use of heavy atoms causes a splitting of bands in spin-selective branches by an electrical field gradient at the surface. A variety of examples are known for surface alloys and as well as metal atoms on semiconductors. Once again, the nanowire system of gold on silicon with a (553)-surface (Au/Si(553) in short) can be used as an examples as it also exhibits a Rashba-type splitted pair of bands [41]. For Au/Si(553) a prediction was made recently on (local) magnetic order for T≠0 K [42] - something which should in principle be prohibited by theory in strict 1D.

This thesis will use gold induced atomic chains on the germanium (001)-surface as the system to study. Au/Ge(001) is well-suited for studying its electronic ground state as it exhibits a spatially confined surface reconstruction [1, 43]. The atomic chains align perfectly in parallel with a low defect-density which results in a highly ordered surface that allows complete coverage [44, 45]. The investigation of this nanowire system will include electronically active orbitals and the question whether they form metallic bands themselves or induced by the substrate. Any electronic states will have to be characterized by their dimensionality in terms of symmetries in the Fermi surface, which determines the size of possible interchain hopping or any nesting conditions required for a CDW. The band dispersion on the other side provides information about possible energy gaps as a function of temperature, band back folding at new zone boundaries or even coupling to quasi-particles in terms of band renormalization manifesting themself

by so called “kinks”. In the absence of these phenomena, the unprecedented case of a strict 1D metallic situation can be analyzed for a Tomonaga-Luttinger liquid.

Apart from the study of the bare reconstruction, further aspects include possible impacts of excessive or co-deposited material, e.g. with alkali metals. In the event of an increased band filling, both scenarios, a CDW and a TLL state, might offer the chance to study the influence on the band structure or even a possible cross-over from a TLL to a normal Fermi liquid. Because Au/Ge(001) also involves a heavy element (Z_{Au}=79), the role of a spin-orbit coupling of Rashba type has to be considered.

Experimental access will be given mainly by angle-resolved photoelectron spectroscopy (ARPES), which is the method of choice when studying the band structure. It offers k-space selective analysis of electronic states and their symmetries (dimensionality) from their Fermi surface or constant energy surfaces. A detailed analysis of the band structure can reveal different dispersions, especially interesting in case of spin-charge separation in a TLL state. Furthermore, the effective masses, band widths and energy gaps are necessary parameters for any classification of the system. The k-integrated spectral function may serve as a direct measure of the density of states yielding the many-body physics of the system. The previous metal-insulator transitions reported energy gaps on the meV energy range in such atomic chain systems [46, 47]. As the TLL physics is also a low energy scale effect [48, 49], high energy resolution is required. This, together with the need for different photon energies to account for $k_\perp$ dispersion as a sign of 3D behavior, makes it necessary to use a tunable light source, i.e. a synchrotron facility, to match all experimental requirements.

Since a detailed understanding of any experimentally observed phenomena cannot rely on experimental evidence alone, additional theoretical modeling is desirable. To verify the experimentally obtained band structure in terms of involved orbitals, bondings etc., calculations can only be performed on the basis of a structural model. First steps towards such a model are achieved by surface x-ray diffraction (SXRD), which provides the distance vectors of the gold atoms within the unit cell.

Both types of experiments, ARPES and SXRD, create different laboratory conditions for the growth of these nanowires. This, on the other hand, demands a highly reproducible and reliable growth recipe for a quick adaption of all necessary parameters. The present thesis will therefore be organized as follows: Initially a short description of the expected correlated phenomena and how they can be identified in the experiments will be given in chapter 2 and 3. Afterwards the recipe for the cleaning procedure of the bare Ge(001) substrate will be presented (chapter 4), on which basis the experimental results from SXRD (chapter 5) and ARPES (chapter 6 and 7) were acquired. Chapter 8 gives a short hint on the possible manipulations of such a surface system and their impact on the physics. The summary is given in chapter 9 followed by a short outlook on potential future investigations.

2. Theoretical concepts of electrons in low dimensions

2.1. The route to the Tomonaga-Luttinger liquid (TLL)

In recent decades a variety of materials where electronic correlation effects dominate have emerged, such that these systems can not longer be described by the common Fermi Landau model. Examples comprise, among others, Mott-Hubbard insulators [16], high-T_c superconductors [50] or the fractional quantum Hall effect [51]. The correlation effects are often influenced by the effective dimensionality of the electron gas [48]. Hence, the impact of the spatial confinement on the electronic system in particular will be traced in the following.

2.1.1. Dimensionality

The influence of reduced dimensions can be observed already in the density of states (DOS) $\rho(E)$ as a function of energy E, which is defined as the number of discrete energy levels per unit volume [52]:

$$\rho(E) = 2\frac{V}{(2\pi)^3}\int_{E=E_k}\frac{1}{\nabla_k E_k}d\Omega_k, \tag{2.1}$$

which is a surface integral of fixed energy E=E_k with volume V, element $d\Omega_k$ in momentum space and wavevector k. As a function of dimensionality one gets:

$$\rho_{3D}(E) = \frac{V}{\pi^2}k^2\left(\frac{dE_k}{dk}\right)^{-1}, \tag{2.2}$$

$$\rho_{2D}(E) = \frac{A}{\pi}k\left(\frac{dE_k}{dk}\right)^{-1}, \tag{2.3}$$

$$\rho_{1D}(E) = \frac{L}{\pi}\left(\frac{dE_k}{dk}\right)^{-1}, \tag{2.4}$$

where V represents the volume, A the area and L the length. Assuming a quasi-free electron with parabolic dispersion $E_k = \hbar^2 k^2 / 2m^*$, where m^* is the effective electron mass. ρ_{dim} accounts to:

$$\rho_{3D}(E)dE = \frac{V}{\pi^2}\left(\frac{2m^*}{\hbar^2}\right)^{\frac{3}{2}}\sqrt{E}dE, \tag{2.5}$$

$$\rho_{2D}(E)dE = \frac{A}{\pi}\left(\frac{2m^*}{\hbar^2}\right)dE, \tag{2.6}$$

$$\rho_{1D}(E)dE = \frac{L}{\pi}\left(\frac{2m^*}{\hbar^2}\right)^{\frac{1}{2}}\frac{dE}{\sqrt{E}}, \tag{2.7}$$

with a 2D DOS being constant over energy and a $\frac{1}{\sqrt{E}}$ behavior in the 1D case. The dimensionality has great impact on the electron-electron (e-e) interactions. In 3D the electrons have enough space to almost "avoid" each other due to the large phase space. Their low-energy excitations are well described within Landau's Fermi liquid quasi-particle picture (see next section). A deviation appears already going from 3D to 2D where a magnetic field B perpendicular to the surface leads to Landau quantization, i.e. discrete levels of energy $E_N = E_0 + (N + \frac{1}{2}) \cdot \hbar w_c$ for $N \in \mathbb{N}$ with cyclotron frequency $w_c = eB/mc$ [52]. In a naive 1D picture of electrons aligned in a row, single-particle excitations seem impossible without influencing neighboring electrons by e-e interaction. Thus, only collective excitations of spin and charge in types of density waves remain, which are predicted to exhibit different group velocities, called *spin-charge separation* [53, 54]. The reduced spatial dimension causes an ideal Fermi surface in 1D of two Fermi points $\pm k_F$, where particle-hole excitations are only possible in a very small regime enabling an essential simplification, namely the *linearization of the fermionic dispersion relation*. As a consequence the k-integrated DOS will scale with a *power-law* towards the chemical potential. The Fermi liquid model now has to be replaced by the Tomonaga-Luttinger liquid [39]. A brief overview of the formal description within the framework of *bosonization* and its impacts on the experiment will be given within the next sections.

2.1.2. The Fermi liquid

Simple 3D metals are well described by Landau's theory of the Fermi liquid, with excitations that are small compared to the Fermi energy. In this case, the system can be expressed by its ground state and its lower-lying elementary excitations, denoted as a diluted gas of "quasi-particles" evolving when interactions are switched on adiabatically [48]. These quasi-particles have a one-to-one correspondence to the bare particles (adiabatic continuity), e.g. the same quantum numbers. Only their dynamical properties, such as the electron mass, are renormalized by the interactions [52]. This scenario is caused by the Pauli exclusion principle and the corresponding Fermi statistic, which

suppresses the scattering induced by the switched-on interactions.
The corresponding one-particle propagator (Green's function) $G(\mathbf{k}, E)$ has the form [48]:

$$G(\mathbf{k}, E) = \frac{Z}{\epsilon_0(\mathbf{k}) - w - \Sigma(\mathbf{k}, E)}, \tag{2.8}$$

with the bare dispersion $\epsilon_0(\mathbf{k})$, the self-energy $\Sigma(\mathbf{k}$, E) and the quasi-particle residue Z. From the self-energy both, the effective mass m^* and the quasi-particle residue Z, can be calculated as follows:

$$m^* = m\left(1 - \frac{\partial\Sigma}{\partial E}\right)\left(1 + \frac{m}{k_F}\frac{\partial\Sigma}{\partial E}\right)^{-1} \tag{2.9}$$

$$Z = \left(1 - \frac{\partial\Re\Sigma}{\partial E}\right)^{-1}_{E=\epsilon(k)}. \tag{2.10}$$

Z is also known as the amplitude of the quasi-particles (quasi-particle weight), which smears out a step-like momentum distribution with its discontinuity at k_F as depicted in Fig. 2.1, where $Z = 1$ represents the non-interacting case (see description of the ARPES process in the one-electron picture in eq. 3.19). Z can also be understood as the order parameter of the Fermi liquid at T = 0 K [48].

It can be accessed via the spectral function $A(\mathbf{k}, E)$ which is connected to the Green's function by $A(\mathbf{k}, E) = -(1/\pi)\Im G(\mathbf{k}, E)$. In the non-interacting system one ends up with a delta function $\delta(E-\epsilon(k))$ because the single electrons are eigenstates of the system, see Fig. 2.2(a). For the interacting system an electron can participate in many eigenstates resulting in a broadening of the spectral function in energy as depicted in Fig. 2.2(b). Still for momenta close to k_F, the electron can be found in the quasi-particle eigenstate

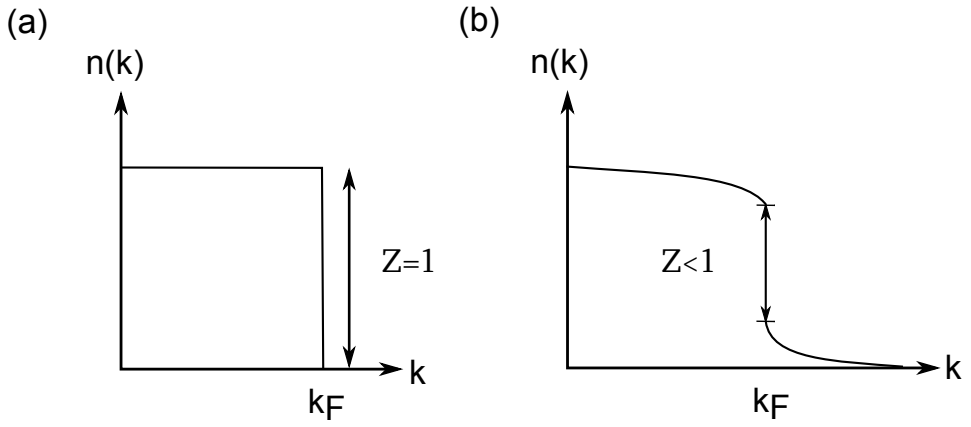

Figure 2.1.: *Single-particle momentum distribution $n(k)$ at $T = 0$ K: (a) In case of a free Fermi gas n switches from 1 to 0 at k_F ($Z = 1$). (b) In the presence of interactions the discontinuity is modified by the quasi-particle residue $Z < 1$ [55].*

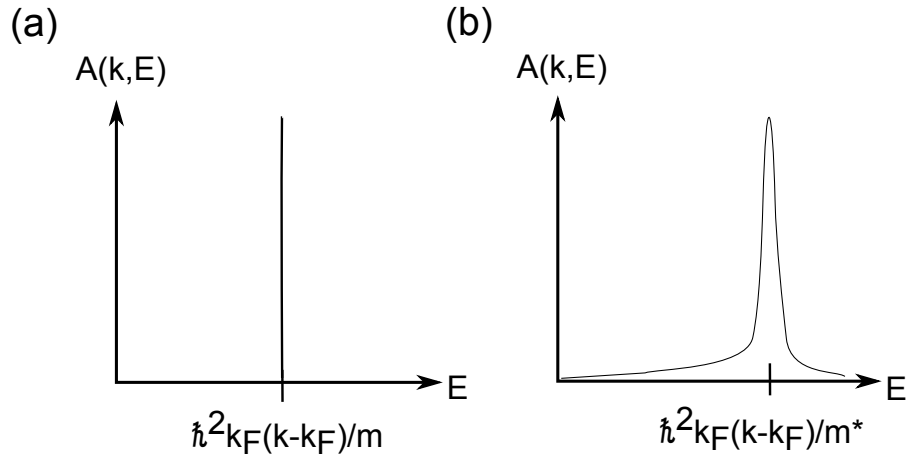

Figure 2.2.: *Spectral function $A(\boldsymbol{k}, E)$, i.e. the probability to find an electron with momentum $\boldsymbol{k}$ at given energy E: (a) For a free Fermi gas without interactions electrons are eigenstates leading to delta functions. (b) The spectral function including interactions is broadened in energy but still contains a peak at the new quasi-particle energy [55].*

with probability Z. At $T = 0$ K the spectral function exhibits a sharp peak with a width proportional to $(k - k_F)^2$ accommodating for the finite lifetime. The integrated peak area corresponds to the quasi-particle weight Z [55].

Note that the self-energy contains all the many-body effects. The poles of the Green's function represent the single-particle excitation energies, its imaginary part the damping of these excitations. The quasi-particles and holes are treated as approximate eigenstates of the system. This allows to calculate their decay rate τ_ϵ for three dimensions by using Fermi's golden rule [55], where all final states f are summed up:

$$\frac{1}{\tau_\epsilon} = \frac{2\pi}{\hbar} \sum_f |V_{if}|^2 \delta(E - E_f). \tag{2.11}$$

With the assumption of a constant scattering matrix element $|V_{if}|$ between initial i and final states f, considering energy conservation and the Pauli principle, the sum becomes:

$$\begin{aligned} \frac{1}{\tau_\epsilon} \sim & \frac{2\pi}{\hbar} \sum_f |V|^2 \int_0^E \rho(E_F) dw \int_0^E \rho(E_F) dE' \\ & \int_{-\infty}^{\infty} \delta(E - w - E' + E'') \rho(E_F) dE'' \qquad (2.12) \\ \sim & \frac{\pi}{\hbar} |V|^2 \rho(E_F)^3 E^2. \qquad (2.13) \end{aligned}$$

The adiabatic continuity is no longer valid for high energies E far away from the Fermi surface, because the quasi-particles decay before the interaction sets in completely [55].

Therefore only small E close to the Fermi surface must be considered. Here the quasi-particles are well defined since the decay rate ($\propto E^2$) is smaller than their excitation energy E. Equation 2.13 can be rewritten by changing the variables [55]:

$$\frac{1}{\tau_\epsilon} = \frac{2\pi}{\hbar}\int_0^E \rho(E_F)wdw \int_{w/\hbar v_F}^{2k_F} \frac{k^{d-1}dk}{(2\pi/L)^d}\frac{|D(k,w)|^2}{(\hbar v_F k)^2}. \tag{2.14}$$

The integral over w accounts for all possible hole excitations. The lower limit of the momentum integral assures a minimum of momentum transferred in the scattering process where $D(w,k)$ represents the scattering matrix element. With the matrix element set constant one gets the same result ($\tau^{-1} \propto \rho(E_F)E^2$) as in equation 2.13 [55].

2.1.3. Deviations from the Fermi liquid - the TLL scenario

For the 1D case the k integral gets singular leading to $\tau_\epsilon \propto \epsilon$ which is equivalent to the breakdown of adiabatic continuity since the quasi-particles are no longer defined in any energy limit. This means: there is no 1D Fermi liquid. The only excitations which are allowed in this case are of collective nature, i.e. density waves for spin and charge, which is a consequence of the dimensionality, see Fig. 2.3.

These collective excitations are described as bosons (spinon and holon) by the Tomonaga-Luttinger liquid concept [39, 48, 55]. Spinon and holon exhibit different velocities ($\nu_{\sigma,\rho}$ for spin σ and charge ρ) thereby leading to the first hallmark of TLL physics: *spin-charge separation*. Its formation is often illustrated using the 1D t-J-model. Here, in the presence of strong inter-electron repulsion (Coulomb U) each site within a 1D chain is occupied by a single electron (half filling) with different spin (anti-ferromagnetic order). Since the electrons now prefer to keep at their sites, the material is an insulator.

If the system is now excited by removal of one electron, see Fig. 2.4, the electrons can lower their kinetic energy by the amount t when switching their positions. Simultane-

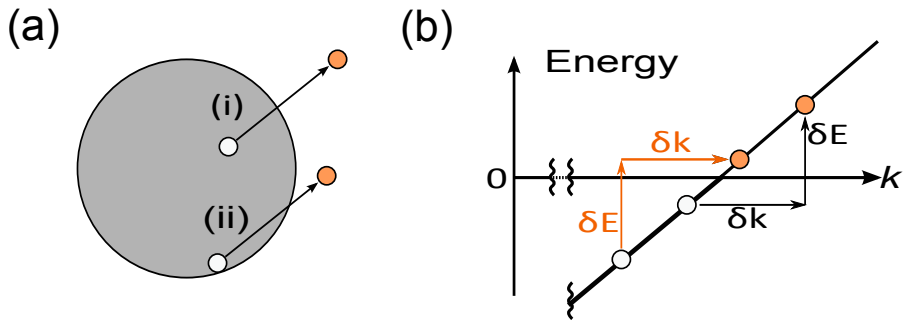

Figure 2.3.: *(a) For dimensions $d > 1$ a manifold of excitations is possible, whether they have (i) high or (ii) low energy and the momentum vector k is normal or transverse to the Fermi surface. (b) In the 1D scenario the direction is restricted such that a fixed momentum transfer δq determines δE. The appropriate description of the systems excitations are density waves [55].*

ously, the systems still prefers to stay anti-ferromagnetically ordered, which is expressed by the strength J. Thus, the movement of the electrons and the antiferromagnetic order are competing processes. In two dimensions this model is used to describe the doped Mott insulator [55]. In 1D, the movement of the excited hole along the chain is called the *holon*, while the pairing of electrons with equal spin orientation is called *spinon*.

The spectral function is modified in a way that for fixed momentum k the quasi-particle peak is replaced by two individual features representing spinon and holon dispersions. The momentum-resolved spectral function which reveals the different propagating velocities is depicted in Fig. 2.5. Notably, two distinct dispersion branches are only observed up to $\alpha \leq 0.5$, i.e. $K_\rho \geq 0.27$. In the opposite case the spinon peak is reduced to an edge as depicted in Fig. 2.5(b).

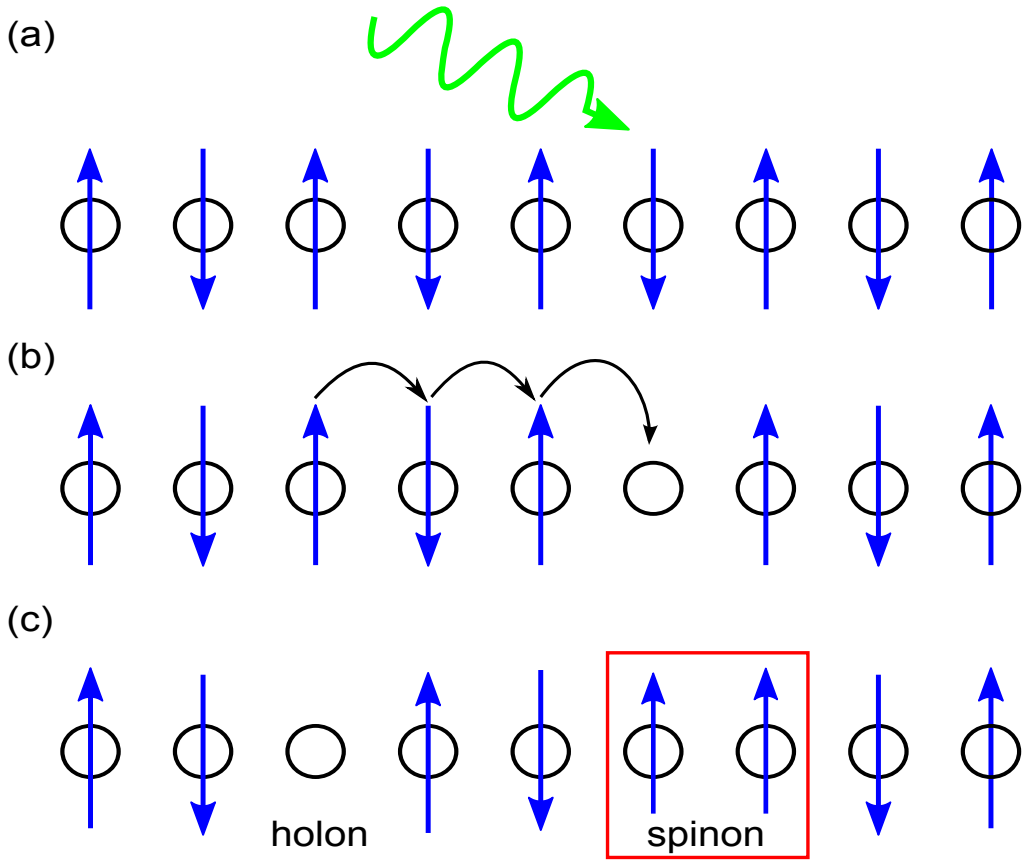

Figure 2.4.: *Cartoon to visualize spin-charge separation in case of a 1D t-J-model: (a) A chain of electrons (half filling, i.e. one electron per lattice site) ordered anti-ferromagnetically is excited, e.g. by ARPES, where one electron is removed. (b) The remaining hole can now be filled by neighboring electrons switching their positions. (c) A pair of spins (spinon in red) with the same orientation is now located at the former position of the hole, while the hole moves to the left (holon = moving site with electron vacancy) [55].*

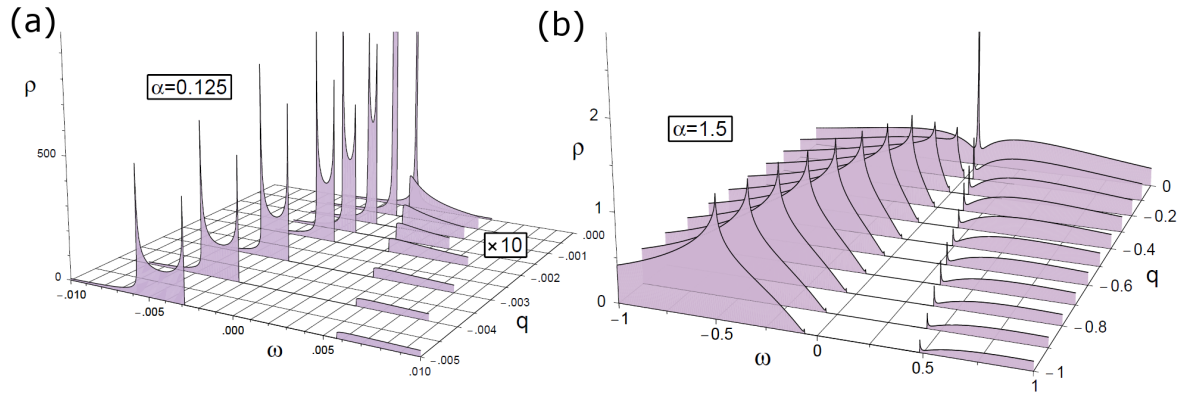

Figure 2.5.: *Momentum-resolved spectral function calculated for two different exponents: (a) In case of weak/short-range interaction ($K_\rho = 0.5$ results in $\alpha = 0.125$) two distinct spectral features are visible with the high energy peak being the holon and the branch close to E_F being the spinon. (b) For strong/long-range interaction ($K_\rho = 1/8$ causes $\alpha = 1.5$) the spinon is smeared out to an edge leaving only the holon peak. Reprinted from [56], Copyright (2013), with permission from Elsevier.*

The single-particle spectral function $\rho(k, E)$ can be approximated close to its singularities according to [56]:

$$\begin{aligned}
&\sim |E|^{\alpha-1}, (k=0) && (2.15)\\
&\sim \Theta(E-\nu_\sigma k)(E-\nu_\sigma k)^{\alpha-1/2}, (E \approx \nu_\sigma k) && (2.16)\\
&\sim |E-\nu_\rho k|^{(\alpha-1)/2}, (E \approx \nu_\rho k) && (2.17)\\
&\sim \Theta(-E-\nu_\rho k)(-E-\nu_\rho k)^{\alpha/2}, (E \approx -\nu_\rho k) && (2.18)
\end{aligned}$$

, where it takes the form of a power-law with the TLL exponent α combined with the Heaviside step function which is denoted by a Θ. In case of translation invariance α generally can be expressed through the stiffness coefficients K_ρ and K_σ:

$$\begin{aligned}
\alpha_{bulk} &= \frac{1}{4}(K_\rho + K_\rho^{-1} + K_\sigma + K_\sigma^{-1} - 4) && (2.19)\\
&\overset{K_\sigma=0}{=} \frac{1}{4}(K_\rho + K_\rho^{-1} - 2). && (2.20)
\end{aligned}$$

The latter applies for the spinless case where $K_\sigma = 1$. For open boundary conditions α, now denoted with an OB, accounts in the spinless case to [57]:

$$\alpha_{OB} = \frac{1}{2}(K_\rho^{-1} - 1). \tag{2.21}$$

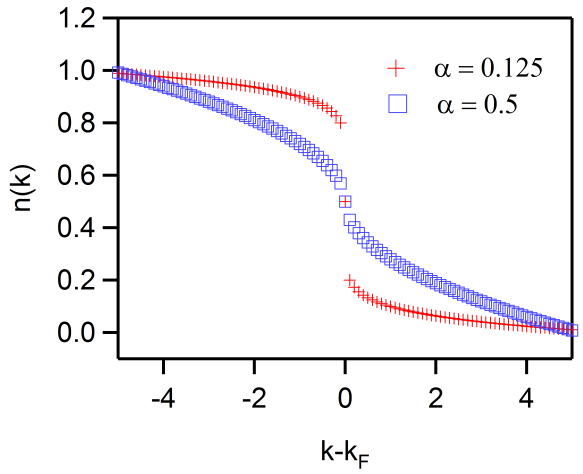

Figure 2.6.: *Momentum distribution according to eq. 2.24 for weak/short-range interactions ($K_\rho = 1/2$) $\alpha = \frac{1}{8}$ (red crosses) and for strong/long-range interaction $K_\rho = 1/8$, i.e. $\alpha = \frac{1}{2}$ (blue squares).*

Both situations will be of importance when dealing with finite chains of atoms as experimentally realized in this thesis by putting metal atoms on a semiconductor surface. By k-integration one obtains the density of states $\rho(E)$ in the limit of $T = 0$ K showing an asymptotic power-law behavior according to:

$$\rho(E) \propto |E|^{\alpha}, \tag{2.22}$$

which will be an important finger print to identify a TLL system in experiments. The more precise equation including the temperature denotes to [58]:

$$\rho(E,T) \sim AT^{\alpha} \cosh\left(\gamma \frac{E}{2k_b T}\right) \left|\Gamma\left(\frac{1+\alpha}{2} + \gamma \frac{iE}{2\pi k_B T}\right)\right|, \tag{2.23}$$

where $\Gamma(x)$ is the Gamma-function, while γ and A are constants. Note that the scaling is dominated solely by the ratio of temperature T and energy E [59]. If the k-resolved spectral function is only integrated for $k < 0$ one gets n(k), which takes the form:

$$\langle n_{k,+} \rangle \sim \frac{1}{2} - |k - k_F|^{\alpha} \, sign(k_F - k), \tag{2.24}$$

for $k << k_F$ [56, 59, 60]. The momentum distribution has no discontinuity at k_F like in the Fermi liquid, i.e. no quasi-particles, but a continuous power-law variation, see Fig. 2.6.

2.1.4. Theoretical treatment of TLL - Bosonization

To understand the origin or rather the essence of the Luttinger parameters $v_{\rho,\sigma}$ and $K_{\rho,\sigma}$ one has to get a glimpse of bosonization. The starting point is the fermionic, non-interacting many-particle Hamiltonian in 3D written in second quantization:

$$H_0 = \sum_{k,\sigma} \epsilon(k) c^\dagger_{k,\sigma} c_{k,\sigma}, \tag{2.25}$$

with the fermionic creation (annihilation) operator $c^\dagger_{k,\sigma}$ ($c_{k,\sigma}$) with spin index $\sigma = \uparrow, \downarrow$ and the well known quadratic energy dispersion relation $\epsilon(k) = \hbar^2 k^2 / 2m$, see Fig. 2.7(a). The corresponding spectrum for particle-hole excitations displayed in Fig. 2.7(b) allows a continuum of excitations with momentum $k < 2k_F$ and arbitrary low energy E. Changing the dimensionality to 1D, the reduced k-space of $\pm k_F$ limits the momentum transfer to $q \sim 0$ or $q = 2k_F$, as sketched in Fig. 2.7(c) and its excitation spectrum in (d).

For low-energy excitations close to the Fermi level one approximates the dispersion to be linear as shown in Fig. 2.8(a). Tomonaga first introduced a band cut-off in momentum as sketched in Fig. 2.8(b) and the concept of left(right) movers for each branch. The

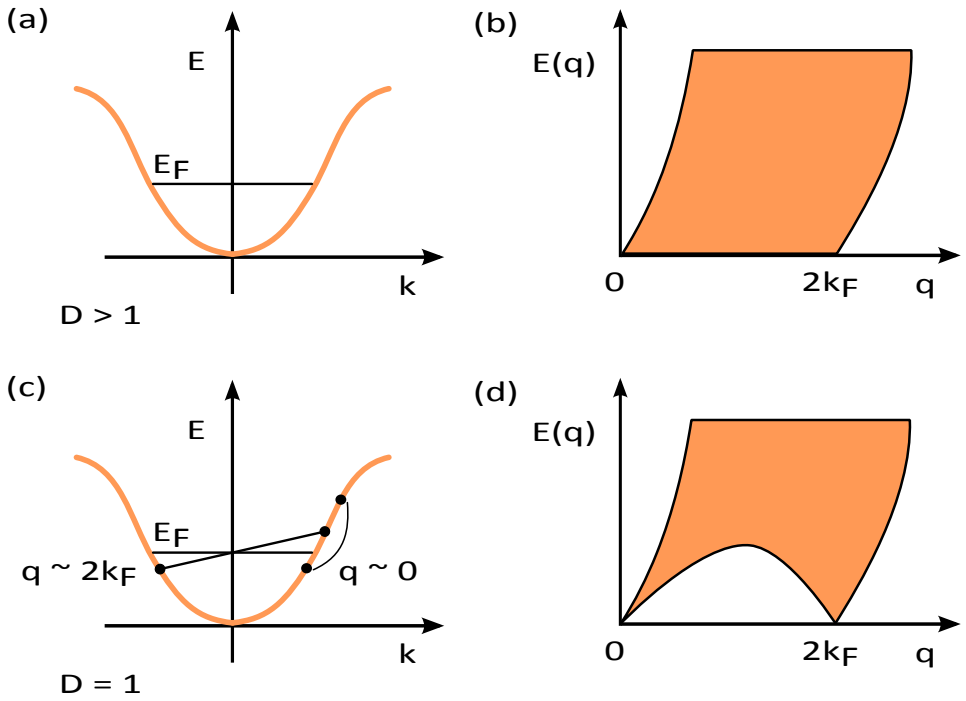

Figure 2.7.: *(a) Quadratic energy dispersion for $D > 1$ with Fermi energy E_F. (b) Corresponding particle-hole excitation spectrum. A continuum of excitations is formed with momentum $q \leq 2k_F$. (c) and (d) counterparts for $D = 1$. The Fermi surface allows only scattering with momentum transfer of $q \sim 0$ or $2k_F$, resulting in a forbidden regime for low energies in the particle-hole spectrum [48].*

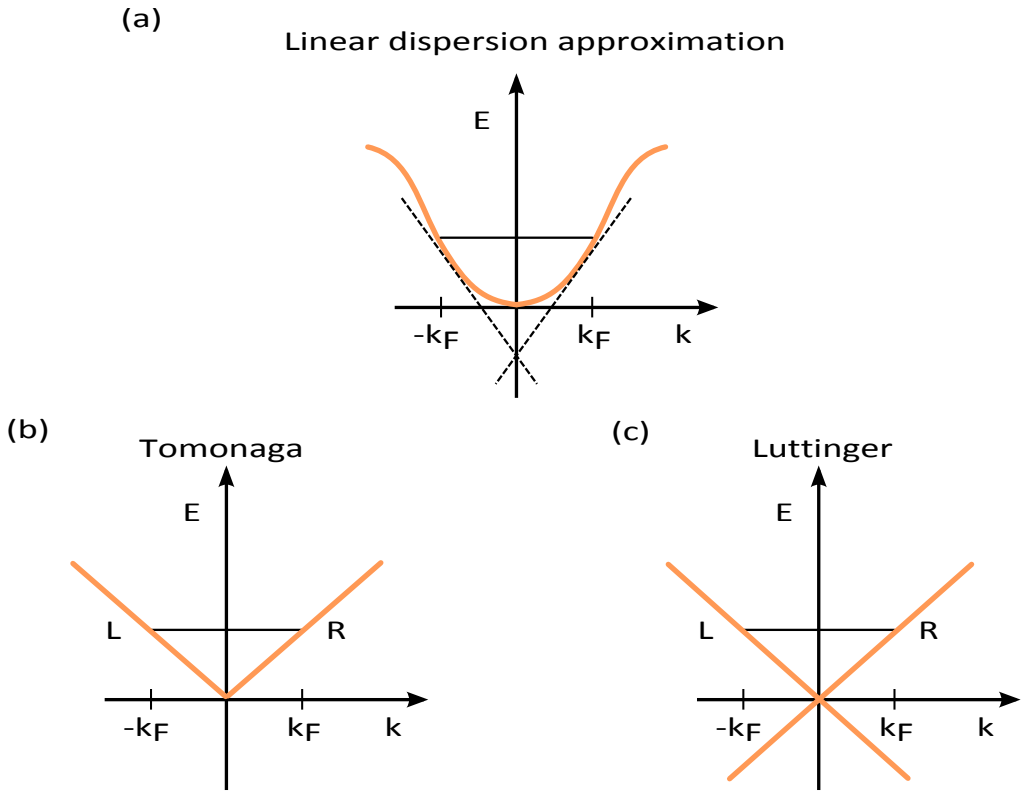

Figure 2.8.: *(a) Linear approximation of the quadratic energy dispersion of free electrons. (b) In the Tomonaga model [37] the linearization is limited with a band cut-off in momentum, while in Luttinger [38] introduced an extension to $-\infty$ as depicted in (c) [61].*

linear dispersion was afterwards extended to $-\infty$ by Luttinger, Fig. 2.8(c). Within this concept the Hamiltonian can still be written with fermionic operators which are now classified for left movers $c^{\dagger}_{+,k}$ for $k \geq 0$ and right movers $c^{\dagger}_{-,k}$ for $k < 0$. The Hamiltonian then becomes [48]:

$$H_0 = \sum_{\pm,k} v_F(\pm k - k_F) c^{\dagger}_{\pm,k} c_{\pm,k} - \Theta(k_F - \pm k). \tag{2.26}$$

In short, bosonization now implies that one can exchange the fermionic operators by bosonic ones if the particle-hole excitations are gapless in both spin and charge channel. In the non-interacting case this leads to an Hamiltonian consisting only of kinetic energy [39, 62, 63]:

$$H = v_F \sum_{q \neq 0} |q| b^{\dagger}_q b_q + \frac{\pi}{2L} \left(v_F (N - N_0)^2 + v_F J^2 \right), \tag{2.27}$$

with the bosonic creation/annihilation operators $b_q^\dagger$ (b_q), the particle number operator $N = N_0 + \sum_\pm N_\pm$ and the particle current $J = \sum_\pm \pm N_\pm$. Alternatively, one can also express the Hamiltonian in phase field variables (for details see Haldane [39]).

Introducing interactions gives four different scattering channels, called g-ology [64], as sketched in Fig. 2.9:

(a) Forward scattering on different branches. Two particles from left and right branch couple to each other, but stay on their own branch involving momentum transfer $q \sim 0$. The corresponding coupling constant is labeled g_2.

(b) Forward scattering on the same branch. Both coupled particles originate from the same branch. The momentum transfer is $g \sim 0$ with the coupling constant g_4.

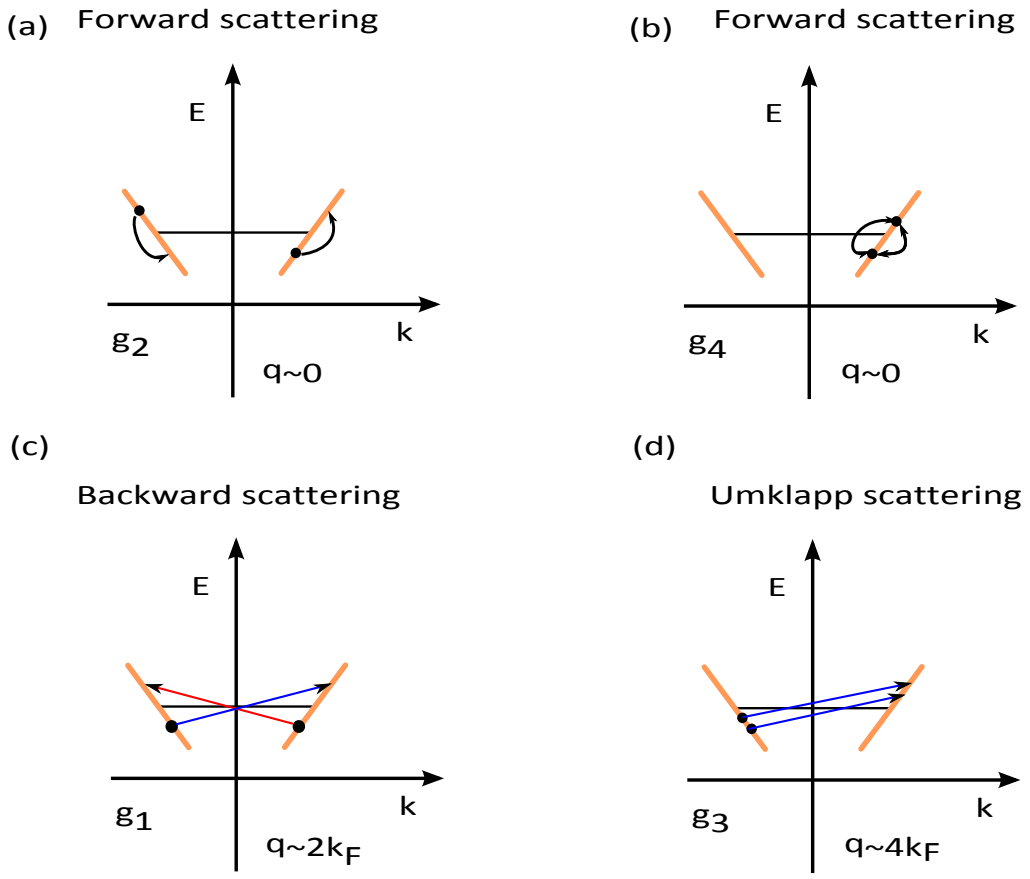

Figure 2.9.: *Possible interactions caused by reduced k-space in 1D. Forward scattering without momentum transfer ($q \sim 0$) on different (a) and same (b) branches with coupling constants g_2 and g_4 respectively. (c) Backward scattering by $q \sim 2k_F$. Two particles with opposite spin change their branch and break local spin conservation (coupling constant g_1). (d) Umklapp scattering with momentum $q \sim 4k_F$ and coupling constant g_3 [48].*

(c) Backward scattering with momentum $q \sim 2k_F$ (coupling constant g_1) where two particles switch branches (direction of motion) but not their spins.

(d) Umklapp scattering. Appears when two particles on the same branch with opposite spin orientation switch to the other branch. This process requires half-filling and momentum transfer $q \sim 4k_F$ (constant g_3).

In case of spinless particles only forward scattering occurs which is accounted for by the coupling constants g_2 and g_4. At this point one can define new coupling constants K_ν and v_ν for $\nu = \rho, \sigma$ according to [48, 54, 63]:

$$K_\nu \equiv \sqrt{\frac{2\pi v_F + g_{4\nu} - g_{2\nu}}{2\pi v_F + g_{4\nu} + g_{2\nu}}} \tag{2.28}$$

$$v_\nu \equiv v_F \sqrt{\left(1 + \frac{g_{4\nu}}{2\pi v_F}\right)^2 - \left(\frac{g_{2\nu}}{2\pi v_F}\right)}. \tag{2.29}$$

A TLL is formed only if both spin and charge channels are gapless. Here, electron-electron interaction causes $v_{spin} \neq v_{charge} \neq v_{Fermi}$ resulting in *spin-charge separation*. Nevertheless, spin and charge channel can individually open up a gap: in case of a charge gap a Mott-Hubbard insulator is formed, while for a spin gap the conducting system is comprised of charge density wave or superconducting correlations. A gap in both channels leads to a bandgap insulator.

Comparison of the individual velocities with the non-interacting case v_ν determines the correlation exponent K_ν, which only depends on the low-energy properties of the Hamiltonian. The TLL system then can be completely described with two parameters v_ν and K_ν per degree of freedom (i.e. spin and charge).

Theoretical studies on the 1D Hubbard and related models [48, 60] have shown that:

(i) $K_\rho = 1$ represents free electrons, while for spin-rotation invariance K_σ=1 is required,

(ii) $K_\rho > 1$ applies for attractive and

(iii) $K_\rho < 1$ for repulsive interactions.

The 1D Hubbard model represents a special case where K_ρ decreases from 1 to 1/2 when the electron repulsion U is increased from zero to infinity. In the repulsive regime, K_ρ decreases as the interaction range is increased going to zero for an infinite interaction range. In the presence of repulsive interactions $\mathrm{v}_\sigma \leq v_F$ (vice versa for v_ρ) applies, where the size of v_σ is a measure for the interaction range. Both the v_ν and K_ν can be decreased by additional electron-phonon interactions.

2.1.5. Extensions to the TLL model

The Tomonaga-Luttinger model described above uses a lot of approximations for which extensions have been brought forward mostly on theoretical grounds. These include:

Nonlinearity of the dispersion relation

The spectral function derived from the Tomonaga-Luttinger model is only asymptotically exact in the low-energy limit around the two Fermi points, where the dispersion relation is linearized. The long-distance asymptotic behavior of the correlation functions turns out to be correct since the band curvature in the Hamiltonians are formally irrelevant [39, 65]. One possibility to account for a nonlinearity is to add higher orders than the linear order in k to the dispersion relation, which is now denoted by $\xi(k)$ for right (R) and left (L) moving holes/particles:

$$\xi(k)^{R/L} = \pm v\tilde{k} + \frac{\tilde{k}^2}{2m} + ..., \tag{2.30}$$

and $\tilde{k} = k \mp k_F$ represents the momentum around the k_F values [39, 66]. The new quadratic term including the finite mass m can break the particle-hole symmetry of the TLL [66] and affect the momentum-resolved quantities, i.e. the k-resolved spectral function, by new power-law exponents [67]. The power-law asymptote for local properties, e.g. for the density of states at low-energies, are preserved [66, 67].

Multi band situations

The Tomonaga-Luttinger model relies on one single band with two Fermi crossings symmetrically located in momentum space (particle-hole symmetry). As will be shown later, Au/Ge(001) exhibits four branches, which can also be accounted for in bosonization [68, 69]. In this case even and odd pairs of charge and spin density bosons apply with corresponding K_ν and v_ν values. If only the even charge channel is different in K from the noninteracting value $K_\rho = 1$, i.e. $K_{\rho,even} = K_\rho \neq 1$, the same TLL power-law behavior is found for the local spectral function as a function of energy but with slightly modified exponents:

$$\alpha_{bulk} = \frac{1}{8}(K_\rho + K_\rho^{-1} + K_\sigma + K_\sigma^{-1} - 4), \tag{2.31}$$

$$\overset{K_\sigma=0}{=} \frac{1}{4}(K_\rho + K_\rho^{-1} - 2), \tag{2.32}$$

which is just half the values from eq. 2.20.

Spin-orbit interactions

Since Au/Ge(001) will contain a heavy Z atom in terms of gold, one may ask if spin-orbit interaction (Rashba-type) on the surface will play a role. The spin-orbit interaction can again be implemented in the bosonization [70], which results in two different Fermi velocities $v_F(1 \pm \xi)$ with ξ representing the strength of the SOI. As before, the spectral function keeps its power-law shape but with exponents [57]:

$$\alpha^{SOI} = \alpha_{bulk} - \frac{(K_\rho - 1)^2}{2(1 + K_\rho)}\xi + O(\xi^2), \tag{2.33}$$

$$\alpha^{SOI}_{Boundary} = \alpha_B + \frac{K_\rho - 1}{1 + K_\rho}\xi + O(\xi^2). \tag{2.34}$$

According to Ref. [57] the exponent α is only marginally affected by SOI interaction for realistic numbers of the velocities. The same applies for the k-resolved spectral function for SOI of realistic size.

Electron-phonon interactions

Voit and Schulz have investigated the influence of both electron-electron and electron-phonon interactions in one-dimensional metals [71]. They analyzed two limits for an incommensurate system, where Umklapp-scattering is neglected:

(i) Weak el-ph interaction with respect to the electronic Coulomb interaction and/or high phonon frequencies (comparable to the Fermi energy). Within this scenario the excitation channels are gapless, i.e. the system is described by the TL model.

(ii) Stronger el-ph interaction or likewise lower phonon frequencies. In this regime the attractive electron-phonon interaction by far exceeds the repulsive electron coupling. Thus, the spin-density excitation spectrum exhibits a finite gap, while the charge-density remains gapless for any nonzero phonon frequency. For details see Ref. [71].

The latter case, where a charge-density wave may occur, will be discussed in more detail in the following section.

2.2. In the presence of electron-phonon interaction - Peierls instability

In the previous chapter scattering processes were introduced to the TLL model which consider (strong) electron-electron interaction only. The alternative case considers distinct electron-phonon (el-ph) coupling while electron-electron interaction is vanishing or even missing. Under such conditions Peierls showed, that a 1D metal is unstable against a *periodic lattice distortion* (PLD) which causes an insulating ground state [72]. The applied model is based on a linear chain of atoms with a lattice periodicity a. Its charge density is constant along the chain in the undistorted state (ρ_0), while it is modulated in a cosinoidal fashion in the distorted state:

$$\rho(\mathbf{r}) = \rho_0(\mathbf{r})[1 + \rho_1 cos(\mathbf{q_0}\mathbf{r} + \phi)], \tag{2.35}$$

where ρ_1, $\mathbf{q_0}$ and ϕ represent the amplitude, wavevector and phase of the modulated electron density. The distortion term is called the *charge-density wave* (CDW) of wavelength $\lambda_0 = 2\pi/|\mathbf{q_0}|$. The ions of the underlying chain now move to new equilibrium positions due to the change in the electronic potential causing a PLD, see sketch in Fig. 2.10(a) [17, 31]. The amplitude of the PLD u_n can be expressed as a function of the integer position n of the ion in the chains as:

$$u_n = u_0 \sin(n|\mathbf{q_0}|a + \phi), \tag{2.36}$$

with the amplitude u_0 being small compared to the lattice constant a. The process is unchanged when first considering a PLD, which vice versa causes the CDW. Hence, both phenomena coexist and mutually depend on each other.

From an energetical point of view the CDW/PLD costs Coulomb and elastic energy which are overcompensated by lowering occupied electron states close to the Fermi energy. Unoccupied close to the Fermi level are lifted as well. A symmetric gap is formed and band backfolding appears as depicted in Fig. 2.10(b). This process is referred to as the *Peierls instability* or *Peierls transition*. Both features, the structural phase transition and the electronic transition from a metal to an insulating state appear simultaneously.

2.2.1. Mean-field approach

A simplified description of the Peierls transition to a CDW/PLD ground state is given by mean-field theory in the weak-coupling limit [17]. Within the approximation of independent electrons in the adiabatic limit (neglecting Coulomb and e-e interaction), the electron-lattice system can be modeled using creation (annihilation) operators for electrons (c) and phonons (p) as done by Fröhlich [73, 74]:

$$H = H_{el} + H_{ph} + H_{el-ph} \tag{2.37}$$

$$H = \sum_k \epsilon(k) c_k^\dagger c_k + \sum_q \hbar w_q p_q^\dagger p_q + \frac{1}{\sqrt{N}} \sum_{k,q} g_q c_{k+q}^\dagger c_k (p_{-q}^\dagger + p_q). \tag{2.38}$$

$\epsilon(k)$ denotes the tight-binding energy which is modeled by a cosine function $\epsilon(k) = -E_F cos(ka)$, g_q represents the el-ph coupling constant, w_p is the phonon frequency of the phonon normal mode q and N is the number of lattice sites per unit length. A

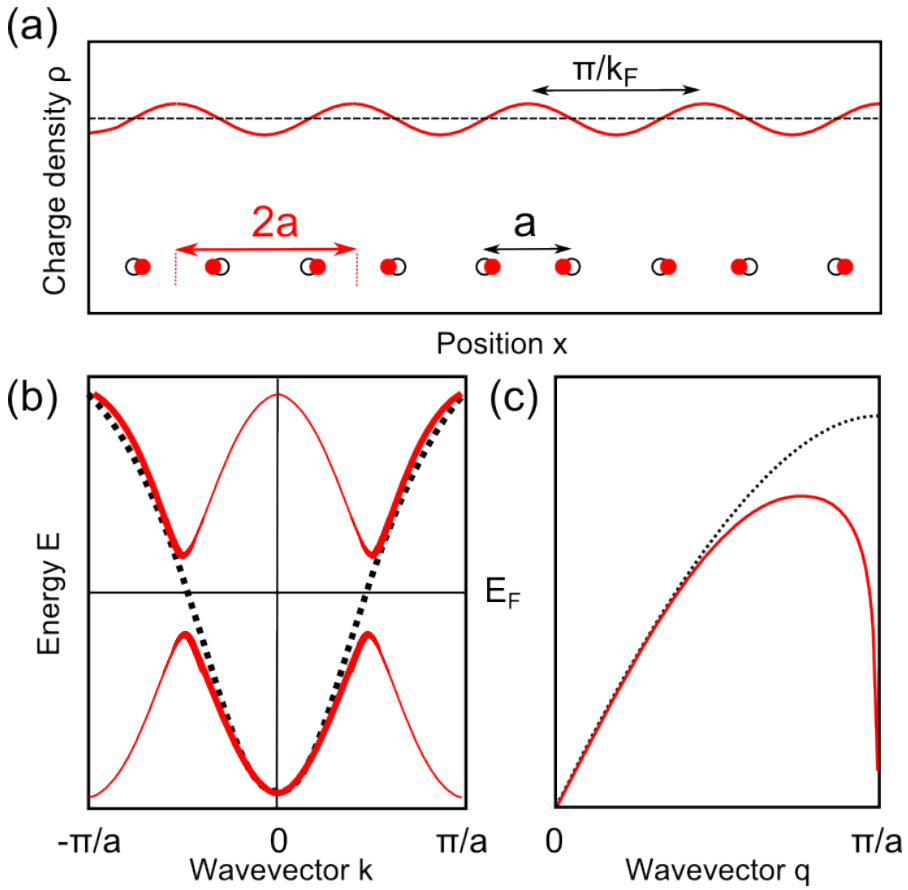

Figure 2.10.: *Peierls instability in 1D chain with a half-filled band. Undistorted properties are labeled by black dashed lines, the CDW state by red solid lines. (a) Constant charge density $\rho(x)$ for an undistorted chain of lattice constant a (open black circles) and cosinoidal modulation in the Peierls phase. The periodic lattice distortion (pairing of atoms) is displayed by red circles. (b) Parabolic band dispersion for 1D chain and corresponding DOS above the Peierls transition and in the CDW state (red lines, thickness proportional to spectral weight). (c) Phonon dispersion in 1D (acoustic only) well above (dashed) and at the transition temperature T_0 (solid red). After [31].*

condition for the stability of a CDW/PLD can be derived from the involved energies. The lattice strain energy is given by [31]:

$$\delta E_{lattice} = \frac{1}{2} M w_q^2 u_q^2, \tag{2.39}$$

with lattice displacement u_q and the ionic mass M. The total band energy can be expressed with the induced potential $v_q = g_q u_q \sqrt{\frac{2Mw_q}{\hbar}}$ in second order perturbation theory:

$$\delta E_{band} = -|v_q|^2 \chi_0(q). \tag{2.40}$$

χ_0 represents the non-interacting electron susceptibility

$$\chi_0 = \frac{1}{L} \sum_k \frac{f_{k+q} - f_k}{\epsilon_k - \epsilon_{k+q}} > 0, \tag{2.41}$$

which depends on the Fermi function f_k and the length of the atomic chain L. The CDW/PLD is now stable, if $\delta E_{lattice} + \delta E_{band} < 0$ for a certain phonon mode q_0. Putting equations 2.39 and 2.40 together yields the stability condition:

$$\frac{4g_q^2}{\hbar w_q} > \frac{1}{\chi_0(q)}. \tag{2.42}$$

This condition can be extended by including Coulomb (U_q) and exchange interactions (V_q) according to Chan and Heine [75]:

$$\frac{4g_q^2}{\hbar w_q} - 2U_q + V_q \geq \frac{1}{\chi_0(q)}, \tag{2.43}$$

where $\frac{4g_q^2}{\hbar w_q} > 2U_q > V_q > 0$ applies. Equation 2.42 and 2.43 tell us that a Peierls transition requires:

- strong electron-phonon interaction (large g_q)
- strong exchange interaction (large V_q)
- large non-interacting susceptibility $\chi_o(q)$
- weak Coulomb interaction (small U_q)
- small phonon frequencies w_q.

2.2.2. Nesting and the role of the Fermi surface contour

When electron-electron interactions are neglected ($U_q = V_q = 0$) the susceptibility becomes:

$$\chi_0(2k_F, T) = \frac{1}{2}\rho(E_F) ln \left(\frac{2.28E_F}{k_B T}\right) \tag{2.44}$$

at $q = 2k_F$ and diverges for $T \to 0$ and large $\epsilon_F/k_B T$. The divergence of the susceptibility is related to the Fermi surface topology. In 1D a large number of empty and occupied states can be linked at the Fermi level by the very same wave vector $q = 2k_F$. This *nesting* within the Fermi surface is strongly reduced in 2D, but can be conserved in the quasi-1D case. Here, a cosinoidal warping allows diagonal nesting in parts of the Fermi surface. The individual scenarios are sketched in Fig. 2.11.

This causes a renormalization (denoted with a $\tilde{w}$) of the phonon frequencies (see Fig. 2.10(c)) according to

$$\tilde{w}_q = w_q^2 \left(1 - \frac{4g_q^2}{\hbar w_q}\chi_0(g)\right), \tag{2.45}$$

which is also known as the *Kohn anomaly*.

From equation 2.45 one can derive an expression for the CDW transition temperature T_0 by setting the renormalization term (brackets) to zero. With the dimensionless electron-phonon constant λ this yields

$$k_B T_0 = 2.28 E_F exp(-\frac{1}{\lambda}). \tag{2.46}$$

The corresponding phonon momentum q_0 is directly related to the band filling, i.e. $\lambda_{CDW} = 2\pi/|q_0| = \pi/|k_F|$. This leads for an arbitrary band filling to an incommensurate

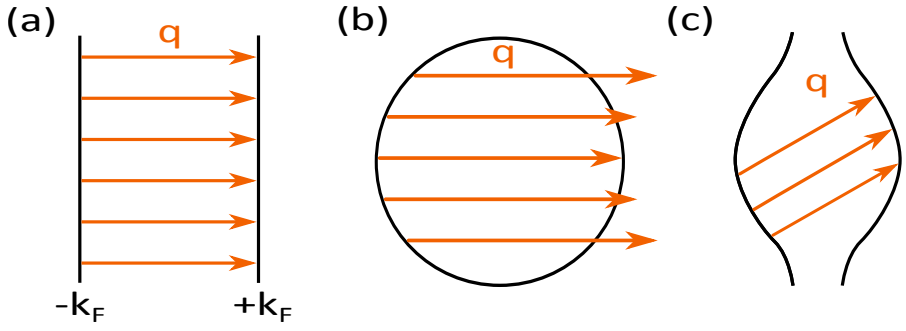

Figure 2.11.: *Nesting of empty and occupied states within the Fermi surface topology for (a) 1D, (b) 2D and (c) quasi-1D systems.*

superstructure, i.e. $\lambda_{CDW} \neq n \cdot a_0$ with $n \in \mathbb{N}$. In the commensurate scenario discussed here (half-band filling) the splitting of the energy dispersion follows:

$$E_{1,2}(k) = \frac{\epsilon_k + \epsilon_{k+q_0}}{2} \pm \sqrt{\left(\frac{\epsilon_k - \epsilon_{k+q_0}}{2}\right)^2 + \Delta^2}, \tag{2.47}$$

with an energy gap of 2Δ appearing at $q_0/2 = k_F$ between the lower (occupied) and upper (unoccupied) branch. At the same time the density of states $\rho(\epsilon)$ diverges at energies $E = \pm\Delta$ and is zero in the gap region. The size of the energy gap is characterized by the BCS (Bardeen-Cooper-Schrieffer) relation [31]:

$$2\Delta(T = 0) = 3.52 k_B T_0 \tag{2.48}$$

and collapses from $T = 0$ K towards the mean-field transition temperature T_0 as a function of $1/T^2$. The description presented so far suffers from its various approximations. These comprise missing fluctuations and the assumption of long-range order at finite temperature (a fact which can be saved by introducing some finite 2D coupling [17]). This is in contrast to entropy considerations, favoring the break up of long-range ordered segments into short-ranged ordered ones.

3. Experimental probes

Photoelectron spectroscopy is a well-established method for a direct access to the band structure of the occupied states. There exists a wealth of comprehensive books and review articles on this topic. Just to mention a few: the book "Photoelectron Spectroscopy" by Stefan Hüfner [76] and the review article by Andrea Damascelli [50]. Since this thesis is meant to elucidate the latest experimental results obtained by this method on Au/Ge(001), the following sections will only give a short overview of the technique with the main terms and equations later used for the data analysis. For a detailed description the reader is referred to the above mentioned references.

3.1. Photoelectron spectroscopy for electronic characterization

The main focus of this thesis is on the electronic structure of gold-induced chains on the germanium (001)-surface. Due to the strong lateral confinement by its unique atomic architecture one expects enhanced correlations of the conducting electrons compared to isotropic bulk materials. The method of choice for exploring the electronic states is photoelectron spectroscopy (PES) when measuring the momentum-dependent many-body spectral function A(E,$\mathbf{k}$) in the angle-resolved mode (ARPES). [1]

In terms of energy, light is able to release valance-electrons of binding energy E_B with kinetic energy E_{kin} from a solid, if the photon energy $h\nu$ exceeds the work function Φ of the sample, or, for higher energies, core-level electrons when using x-ray sources:

$$E_{kin} = h\nu - \Phi - |E_B|. \tag{3.1}$$

The technical process of incoming light extracting the electrons from the solid is displayed in Fig. 3.1(a). The electron energy distribution inside the solid of Fig. 3.1(b) experiences broadening due to the limited lifetime and finite energy resolution when mapped in the experiment. The energy reference in the experiment is determined by the vacuum energy of the sample, which is separated from the Fermi level by the work function Φ. Since photoelectron spectroscopy is restricted to occupied states only, the measured spectrum ends with a Fermi distribution.

[1] Note, that in the following all terms containing vectors like $\vec{k}$ are written in bolt letters instead of an top arrow.

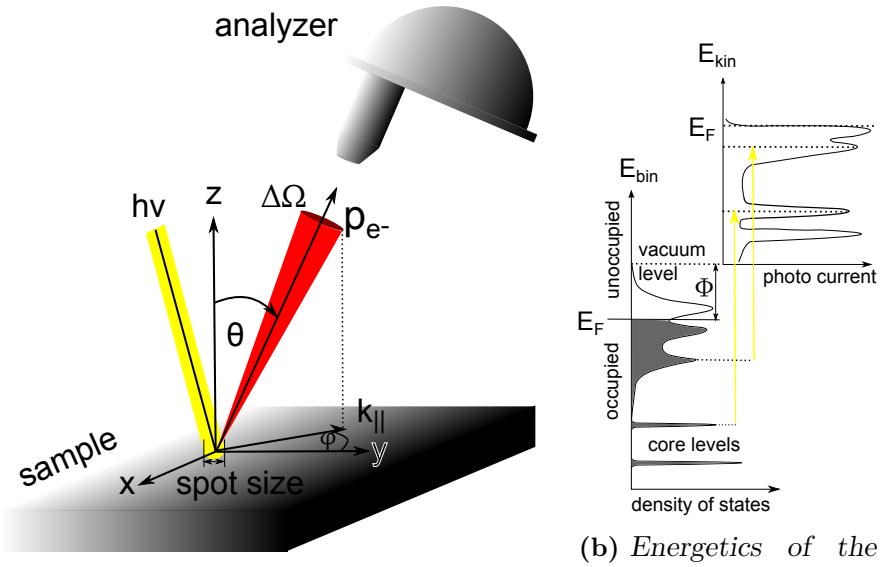

(a) *Typical geometry of the PES process.*

(b) *Energetics of the PES process.*

Figure 3.1.: *(a) The incoming light of energy $h\nu$ excites an photoelectron which is detected under the azimuth angle φ and the polar angle θ. The spot size is typically in the range of 100 μm [50, 76]. (b) Common view on the photoemission process in the single-particle picture in terms of energies. The difference between the Fermi energy E_F and the vacuum level E_{vac} is defined as the work function Φ. Changing into the reference system of the measured spectrum, one typically refers the energy to the binding energy within the sample. All structures are broadened due to the limited lifetime and energy resolution. The spectrum now exhibits a Fermi distribution at E_F.*

Although the term "Fermi energy" in a strict sense is only valid for the chemical potential $\mu(T)$ at $T = 0$ K, it will also be used throughout for finite temperatures as is common in the literature. Usual laboratory light sources are noble-gas discharge lamps for ultra-violet photoemission or x-ray guns commonly using Mg or Al anodes. Depending on the photon energies one differentiates between x-ray photoemission (XPS) and ultra-violet photoemission (UPS). XPS is extensively used for chemical analysis (stoichiometry), since the excited core-levels are element-specific. The energy ranges from hundreds of eV (soft x-rays) to several keV (up to hard x-rays). The excitation energy determines the probing depth d via the energy dependent inelastic mean-free-path λ. Bulk or surface sensitivity can be enhanced by variation of the escape angle θ:

$$d = 3 \cdot \lambda(E_{kin}) \cos(\theta). \tag{3.2}$$

The loss function of the inelastic mean free path is for low energies (around 50 eV) mainly determined by the plasmon frequency which itself depends on the electron density (roughly equal for all elements). Dominant processes below 50 eV are inter-band transitions whereas electron-electron scattering prevails for higher energies than 50 eV

[76]. These loss processes are assumed to be almost element independent, resulting in an universal curve for the inelastic mean free path λ plotted as a function of their kinetic energy, see Fig. 3.2. The graphs are generated among a rough estimate given by Shea and Dench who collected an extensive collection of various experimental data for inelastic mean free paths for four classes of materials: elements, inorganic compounds, organic compounds and adsorbed gases. Their fitting routine was based on the parameters A_n and B_n giving the equation [77]:

$$\lambda_{IMFP} = \frac{A_n}{E_{kin}^2} + B_n E_{kin}^{0.5}, \tag{3.3}$$

where the $\lambda \propto E^{-2}$ term at low energies represents the scattering probability of excited electrons. The $\lambda \propto E^{0.5}$ accounts for the losses due to plasmon excitation which itself mainly depends on the conduction band electron density [77]. The blue line in Fig. 3.2 denotes the inelastic mean free path for inorganic compounds ($A_{inorg} = 641$, $B_{inorg} = 0.096$), the red one represents pure elements ($A_{ele} = 143$, $B_{ele} = 0.054$, for more details see [77]).

A more precise Ansatz was made by Tanuma, Paul and Penn who proposed the TPP-2M equation [78]:

$$\lambda_{IMFP} = \frac{E_{kin}}{E_{plasmon}^2 \left[\beta \ln(\gamma E_{kin}) - (C/E_{kin}) + (D/E_{kin}^2)\right]}, \tag{3.4}$$

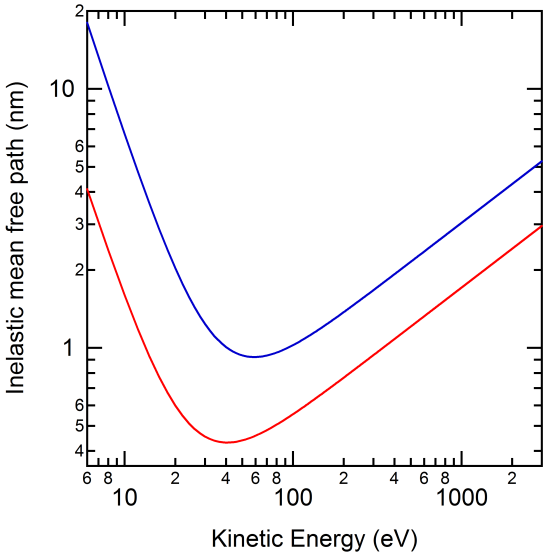

Figure 3.2.: *Inelastic mean free path of electrons as a function of their kinetic energy. In the range of 50 eV to 100 eV the escape depth accounts to ∼5 Å. Both curves were obtained from eq. 3.3 with the blue line representing inorganic compounds and the red line elements [77].*

with the kinetic energy of the electrons E_{kin}, the plasmon energy $E_{plasmon}$ and the material-specific constants β,γ, C and D which are related to the material density, atomic/molecular weight, number of valence electrons and the size of the band gap. The low escape depth of a few Angströms results in the need for clean and stable surfaces, which can only be achieved by ultra-high vacuum (UHV) conditions. Due to the high kinetic energies of the photoelectrons in XPS, the achieved energy resolution is limited roughly to hundred(s) of meV hindering any study of low energy excitations around the chemical potential. In addition, one cannot neglect the photon momentum for energies above 100 eV, which is essential for the calculation of the electron momentum in the solid. Thus, low photon energies in the ultra-violet (UPS) are used to map the valence electrons, especially the $E(\mathbf{k})$ dispersion of the band structure using angle-resolved photoemission (ARPES). Assuming that the photon adds only negligible momentum to the electron momentum, the conservation law yields $\mathbf{k}_i = \mathbf{k}_f$ for initial (i) and final (f) excited electron state. When passing the crystal surface towards vacuum the translation invariance is broken along the surface normal. Therefore, only the electron crystal momentum parallel to the surface $\hbar\mathbf{k}_{||}$ is conserved and can be related to [79]:

$$\mathbf{p}_{||} = \hbar\mathbf{k}_{||} = \sqrt{2mE_{kin}}\sin(\theta), \tag{3.5}$$

$$\mathbf{p_x} = \hbar\mathbf{k_x} = \sqrt{2mE_{kin}}\sin(\theta)\cos(\varphi), \tag{3.6}$$

$$\mathbf{p_y} = \hbar\mathbf{k_y} = \sqrt{2mE_{kin}}\sin(\theta)\sin(\varphi). \tag{3.7}$$

The geometry of the PES process is depicted in Fig. 3.1(a). For $\mathbf{k}_\perp$ one usually assumes a parabolic dispersion for the final state $E_f(\mathbf{k}_f)$ in a constant inner potential V_0 which results in [79]:

$$\mathbf{k}_\perp = \frac{\sqrt{2m_e}}{\hbar}\sqrt{E_{kin}\cos^2(\theta) + V_0}. \tag{3.8}$$

The inner potential V_0 is often approximated by the distance from E_F to the lowest occupied valance band [80]. Since the electron system under study will be of low dimensionality (dim$<$ 3D), the $k_\perp$ dispersion can be neglected. Hence, $E(\mathbf{k}_{||})$ is solely determined by $\mathbf{k}_{||}$. This allows mapping of not only the first but also higher Brillouin zones by variation of θ. To get the reduced zone scheme, one has to retract the reciprocal lattice vector $\mathbf{G}$ to end up in the first Brillouin zone.

Another advantage of using low energy photons is the increased energy and momentum resolution. For the latter applies

$$\Delta\mathbf{k}_{||} = \sqrt{2mE_{kin}/\hbar^2}\cdot\cos(\theta)\cdot\Delta\theta, \tag{3.9}$$

with $\Delta\theta$ representing the final acceptance angle or angular resolution of the spectrometer.

3.1.1. Theoretical description

For UPS, XPS and its inverse (IPES), the photoemission process is described by a transition from an initial to a final state. The transition probability w_{fi} can be written according to Fermi's golden rule from an initial state Ψ_i to a final state Ψ_f mediated via the dipole operator e$\mathbf{r}$ [76]:

$$w_{fi} \propto \int \Psi_{final}\ e\mathbf{r}\ \Psi_{initial}\ d^3r. \tag{3.10}$$

After irradiation all elements except for Hydrogen are positively charged and at the same time still contain electrons which will try to screen the photo hole inside the sample. This means the final state is affected by many body processes, which will be especially important for the analysis of the spectral function A(E,$\mathbf{k}$). Without these effects, a considered core-level photo hole energy will be independent of the k-vector due to its localized wave function. Thus, the core-level line width can be described by a Voigt curve which is a convolution of the instrumental width, i.e. the finite energy resolution (gaussian shape), and the width of the intrinsic life time of the core-hole state (Lorentzian shape). Taking interaction of the remaining photo-ionized system with the core-hole potential into account, satellites appear next to the main core-level at lower kinetic energy (higher binding energy). For metals with an (almost) infinite number of excitations, electron-hole pairs and plasmon excitations must be considered. The electron-hole pairs follow an inverse power-law for their creation probability. It diverges towards infinity for $\Delta \mathrm{E}_{ph} \rightarrow 0$ resulting in an asymmetric line shape while the plasmons induce intrinsic sidebands (satellites). The picture gets more complicated for the valence band (VB) where the created hole strongly depends on the k-vector due to its delocalization.

In more detail, w_{fi} must be written for an N-electron ground state Ψ_i^N and one possible final state Ψ_f^N as

$$w_{fi} = \frac{2\pi}{\hbar} \left| \left\langle \Psi_f^N | H_{int} | \Psi_i^N \right\rangle \right|^2 \delta(E_f^N - E_i^N - h\nu), \tag{3.11}$$

with the delta function representing the energy conservation. The corresponding energies for the initial and the final states are $E_i^N = E_i^{N-1} - E_B^k$ and $\mathrm{E}_f^{N-1}+\mathrm{E}_{kin}$. The photoelectron is described by its binding energy $\mathrm{E}_B^{\mathbf{k}}$, its kinetic energy E_{kin} and its momentum $\mathbf{k}$. H_{int} represents the perturbation Hamiltonian of the interaction with the photon [50]:

$$H_{int} = \frac{e}{2mc}(\mathbf{A}\cdot\mathbf{p} + \mathbf{p}\cdot\mathbf{A}) - e\Phi + \frac{e^2}{2mc}\mathbf{A}\cdot\mathbf{A}, \tag{3.12}$$

where $\mathbf{p}$ is the momentum operator of the electron and $\mathbf{A}$ is the electro-magnetic vector potential. With a gauge chosen to ϕ=0 with $\nabla\phi = -\mathbf{E}$, disregard of $\mathbf{A}\cdot\mathbf{A}$ (two photon processes) and the dipole approximation div$\mathbf{A} = \nabla\mathbf{A} = 0$ ($\mathbf{A}$ is supposed to be

constant on an atomic scale, valid in the ultraviolet), H_{int} is reduced to:

$$H_{int} = \frac{e}{mc}\mathbf{Ap}. \tag{3.13}$$

In case of non-negligible $\nabla\mathbf{A}$, the so-called *one-step model* must be applied, where the adsorption of the photon, the removal of the photoelectron and its detection are merged in one coherent process. In this complex picture, the crystal Hamiltonian must include bulk, surface and vacuum accounting for bulk-, surface- and evanescent-states as well as surface resonances, which is far from being convinient. Thus, the most frequently used description is the *three step model* [76], which includes:

(i) Optical excitation of the photoelectron in the bulk (electron adapts information of intrinsic electronic structure).

(ii) Ascent of the photoelectron to the sample surface (in-/elastic scattering processes).

(iii) Transition of the photoelectron into the vacuum (depending on kinetic energy and work function).

The process is depicted in Fig. 3.3. The total intensity is given as the product of the three independent processes. To account for the relaxation of the (N-1)-electron system the *sudden approximation* is applied, where the photoelectron instantaneously leaves

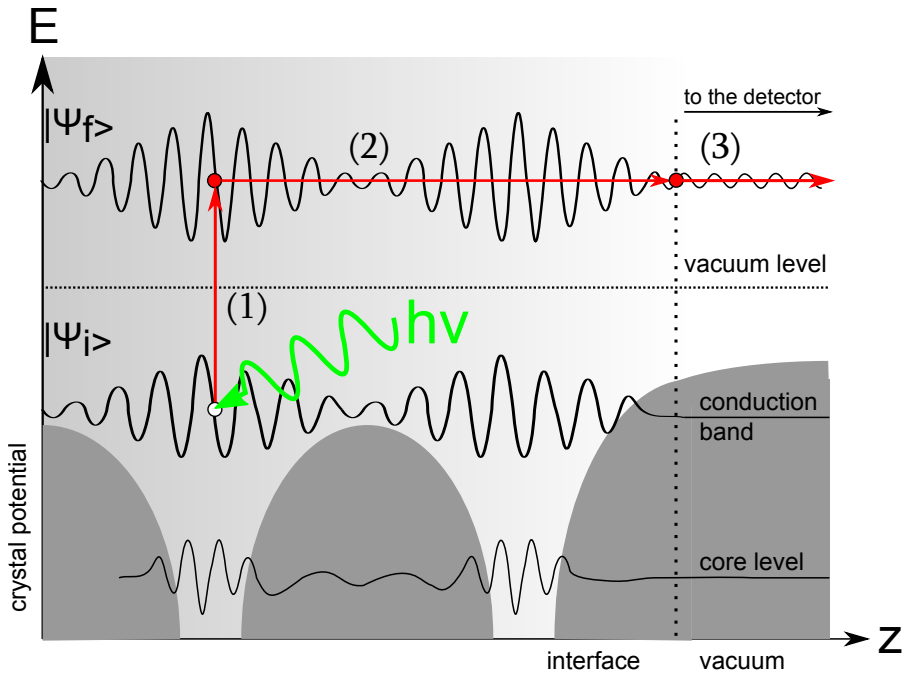

Figure 3.3.: *Three step model of the photoemission process. (1) Excitation of photoelectron. (2) Travel of the latter to the surface. (3) Transition into vacuum and travel to the detector.*

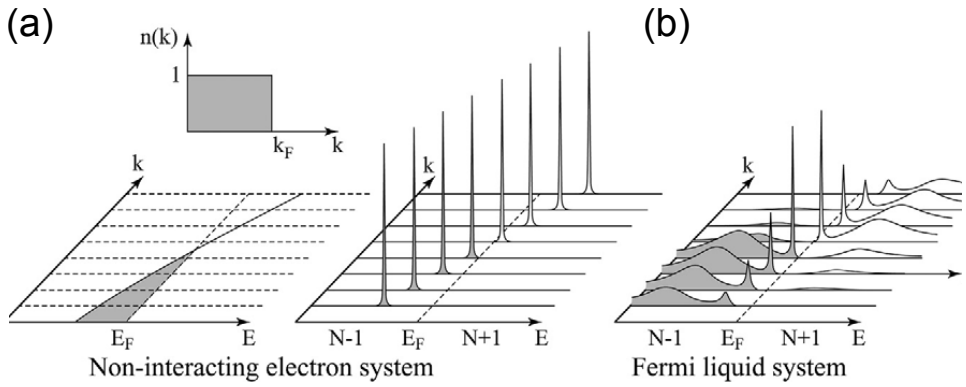

Figure 3.4.: *(a) Non-interacting electron system. The occupied states are shaded in grey with the single band energy dispersion crossing the Fermi energy. (b) The spectra of the non-interacting particles have the shape of a delta function. (c) For an interacting Fermi liquid the spectra are composed of a main line and several satellites due to the additional number of excited states. Figure reprinted with permission from A. Damascelli, Z. Hussain and Z.-X. Shen, Rev. Mod. Phys., Vol. 75, page 473, 2003 [50], http://link.aps.org/doi/10.1103/RevModPhys.75.473. Copyright (2012) by the American Physical Society.*

the solid without further interaction. In this respect, the N-particle final state Ψ_f^N is composed of the antisymmetric operator A multiplied by $\Phi_f^{\mathbf{k}}$, the wave function of the photoelectron with momentum $\mathbf{k}$ and Ψ_f^{N-1}, the final state of the $(N-1)$-system. The latter can be chosen as an excited state with an eigenfunction Ψ_m^{N-1} and energy E_m^{N-1}. For the total intensity probability one has to sum over all possible excited states m. The initial state is assumed to be a single Slater determinant such that it can be written as a product $\Psi_i^N{=}A\Phi_i^{\mathbf{k}}\Psi_i^{N-1}$. Since for Ψ_i^{N-1} one electron has to be annihilated by the annihilation operator $\mathrm{c}_{\mathbf{k}}$ of the N-particle state Ψ_i^N, one can write $\Psi_i^{N-1} = c_{\mathbf{k}}\Psi_i^N$. Now equation 3.11 can be re-written as [50]:

$$\left\langle \Psi_f^N \left| H_{int} \right| \Psi_i^N \right\rangle = \left\langle \Phi_f^{\mathbf{k}} \left| H_{int} \right| \Psi_i^{\mathbf{k}} \right\rangle \left\langle \Psi_m^{N-1} | \Psi_i^{N-1} \right\rangle, \tag{3.14}$$

where the first term represents the one-electron dipole matrix element $\mathrm{M}_{i,f}^{\mathbf{k}}$ and the second term the $(N-1)$-electron overlap integral. The measured quantity of the experiment, the total photoemission intensity $I(\mathbf{k}, E_{kin}) = \sum_{i,f} w_{i,f}$, is now proportional to

$$\propto \sum_{i,f} \left| M_{i,f}^{\mathbf{k}} \right|^2 \sum_m |c_{m,i}|^2 \, \delta(E_{kin} + E_m^{N-1} - E_i^N - h\nu), \tag{3.15}$$

with an electron removal from state i and leaving an $(N-1)$-electron system in the excited state m. The probability of this transition is now labeled $|c_{m,i}|^2$ which is equal to $\left| \left\langle \Psi_m^{N-1} | \Psi_i^{N-1} \right\rangle \right|^2$. In the special case of $\Psi_i^{N-1} = \Psi_{m_0}^{N-1}$ for $m = m_0$ the probability $|c_{m_0,i}|^2$

will turn unity and the remaining $|c_{m,i}|^2$ are zero. For a non-zero matrix element $M_{i,f}^{\mathbf{k}}$ the spectral shape will be a delta function at the Hartree-Fock orbital energy $E_B^{\mathbf{k}} = -\epsilon_{\mathbf{k}}$.

This will not be valid for strongly correlated systems, where the effective potential will be distorted by the removal of the electron. This causes an overlap of Ψ_i^{N-1} with many eigenstates Ψ_m^{N-1}, which appear as additional satellites to the main spectral line. Both scenarios are depicted in Fig. 3.4.

Influence of the photon energy

The optical transition in the PES process allows the selective enhancement of certain electronic states by varying the excitation energy. This is illustrated in Fig. 3.5, where wave functions of the harmonic oscillator are used (although a $1/r$ -potential is sketched for the solid). Here the cross-section is large for low kinetic energies of the photoelectron and states with low angular momentum. This comes from the fact that both low-kinetic final state and the low angular momentum initial state vary only little over the atomic volume which results in a large dipole matrix elmenent (vice versa for high-energy final states).

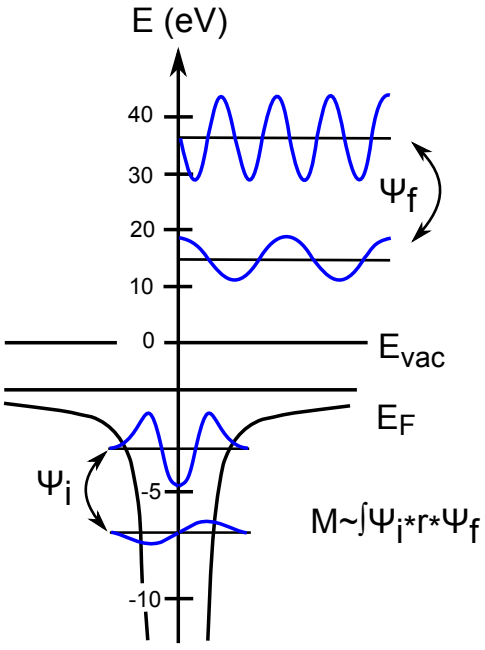

Figure 3.5.: *Schematic sketch of the photoexcitation for two different energies (20 eV and 40 eV). The transition matrix element depends on the angular momentum of the valence orbital and the excitation energy. Low angular momenta prefere low photon energies, while higher angular momenta have an higher overlap with final state wave functions at higher final state energies [76].*

3.1.2. Spectral function and Green's formalism

To describe the propagation of a single electron in a many body system, the most common approach is given by the time-ordered Green's function $G(t-t')$. It represents the probability amplitude of an added electron in the Bloch state with momentum $\mathbf{k}$ at $t=0$ to be in the same state after $|t-t'|$. By Fourier transformation, $G(\mathbf{k},E)$ can be composed by the one-electron removal and addition Green's function $G^{-}(\mathbf{k},E)$ and $G^{+}(\mathbf{k},E)$ [50]. The spectral function $A(\mathbf{k},E)$ is directly related to the imaginary part ($\Im$) of the Green's function [50] according to:

$$A(\mathbf{k},E) = -\frac{1}{\pi}\Im G(\mathbf{k},E). \tag{3.16}$$

$A(\mathbf{k},E)$ is also composed of a removal $A^{-}(\mathbf{k},E)$ and an addition $A^{+}(\mathbf{k},E)$ spectral function:

$$A^{\pm}(\mathbf{k},E) = \sum_{m} \left|\left\langle \Psi_m^{N\pm1}|c_{\mathbf{k}}^{\pm}|\Psi_i^{N}\right\rangle\right|^2 \delta(E-E_m^{N\pm1}+E_i^{N}), \tag{3.17}$$

which are both measurable quantities by PES and IPES. For PES one obtains:

$$I(\mathbf{k},E) = I_0(\mathbf{k},\nu,\mathbf{A})f(E)A(\mathbf{k},E), \tag{3.18}$$

with the electron energy E with respect to the Fermi level, $\mathrm{I}_0(\mathbf{k},\nu,\mathbf{A})$ is proportional to $\left|M_{i,f}^{\mathbf{k}}\right|^2$ and depends on the electron momentum $\mathbf{k}$ and on the energy $h\nu$ of the incoming light and its polarization (vector potential $\mathbf{A}$). Since PES measures only occupied states, the Fermi distribution $f(E) = (exp(^{E}/_{k_BT})+1)^{-1}$ has to be introduced. Here, one has to note that eq. 3.18 does not account for any extrinsic background or energy and resolution broadening.

Up to now the many-body processes, e.g. electron-electron interaction or coupling to phonons or magnons, are neglected. They can be introduced by correcting the Green's function by the self-energy $\Sigma(\mathbf{k},E)$ of the electrons [50]:

$$G(\mathbf{k},E) = \frac{1}{E-\epsilon_{\mathbf{k}}-\Sigma(\mathbf{k},E)}. \tag{3.19}$$

This influences the spectral function $A(\mathbf{k},E)$ such that:

$$A(\mathbf{k},E) = -\frac{1}{\pi}\frac{\Im\Sigma(\mathbf{k},E)}{\left[E-\epsilon_{\mathbf{k}}-\Re\Sigma(\mathbf{k},E)\right]^2+\left[\Im\Sigma(\mathbf{k},E)\right]^2}. \tag{3.20}$$

Its real part $\Re\Sigma(\mathbf{k},E)$ causes a renormalization of the bare electron band with energy $\epsilon_{\mathbf{k}}$ and momentum $\mathbf{k}$. The imaginary part $\Im\Sigma(\mathbf{k},E)$ represents the lifetime of the

photoelectron [50]. The self-energy thereby can be written as the sum of the individual contributions determining the intrinsic quasi-particle spectrum:

$$\Sigma(\mathbf{k}, E) = \Sigma^{el-el}(\mathbf{k}, E) + \Sigma^{el-ph}(\mathbf{k}, E) + \Sigma^{el-imp}(\mathbf{k}, E) + ... \tag{3.21}$$

Final state effects

The above mentioned assumptions were introduced to justify the description of the initial state properties of a system by the spectral function. The influence of the photoelectron final state on the photoemission spectrum can be illustrated comprehensively along the lifetime width [81]. For both photohole (initial state) and photoelectron (final state) a Lorentzian linewidth Γ_i and Γ_f are used. The resulting linewidth Γ_{res} denotes to

$$\Gamma_{res} = \frac{\Gamma_i/|v_{i_\perp}| + \Gamma_f/|v_{f_\perp}|}{|\frac{1}{v_{i_\perp}}(1 - \frac{m v_{i_{||}} \sin^2\theta}{\hbar k_{||}}) - \frac{1}{v_{f_\perp}}(1 - \frac{m v_{f_{||}} \sin^2\theta}{\hbar k_{||}})|}, \tag{3.22}$$

where the $\hbar v_{i_\perp} = \partial E_i / \partial k_\perp$ represent the group velocities [81]. An often considered limit is normal emission, where $\theta = 0$. Now assuming that $|v_{i_\perp}|$ is much smaller than all other group velocities, e.g. the dispersion of the initial state is almost flat, the linewidth at normal emission becomes

$$\Gamma_{res} = \Gamma_i + \left|\frac{v_{i_\perp}}{v_{f_\perp}}\right| \Gamma_f. \tag{3.23}$$

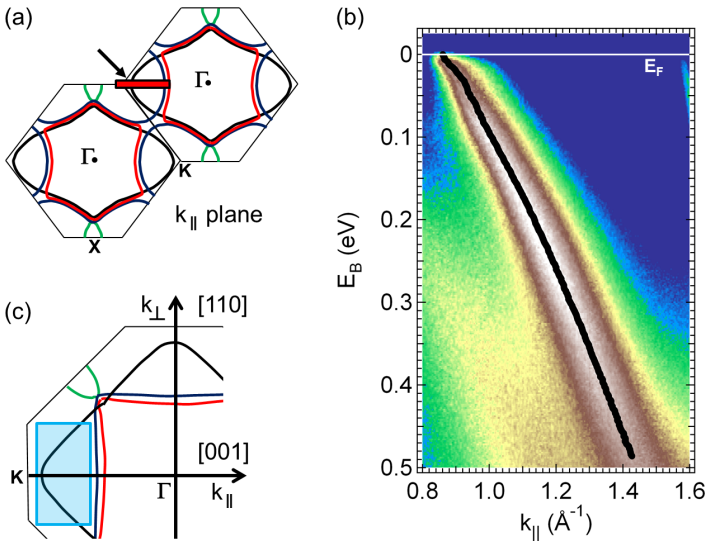

Figure 3.6.: *(a) Schematic Fermi surface of Ni(110) showing the symmetry plane along $k_{||}$. (b) APRES data ($h\nu = 100$ eV) for the minority spin band $\Sigma_{2\downarrow}$ along the $\Gamma - K$-line. (c) Fermi surface of Ni(110) based on a Gutzwiller calculation including $k_\perp$. From [2].*

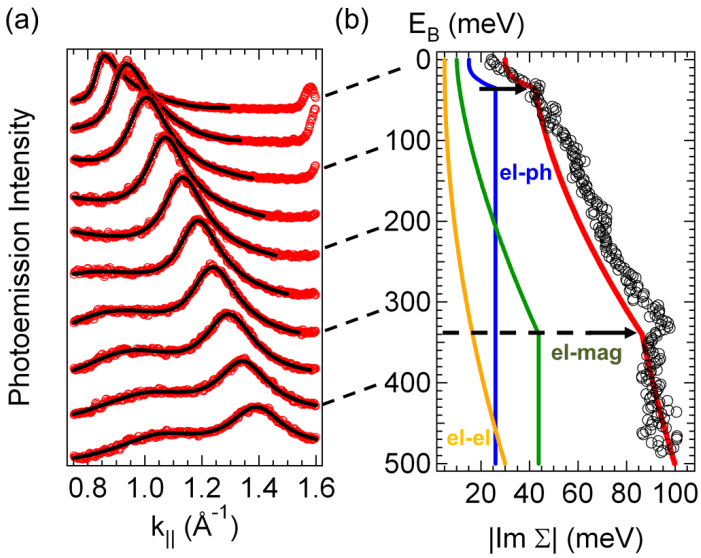

Figure 3.7.: *(a) MDC raw data (red) of Fig. 3.6(b) with corresponding fitting curves (black). (b) Imaginary part of the self-energy exhibiting two distinct features for electron-phonon (blue) and electron-magnon (green) interaction. From [2].*

Thus, for an ideal flat band with vanishing $v_{i\perp}$ the resulting linewidth Γ_{res} coincides with Γ_i, which is nothing else than the imaginary part of the photohole self-energy [81].

To illustrate the role of both self-energy and final state effects in the ARPES analysis, a brief example will be given by nickel (110) [2] in Fig. 3.6. Since Ni is ferromagnetic, the energy scale for the lattice and the magnetic quasi-particle excitation are separated by approximately one order of magnitude. To reduce the influence of the final states on the photoemission spectra, the photon energy is selected such that $k_\perp$ lies in a high symmetry plane where $v_{i\perp} = v_h = 0$, see Fig.3.6(a) and (c). The analyzed minority spin band $\Sigma_{2\downarrow}$ is located at the K-point shown in Fig. 3.6(b). The quasi-particle analysis is performed by fitting the peak position and the width of various momentum distribution curves (MDC) taken along the minority band $\Sigma_{2\downarrow}$ with an asymmetric Lorentzian. The raw MDC data including the fit curves are presented in Fig. 3.7(a). The extracted imaginary part of the self-energy in Fig. 3.7(b) has two pronounced shoulders at $E_B = 35$ meV and $E_B = 340$ meV. These two contributions can be assigned to the electron-phonon (blue curve at lower binding energy) and electron-magnon interaction (green curve at higher binding energies). For more details on Ni(110) see Ref. [2].

Photoemission setups

The experimental setups of the electronic structure factory (ESF) at beamline 7.0.1. Advanced Light Source (ALS), Berkeley USA, and the high-resolution PES (HRPES) endstation at the surface and interface spectroscopy (SIS) beamline of the Swiss Light Source, Villigen Switzerland, will be described in the appendix, see chapter 9.

3.2. Surface x-ray diffraction

The previous chapter introduced ARPES as a k-space technique which gives direct access to the band structure and therefore the single particle spectral function reflecting the (occupied) density of states. Thus, it is the method of choice to study correlated electron systems. Since the electronic effects are always determined by real space properties, like atomic or molecular bondings, there is a strong interest in the underlying structure. Applied methods, also exemplarily presented within this thesis, comprise mostly scanning probe techniques based on scanning tunneling microscopy (STM) [82] or atomic force microscopy (AFM) [83]. Both enable a sufficient spatial resolution on the atomic scale but do not allow chemical sensitivity. Low-energy electron diffraction (LEED) is also a common tool for structural analysis (S(pot)P(rofile)A(nalysis)-LEED, I-V-LEED). However, the strong interaction of the electrons with the sample requires a rather complicated "dynamical scattering theory" due to multiple scattering events [84]. An alternative approach is given by surface x-ray diffraction (SXRD) (comprehensive reviews are available by R. Feidenhans'l [85] and I.K. Robinson [86]). The x-rays only weakly interact with the sample (single scattering events), thereby allowing for the much simpler "kinematic scattering theory". Another advantage is the adjustable probing depth by varying the incidence angle. This also allows one to study subsurface layers or buried interfaces, as well as surface reconstructions below one monolayer [85]. One of the drawbacks of this technique is the exceedingly small scattering intensity which implies the need for synchrotron radiation to get sufficient count rates and signal-to-noise ratios. Another disadvantage lies within the nature of all scattering techniques, where the recorded intensities only represent the squared amplitude of the scattered waves while the phase information is lost.
This problem can be circumvented by model-refinement methods involving some input parameters, e.g. number of atoms per unit cell (coverage), to gain calculated intensities. These intensities can be compared with the experiment leading to an iterative process. Alternatively, "direct methods" have emerged which are based on generic *a priori* properties of the sample, like a positive electron density, and the measured intensities [87]. Phase retrieval thereby also includes iterative procedures to gain the electron density in real space.

3.2.1. Basics on Fourier transformation

Before illustrating the scattering theory within the kinematic approximation one has to recall some basic aspects of mathematical convolution. The convolution of two functions $f(x)$ and $g(x)$ is written:

$$(f \otimes g)(x) := \int_{-\infty}^{+\infty} f(x') \cdot g(x - x')dx'. \tag{3.24}$$

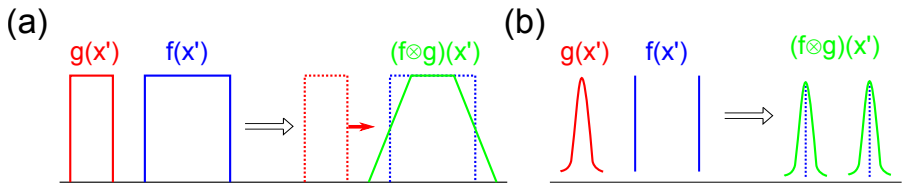

Figure 3.8.: *(a) The convolution of two rectangular functions f and g yields a trapezoid. (b) A Gaussian-like envelope convolved with two delta functions gives the envelope at the former positions of the delta functions.*

This expression can be expanded to the *Faltung theorem*, which states that the Fourier transform of a product of two functions f and g is equal to the convolution of the individual Fourier components of both functions:

$$F(f \cdot g) = F(f) \otimes F(g). \tag{3.25}$$

Two examples to visualize a Fourier transformation are given in Fig. 3.8. In (a) two standard rectangular functions yield a trapezoidal shape after convolution. The second example in Fig. 3.8(b) is an envelope function (e.g. of Gaussian shape) convolved with two delta peaks resulting in a doubling of this shape at the former positions of the two delta functions.

In terms of a scattering process two correlations between real space structure and diffraction pattern can be given. Having a charge distribution of finite width around each atom causes an intensity drop-off as depicted in Fig. 3.9(a), whereas a finite crystal size in (b) results in small oscillations around the diffraction peaks (fringes).

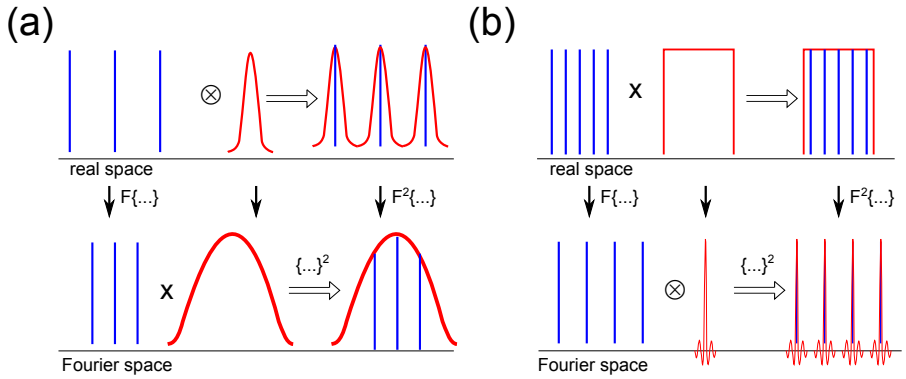

Figure 3.9.: *Real space structure and its impact on the diffraction pattern under Fourier transformation: (a) A finite electron distribution around each atom causes an intensity drop-off of the peaks. (b) Small oscillations around the diffraction peaks appear for a crystal of finite size.*

3.2.2. Kinematic theory

The kinematical approximation is based on the assumption that weak interaction of the x-rays (keV energy range) with matter leads to single scattering events of elastic type. Strictly speaking, this is only valid for grazing incidence, as will be the case in the experiment. Within Huygen's principle every electron/atom acts as a scattering center for the incoming wave. Constructive interference of all secondary waves leads to a Bragg peak. All wave vectors yielding such Bragg reflexes can be combined in what is called the *reciprocal lattice* of the crystal. Both, real space crystal lattice and reciprocal lattice, are directly connected via Fourier transformation. For a unit cell with lattice vectors $\mathbf{a}$, $\mathbf{b}$ and $\mathbf{c}$ the volume accounts to $V = \mathbf{a} \cdot (\mathbf{b} \times \mathbf{c})$. The reciprocal vectors follow [86]:

$$\mathbf{a}^* = 2\pi \frac{(\mathbf{b} \times \mathbf{c})}{V}, \tag{3.26}$$

where $\mathbf{b}^*$ and $\mathbf{c}^*$ result from permutation of $\mathbf{a}$, $\mathbf{b}$ and $\mathbf{c}$. The incoming x-ray wave (ideally monochromatic, labeled with i for initial) has a wave length of λ and momentum $\mathbf{k}_i$ with $|\mathbf{k}_i| = 2\pi/\lambda$. The scattered wave ($f$ for final wave) is denoted by $\mathbf{k}_f$ and is refracted under an angle of 2θ. The momentum transfer to the lattice accounts to $\mathbf{q} = \mathbf{k}_i - \mathbf{k}_f$.

Mathematically, the scattering process can be described using the Laue equations [86]:

$$\mathbf{q} \cdot \mathbf{a} = 2\pi h; \quad \mathbf{q} \cdot \mathbf{b} = 2\pi k; \quad \mathbf{q} \cdot \mathbf{c} = 2\pi l, \tag{3.27}$$

the Ewald-construction with vector

$$\mathbf{q} = h\mathbf{a}^* + k\mathbf{b}^* + l\mathbf{c}^* \tag{3.28}$$

and the Bragg condition

$$2d_{hkl} \ \sin\theta = n\lambda. \tag{3.29}$$

The Miller indices (h, k, l) are integer numbers and label the Bragg points in reciprocal space. d_{hkl} denotes the distance between lattice planes. In case of a cubic crystal d_{hkl} accounts to $a/\sqrt{h^2 + k^2 + l^2}$. n represents the order of the interference maximum (n $\in \mathbb{N}$). The process is visualized in Fig. 3.10: (a) the incoming x-ray is scattered in the direction of the detector in real space. The Laue equations for a finite crystal terminated by a surface lead to a continuous signal of the former Bragg points which takes the shape of rods. The scattering event in reciprocal space can than be understood by constructing the Ewald's sphere for the incoming x-ray wave. Intensity appears wherever the sphere hits one of these crystal truncation rods (CTRs). The complete schematic is displayed in Fig. 3.10(b).
The intensity I_{hkl} at the Bragg points is proportional to the complex structure factor

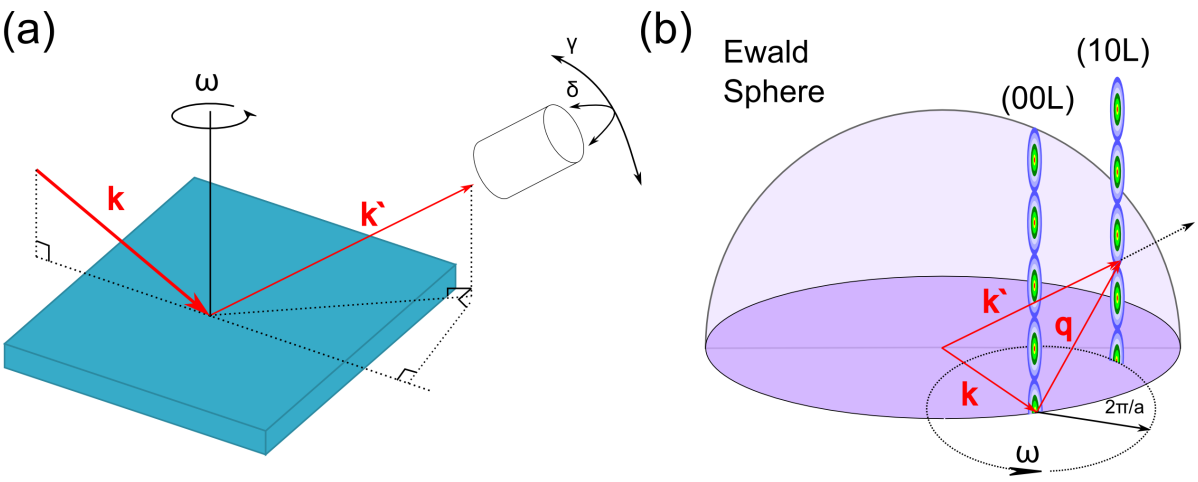

Figure 3.10.: *(a) Experimental configuration of SXRD in real space. (b) Cutting the crystal truncation rods (CTRs) with the Ewald's sphere in reciprocal space. After [88].*

$\propto |F_{hlk}|^2$, with the structure factor being the Fourier transform of the electron density $\rho(\mathbf{r})$ within one unit cell

$$F(\mathbf{q}) = \int_V \rho(\mathbf{r}) \exp(i\mathbf{q} \cdot \mathbf{r}) dV. \tag{3.30}$$

For mathematical reasons one can exchange the integral with the sum over all individual atoms i within the unit cell, which results in $F(\mathbf{q}) = \sum_i f_i(|\mathbf{q}|) exp(i\mathbf{q} \cdot \mathbf{r})$. The f_i denote the atomic form factors, i.e. the Fourier transform of the individual atoms' electron density.
Now adding a surface to the former infinite crystal means to break translational symmetry along the z-axis (surface normal). The corresponding Fourier transform along this axis can not longer be discrete, but causes the diffraction pattern to become continuous as a function of l. This process can be visualized by taking the infinite crystal and multiplying it with a step function in z-direction (idealized view of a surface), see Fig. 3.11.

The equivalent in reciprocal space is the product of the ideal diffraction pattern and a $1/q_z$ function, which smears out the Bragg peaks of the ideal diffraction pattern now taking the form of streaks perpendicular to the surface. If these streaks coincide on a line of Bragg reflexes, they overlap and form the continuous CTRs. Surface roughness, defects and dangling bonds all broaden the step function and at the same time narrow the $1/q_z$ function in reciprocal space. As a result, the intensity of the CTRs will fall off more rapidly around the Bragg reflexes.
Since the crystal is still infinite in the crystal plane, intensity will only occur at discrete values of h and k. Quantitatively, one has to sum over all lattice planes with the structure factor F($\mathbf{q}$) of one unit cell, vector $\mathbf{q} = h\mathbf{a}^* + k\mathbf{b}^* + l\mathbf{c}^*$ and the translation vector $\mathbf{r}_\nu$ between neighboring planes. The complete structure factor of the semi-infinite crystal

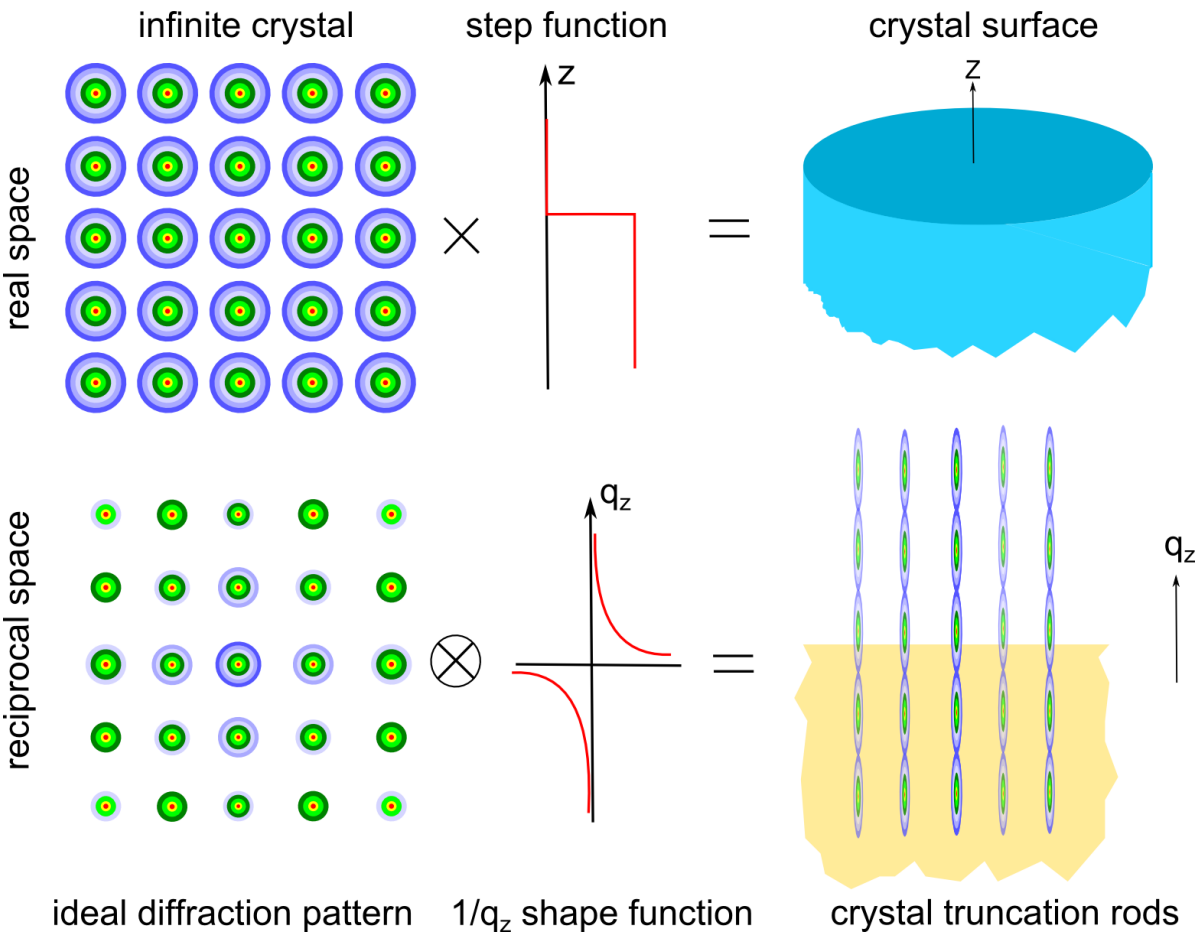

Figure 3.11.: *(a) Convolution of an infinite periodic crystal with a step function resembling the surface yields a semi-infinite crystal with a perfect surface. (b) In terms of reciprocal space the counterparts are the ideal diffraction pattern and a $1/q_z$ function which cause the appearance of the crystal truncation rods (CTRs). After [89].*

results from summing up all crystal planes:

$$F_{ctr}(\mathbf{q}) = F(\mathbf{q}) \sum_{n=0}^{\infty} \exp(-n\nu) \exp(in\mathbf{q} \cdot \mathbf{r}_\nu) = \frac{F(\mathbf{q})}{1 - \exp(-\nu) \exp(i\mathbf{q} \cdot \mathbf{r}_\nu)}. \tag{3.31}$$

The right hand side of the equation uses the limit of the geometric series according to $\sum_{n=0}^{N} q^n = (q^{N+1} - 1)/(q - 1) \overset{N\to\infty}{\to} 1/(1 - q)$. The exponential damping factor $\exp(-n\nu)$ is required to avoid a divergence of the denominator at the Bragg points, where $\mathbf{q}\cdot\mathbf{r}_\nu = 2\pi$. It is a function of the adsorption coefficient and the incidence angle and

can be calculated. For x-rays, ν is in the order of 10^{-4} and can be neglected beside the Bragg points. The phase φ of the structure factor is:

$$\varphi = arctan\left(\frac{\sin(\mathbf{q}\cdot\mathbf{r}_\nu)}{1-\cos(\mathbf{q}\cdot\mathbf{r}_\nu)}\right). \tag{3.32}$$

The intensity can be calculated to

$$I_{CTR}(\mathbf{q}) \propto |F_{CTR}(\mathbf{q})|^2 \overset{\nu\approx 0}{=} \frac{|F(\mathbf{q})|^2}{4\sin^2(\frac{1}{2}\mathbf{q}\cdot\mathbf{r}_\nu)}, \tag{3.33}$$

which results in a $\sin^2(\frac{1}{2}\mathbf{q}\cdot\mathbf{r}_\nu)$ modulation neglecting the $\mathbf{q}$ dependency of F($\mathbf{q}$).
Up to now the CTRs are caused by the surface *per se*. Considering a surface reconstruction with a unit cell that exceedes the one from the underlying substrate leads to additional *surface truncation rods* (STRs), whose intensity at discrete points (h,k) can be calculated in the same manner by

$$I_{STR}(\mathbf{q}) \propto |F_{STR}(\mathbf{q})|^2. \tag{3.34}$$

If all atoms in the surface unit cell lie at the same z-coordinate, the height distribution is a delta function. The Fourier transform of a delta function would be a constant structure factor (neglecting temperature). Typical surface reconstructions involve several re-arranged layers compared to the bulk periodicity. Due to the decreased number of atoms in the surface layer as compared to the bulk, the intensity of the STRs is orders of magnitude weaker than the CTRs.

3.2.3. Patterson Map

The Patterson function is defined as the Fourier transform of $|F_{hkl}|^2$:

$$P(\mathbf{r}) = \sum_{h,k,l} |F_{hkl}|^2 \exp(-i\mathbf{q}\cdot\mathbf{r}). \tag{3.35}$$

The identity of F_{hkl} from equation 3.30 leads to

$$P(\mathbf{r}) = \int_V \rho(\mathbf{r'})\rho(\mathbf{r}+\mathbf{r'}), \tag{3.36}$$

which means the Patterson map represents the autocorrelation function of the electron density. Using the Fourier series of the electron density ρ with the structure factors being the coefficients

$$\rho(x,y,z) \propto \sum_{h,k,l} F_{hkl}\exp(-2\pi(hx+ky+lz)), \tag{3.37}$$

one obtains

$$P(x,y,z) \propto \sum_{h,k,l} |F_{hkl}|^2 \cos(2\pi(hx+ky+lz)). \tag{3.38}$$

Additional information on the structure can be extracted from the projection of the Patterson map on the surface plane, where

$$\rho(x,y,z=0) = \rho(\mathbf{r})dr_z \propto \sum_{h,k,l} F_{hkl} \exp(-i2\pi(hx+ky)) \tag{3.39}$$

leads to

$$P(x,y) \propto \sum_{h,k,l=0} |F_{hkl}|^2 \cos(2\pi(hx+ky)). \tag{3.40}$$

As is obvious from this equation, only an in-plane data set of l close to zero instead of a full 3D scan is necessary to calculate $P(x,y)$. The dominating maxima of this projection correspond to interatomic distances within the unit cell, which do not yield direct coordinates but the length and the direction of the lattice vectors . The height of the Patterson peaks scales with the product of the electron densities of the contributing atoms. Thus, the largest peak will be at the origin, which is also the center of symmetry. These informations are often very helpful in creating starting models which can be further verified by measuring the CTRs and STRs.

Surface x-ray diffraction on the Ge(001)-c(4×2) reconstruction

Just to briefly document how powerful the Patterson map can be in the process of developing a structural model, the analysis of Ferrer and co-workers will be presented in the following [90].

They investigated the c(4×2)-reconstruction of plane Ge(001) with a miscut less than 0.1°. The sample was cooled down to 150 K to reach the c(4×2) symmetry. In-plane data were recorded for the lowest possible l of 0.1 for 46 nonequivalent reflexes of one of the two surface domains which are orthogonal to each other. The calculated Patterson map is displayed in Fig. 3.12. Using the five vectors A to E from the Patterson map, they derived a model with five different Ge atoms involved, see Fig. 3.13. From the out-of-plane reflexes they calculated the coordinates of the vertically relaxed form of the model, which is in line with other reports, e.g. STM and DFT calculations [91]. For more details see Ref. [90].

Material Science Beamline at the Swiss Light Source

The experimental setup of the Material Science beamline at the Swiss Light Source is depicted in the appendix 9.

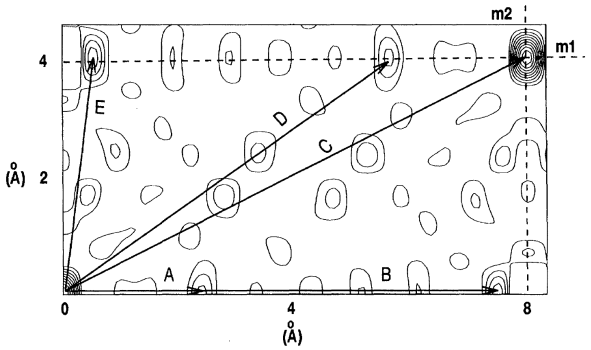

Figure 3.12.: *Contour plot of the Patterson map for Ge(001) by Ferrer et al. obtained from the lower temperature c(4×2)-phase of Ge(001). The highest maxima are connected from the origin by the vectors* **A** *to* **E** *within the projected unit cell. Figure reprinted with permission from S. Ferrer, X. Torrelles, V. H. Etgens, H. A. van der Vegt and P. Fajardo, Phys. Rev. Lett., Vol. 75, page 1771, 1995, http://link.aps.org/doi/10.1103/PhysRevLett.75.1771 [90]. Copyright (2012) by the American Physical Society.*

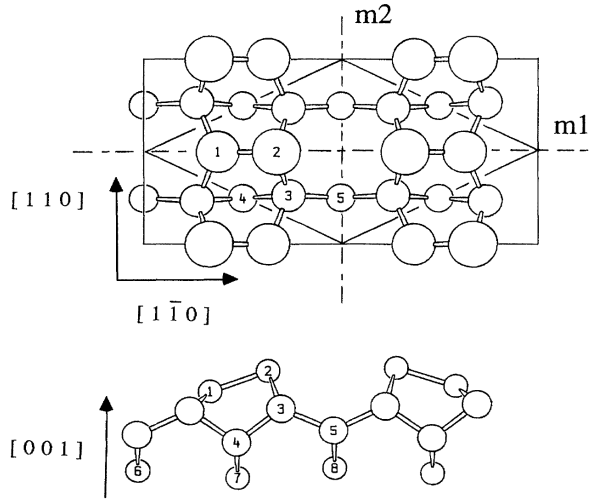

Figure 3.13.: *Top and side view of the structural model of the c(4×2)-reconstruction of Ge(001). The asymmetric top dimer is built by atom 1 and 2, while the two sublayers contain atoms 3, 4 and 5.* m_1 *and* m_2 *indicate the symmetry planes. Figure reprinted with permission from S. Ferrer, X. Torrelles, V. H. Etgens, H. A. van der Vegt and P. Fajardo, Phys. Rev. Lett., Vol. 75, page 1771, 1995, http://link.aps.org/doi/10.1103/PhysRevLett.75.1771 [90]. Copyright (2012) by the American Physical Society.*

4. Substrate - template for self-assembly

From a structural point of view silicon and germanium are very similar. Both crystallize in a diamond lattice, are semiconducting at room temperature and have an indirect bandgap. The unique property that makes silicon so dominant for device application, like in CMOS structures, is its stable oxide [92]. In contrast, germanium oxide is soluble by water, thus preventing a long-lasting lifetime of any devices [93]. Cutting silicon and germanium along the (001)-plane results in two dangling bonds per surface atom, see Fig. 4.1(a). To minimize the total free energy, these sp^3 dangling bonds de-hydridize into a surface normal (sp_x) and a parallel ($p_{y/z}$) component, as illustrated in Fig. 4.1(b).

The pairing of two nearest-neighbor surface atoms is achieved by σ-bonding along the [011] direction in Fig. 4.1(c). At this point additional energy can be gained by asymmetric buckling of one of these dimer atoms causing a doubling of the surface unit cell from a p(2×1) to a c(4×2) pattern [94]. The energy gain of this buckling is almost three times larger for germanium (0.3 eV/dimer) [95] than for silicon (0.1 eV/dimer) [96] such that the flipping frequency of the dimers is 10^3 times larger for silicon than for germanium. This fact allows for germanium the coexistence of both

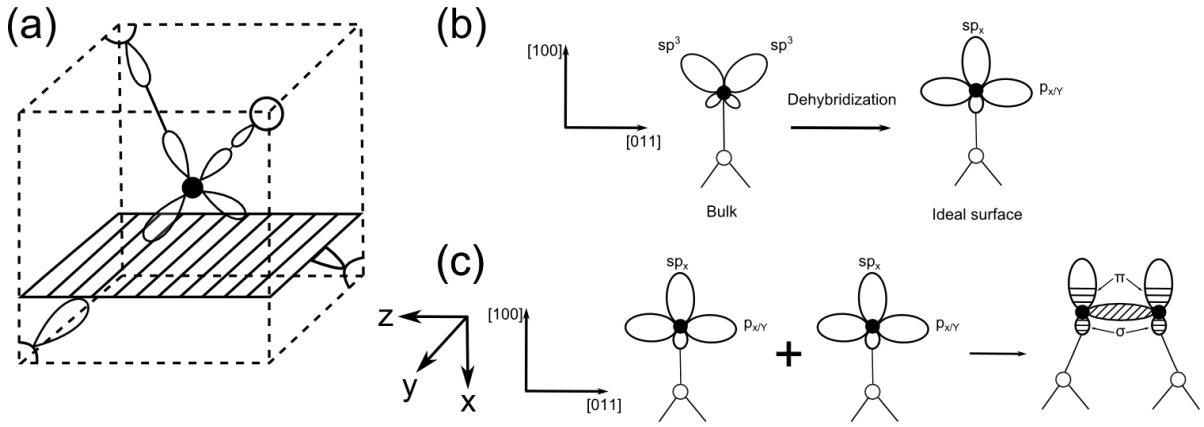

Figure 4.1.: *Reconstruction of Ge(001): (a) Cutting of bulk Ge in the (001) plane results in two dangling sp^3-bonds per surface atom. (b) Due to symmetry reasons these dangling bonds de-hybridize into a surface normal component sp_x and a parallel component $p_{y/z}$. (c) The total free energy is now minimized by dimerization along the [011] direction forming a σ-bond between contributing surface atoms. Thus, the first surface layer is twisted compared to the second one. From [94].*

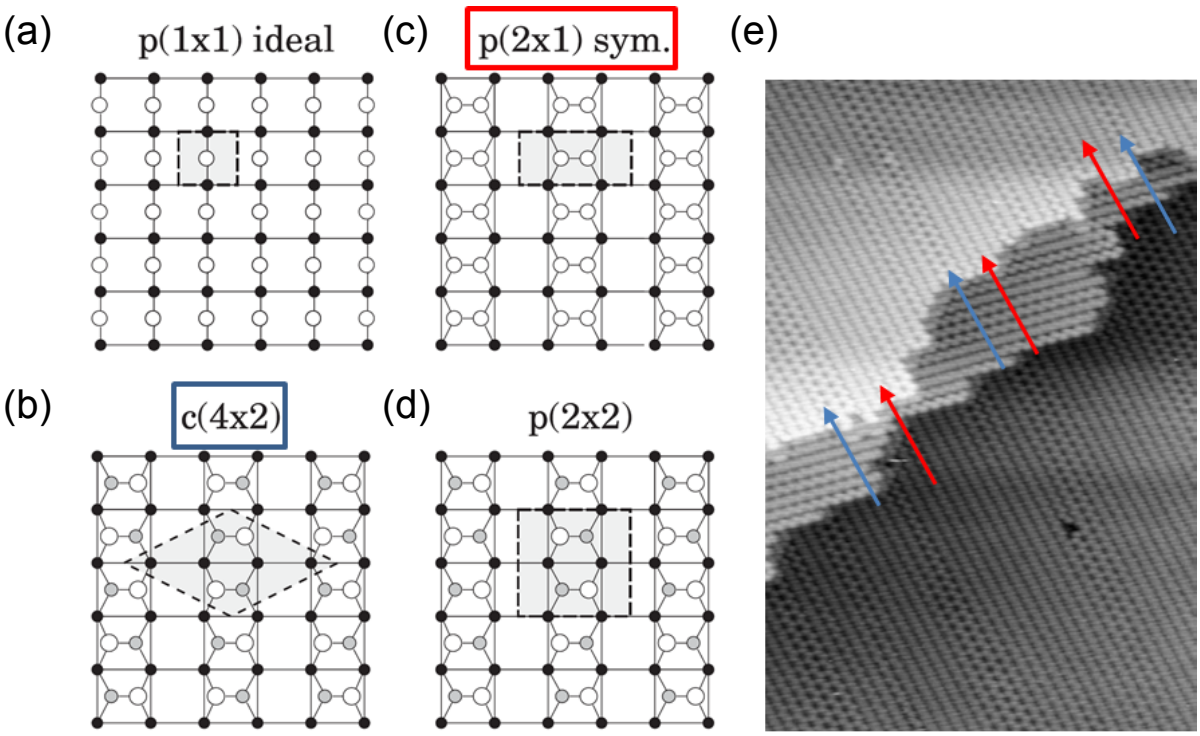

Figure 4.2.: *Reconstructions on the Ge(001) surface: (a) Primitive (p)(1×1) sharing the periodicity from the bulk crystal. (b) Dimerization along the horizontal line forming a p(2×1) symmetry, where both dimer atoms flip alternately between the up and down position. (c) The static (frozen in) form of (b) is a c(4×2) pattern with a zig-zag along one dimer row and a phase shift of the buckling between neighboring dimer row. (d) In-phase configuration of (c) leading to a p(2×2) symmetry. The corresponding unit cells are highlighted by the dashed black lines. Reprinted from [97], Copyright (2013), with permission from Elsevier. (e) STM image by Zandvlied taken at room temperature showing the coexistence of both c(4×2) and (2×1), reprinted from [98], Copyright (2013), with permission from Elsevier.*

phases (2×1) and c(4×2) at room-temperature (presented in Fig. 4.2, where for higher [lower] temperatures only the (2×1) [c(4×2)] appears [97]. The reason for this domain pattern is the anisotropic stress tensor that comes along with the dimerization. An additional p(2×2) reconstruction is also observed, which is close in energy to the lowest energy configuration of c(4×2) [97]. Note that two surface domains already exist on the bare Ge(001) surface. They are rotated by 90° to each other going from one terrace to the next underlying terrace by a single step of 1.4 Å height, see STM image in Fig. 4.2(e). The dual domain nature originates from the stacking sequence ABAB for germanium.

In our case the dimer pattern will act as a template for the growth of atomic chains / nanowires after the adsorption of metal on the semiconductor surface. However, the nanowires are always limited to the perfection of the substrate, i.e. terrace size and low defect density, for which an effective cleaning process is inevitable.

4.1. Common cleaning methods

A clean surface is required not only for nanostructures, e.g. atomic chains, but also for depositing thin films. One example that has recently emerged are high-permitivity (κ) materials such as HfO_2 or ZrO_2. They are discussed as alternative gate oxides to SiO_2 with reduced current leakage for lower power consumption, combined with an increase in bulk electron and hole mobility when grown on germanium as a channel material compared to silicon [93]. GeO_2 is discussed in this sense as a passivation layer, whose thermal stability is mandatory to maintain the electrical characteristics of the device [99].

The most common in situ cleaning procedure for the Ge(001) surface involves several cycles of Ar^+ ion bombardment to remove impurities on the surface, but surface roughness is enhanced. To a certain extent this can be compensated by thermal heating (annealing). Thermal energy on the other side enables (hydro-)carbon (e.g. from the surrounding UHV) to stick on or react with the surface, which hinders further self-organized growth on the surface [100, 101]. Dopant segregation at the surface must be considered as well. An additional disadvantage is the time consumption of Ar^+ sputtering, where each cycle requires $\sim$ 60 min, and often various cycles are needed. High quality smoothing of the surface can be achieved by Ge buffer layer growth using molecular beam epitaxy [100, 102].

Alternatives are wet-chemical treatments which include multiple cycles of surface-oxidization with hydrogen-peroxide (H_2O_2) and subsequent oxide stripping with acid. Here, mostly the use of HCl or HF is reported [103–105]. The final oxide acts as a passivation layer which is removed thermally in UHV. In terms of protrusion density the surface quality is comparable to sputtering and annealing following these treatments, yet still some carbon remains [100]. A shortcoming is the passivation with GeO_2 by liquid oxidizers (H_2O_2/H_2O, $NH_4OH/H_2O_2/H_2O$ or HNO_3) [103, 104]. These are inefficient to a certain extent, since the hexagonal phase of GeO_2 (phase transition to tetragonal phase above 1030 C°[93]) is water soluble, causing a constant etching of the oxide in aqueous solutions [104, 105]. Other approaches comprise UV/ozone based oxidations [105] or the *in situ* use of molecular oxygen [106], yet these approaches require additional technical procedures.

4.2. Own cleaning procedure for Ge(001)

The cleaning method used in this thesis is a combination of wet-chemical etching with *Piranha* solution (H_2SO_4, H_2O_2, H_2O), followed by dry oxidation to form a GeO_2 passivation layer. Piranha is known as a strong oxidizer and effective for removing organic compounds and metal contaminations [107, 108]. The use of sulfuric acid has proven to gain the same results as HF - without its toxicity allowing simple handling and easy waste management. Its etching capabilities are already reported for GaAs [109] and are

comparable for Ge(001). The passivating oxide is produced at elevated temperature (∼ 380 °C) and yields ultra-thin amorphous GeO_2 layer, which buries residual contaminants. Desorption of the oxide in UHV takes place according to [93]:

$$GeO_2\ (solid) + Ge\ (solid) \rightarrow 2GeO\ (gaseous)\ (T > 400°C), \tag{4.1}$$

resulting in a complete removal by conversion of the solid dioxide into the gaseous phase in UHV. This procedure is highly reproduceable and requires less time/technical effort than the former quoted methods. The final Ge(001) terraces are of high quality with low defect concentrations and typical diameters of ∼ 100 nm.

Technical treatment

Before the etch process the Ge(001) samples (n-type doped (Sb), <1 Ωcm) are rinsed in acetone to remove the photo resist. This is done in a clean room environment, provided by a flow-box. Adsorbed hydrocarbons are subsequently removed by stirring the samples in ultra-pure acetone, propanol and methanol for 2 min each. To get rid off residual solvents, the samples are blown off with dry nitrogen. The following etching with H_2SO_4:H_2O_2:H_2O (7:2:1) for 5 s does not only strip the native oxide but also etches several layers of the Ge surface. The blown dry samples are oxidized in an oven at ∼380 °C in high purity synthetic air for 5 min to produce a clean passivating oxide layer. The chosen temperature regime provides the activation energy for the oxidization [110] and ensures the growth of GeO_2. Finally, the samples are mounted on a sample holder and put into UHV.

Adsorbed hydrocarbons are desorbed at a sample temperature of ∼ 250 °C with a pressure typically not exceeding $\leq 1 \times 10^{-9}$ mbar. This avoids any reaction of the

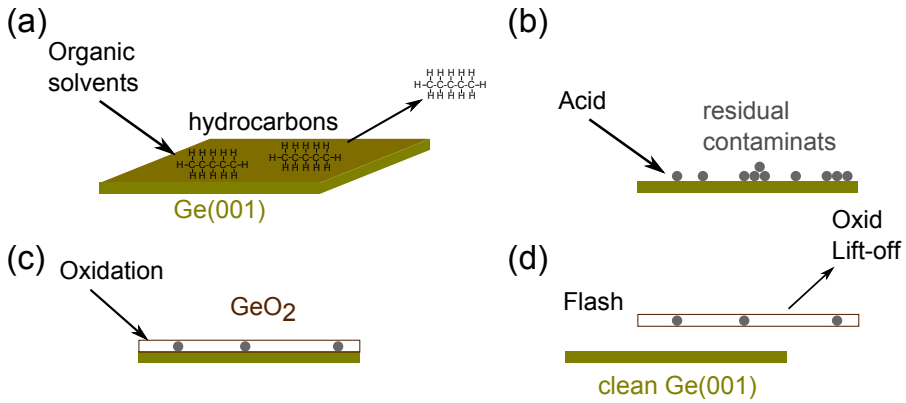

Figure 4.3.: *(a) Adsorbed contaminants, i.e. mostly hydrocarbons, are partially removed. (b) Further cleaning is performed by wet chemical etching using a mixture of H_2O:H_2O_2:H_2SO_4 (1:2:7) for 10 seconds. (c) Residual contaminants are buried in the thermally grown oxide at 380 °C. (d) Short heating (flash) for ∼1 seconds at 600 °C removes the oxide yielding a clean Ge(001) surface.*

substrate with residual gas. Samples are heated with direct current to avoid a complete warming of the sample holder, as would be the case for resistive heating. Oxide removal is performed by short (t $\sim$ 1 sec) current pulses (flash) that heat the sample quickly above 600 °C. The whole process is depicted in Fig. 4.3.

XPS analysis of the oxide

GeO_2 forms via sub-oxides and only gradually leads to a closed packed film due to the lattice mismatch of 21% and strain relaxation between Ge and GeO_2 [111, 112]. The quality and thickness of the thermally grown oxide layer can be studied by x-ray photoelectron spectroscopy (XPS) for different escape angles. Electrons escaping the sample normal to the surface provide the highest probing depth, while surface sensitivity is enhanced at shallow angles. Due to the small oxide thickness both the bulk Ge and its oxide contribute to the XPS signal. Both exhibit different components which are energetically separated (chemical shift). The passivating oxide's thickness can be determined from the angular dependence of the oxide-shifted Ge 3d core-level component.

The corresponding data are plotted in Fig. 4.4(a) for the thermally grown oxide layer. At normal emission ($\alpha = 0°$), both contributions from the Ge bulk (29.4 eV) and GeO_2 (32.4 eV) are present. According to the maximized probing depth the spectrum is dominated by the Ge bulk signal. Increasing the angle in steps of 10° and thereby enhancing the surface sensitivity yields an increase in the GeO_2 signal at the expense of bulk Ge

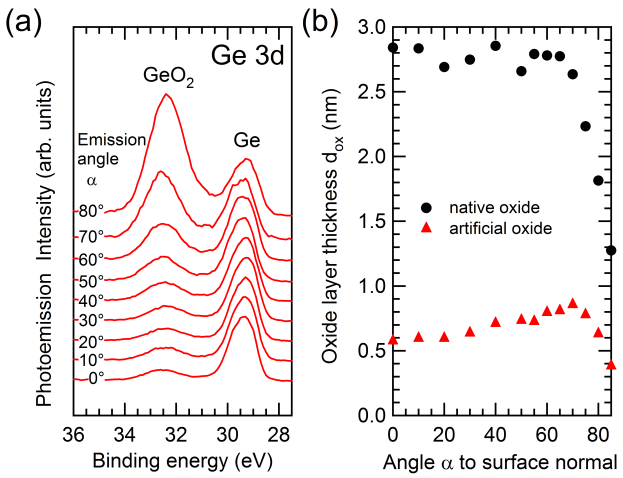

Figure 4.4.: *(a) Ge 3d core-level spectra as a function of electron emission angle α to surface normal starting from normal emission towards in-plane. All spectra are normalized to the Ge 3d bulk peak. (b) Calculated oxide layer thickness for thermally oxidized (red triangles) and native oxide samples (black dots). Data at normal emission yield an oxide thickness of 2.8 nm for the native oxide samples while only 0.6 nm for the thermally grown oxide. The intensity drop-off for $\alpha > 70°$ must be ascribed to elastic scattering of the photoelectrons. From [7].*

(spectra are normalized to Ge 3d bulk core-level). The quantitative determination of the oxide layer thickness is done by comparison of the substrate intensity (I_{sub}) and GeO_2 intensity (I_{ox}) of the Germanium 3d core-level as a function of the escape angle according to refs. [113, 114]:

$$d_{ox} = \lambda_{ox} \ln\left(\frac{\rho_{sub}\lambda_{sub}}{\rho_{ox}\lambda_{ox}}\frac{I_{ox}}{I_{sub}} + 1\right)\cos\alpha, \tag{4.2}$$

with ρ representing the atom densities. The inelastic mean free path for the oxide $\lambda_{ox} = 2.89$ nm and the Ge substrate $\lambda_{sub} = 2.99$ nm are calculated according to Tanuma, Paul and Penn *et al.* [78], see eq. 3.4. The calculated oxide layer thickness d_{ox} over α yields a nearly flat curve for $0 < \alpha < 60°$, see Fig. 4.4(b). This is a first indication of a homogeneous and smooth oxide layer. The drop-off around 70° is dedicated to elastic scattering of the photoelectrons. Thickness values of 0.6 nm ($\sim$ 3 monolayer (ML) [112]) for the thermally grown oxide and a more than four-fold larger value of 2.8 nm for the native oxide are derived at normal emission. The latter is consistent with previous reports on the typical native oxide layer thickness [99, 114]. The reduced thickness for the thermally grown oxide is advantageous as it allows easy removal by short-time heating. Thicker oxides can last due to the high stability of bulk GeO_2. This implies a *thin* oxide layer is essential. The stoichiometric composition of GeO_x is mainly concluded to be GeO_2 from the chemical shift of about 3 eV in the upper Ge 3d core-level of Fig. 4.4(a). This matches previous results by Molle *et al.*, who report a preference for GeO_2 compared to GeO in the growth temperature regime below 400°C [99].

Homogeneity of the oxide

Atomic force microscopy (AFM) is used to judge the roughness of the insulating GeO_2 face. The typical terraced topology of the oxidized surface is shown in Fig. 4.5(a). A root-mean-square value of about 0.28 nm is observed for an area about 1 μm^2, which is comparable in size with a double height step on the bare Ge(001) [97].

Oxide removal in XPS

The oxide removal and the achieved cleanliness of the substrate is monitored by XPS. Here, the initial oxygen contribution of both Ge 3d and O 1s core-level vanishes, see Fig. 4.5(b) and (c). In place of the former O 1s the Ge Auger $L_2M_{23}M_{23}$ peaks (534 eV and 525 eV) can now be observed [115]. The contamination level, mainly attributed to hydrocarbons, is accessed by the C 1s core-level before (red) and after oxide desorption (blue). In the latter case in Fig. 4.5(d) almost no detectable C 1s signal is found compared to the oxidized sample. For comparison, the spectrum for 1 min exposure to atmosphere is plotted (black) in Fig. 4.5(d). This proves the effective burying of residual contaminations within the oxide and their removal afterwards during flash annealing.

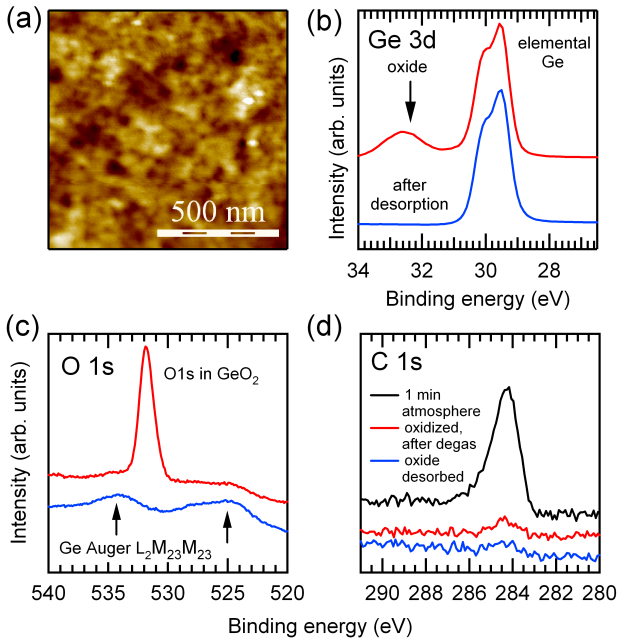

Figure 4.5.: *(a) AFM image of 1 μm^2 thermally grown GeO_2 yielding a root-mean-square roughness of 0.28 nm. Core-level spectra taken before (red, upper curve) and after (blue, lower curve) desorption of thermally grown oxide. (b) Ge 3d, (c) O 1s and (d) C 1s. In the latter case almost no traces of carbon or oxygen are detectable, pointing to a complete lift-off of the oxide. From [7].*

Purity of the process

Since other wet-chemical treatments are reported to leave detectable amounts of carbon residue at the surface [100, 101, 105], only spatially resolved techniques allow to judge the surface quality on the atomic scale. Any remaining carbon impurities may hinder surface mobility (i.e. by acting as nucleation centers for clustering of adsorbate material) and the development of larger terraces [100, 101], thereby limiting the length scale of potential nanowires.

STM images recorded on the 250 nm scale yield regular flat terraces with a mean diameter of $\sim$ 100 nm. An example is given in Fig. 4.6(a). The surface roughness on this large scale essentially reflects the roughness caused by the polishing of the wafer during manufacturing. As expected from the XPS C 1s spectrum, the protrusion density is very low and comparable to or even better than for other chemical cleaning procedures or ion bombardment followed by annealing [100, 101, 105]. This does not hinder the intrinsic dimer rows [116] of the reconstructed surface to be resolved in STM, Fig. 4.6(b). To check for the long-range order, LEED images are recorded which represent a spatial average due to the LEED spot size in the mm^2 range. The pattern at 41 eV yields sharp reflexes of the (2×1) reconstruction in Fig. 4.6(c), which predominates the local c(4×2)

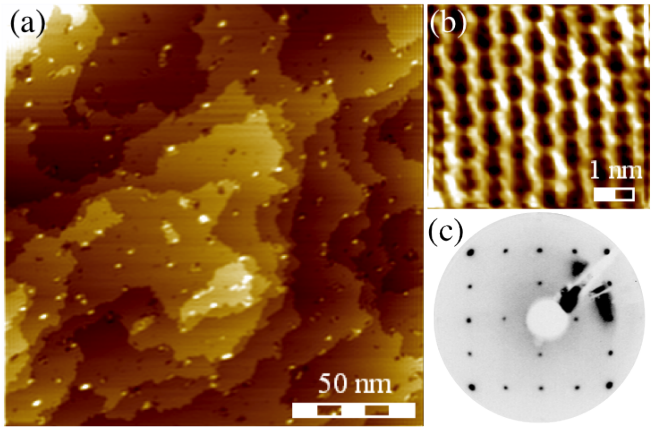

Figure 4.6.: *(a) STM image of unoccupied states (+1.7 V, I = 0.5 nA) of the Ge(001) surface after oxide desorption. The terrace width is typically about 50-100 nm accompanied by some point-like protrusions most probably due to C-atoms. (b) Zoomed STM image (+1.5 V, 0.5 nA) reveals a defect-free c(4×2) reconstruction. (c) Corresponding LEED pattern at 41 eV proves the surface quality by sharp reflexes and low background. From [7].*

when averaging over several terraces. The low background is an indication for the low defect and contamination density. The chosen energy of 41 eV is close to the minimum of the inelastic mean free path of the electrons to ensure a maximum of surface sensitivity. The resulting linear dimer pattern of the Ge(001) surface can now act as a template for the growth of atomic nanostructures [1, 3, 117].

5. Structural investigations of Au/Ge(001) by surface x-ray diffraction

To understand the electronic behavior of a material it is inevitable to take a look at the underlying real space structure. Among other things, modern density functional theory methodes allow the calculation of the electronic band structure if the exact atomic arrangement is identified. Experimental access to the structural composition of such a surface system is a complex task, such that ultra high vacuum is experimentally required to maintain the sample quality. The most common approach for Au/Ge(001) has been scanning tunneling microscopy (STM) with the most prominent data being presented in the next section. As a note of caution the reader is reminded that STM images always represent a mixture of topography and local charge density with the latter being affected by the applied bias [118]. Thus, interpreting STM images in terms of the structural components has to be done with care. Atomic force microscopy does not suffer from this electronic screening and has recently improved in resolution by introducing the q-plus sensor [83, 119, 120]. Unfortunately, this method is fairly used in the literature on self-assembled nanowires.

5.1. Previous work on Au/Ge(001)

Gold-induced chains on Ge(001) with short-range order were first reported by Wang *et al.* [44, 45]. They deposited 0.5 ML of gold at 675 K on Ge(001) yielding a (4×2) or c(8×2) pattern compared to the (2×1) of the bare Ge surface, see Fig. 5.1(a). In STM two types of wires of different electronic contrast were observed, each with a 16 Å spacing corresponding to four times (4×) the surface lattice constant a_0. The length scale of these wires was only limited by the underlying terrace size. As not the whole surface was covered by wires for this amount of gold, line profiles including the bare Ge and the gold reconstructed surface could be performed. For the two types of wires a height difference of only 0.13 nm and 0.03 nm compared to the bare Ge surface was found. The zig-zag pattern along the wire direction had a 8 Å periodicity ($\times 2a_0$) leading to the conclusion of two types of dimer rows as displayed in Fig. 5.1(b): One row being made by Au-Au dimers, the other by mixed dimers of Au and Ge. The height difference of both types compared to the bare Ge surface was interpreted as different charge contributions of the

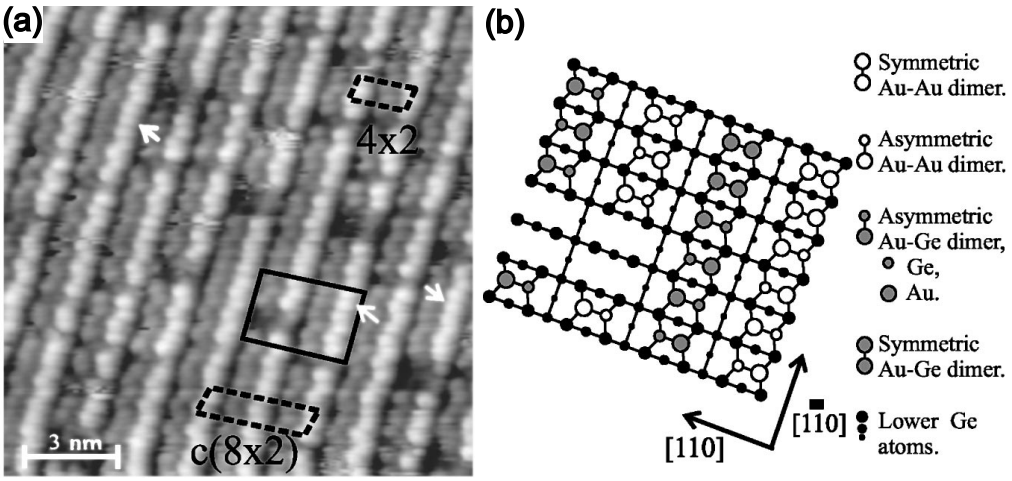

Figure 5.1.: *Occupied states (-0.7 V) image by Wang et al. after 1.5 ML of Au deposited on Ge(001) at 675 K. (b) Ball and stick model of the marked area in (a). Two types of wires were identified: Au-dimer rows of bright contrast and mixed Au-Ge dimers with less contrast. Both symmetric and asymmetric arrangements were observed. Figure reprinted with permission from J. Wang, M. Li and E. I. Altman, Phys. Rev. B, Vol. 70, page 233312, 2004, http://link.aps.org/doi/10.1103/PhysRevB.70.233312 [44]. Copyright (2012) by the American Physical Society.*

involved atoms rather than a structural height difference. Thus, both types of wire were proposed to *lie on the very same height*. Complete coverage of Ge(001) could be realized with 1.5 ML Au on the surface demonstrating an astonishing wettability of Ge(001) by Au. The nanowire growth hereby followed the underlying dimer direction guiding a template-driven self-assembly on the surface. Since Ge exhibits two types of surface orientations by its stacking sequence of ABAB, the corresponding nanowire direction rotated by 90° was also found when going in Ge single-height steps (1.4 Å) from one terrace to the next one.

Growth conditions

Detailed studies on the influence of the growth temperature and deposited gold amount revealed that for a small initial amount of gold (0.03 ML) a highly distorted Ge(001) surface with various vacancies occurred already at room temperature [45]. This behavior was already known for Pt on Ge(001) where Pt drops below the Ge surface. This so called β-terrace exclusively allows the growth of Pt-induced atomic chains on top [121]. Increasing the amount of Au to 0.1 ML lead to two-dimensional islands on the surface in the temperature range of 475 K to 575 K. A further increase of gold enabled the first chain formation at $\sim$0.4 ML and subsequent annealing at 475 K. By analyzing the step height for partially covered surfaces, e.g. 0.5 ML Au in Fig. 5.2(a), a preference for double height steps was observed with the chains aligned in parallel to the step edges.

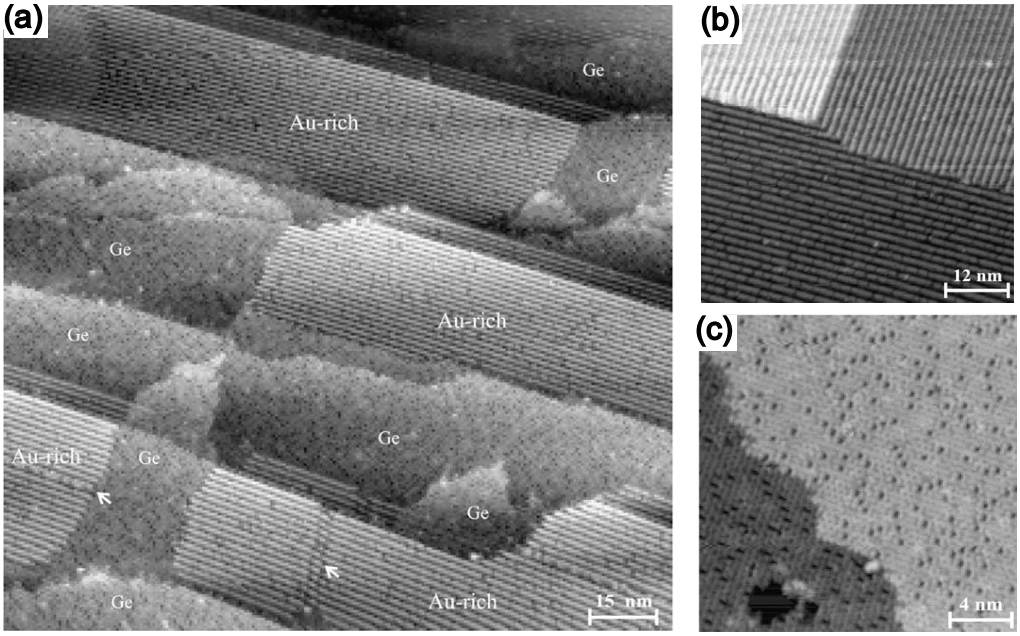

Figure 5.2.: *STM images showing occupied states (-1.5 V) for Au/Ge(001) after depositing 0.5 ML of Au at 675 K (a). Notably, the chains prefer to align parallel to the step edges. A completely covered surface is observed for 1.5 ML of Au at 675 K (b). (c) Heating of a 0.5 ML Au covered sample to 1000 K leads to a defect-rich surface caused by bulk migration of gold. Reprinted from [45], Copyright (2013), with permission from Elsevier.*

Best growth conditions were found at 675 K with 100 % coverage for 1.5 ML of Au deposited, as depicted in Fig. 5.2(b) [45]. Exceeding this amount resulted in three-dimensional clusters of rectangular shape with a surface normal component in the [110]-direction. The chain reconstruction itself remained stable up to 1000 K. For higher temperatures bulk migration was dominant leaving a highly distorted surface with various vacancy defects as shown in Fig. 5.2(c) [45].

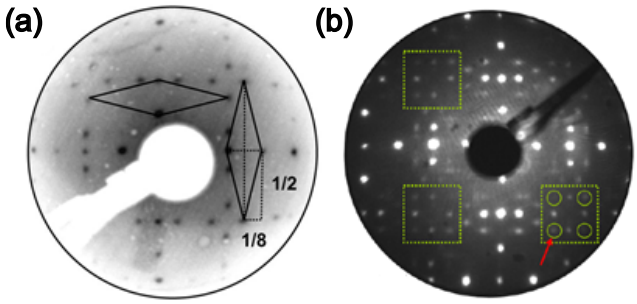

Figure 5.3.: *(a) LEED pattern at 29 eV only resolving the basic c(8×2) pattern [1]. (b) Additional LEED spots of p(4×1) symmetry recorded at 18 eV for a highly ordered surface [123].*

Subsequent studies by our group revealed the true symmetry of the reconstruction to be c(8×2) both from LEED, shown in Fig. 5.3(a), and STM. This means a 8 Å charge modulation along each wire and a phase shift of neighboring wires by one surface lattice constant a_0 [1]. The lateral extent from full width half maxima (FWHM) STM line-profiles accounted to ∼7 Å for which a best match was found for single gold atoms with a calculated FWHM of 9 Å on aluminum, whereas a Au-dimer leads to a FWHM of 16 Å respectively [122].

Structural components deduced from STM

The nanowire height of ∼1.5 Å measured by us is close to the reported values of Wang and co-workers. In contrast, van Houselt *et al.* reported an increased value of 6 Å [124]. They proposed a model of buckled Ge-dimers on top of the wire ridges and sidewalls of Au-$\sqrt{3}$-facets. Their comparison of line-profiles for the bare germanium surface with

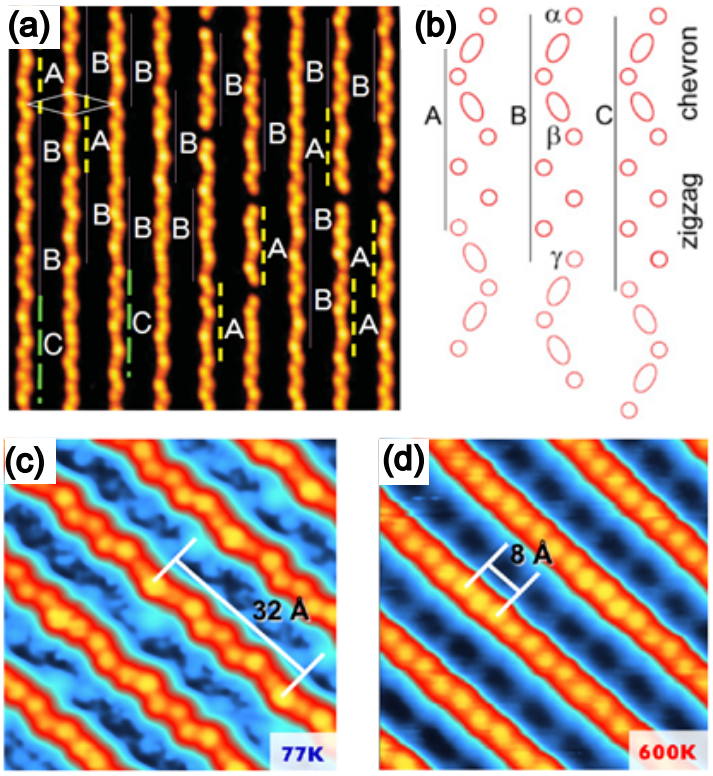

Figure 5.4.: *(a) Pronounced charge protrusions in occupied states at -1 V of V- and W-shape with corresponding explanation in (b) by Niikura et al.. Figure (a) and (b) with permission from R. Niikura, K. Nakatsuji and F. Komori, Phys. Rev. B, Vol. 83, 035311, 2011, http://link.aps.org/doi/10.1103/PhysRevB.83.035311 [127]. Copyright (2012) by the American Physical Society; phase transition in occupied states (-0.8 V) upon temperature (c) 77 K and (d) 600 K by Blumenstein et al. [123]. The former V- and W-shapes are stretched at elevated temperatures.*

Au/Ge(001) yielded an overall good agreement suggesting structural similarities to the dimers of the bare Ge(001) surface. In contrast, a more narrow envelope was observed for Pt/Ge(001) chains which are thought to resemble true single-atom chain [125]. The assumption of buckled dimer on top of the Au/Ge wires was further supported by STM data by Mocking *et al.* showing noisy wire segments in the vicinity of anti-phase boundaries with the next two nearest neighboring dimers being buckled with a phase shift [126]. Recording the tunneling current with an opened feedback loop over such a flipping feature provided a flipping frequency of 25 Hz. No flipping was observed at 77 K, thus indicating a thermal driven process [126].

In general, one has to be careful with interpretation of STM data since these measurements depend highly on the applied bias voltage, thermal stability and the tip performance. Van Houselt *et al.* proposed their model of $\sqrt{3}$-side facets by using an asymmetric tip apex [124]. A subsequent study which was run by our group at liquid nitrogen temperature (77 K) lead to the first observation of local protrusions on top of the wires [3]. This must be ascribed to the improved thermal stability and instrumental resolution compared to all other data which were acquired at room temperature. These protrusions of V- and W-shape at 77 K were later confirmed by Niikura and co-workers [127] as depicted in Fig. 5.4(a) and (b). However, they discussed these shapes still in the presence of the c(8×2) symmetry although an additional symmetry was already apparent in their low-energy electron diffraction data. Here, the very same group had already observed extra reflexes with a seemingly 8× periodicity some years earlier [128], but could not draw a conclusion on it.

Additional p(4×1) finestructure

Clarification came from a combined LEED and STM study in our group proving a correlation between the observed protrusions of 32 Å periodicity in STM and the extra LEED spots beside the basic c(8×2) pattern [123]. Here, a complex fine structure of p(4×1) symmetry on top of the basic c(8×2) was identified in LEED. Both the basic c(8×2) and the additional p(4×1) superstructure are shown in Fig. 5.3(b) for comparison. The superstructure appears in STM in terms of triplets of spherical charge clouds in the unoccupied states of Ref. [123]. They turn into the V- and W-shapes upon change in polarity (occupied states) located at the very same position of the triplets. Increasing the sample temperature leads to a gradual disappearance of the p(4×1) spots in LEED and likewise of the protrusions in STM (transition displayed in Fig. 5.4(c) and (d)). The transition temperature is determined by $T_C = 585 \pm 10$ K. This reversible, second order phase transition is supposed to be of purely structural origin that leaves the electronic states unaffected.
To summarize:

- Au/Ge(001) exhibits two domains of wires rotated by 90° due to the stacking sequence of Ge.

- Two symmetries are present - a basic c(8×2) pattern and a p(4×1) superstructure.
- The c(8×2) exists at all temperatures and represents the basic spacing along the wire and perpendicular to it.
- The p(4×1) is called superstructure, because it sits on top of the c(8×2). It manifests itself in terms of a triplet and V-/W-shape (chevron/zig-zag) in STM. These shapes disappear with increasing temperature in both STM and LEED.

Epitaxy recipe for Au/Ge(001)

All samples used in this thesis have been fabricated by hot deposition, i.e. the substrate was held at $\sim$ 675 K by direct current heating. Gold (purity typically 99.995 %)was evaporated from electron beam evaporators with rates up to 2.4 ML/min as recorded by a quartz crystal. The correct surface reconstruction with both c(8×2) and p(4×1) symmetries was checked by LEED (typical LEED images are presented in Appendix Fig. A.3). The total amount of Au is assumed to be $\theta = 0.75$ ML according to Gallagher *et al.* [43].

5.2. In-plane distances from SXRD autocorrelation maps

The data that were presented in the previous section mostly rely on scanning tunneling microscopy. They do not explicitly show topography only, but also depend on the experimental performance including tip shape and thermal stability. Thus, any proposition of a structural model on STM alone remains somehow speculative. Nevertheless, the data provide a first insight and can be compared for instance with DFT calculations, which provide a check for energetical stability. An alternative access to the structural arrangement is given by surface x-ray diffraction (SXRD). Although the investigated structure cannot be determined directly from the diffraction pattern due to the *phase problem* (see chapter 3.2), a solution is provided by the Patterson function. $P(\mathbf{r}) = \int \rho(\mathbf{r}')\rho(\mathbf{r}'+\mathbf{r})d\mathbf{r}'$ represents the pair-correlation function of the electron density $\rho(\mathbf{r})$. This means, all inter atomic distances in $\rho(\mathbf{r})$ are present in $P(\mathbf{r})$ revealing their length scale and directions between atoms, but not absolute atom positions. Technically, $P(\mathbf{r})$ is generated by applying a Fourier transformation directly to the corrected in-plane diffraction intensities (h, k, $l = 0$), thus ignoring the unknown phases. More precisely, l is limited by the lowest achievable grazing incident angle due to the sample/sample-holder geometry and the angle for total reflection. In the present case $l_{min} = 0.05$ r.l.u. (reciprocal lattice units) was used.

In-plane scattering

The bare Ge(001) surface exhibits two domains which are rotated by 90° going from one terrace to the next by one single atom height step (1.4 Å). The construction of the basic c(8×2) LEED pattern is displayed in Fig. 5.5. The LEED pattern for one c(8×2) domain, e.g. the red dots, consists of reflexes with a periodicity of $2\pi/8a_0$ while neighboring rows of reflexes are $2\pi/2a_0$ apart as well as phase shifted by $\pi/8a_0$. The dual domain image is now achieved by duplicating the single domain pattern, 90° rotating (blue dots) and overlaying both. The (1×1) unit cell vectors $\vec{a}$ and $\vec{b}$ are indicated in black. Both domains are well separated in the diffraction experiment and represent the very same structure. With this in mind it is sufficient to record reflexes for one domain only.

The experimental LEED pattern also contains the extra p(4×1) superstructure [overlay with black dots in Fig. 5.5(b)], which is weaker in intensity compared to the basic c(8×2) structure. In turn they were also too weak to be addressed within the SXRD experiment which therefore focused on the basic c(8×2) reconstruction only [grey-shaded quadrant in Fig. 5.6(a)]. Here, 69 symmetrically inequivalent reflexes were recorded in the hk-plane at lowest possible surface normal component $l = 0.05$ r.l.u. presented in Fig. 5.6(b) for the in-plane data set. The use of one domain causes h to be multiples of (n-1)·0.5, while k takes only values of (0.5n+0.5)+0.25 with n ∈ ℕ. Measured intensities

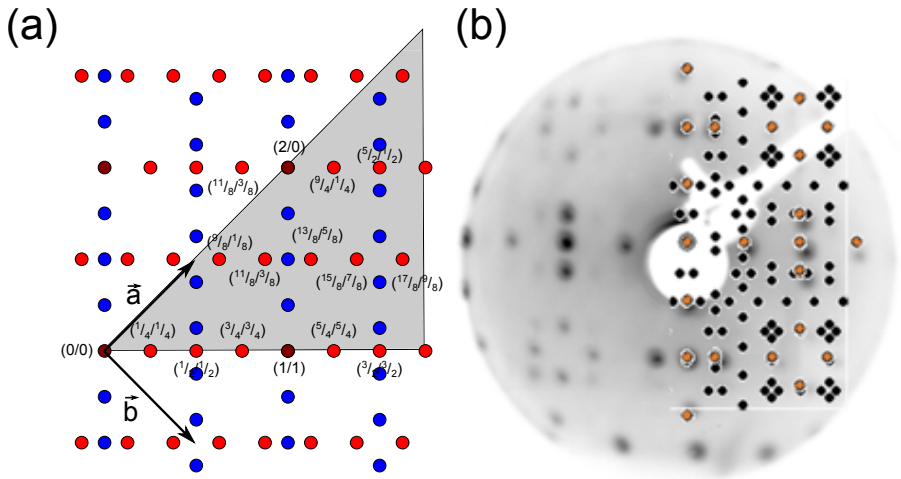

Figure 5.5.: *(a) Schematic c(8×2) LEED pattern for a dual domain sample of Au/Ge(001). The individual domains are displayed in red and blue. The reflexes are labeled by (h, k) according to their location in terms of the (1×1) unit cell vectors $\vec{a}$ and $\vec{b}$. The grey-shaded area corresponds to the measured quadrant in SXRD. (b) Experimental LEED pattern recorded at 29 eV showing both the c(8×2) reconstruction (orange dots) and the p(4×1) superstructure (black dots).*

are corrected for background, the Lorentz-factor, polarization factor and active sample area.

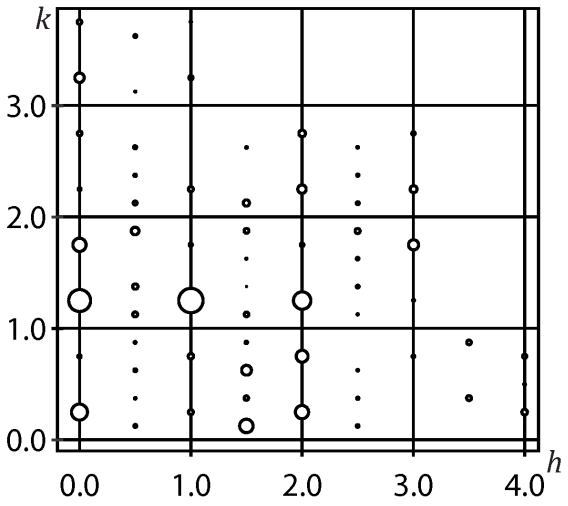

Figure 5.6.: *Reflexes of the c(8×2) symmetry in the hk-plane for $l = 0.05$ r.l.u.; h takes multiples of (n-1)·0.5, while k denotes to (0.5n+0.5)+0.25 with $n \in \mathbb{N}$. Circle diameters are proportional to the structure factor $|\vec{F}|^2$. From [10].*

Patterson map

Applying a Fourier transformation to the in-plane data set yields the experimental Patterson map (PM). A contour plot of the corresponding Patterson function with only positive contour lines is presented in Fig. 5.7(a). In a most simplistic picture the scattering process in SXRD scales with the product of the atomic masses of the contributing atoms. Hence, the most intense peaks, which lie on the horizontal line of the unit cell, can be attributed to scattering between two gold atoms. Note that the point of origin (highest intensity in PM) resides at the left corner of the flat lying diamond, as indicated by the line-profile along the horizontal line through the main peaks in Fig. 5.7(b).

To relate the peak maxima of the PM to individual gold atoms in the unit cell one requires the knowledge of the precise coverage. Unfortunately, all common determinations, i.e. by a quartz crystal monitor or scaling from a known reconstruction like the $\sqrt{3} \times \sqrt{3}$ (coverage = 1/3 ML), bare some uncertainties, i.e. assumptions of sticking coefficients or unknown influence of the applied temperature during the growth process. In addition, two different growth procedures are reported, which both evidently yield the same structure [125, 127]: Room temperature deposition followed by a post-annealing and alternatively, Au deposition on heated Ge substrates. In the latter case little is known about possible desorption or bulk segregation rates of Au, while at least for the

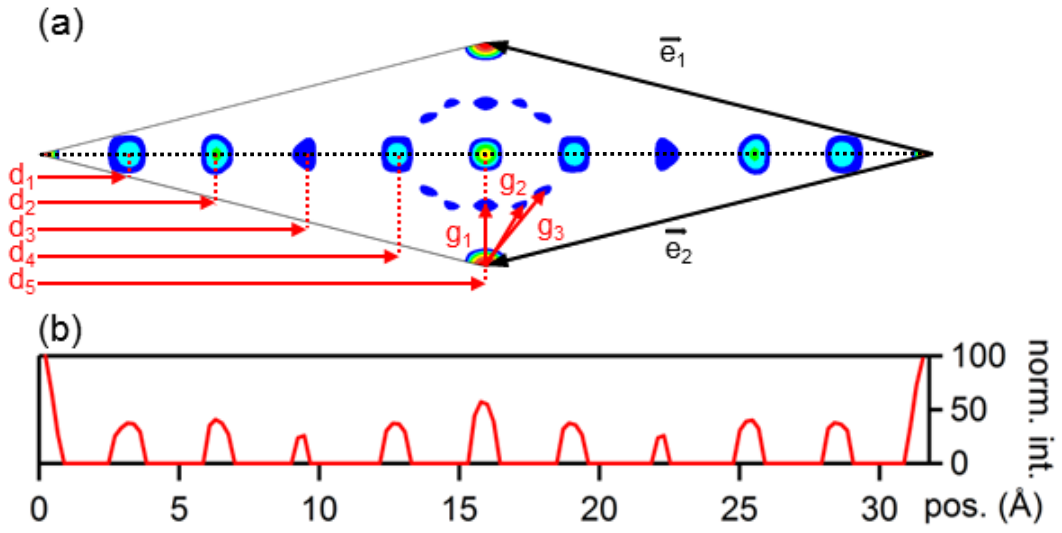

Figure 5.7.: *(a) Projected Patterson function calculated from the fractional order in-plane reflections. The c(8 × 2) unit cell is indicated by the vectors $\vec{e}_1$ and $\vec{e}_2$. Distances $\vec{d}_1$ to $\vec{d}_5$ from the most intense maxima are allocated to Au-Au distances, while $\vec{g}_1$ - $\vec{g}_3$ most probably involve Au-Ge bonds. (b) Line-profile along the horizontal crossing the main peaks of $\vec{d}_1$ to $\vec{d}_5$. Normalized intensity is highest at the point of origin, which is the left corner of the lying diamond unit cell. From [10].*

heated substrate segregation was observed by Wang *et al.* [45]. As a consequence, the reported Au coverage ranges from 0.2 to 1.5 ML of Au, see Tab. 5.1 for comparison.

1st Author	coverage [ML]	year	Ref.
van Houselt	0.2-0.3	2008	[124]
Schäfer	0.5	2008	[1]
Mocking	0.5	2010	[125]
Gallagher	0.75	2011	[43]
Nakatsuji	1.1-1.2	2009	[128]
Wang	1.5	2004	[44]

Table 5.1.: *The reported Au coverage varies in the range from 0.2-1.5 ML from the various publications. The probably most precise analysis is done by Gallagher et al. and states 0.75 ML.*

Using the probably most precise coverage determination (0.75 ML) by Gallagher and co-workers [43] results in six Au atoms and eight Ge atoms per unit cell. For 6 inequivalent Au positions one would expect five different vectors within the Patterson map of one unit cell. Instead the experimental data exhibit nine maxima from the left corner of the lying diamond, which marks the point of origin of the Patterson map, to the right corner of the diamond, see dotted line in Fig. 5.7(a). Due to the present symmetry with its inversion center in the middle of the Patterson map not all of these maxima are inequivalent. As a consequence, one has to concentrate only on half the unit cell with five vectors $\vec{d_1}$ to $\vec{d_5}$ drawn in Fig. 5.7. With the already known Au coverage 3 Au atoms have to be attributed to certain locations using these five vectors within half the unit cell.
All distances $\vec{d_1}$-$\vec{d_5}$ are multiples of $\vec{d_1}$ = 3.2 Å, where $\vec{d_5}$ corresponds to the wire periodicity of 16 Å. Three Au positions can be defined from this symmetry by combining two of these vectors to give $\vec{d_5}$ in total, i.e. adding $\vec{d_1} + \vec{d_4}$ or $\vec{d_2} + \vec{d_3}$. These two pairs of vectors match the same position if one is drawn from one corner of the Patterson map and the other from its center. The remaining off-axis reflexes labeled $\vec{g}_1$ - $\vec{g}_3$ are less intense and therefore related to Au-Ge distances. This is plausible from their decreased scattering intensity, which qualitatively scales with the reduced product of the atomic masses involved (by a factor of ∼2, matching approximately the mass ratio $Z_{Au}^2 : Z_{Au}Z_{Ge} = 79^2 : 79 \cdot 32$=2.5:1).

Autocorrelation map from STM

To further verify the distances found in SXRD an autocorrelation map is generated from STM topography data (≈60 nm)^2. By using high temperature data recorded at 600 K, i.e. above T_C, one should in principle only get information on the basic c(8×2) reconstruction, see Fig. 5.4(d). The unit cell shows two types of intensity profiles, a sharp and a broad one, where the broad shape appears to be a double row, see marker in Fig. 5.8(a). The line-profile across the central maxima of Fig. 5.8(b) along the white

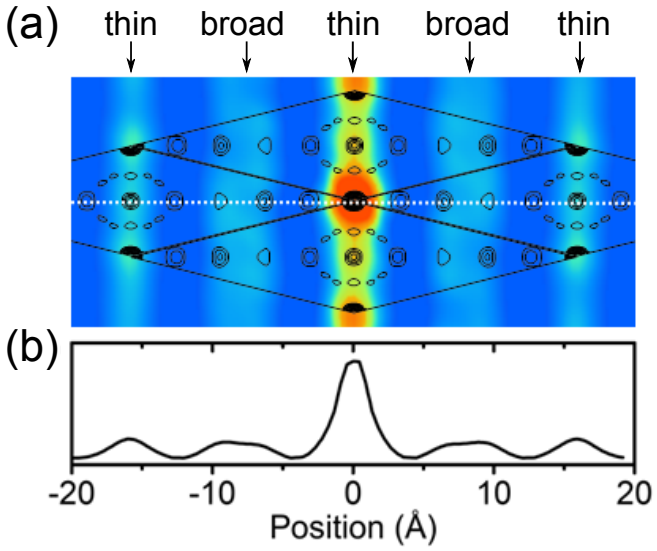

Figure 5.8.: *(a) Autocorrelation map generated from defect-free STM image of ∼60 nm². Two types of intensity distributions are present of broad and thin shape. The overlay with the SXRD Patterson map already indicates qualitative agreement for maxima leading to $\vec{d}_{2,3,5}$ which is supported within a 10% error by the line-profile of (b). From [10].*

dotted line in (a), reveals a distance of 16 Å ($\vec{d}_5$) between sharp lines, which directly reflects the wire periodicity. The distances from a sharp line to both maxima of a neighboring broad line account to 7 Å and 8.6 Å, which can be related to $|\vec{d}_2|$ and $|\vec{d}_3|$ within a 10% error bar. Thus, the three most intense maxima ($|\vec{d}|_{2/3/5}$) found in SXRD can be confirmed by the autocorrelation map from STM. The quantitative match is indicated by the overlay of the SXRD Patterson map in Fig. 5.8(a). The lack of the remaining SXRD distances $|\vec{d}_1|$ and $|\vec{d}_4|$ might be due to the technical limitation of STM i.e. probing the local charge densities of the top most layer or thermal drift during the measurement.

The obtained distances can now be used to check for consistencies by means of the already proposed structural models. On the basis of Au coverage and the distance vectors some formerly proposed complex structures can be excluded. Among them is the Giant-Missing-Row model by van Houselt et al. [124], where Ge dimers are on top of the ridges with $\sqrt{3} \times \sqrt{3}$-Au facets at the sidewalls of the nanowires. The model was originally proposed on a reported coverage of 0.2-0.3 ML of Au [124], yet a refined modeling states an Au coverage of 1 ML [129]. Both values do not fit to the results by Gallagher *et al.* [43]. Furthermore; the calculated total free energies in DFT render the model unfavorable [129]. Here, a modified version was proposed by Sauer et al. [129] to account for the right coverage of 0.75 ML Au with initial Au-dimers on top of the wire ridges which switch to sidewall facets after relaxation in DFT. This ATSGR-model (Au trimer stabilized Ge ridge) can be excluded from SXRD and will not be discussed in more detail because it is incompatible with the Patterson map presented here.

5.3. Minimal Structural Model

In order to construct a "minimal structural model", one has to consider how the three Au atoms per half unit cell can be arranged to account for the distances found in SXRD. Indications come from STM topography at ∼600 K, where only the c(8×2) reconstruction is present [123]. The occupied states at -0.8 V in Fig. 5.4(d) still exhibit a faint buckling along the wire, although with a small amplitude. The typical substructure of V- and W-shape observed at low temperature has vanished. The remaining shape reminds of a rope of pearls which is elongated such that the former sideward displacement is reduced. STM line-profiles across the wire at room temperature were already interpreted in terms of a single atom width [1]. This impression is substantiated by the subsequent studies at elevated temperatures where the nanowire ridge appears too sharp to result from a flat dimer [123].

The zig-zag along the wire can have two possible origins: a structural buckling or alternating electronic contrast that originates from different orbitals. Both scenarios are plausible for (i) a buckled hetero-dimer of Au and Ge, or (ii) a single atom, exhibiting a small zig-zag along the wire. For both options one of the three Au atoms per half unit cell is required. Experimental evidence for a buckled dimer within the wire architecture was brought forward recently by Mocking *et al.*, who reported a dynamical flipping mode of wire segments close to defects in STM images [126].

Allocating one of three Au atoms to the wire ridge leaves two remaining Au atoms to be incorporated in the trenches. The fact that any applied voltage causes a homogeneous and flat appearance of the trenches in STM makes it plausible to assume a flat Au homo-dimer as a structural building block. On the basis of these two elements, i.e. a

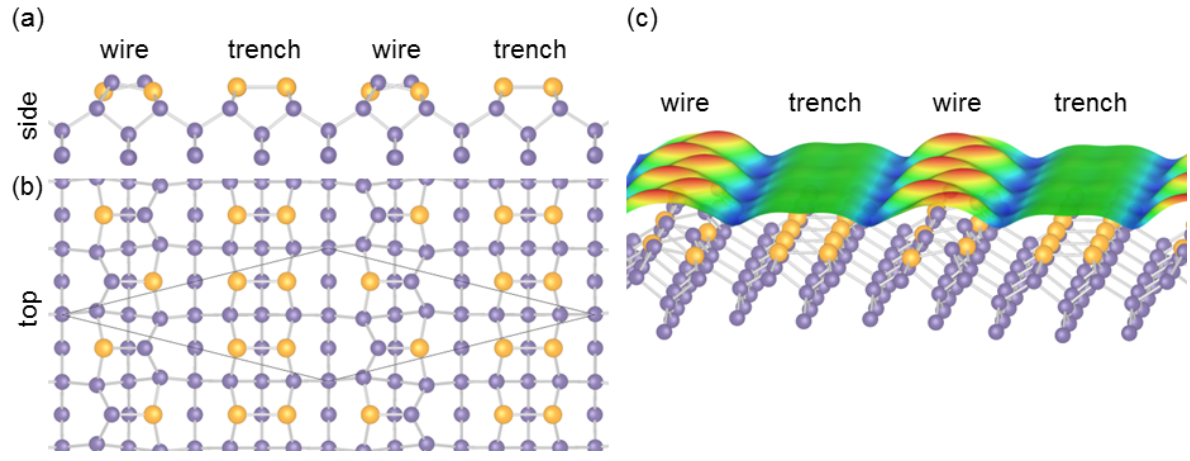

Figure 5.9.: *(a) Side view of "minimal model" after relaxation in DFT. Au-Ge hetero-dimers are buckled with Ge on top, while the Au homo-dimers remain flat. (b) Corresponding top view. (c) 3D view with overlay of occupied states at -1 V. The trenches appear flat, while the pronounced zig-zag along the wires originates from Ge, not from Au. From [10].*

hetero-dimer for the wire and homo-dimer for the trench, a "minimal structural model" can be constructed. Thereby only the Au-Au distances from the Patterson map are considered. The Au-Ge distances have to be neglected to reduce the parameter set, which explains the "minimal" character of the model.

These two types of dimers can be implemented in the bare Ge(001) surface by substituting one Ge (2×1) double-row completely with Au homo-dimers and the neighboring row only partially, i.e. one of two Ge-dimer atoms is replaced by Au, see Fig. 5.9(a). Both elements are located at the same height since no information on the vertical arrangement has been included up to this point. This arrangement of double rows resembles the proposal by Wang *et al.* [44], but with both building blocks switching position. The wire is made of Au-Ge hetero-dimers instead of Au-Au homo-dimers, whereas it is the other way round for the trench. This configuration now also matches the right c(8×2) symmetry as concluded from LEED, while Wang and co-workes favored a (4×2) reconstruction.

Relaxation of the "minimal" model by DFT

To gain a relaxed version of the model, DFT calculations were performed with an exchange-correlation functional within the generalized gradient approximation (GGA). The energy gain amounts to $\Delta\Omega_f^{GGA} = -0.7$ eV per unit cell compared to the bare

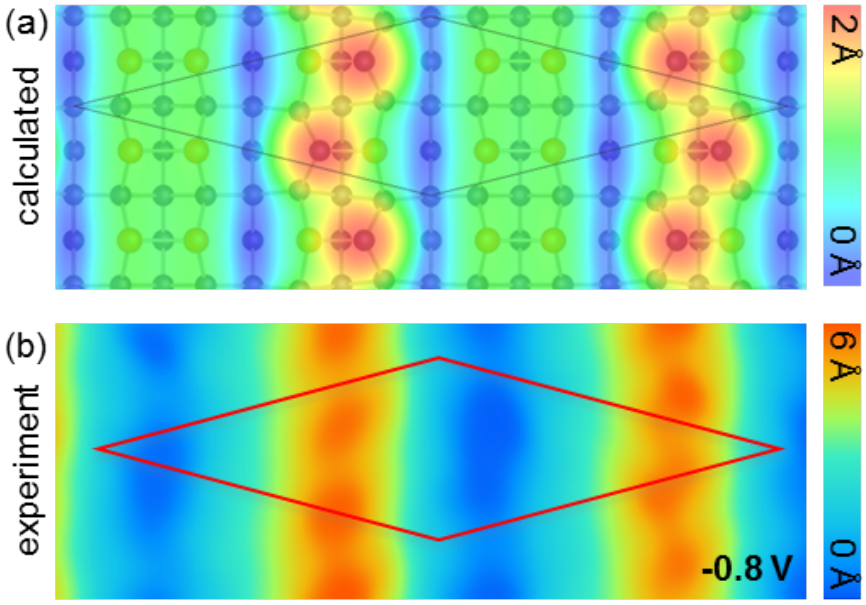

Figure 5.10.: *Occupied states at (a) -1V from DFT calculations showing a pronounced zig-zag along the wire originating from the Ge atom within the hetero-dimer. The shape of both wire and trench qualitatively match the experimental data at -0.8V recorded at $T = 600$ K (b). From [10].*

Ge(001) surface, as already reported in Ref. [129], see the equivalent *AD/HD* model therein. The minimization of the total free energy yields the modified coordinates also in the vertical direction. The relaxed form is presented in Fig. 5.9. The relaxation causes the hetero-dimers to get buckled with the Ge atom slightly located above the Au atom, while the homo-dimers in the trenches remain flat and are on the same height as the Au atom of the mixed dimer (see side view). From the top view of Fig. 5.9(b) a ladder structure for the trenches and a zig-zag along the wire is apparent. The overlay of the model and the corresponding calculated STM topography image from DFT in Fig. 5.9(c) reveals Ge as the origin of the pronounced charge clouds building the zig-zag along the wire direction, while the electronic contribution of the Au atoms is rather low.

The direct comparison of both calculated and experimental topography is presented in Fig. 5.10. There is an overall qualitative agreement concerning the shape of the trenches and the wires, albeit with a reduced height of the calculated wires. They also experience a more pronounced zig-zag along the chain direction. Nice agreement exists for the rather structureless trenches of the non-buckled Au homo-dimers exhibiting a ladder arrangement with a 4 Å periodicity.

Calculated Patterson maps for minimal model

Since the DFT relaxation varies all three real space coordinates, the Patterson map was calculated for (i) the non-relaxed version and (ii) the refined set of atom positions

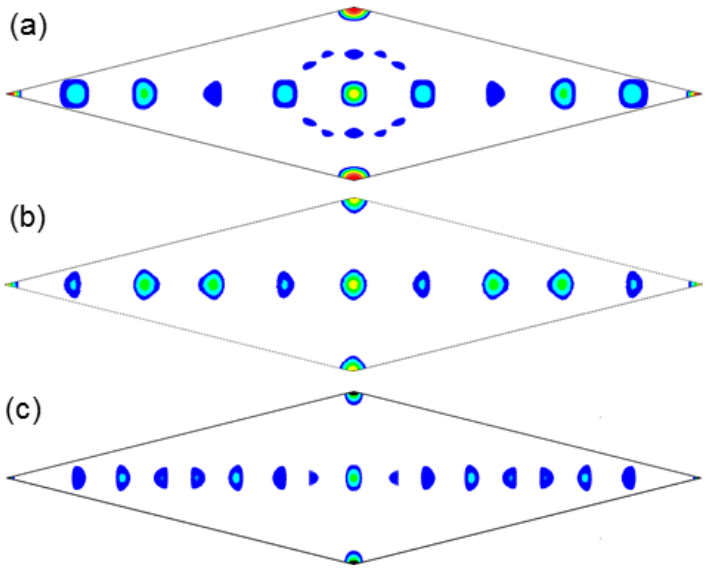

Figure 5.11.: *Patterson maps: (a) Experimental results. (b) Calculation for the unrelaxed "minimal" model. The positions of the experimental maxima are nicely reproduced. The intensity distribution is slightly changed. (c) In case of the relaxed configuration a splitting of the maxima corresponding to* $|\vec{d}_{2/3/4}|$ *is observed. From [10].*

as an additional cross-check. The comparison is presented in Fig. 5.11. For the non-relaxed version in (b) all 5 different main maxima from the experiment in (a) are present, although with a different intensity modulation. While in experiment all maxima have different intensities, the non-relaxed model yields the same values for peak 1(2) and 4(3). Note that the circularly arranged peaks from the experiment related to Au-Ge are always missing in the calculation due to the chosen simplification. Observing the relaxed version of the model in Fig. 5.11(c) one finds noticeable discrepancies. The former peaks related to $|\vec{d}_{2/3/4}|$ are split, giving rise to a number of new vectors which obviously do not match the experiment. Since the change mainly concerns $|\vec{d}_{2/3}|$, which are the vectors related to the hetero-dimer of the wire, the deviations must be primarily a consequence of the buckling of the dimer caused in DFT.

5.4. Chemical environment from X-ray core-level spectroscopy

As already stated in the introductory part on photoemission (see chapter 3), the x-ray regime gives access to the core-level electrons and their element specific binding energies. Here, different types of bonding environments that are element-specific individually contribute to the corresponding XPS spectra. The following analysis of the XPS data on Au/Ge(001) will assess the chemical surroundings for both Au and Ge to understand whether there is evidence for or against the "minimal model". Successful analyses of the chemical shifts that are involved in such nanowire systems are reported for In/Si(111) [130], Au/Si(5 5 12) [131] and Pb/Si(557) [132].

XPS analysis of bare Ge(001) as described in literature

To understand the influence of the gold-induced reconstruction on the bare germanium substrate, it is inevitable to apprehend the core-level spectra of Ge(001). As an example the analysis of Eriksson and Uhrberg is presented in Fig. 5.12. They used a model of five Ge layers for the c(4×2) reconstruction of Ge(001) [133], see Fig. 5.12(a). Layer four represents the bulk, while the next layer (number 3) is relaxed in the vertical direction due to the onset of the surface reconstruction. Layer two is already shifted within the surface plane and does not share the bulk periodicity. The topmost layer contains the two buckled configurations "up" and "down" of the top dimer atoms which are frozen in within the c(4×2) reconstruction.
According to these layers the Ge 3d core-level is deconvoluted using five Voigt doublets, see dotted line in Fig. 5.12(b). The fitting parameters are used from calculations within a final state picture (for details see Ref. [133]). The parameters are listed in table 5.2 together with those from Goldoni *et al.* [134] and Pi *et al.* [135]. Although not all values coincide, this set of parameters gives a confined interval for the XPS analysis

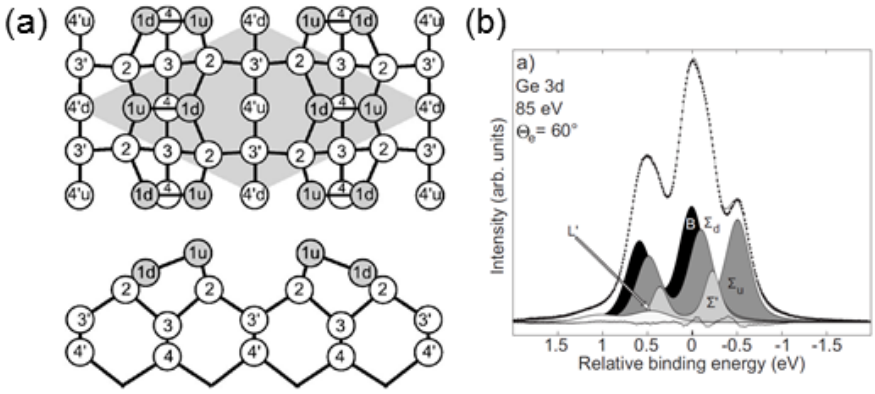

Figure 5.12.: *(a) Top and side view of the four top layers of the c(4×2) reconstruction of Ge(001). (b) Ge 3d core-level and corresponding deconvolution with five different components. Figure reprinted with permission from P.E.J. Eriksson and R.I.G. Uhrberg, Phys. Rev. B 81, 125443 (2010), http://link.aps.org/doi/10.1103/PhysRevB.81.125443 [133]. Copyright (2012) by the American Physical Society.*

on Au/Ge(001) concerning the Lorentzian width (LW), the Gaussian width (GW), the spin-orbit splitting Δ_{SO} within the Ge 3d level and the branch ratio of $3d_{3/2}$ and $3d_{5/2}$.

Author	Ref.	LW	GW	Δ_{SO}	$3d_{3/2}/3d_{5/2}$
Uhrberg	[133]	0.15 eV	free	0.59 eV	0.64-0.707
Goldoni	[134]	0.15 eV	0.35 eV	0.59 eV	0.61
Pi	[135]	0.18 eV	0.27 - 0.44 eV	0.561-0.594 eV	0.66

Table 5.2.: *Fitting parameters for Voigt doublets (convolution of a Lorentzian and a Gaussian line shape) used in Ge 3d core-level analysis.*

XPS on Au/Ge(001)

The Ge 3d core-level of Au/Ge(001) has been measured as a function of the photo-electrons' emission angle. The spectra were best deconvoluted when using three Voigt doublets. The free parameters were the Gaussian width, the peak positions and the peak height. The Lorentzian width was fixed at 0.15 eV, the spin-orbit splitting Δ_{SO} was set within the range of 0.56 eV to 0.59 eV, and a branch ratio between $3d_{5/2}$ and $3d_{3/2}$ of 0.65 to 0.7 was used. For Ge 3d a photon energy of $h\nu = 130$ eV results in a kinetic energy of roughly 100 eV, which is not exactly the surface sensitive minimum from the inelastic mean free path (see Fig. 3.2). To increase surface sensitivity, the spectra were recorded as a function of the emission angle.

The deconvolution of the spectrum recorded at normal emission in Fig. 5.13(a) yields three components: The main line (bulk) located at -29.3 eV and two surface-derived

Author	Ref.	bulk	surface	up	down
Uhrberg	[133]	0 eV	-0.23 eV	-0.51 eV	-0.10 eV
Goldoni	[134]	0 eV	-0.24 eV	-0.53 eV	+0.19 eV
Pi	[135]	0 eV	+0.09 eV	-0.442 eV	-0.10 eV

Table 5.3.: *Surface core-level shifts accounting for four different surface components within the Ge 3d core-level.*

components at -29.15 eV (SC 1) and -29 eV (SC 2). Increasing the angle from the surface normal towards the surface by 25° does not affect the spectrum significantly, see Fig. 5.13(b). For 45° off normal, which represents the most surface-sensitive measurement, a slight transfer of spectral weight appears from the supposed bulk component at -29.3 eV to the first surface component at -29.15 eV, while the lowest binding energy component at -29 eV remains unaffected. The fitting parameter are listed in Tab. 5.4. The XPS surface components for Au/Ge(001) are shifted by -0.15 eV and -0.3 eV relative to the bulk. This is in qualitative agreement with the results by Eriksson and Uhrberg in Tab. 5.3 on the bare Ge(001) surface, where surface core-level shifts of -0.1 eV and -0.23 eV were reported. The component for the up-dimer of the bare Ge(001) with a shift of -0.5 eV seems lacking in the spectra for Au/Ge(001). This was already reported by Niikura *et al.* [127], although without mentioning explicit values used for their fit analysis. They interpreted this fact as an exclusion of Ge homo-dimers as building blocks for Au/Ge(001).

Using the "minimal structural model" according to the layer assignment by Uhrberg *et al.* yields four positions for Ge: The up position within the hetero-dimer, the second,

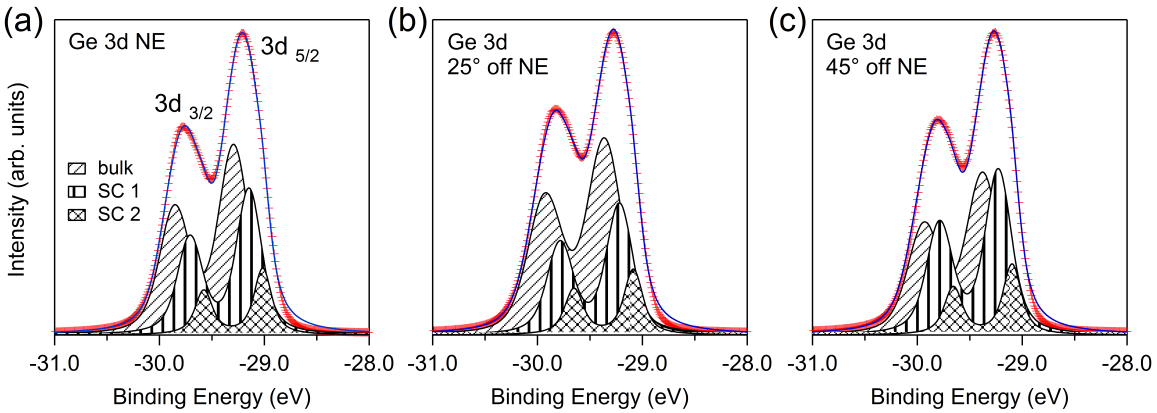

Figure 5.13.: *Germanium 3d core-level of Au/Ge(001) as a function of electron emission angle: (a) Normal emission (NE), (b) 25° off normal and (c) 45° off normal. All spectra can be deconvoluted using three Voigt doublets (bulk, SC 1 and SC 2) and a Shirley background subtraction. A slight transfer of spectral weight is observed between the bulk and the SC 1 peak at 45° off normal.*

Component	abs. Energy	rel. E_B	LW	GW	Δ_{SO}	ratio
Ge bulk	-29.3 eV	0 eV	0.15 eV	0.2 eV	0.56 eV	0.66
Ge SC 1	-29.15 eV	-0.15 eV	0.15 eV	0.15 eV	0.56 eV	0.66
Ge SC 2	-29.0 eV	-0.3 eV	0.15 eV	0.1 eV	0.56 eV	0.66

Table 5.4.: *Fitting parameters for all three Voigt doublets used in the Ge 3d core-level analysis.*

third and fourth layer. From the three XPS components in Fig. 5.13 the peak at highest binding energy of -29.3 eV must be attributed to bulk Ge, i.e. in a rough estimate the third and fourth layer of the bare Ge(001) model by Uhrberg. The next component at -29.15 eV would best fit the down Ge dimer of the bare Ge(001) surface, see Fig. 5.12(b), although the energy shift by 150 meV is slightly increased compared to the 100 meV in Tab. 5.3. Since the "minimal structural model" does not contain a down Ge-dimer, one may speculate if the bonding to an Au atom can account for such a chemical shift.

The remaining peak at -29 eV provides a closest match with the surface layer (Σ') described by Erikson and Uhrberg [133]. Thus, the one-to-one comparison with the bare Ge(001) surface supports the existence of the second, third and forth germanium layer as implemented in the "minimal structural model". The peak at -29.15 eV provides evidence for an additional Ge atom, but would better fit a down Ge-dimer as concluded from the bare Ge(001) surface rather than the Au-Ge hetero-dimer used in the model.

The same analysis was performed for the Au $4f_{5/2}$ and Au $4f_{7/2}$ core-levels. The photon energy of $h\nu = 130$ eV gives a kinetic energy of about 50 eV which is close to the minimum of the universal curve of the inelastic mean free path. The surface sensitivity was further enhanced by choosing an escape angle of 25° off normal. The corresponding spectrum of Fig. 5.14 can be deconvoluted by two Voigt doublets with a

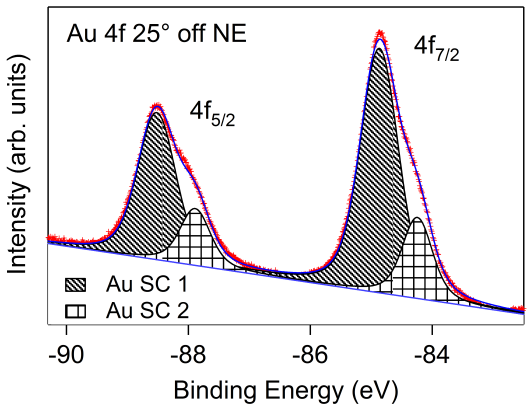

Figure 5.14.: *Gold 4f core-level of Au/Ge(001) at 25° off normal emission. The spectrum can be deconvoluted with two Voigt doublets which exhibit a spin-orbit splitting Δ_{SO}=3.65 eV. In contrast to the Ge 3d core-level a linear background subtraction yielded the best fitting results.*

Component	Energy	LW	GW	Δ_{SO}	ratio
Au SC 1	-84.87 eV	0.25 eV	0.59 eV	3.65 eV	0.6
Au SC 2	-84.24 eV	0.27 eV	0.42 eV	3.65 eV	0.7

Table 5.5.: *Fitting parameters from both Voigt doublets used in the Au 4f core-level analysis.*

spin-orbit splitting of $\Delta_{SO} = 3.65$ eV [115]. Both the Lorentzian (LW), the Gaussian line width (GW) and the spin-orbit splitting were free fitting parameters. The branch ratio was set within the range of 0.6 - 0.7. The resulting values of the converged fit are given in Tab. 5.5.

Both binding energies -84.87 eV and -84.24 eV are slightly increased compared to the general accepted position of -84 eV. The Lorentzian widths from the fit qualitatively match results of polycrystalline Au films in Ref. [136]. Fitting a Doniach-Šunjić line shape [76] to the data did not produce any asymmetry as one would expect for a metallic material. In terms of chemical components, the two doublets of the Au 4f core-level spectrum favor two different bonding sites, which would be consistent with the "minimal structural model". However, the intensity ratio of both components from their integrated spectral weight accounts to 77%:23%. This is close to 3:1 which diverges from the 2:1 ratio that we would expected from the "minimal structural model". One explanation for this deviation might be further contributions to SC1 by additional, bulk-segregated Au atoms. In principle the core-level analysis does qualitatively support the bonding sites for Ge and Au as proposed in the "minimal model".

Asymmetries in core-level line shapes

An asymmetric line shape is expected in case of pronounced interaction between the positively charged core-hole and any mobile conduction electrons in the Fermi sea, i.e. mainly in a metal. This process was first theoretically described by Mahan [137]. According to Doniach and Sunjic [138] the line shape follows:

$$I(E) = \frac{\Gamma(1-\alpha)}{(E^2+\gamma^2)(1-\alpha)/2} \cos\left(\frac{1}{2}\pi\alpha + \Theta(E)\right), \tag{5.1}$$

$$\Theta = (1-\alpha)\tan^{-1}(E/\gamma), \tag{5.2}$$

with the Γ-function and the natural line shape γ of the hole state . $0 < \alpha < 1$ leads to additional intensity on the side of higher binding energies which results in an asymmetric line shape. Investigations of elemental 4d and 5d metals [139] revealed a pronounced asymmetry for Rh and Pd for the 3d core-level whereas the effect appeared to be very weak for Ag. In case of the 5d metals Ir and Pt showed a discernable asymmetry, while Au did not.

Applying a corresponding fit model to the data of Au/Ge(001) yields a vanishing asymmetry parameter. This behavior may be related to the unusual phase of the electronic states of Au/Ge(001) which deviates from a simple metals as will be discussed in the following chapters. Reports from the literature of truely metallic nanowire systems that show an asymmetric core-level line shape comprise:

- Au/Si(5 5 12) [131], although very faint without quantitative evaluation.
- In/Si(111), with an asymmetry of 0.09 at RT and 0.18 in the low-temperature phase [130].
- Pb/Si(557), with $\alpha = 0.11$ [132].

For all these mentioned systems the asymmetry was interpreted as an indication of metallicity in accordance with metallic surface states observed in the band structure.

Summary of the structural investigations

To summarize, the structural experiments by SXRD, STM and DFT provide:

- The in-plane distances between the gold atoms for the c(8×2) unit cell.
- A cross-check for any model by calculating its Patterson map and compare it with the experiment.
- Two structural building blocks - Au-Ge hetero-dimers and Au homo-dimers.
- The germanium orbitals dominate the charge distribution along the wire in the present model, as judged from DFT. Thus, Ge may play an important in the wire architecture.

To finally resolve the complete atomic arrangement, one has to include:

- The Au-Ge distances, which had been neglected so far.
- Surface truncation rods as a function of l (surface normal) to account for vertical relaxation.
- The additional p(4×1) superstructure, which was not accessible so far by SXRD due to the low signal. But also for theoretical investigations an increased real space unit cell causes a much more complex handling and increased computing power.

Thus, further experimental evidence, e.g. by SXRD, is necessary to refine the “minimal structural model”, which then should finally allow to calculate its band structure by DFT. XPS can support proposed bonding sites, as in case of the “minimal structural model”. Again, an extended data set mostly for Au is desireable to refine the 4f spectra. Here, partially covered Au/Ge(001) might be suitable to study the contributions of subsurface or randomly adsorbed Au atoms to XPS spectra.

6. Electronic states of Au/Ge(001) from ARPES

As apparent from its real space appearance, Au/Ge(001) provides all requirements to allow electronic phenomena emerging in reduced dimensions. Thus, the band structure will be analyzed in detail for new reconstruction-induced states. The dimensionality of the electronic states will be checked by their Fermi surface topology. Temperature dependent measurements are performed to look for metal-insulator or metal-superconductor transitions within the band structure. A detailed description of the electronic ground state properties will be obtained from line shape analysis of the individual bands.

Bulk Germanium is known to be insulating with an indirect band gap of ~ 0.67 eV at room temperature (RT) [52]. First angle-resolved photoemission data on the reconstructed Ge(001) surface revealed a surface state close to E_F. It was interpreted to be metallic and related to the (2×1) reconstruction since it vanished simultaneously to the phase transition from the (2×1) to the c(4×2) reconstruction upon cooling [140, 141]. Subsequent ARPES studies [142–144] consistently reported an energy gap at RT (although varying in size, but in the order of several 100 meVs) with an anti-bonding π^* band above E_F resulting from the dimer down atoms. Recent scanning tunneling spectroscopy data suggested a metallic surface state to originate from the (2×1) reconstruction, while the c(4×2) did not show a finite density of states at the Fermi level [116]. Thus, under the assumption of an insulating substrate, any states found for Au/Ge(001) in the Ge gap region around E_F can be attributed to the new surface reconstruction formed by metal adsorption.

6.1. Surface Brillouin zone and high-symmetry lines

An orientation guide to the high-symmetry points and lines in k-space is provided by the surface Brillouin zone (SBZ). Therefore the real space lattice of one single domain of Au/Ge(001) with a c(8×2) symmetry ($2\times a_0$ periodicity along the wire and a $8\times a_0$ perpendicular to it) has to be Fourier-transformed, see Fig. 6.1. The resulting SBZ for Au/Ge(001) is of hexagonal shape.

The full SBZ scheme for a dual-domain sample is obtained by doubling, rotating of the second SBZ by 90° and overlay with the first one as sketched in Fig. 6.2. Three high symmetry points exist: $\bar{\Gamma}$, $\bar{K}$ and $\bar{M}$. The sample can be aligned with the six-axis goniometer, see Appendix 9, such that the wire direction for one domain coincides with

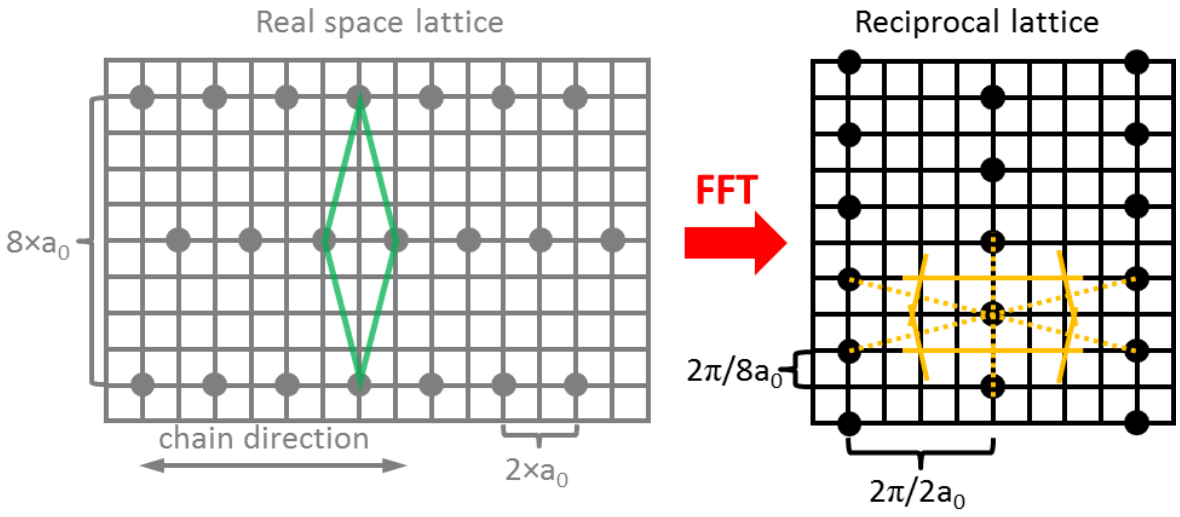

Figure 6.1.: *Real space lattice for one domain of c(8×2) symmetry (primitive cell in green), where the periodicity along the wire accounts to 2×a_0 and 8×a_0 perpendicular to it. After Fourier transformation the SBZ can be constructed connecting all nearest neighbor sites for one lattice point (dotted orange). The orthogonal lines on these connections yield the surface Brillouin zone (solid orange), which is of hexagonal shape.*

the dispersion detecting window of the analyzer. The measurement direction including normal emission (the $\bar{\Gamma}$ point) thereby follows the $\bar{\Gamma}$-$\bar{K}$ line within the first SBZ and crosses the $\bar{M}$-point along the outer border of the second SBZ.

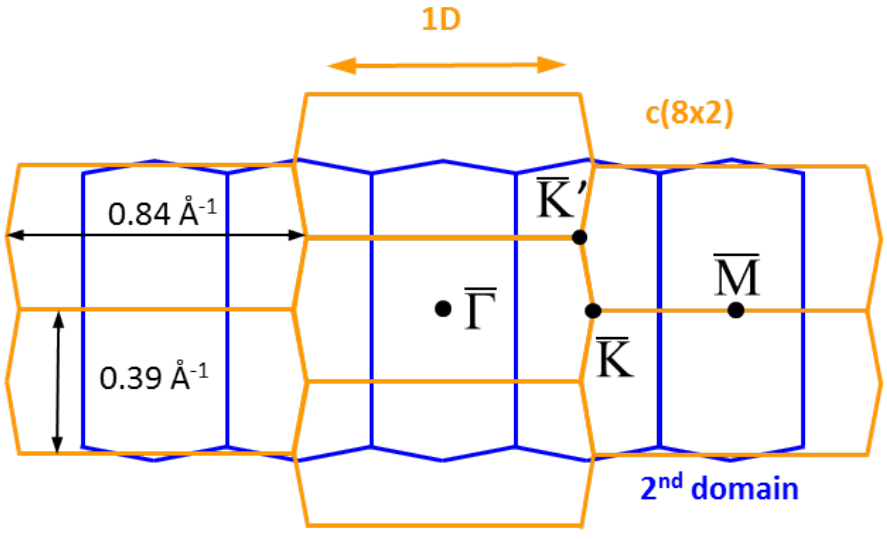

Figure 6.2.: *Surface Brillouin zones for a dual-domain Au/Ge(001) sample. The long side of the hexagon corresponds to the nanowire direction (orange). The high symmetry points $\bar{\Gamma}$, $\bar{K}$ and $\bar{M}$ are labeled for the same domain.*

6.2. Main dispersions along the $\bar{\Gamma}$-$\bar{K}$ line

Electron-like dispersion and its characteristics

The central dispersion along the high-symmetry line along $\bar{\Gamma}$-$\bar{K}$ is presented in Fig. 6.3(a) for $h\nu = 100$ eV. Thise photon energy is a compromise between the beamline limitation ($80 - 200$ eV, beamline 7.0.1 Advanced Light Source, Berkeley USA) and the energy dependent spectral weight given to the observed states. The combined energy resolution of beamline optics and electron analyzer was set to $\sim$ 30 meV. The band maps were recorded at T = 15 K to reduce the thermal broadening. The light polarization was limited to linear horizontal with the light wave vector being parallel to one of the nanowire directions and perpendicular to the other domain.

The main feature of the band map are two small bands located on either side of the $\bar{\Gamma}$-point at $k_x = \pm 0.2$ Å^{-1} right below the Fermi energy E_F. Their dispersion is reminiscent of an upward parabola, i.e. the state is "electron" like. The band depth as judged from the energy distribution curve (EDC) in Fig. 6.3(b) accounts to $\sim$ 130 meV below the Fermi energy. The band crosses E_F at the Fermi vectors of $k_F = \pm 0.26$ Å^{-1} and $k_F = \pm 0.14$ Å^{-1}. Assuming a parabolic shape for this electron pocket, one can determine the *effective mass* m^* according to $E(k) = \frac{\hbar^2(k-k_{BB})^2}{2m^*} + E_0$, where $k_{BB} = 0.2$ Å^{-1} represents the location of the band bottom (BB) at binding energy $E_0 = -0.13$ eV. The calculation yields an effective mass $m^*_{pocket} \sim 0.1 m_e$, where m_e denotes the free electron mass. By tuning the color code and contrast of the very same data set, a second state is revealed at the $\bar{\Gamma}$-point, see Fig. 6.3(c). It was only faintly visible in Fig. 6.3(a) and is of hole-like character with a downward dispersion of parabolic shape. This band

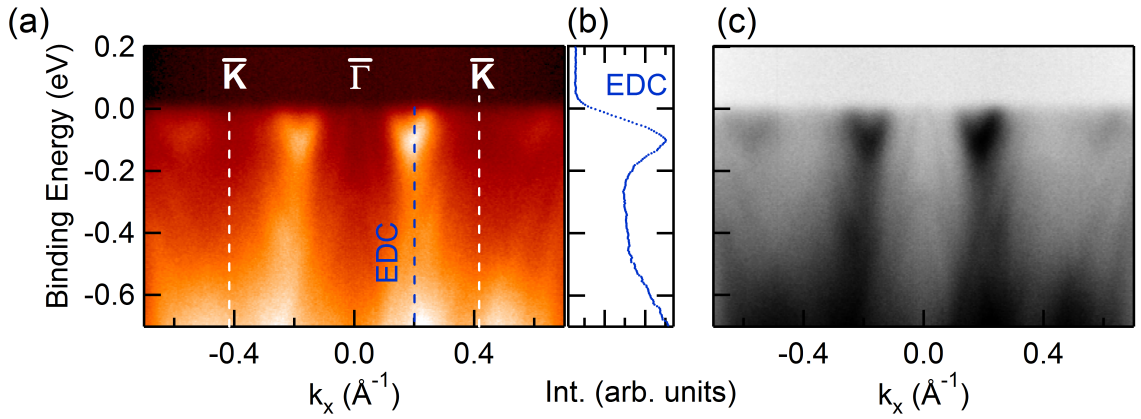

Figure 6.3.: *(a) Band map along the high symmetry line $\bar{\Gamma}$-$\bar{K}$ recorded at $T = 15$ K with $h\nu = 100$ eV. Two shallow electron pockets induced by the metal reconstruction are observed on either side of $\bar{\Gamma}$. The band width as judged from the EDC (blue line) in (b) is approximately 130 meV. (c) Tuning the color contrast reveals a second band cutting the Fermi level which is centered at the $\bar{\Gamma}$-point. It exhibits the shape of a downward parabola like the Ge heavy- and light-hole branches.*

seems to resemble the well known valence band of Ge with heavy- and light-hole branches [142] and will be discussed in detail in the following sections.

To prove the origin of the electron pocket, slight variations of the photon energy were performed, i.e. $h\nu = 90$ eV and $h\nu = 110$ eV, yielding the same band situation with the same $k_{(x/y)}$ values. The absence of any perpendicular ($k_\perp$) dispersion determines the *surface character* of this state. Since no such dispersion is known from the bare Ge(001) surface [142], it must be induced by the chain formation.

Assignment of the dispersion direction

The band bottom of the electron pocket is located at $k_x = \pm 0.2$ Å^{-1}. As apparent from the sketch of the Brillouin zone scheme for two domains in Fig. 6.2, two different scenarios are possible to assign the dispersion direction. From a structural point of view only a dispersion along the nanowire direction seems reasonable. Within this picture the yellow flat hexagon would apply with the band bottom ($k_x = 0.2$ Å^{-1}) roughly at half way from $\bar{\Gamma}$ towards the zone boundary ($k_x = 0.42$ Å^{-1}) as sketched in Fig. 6.4(a). In contrast, the counterintuitive case of a dispersion direction perpendicular to the real space wire direction yields a band bottom for the electron pocket directly at the zone boundary, see Fig. 6.4(b).

In the latter case one would expect conducting channels perpendicular to the chain direction in STM images. These channels would also be aligned in parallel and thus should interrupt the chains forming segments. This is obviously not observed in the experiments [1, 123]. In fairness, a clear assignment of the band to a real space axis cannot be made using a dual-domain sample. Following the above given arguments, the dispersion will be related to the wire direction in the following discussion. Within this scenario the electron pocket is assumed to be a one-dimensional (1D) band with a detailed dispersion analysis given in the next chapter.

Using the size of the surface Brillouin zone one can determine the band occupation f, which is the ratio of the occupied k-space $\Delta k_F = 0.12$ Å^{-1} compared to the long side of the SBZ hexagon (0.84 Å^{-1}, see Fig. 6.2(b). For one band $f = 0.142 = \frac{0.12}{0.84}$, while f accounts to ~ 0.3, if two bands are considered within the first SBZ. Notably, the

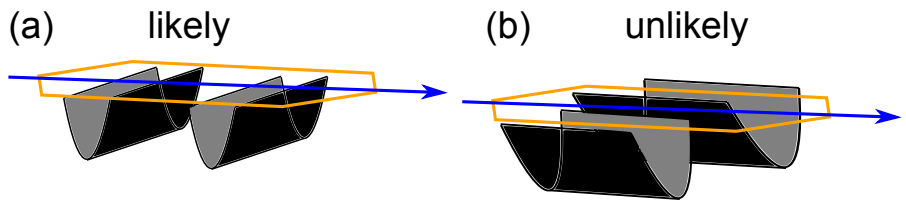

Figure 6.4.: *Scenarios for assigning the dispersion direction to the real space direction: (a) Dispersion along the wire direction with a band bottom of the electron pocket located roughly half way from $\bar{\Gamma}$ to the zone boundary. (b) Dispersion assigned to the direction perpendicular to the wires. Here, the band bottom is located at the zone boundary.*

band filling is incommensurate, which will be important when discussing the electronic ground state in terms of a Peierls instability or every other theoretical model typically assuming a filling of $f = \frac{1}{2}$.

Repetition scheme of the electron pocket

The repetition of the electron pocket in the next SBZ is already visible at $k_x = \pm 0.59$ Å^{-1} in Fig. 6.3(a), however with decreased intensity which must be attributed to matrix element effects [5]. By extending the detection window beyond the first SBZ as sketched in Fig. 6.5(a), both types of states are present along the SBZ boundary in (b). The electron pocket is located at $k_x = 0.59$ and 0.98 Å^{-1} (see white overlay) and the hole-like band at the $\bar{M}$-point ($k_x \sim 0.8$ Å^{-1}). Notably, the hole-like band is much more pronounced than within the first SBZ, while the electron pocket experiences a decrease in intensity in the second SBZ as indicated by the dotted red lines in the sketch of Fig. 6.5(a). To improve the contrast, the band situation is also depicted as a stack of energy distribution curves in Fig. 6.5(c), which clearly demonstrates the presence of three bands within the detection window.

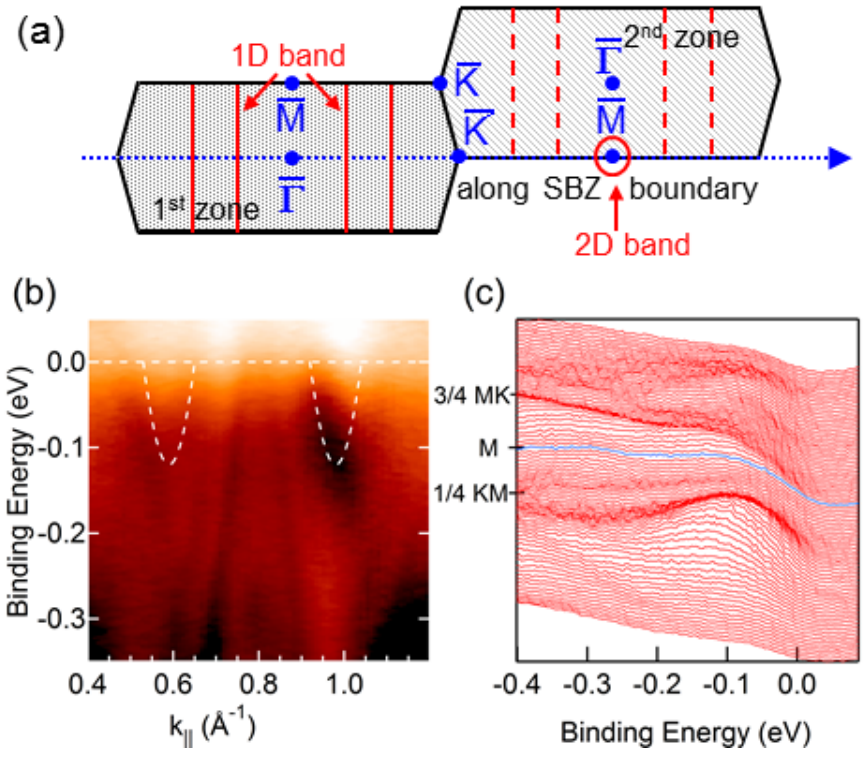

Figure 6.5.: *(a) Sketch of the band situation of the first and second SBZ. (b) Band map along the zone boundary of the second SBZ ($\bar{\Gamma} - \bar{K}' - \bar{M} - \bar{K}'$) with $h\nu = 100$ eV at $T = 15$ K revealing a parabolic band at the $\bar{M}$-point which is cut slightly below its top by the Fermi energy. (c) EDC stack revealing the presence of three bands along $\bar{K}' - \bar{M} - \bar{K}'$. From [5].*

6.3. Interface states and symmetries

Band maps as a function of photon energy

To study the influence of the photon energy on the two surface states observed for Au/Ge(001), additional ARPES measurements were conducted at the high-resolution photoemission (HRPES) endstation, surface and interface spectroscopy (SIS) beamline, the Swiss Light Source (SLS) Villigen CH. Here, a series of band maps was obtained along the high symmetry line along $\bar{\Gamma}$-$\bar{K}$ at $T = 10$ K. Starting again at $h\nu = 100$ eV in Fig. 6.6(a) the same band situation is found as for the ALS measurements. Notably, the hole-like state can be found at the $\bar{\Gamma}$-point as well as indicative for the repetition of the band at $k_x = 0.4$ Å^{-1} and $k_x = 0.8$ Å^{-1}.

The distribution of spectral weight changes only little at $h\nu = 80$ eV in Fig. 6.6(b), where the most intense electron pocket is found in the second SBZ at $k_x = -0.59$ Å^{-1}. Further lowering of the photon energy to $h\nu = 65$ eV reveals the hole-like parabola very clearly at $\bar{\Gamma}$ and $k_x = 0.4/0.8$ Å^{-1}, see Fig. 6.6(c), giving a repetition periodicity from band top (BT) to band top of $\Delta_k = 0.4$ Å^{-1}. For $h\nu = 55$ eV a second hole-like branch can clearly be identified below the initial parabola with its top at $E_B = -0.3$ eV which is reminiscent of the Ge split-off (SO) valence band. Thus, the parabola at the Fermi energy is related to the light-hole (LH) branch of the former Ge valence band. The determination of the effective mass by assuming a quadratic dispersion relation yields $m^* \in [0.03, 0.09]$, which is close to the literature value of 0.04 [145–147] [Note that m^* does not change significantly for different high-symmetry directions as concluded from the before mentioned references]. Within the band map series of Fig. 6.6 indications of the heavy-hole (HH) branch can be found at higher binding energies at $k_x = \pm 0.2$ Å^{-1}, whereas no intensity is observed for this branch for energies close to E_F.

Concerning the location of the hole-like states (LH, HH and SO) in real space, an interface state seems likely. Tunneling spectroscopy does not report a step in the spectrum above the Fermi energy [1], which is expected to appear for a true two-dimensional state whose density of states is constant over energy. Thus, the hole-like state must be attributed to *subsurface layers*. Similar dispersions of hole-like character have been observed for other metal-adsorbed Ge surfaces [148, 149] as well as for the related system of Au/Ge(111) [6], where the origin of these bands could be related to $\sim 10 - 20$ layers below the surface. Further decrease of $h\nu$ does not change the appearance of the electron pocket, see Fig. 6.6(e)-(h), but the distribution of spectral weight for the electron band changes quite strongly. While at $h\nu = 45$ eV in Fig. 6.6(e) only the outer branches of the two electron pockets around $\bar{\Gamma}$ are visible, the pocket at $k_x = 0.2$ Å^{-1} gets a symmetric shape for $h\nu = 35$ eV in Fig. 6.6(f). The very same band looses intensity at $h\nu = 30$ eV in Fig. 6.6(g) and disappears completely at $h\nu = 25$ eV in Fig. 6.6(h). This behavior demonstrates the strong influence of the matrix element effects in Au/Ge(001), where $h\nu = 100$ eV provides the best observation condition for the electron pocket, while the hole-like band dominates at $h\nu = 55$ eV.

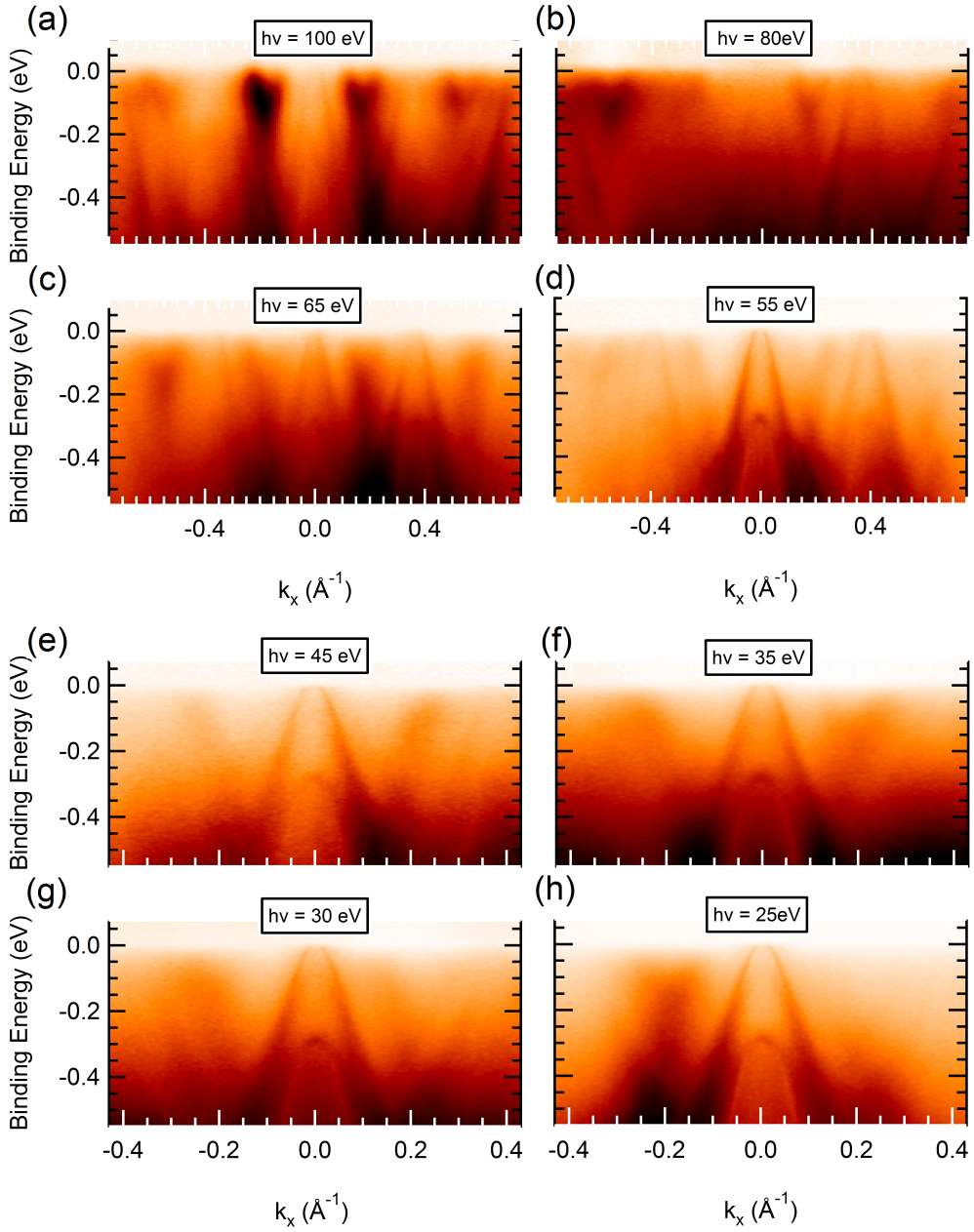

Figure 6.6.: *Band maps along $\bar{\Gamma}$-$\bar{K}$ as a function of $h\nu$ at $T = 10$ K: (a) at 100 eV main intensity is given to the 1D band. A second state is fairly visible in between with the shape of a downward parabola. The latter gains intensity at $h\nu$=80 eV, where the most intense 1D band is observed at $k_x = -0.59$ Å^{-1}. (c) An intermediate intensity distribution appears at $h\nu = 65$ eV, where both states are present. (d) $h\nu = 55$ eV suppresses the electron pockets, while the hole-like bands are well resolved. Lower photon energies (e) to (g) reveal the splitting of the hole-state with a split-off part at lower binding energies (top at $E_B = -0.3$ eV), while the distribution of spectral weight for the electron pocket changes such that no symmetric appearance on both sides of $\bar{\Gamma}$ is given at these energies.*

Constant energy contours

To reveal the presence of the heavy-hole branch and the symmetries of the electronic states, constant energy surfaces have been recorded for $h\nu = 55$ eV. These allow to trace the band dispersion in k_y direction, i.e. perpendicular to the wire direction as drawn in

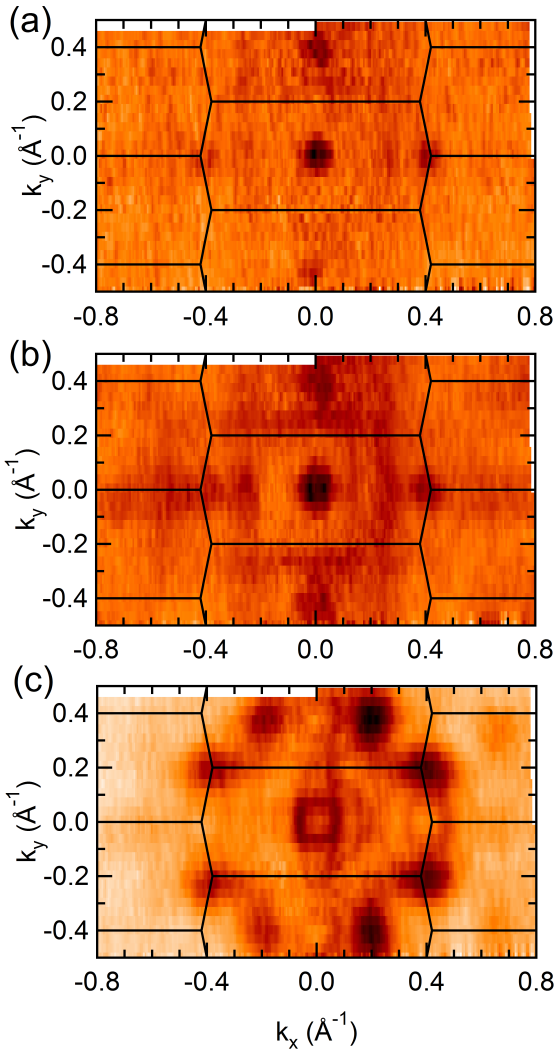

Figure 6.7.: *Constant energy surfaces recorded at $h\nu = 55$ eV and $T = 10$ K. (a) The Fermi surface is dominated by circular contours from the hole-like states located at $k_{(x/y)}$=(0/0), (0/±0.4) and (±0.4/0) Å^{-1}. No intensity is observed for the electron pockets which must be attributed to matrix element effects or the suppression of spectral weight. (b) Decreasing the binding energy by 40 meV reveals a square-like structure formed by the 1D band. (c) At $E_B = -0.22$ eV the 2D band dispersion clearly exhibits a circular shape. Additional features appear roughly at the corner of the hexagon, i.e. at $k_{(x/y)}$=(±0.2/±0.4) and (±0.4/±0.2) Å^{-1}.*

the 1D scenario. The Fermi surface displayed in Fig. 6.7(a) contains only contributions from the LH band which are of circular, i.e. clearly two-dimensional shape, located at $k_{(x/y)}$=(0/0), (0/±0.4) and (±0.4/0) Å^{-1}. The overlay of the surface Brillouin zone for one domain in black indicates that the LH bands are located at the outer tip of the lying hexagon (along $k_y = 0$), but for the equivalent direction where $k_x = 0$, the top of every LH parabola marks a middle of SBZ.

The 1D band cannot be distinguished, which must be related either to matrix element effects or suppressed spectral weight. The latter effect seems plausible since lowering binding energies by 40 meV leads to an intensity onset for the 1D band of square-like structure, see Fig. 6.7(b). The square-like shape can be understood from an electron parabola in one direction which is stretched in the perpendicular direction. The fourfold

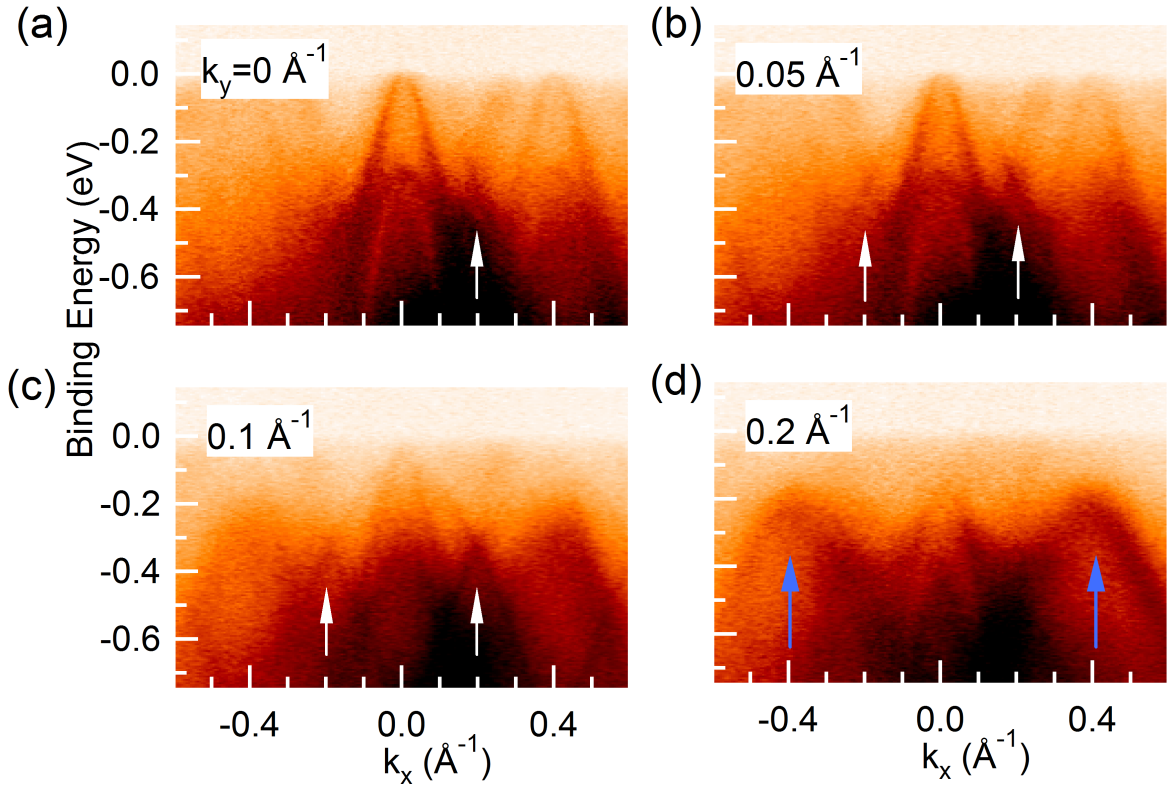

Figure 6.8.: *Band maps recorded at $h\nu = 55$ eV and $T = 10$ K as a function of k_y. (a) Already at $k_y = 0$ Å^{-1} a second branch of the 2D state disperses towards E_F (see white arrow). (b) Increasing k_y to 0.05 Å^{-1} reveals a crossing of this outer branch with its replica from the neighboring surface Brillouin zone. (c) At $k_y = 0.1$ Å^{-1} the crossing is best resolved while an additional occupied band appears at $k_x = 0.4$ Å^{-1}. (d) The band top of this additional hole-like state is located at $E_B = -0.25$ eV at for $k_y = 0.24$ Å^{-1} as marked by the blue arrows.*

symmetry results simply from the overlay with the second domain, which is rotated by 90°.

Cutting at higher binding energies, i.e. $E_B = -0.22$ eV as presented in Fig. 6.7(c), reveals the opening of the circular shapes at the positions of the hole-like band which exhibits a two-dimensional shape. The 1D bands have vanished due to the small band width of only ∼130 meV. In addition, new features appear at $k_{(x/y)} = (\pm 0.2/\pm 0.4)$ and $(\pm 0.4/\pm 0.2)$ Å^{-1}, which roughly marks the corner of the hexagonal SBZ. They also exhibit a circular shape.

To identify the new contributions at lower binding energies in the constant energy surfaces, band maps are inspected as a function of k_y, see Fig. 6.8. Starting at $k_y = 0$ Å^{-1} the LH state is visible at $k_x = 0$ and 0.4 Å^{-1}. At $k_x = 0.2$ Å^{-1} and $E_B = -0.3$ eV one gets the impression of a band crossing which is caused by the appearance of the heavy-hole (HH) branches now visible (see white arrow). Changing k_y to 0.05 Å^{-1} in Fig. 6.8(b) intensifies the impression of a crossing, which is now present on both sides of $\bar{\Gamma}$. The HH branch is best resolved for $k_y = 0.1$ Å^{-1} in Fig. 6.8(c). Increasing k_y to 0.2 Å^{-1} reveals an additional state at $k_x = 0.4$Å^{-1} (blue arrows) which exhibits a broad hump with its top at $E_B \sim -0.25$ eV. The top of this fully occupied state with a

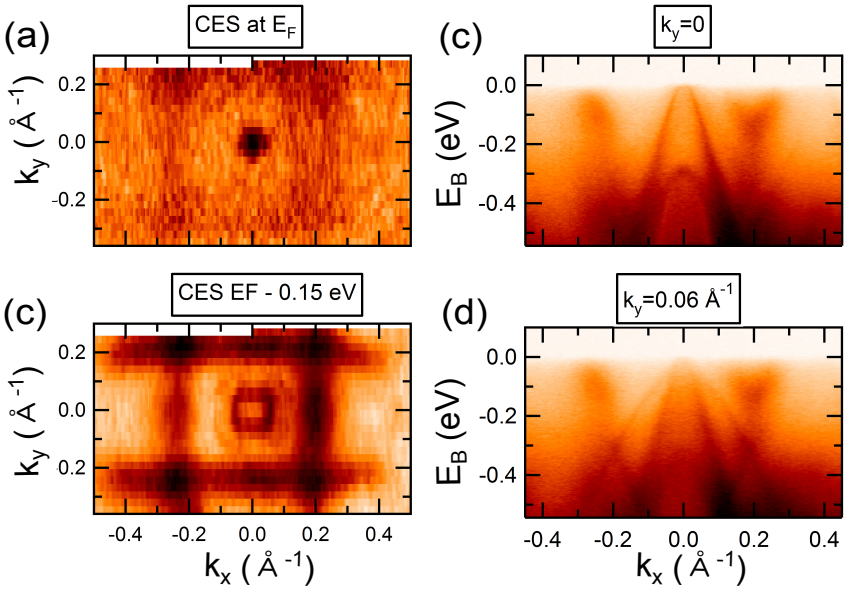

Figure 6.9.: *(a) Fermi surface at $h\nu = 35$ eV and $T = 10$ K. Beside the circular shape of the 2D band around $\bar{\Gamma}$ the intensity onset for the 1D band is already present at E_F. The enhanced intensity compared to the measurement at $h\nu = 55$ eV must be attributed to the different matrix elements at lower photon energies as concluded from the band map series. (b) Cutting the energy surface around the band bottom of the 1D band, i.e. $E_B = -0.15$ eV shows a twofold splitting of the 2D circular contour which originates from the two types of branches (light- and heavy-hole) being degenerate at the band top.*

hole-like dispersion is located at $k_y = 0.2$ Å^{-1} which coincides with the intense circular shapes found in the constant energy surfaces at $E_B = -0.22$ eV in Fig. 6.7(c). Due to the shape of this band it is called "garland band".

The same inspection is performed at $h\nu = 35$ eV, where the recorded k-window shrinks and narrow features can be better resolved. The changed matrix element allows the observation of the 1D band within the Fermi surface, although with weak intensity as seen in Fig. 6.9(a). Remarkably, the 1D band located at $k_x = -0.2$ Å^{-1} exhibits only the outer branch cutting the Fermi energy ($k_x = 0$ Å^{-1}) in Fig. 6.9(b) which causes an asymmetric appearance of the Fermi contour of the 1D band. Going to higher binding energies of $E_B = -0.15$ eV in Fig. 6.9(c) still reveals a square-like structure from the fading band bottom of the 1D band while the 2D state is now split into two circular shapes of light- and heavy-hole character, see Fig. 6.9(c). These two branches can be very well distinguished in the band map recorded at $k_y = 0.06$ Å^{-1} of Fig. 6.9(d) where two neighboring heavy-hole branches seem to cut each other well below the band bottom of the 1D band at $k_x = 0.2$ Å^{-1} at a binding energy of $E_B = -0.3$ eV. Since both HH branches share the same origin a hybridization gap should be observable, which in the present case must be of small size and thus below the detection limit. Any interference of the HH branch with the 1D electron pocket can be excluded since both do not overlap and are well separated in energy and momentum.

6.4. Electronic confinement of the electron pocket

The dimensionality of the two reconstruction induced states has already been revealed qualitatively from the constant energy surfaces at low photon energies (35 eV and 55 eV). The $h\nu$ dependent band maps have shown that the shape of the electron pocket can best be identified at $h\nu = 100$ eV. The idealized 1D situation is sketched in Fig. 6.10(a), where the electron pocket is stretched in k_y direction forming a Fermi surface without any lateral dispersion. The experimental counterpart is displayed in Fig. 6.10(b). It closely matches the ideal sketch just by adding a fourfold symmetry caused by the superposition of the two orthogonal domains. These are always included due to the photon spot size of ARPES ($\sim 100 - 200$ μm^2), which typically exceeds the terrace size for one single domain in STM ($\sim$100 nm^2) by several orders of magnitude, causing all constant energy contours to be a superposition of the two individual domains.

Nevertheless, the individual Fermi sheets of one domain are well separated in momentum from their rotated counterpart if one does not come close to the SBZ boundary. The overlay of the c(8×2) SBZ reveals a strong influence from matrix elements involved in the ARPES process as already stated from the band maps. Main intensity is seen in the first SBZ, while higher zones experience a suppression of intensity. The p(4×1) superstructure seen in LEED and STM does not affect the electronic states, because the resulting Brillouin zone would be too small to host the electron pocket.

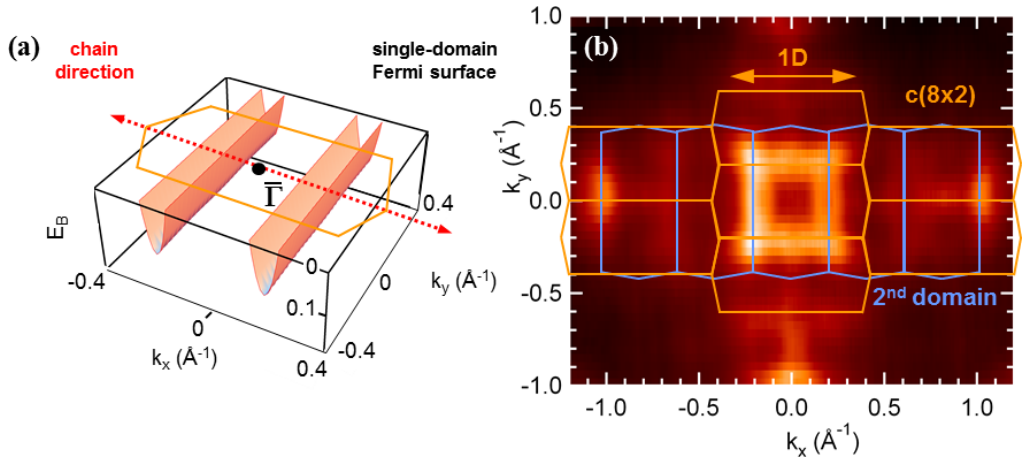

Figure 6.10.: *(a) Sketch of the band situation assuming a single c(8×2) symmetry as indicated by the SBZ of hexagonal shape. In a strict 1D scenario the dispersion should be limited to the direction of the real space structure, i.e. the nanowire direction, leading to a gutter-like structure when mapped in the perpendicular direction (variation of k_y). (b) Coarse Fermi surface overview at $T = 15$ K and $h\nu = 100$ eV. A square-like shape is observed in the first SBZ. The fourfold symmetry results from the superposition of the two domains rotated by 90°. From [5].*

Already from this coarse overview the strikingly linear shape of the Fermi surface sheets is apparent, which strongly supports the 1D scenario drawn for the small electron pockets found around the $\bar{\Gamma}$-point. Concerning the 2D hole-like band a small circular shape of two-dimensional character should be present at $\bar{\Gamma}$, but is not visible in the

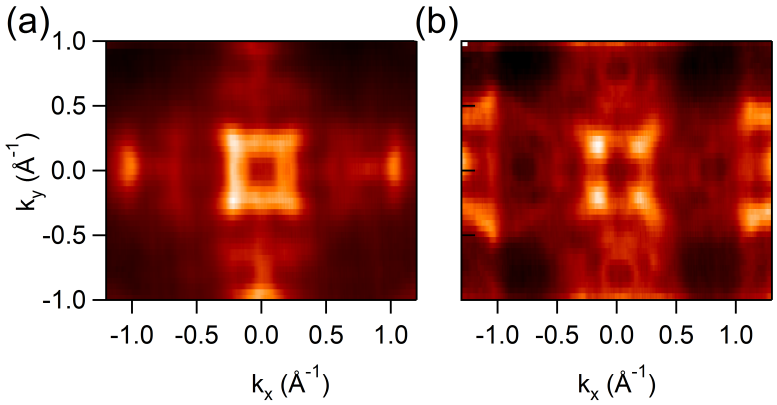

Figure 6.11.: *(a) Fermi surface of Fig. 6.10(b) without overlay. The individual Fermi surface sheets appear as straight lines and are well separated in k around the center of the SBZ. Higher SBZ are remarkably suppressed in intensity. Noticeable, an H-shape is observed at the $\bar{M}$-points ($k_x/k_y = 0/\pm 0.8$ Å^{-1} and $\pm 0.8/0$ Å^{-1}). (b) Constant energy surface at $E_B = -0.6$ eV. The H-shape around the $\bar{M}$-point converts to a circular shape demonstrating the 2D character of the observed hole-like band.*

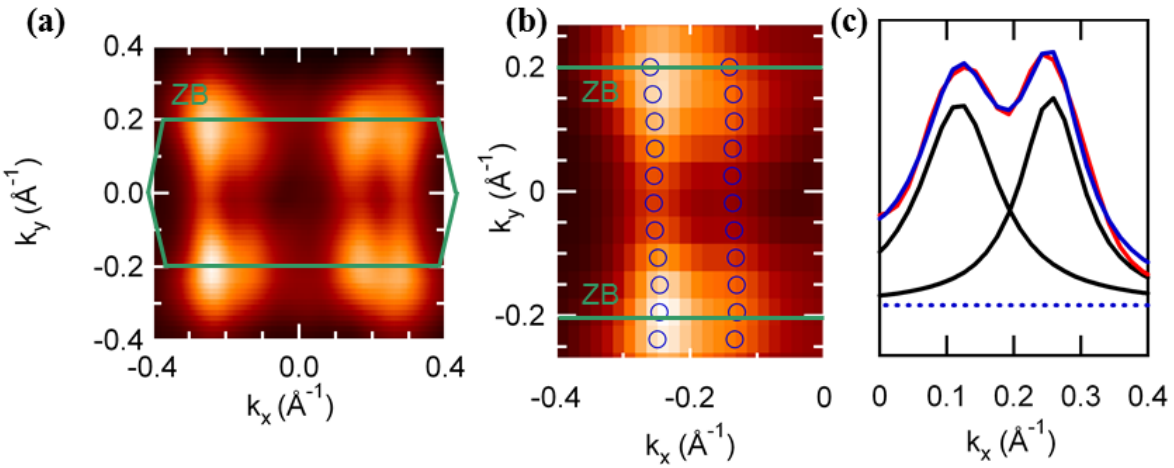

Figure 6.12.: *(a) Constant energy surface averaged from μ to $\mu - 30$ meV for a sample with a slight miscut angle leading to a domain imbalance. The individual branches cutting μ are well resolved and can be traced with the MDC analysis of (b) up to the zone boundary. The maxima of each MDC (c) represent the k_F values as a function of k_y (perpendicular to the dispersion direction) which suggests a lack of lateral dispersion within the measurement accuracy.*

data. The contribution from the hole-like state to the Fermi surface around the $\bar{\Gamma}$-point is completely suppressed in Fig. 6.11(a). For $k_x > \pm 0.4$ Å^{-1} an H-shaped intensity is present in the Fermi surface, which is mainly arising from the electron pockets of the second SBZ located at k_x=0.59/0.98 Å^{-1} and then stretched to Fermi lines in k_y (likewise for swapping x- and y-axis). The faint intensity between the two sets of Fermi sheets of the two electron pockets, i.e. the middle of such an H-shape at $k_x \sim 0.8$ Å^{-1} results from the hole-like state. The circular shape of the LH band can better be observed at lower binding energies, e.g. for $E_B = -0.6$ eV and $k_x \sim 0.8$ Å^{-1} in Fig. 6.11(b).

The electronic confinement of the electron pocket is precisely determined by tracing the dispersion in constant energy contours close to μ, where the 1D band is located. Using a substrate with a small crystal miscut angle leads to a slight domain imbalance. The corresponding data are presented in Fig. 6.12(a). On both sides of $\bar{\Gamma}$ two pairs of Fermi sheets are located which result from the crossing of the two parabola branches of each electron band at the chemical potential. Note that the energy is averaged down to 30 meV below E_F to gain sufficient intensity/signal-to-noise ratio as necessary for detailed momentum distribution curve (MDC) analysis.

The quantitative analysis is performed using the MDCs. The MDC peak positions reflecting the k_F-values are evaluated using Lorentzian fit profiles for each Fermi crossing [50]. The peak maxima are well separated in momentum and can be recorded up to the zone boundary, see Fig. 6.12(b) and (c). The fit results yield the same position as a function of $k_\perp$ with a statistical scatter of $\delta k = 0.004$ Å^{-1}. This directly reflects the 1D character of the electron dispersions.

Tight-binding modeling of the Fermi surface

Although the E(k_y) band dispersion from the MDC fitting with Lorentzian curves indicates a vanishing lateral coupling, an upper boundary can be given within a tight-binding approximation of the band dispersion. To quantify the band parameters the data are modeled with two coupling parameters t_1 and t_2 representing the next nearest neighbors hopping along the chains (×2 periodicity) and perpendicular to the chains (×8 periodicity):

$$E(\mathbf{k}) = E_0 + \sum_{n.n.} t_n \cos(\mathbf{k} \cdot \mathbf{R}_n). \tag{6.1}$$

Within the basic c(8×2) pattern the nearest neighbor along the chains sits at $R(x, y) = (a, 0)$ while for the interchain coupling the next atom is located at $R(x, y) = (\frac{a}{2}, b)$ with $a = 2a_0$ and $b = 4a_0$, see Fig. 6.13(a). Using eq. 6.1 leads to:

$$E(\mathbf{k}) = E_0 + 2t_1 \cos(k_x a) + 2t_2 \cos(k_x \frac{a}{2}) \cos(k_y b). \tag{6.2}$$

The band bottom at $E(\mathbf{k} = \pi/2a) = -130$ meV and the Fermi crossings ($k_F = 0.26$ Å$^{-1} \sim 2\pi/3a$) of a band map at $k_y = 0$ Å^{-1} (see Fig. 6.3) yield E_0 and t_1 according to:

$$\begin{aligned} E(k_x &= \frac{\pi}{4a_0} = \frac{\pi}{2a}) = -0.13eV, && (6.3)\\ -0.13eV &= E_0 + 2t_1 \cos(\frac{\pi}{2a} a), && (6.4)\\ -0.13eV &= E_0, && (6.5) \end{aligned}$$

and

$$\begin{aligned} E(k_F) &= 0, && (6.6)\\ 0 &= -0.13eV + 2t_1 \cos(\frac{2\pi}{3a} a), && (6.7)\\ t_1 &= \frac{0.13eV}{2\cos(\frac{2\pi}{3})} = -0.13eV. && (6.8) \end{aligned}$$

Within the next nearest neighbor calculation of Eq. 6.2 the $\cos(k_x a)$ turns 0 at the band bottom for $k_x = \pi/2a$ instead of -1 as necessary to generate a band minimum. This must be compensated by using second nearest neighbors along the wire, instead of next nearest neighbors as sketched in Fig. 6.13(a). In this case the dispersion relation can be written as:

$$E(\mathbf{k}) = E_0 + 2t_1 \cos(k_x 2a) \pm 2t_2 \cos(k_x \frac{a}{2}) \cos(k_y b). \tag{6.9}$$

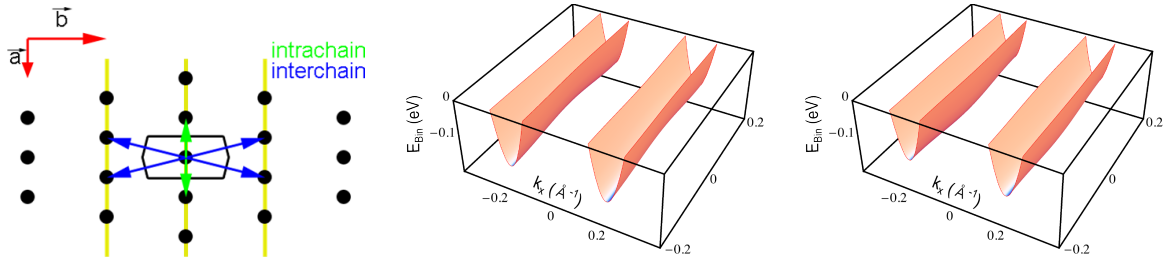

(a) *Geometry for next nearest neighbors for one single domain.*

(b) *TB band structure without phase shift in k_y-direction*

(c) *TB band structure with phase shift of π in k_y-direction.*

Figure 6.13.: *(a) Tight-binding model for next nearest neighbors. The basis vectors* **a** *and* **b** *correspond to $\times 2a_0$ and $\times 4a_0$. To obtain the experimental band structure with electron pockets at $k_x = \pm 0.2 \text{Å}^{-1}$ second nearest neighbors along the chain have to be considered. (b) The band structure has the lowest band bottom at the middle of the Brillouin zone, while its maximum lies at the zone boundary, i.e. $k_y = 0.2$ Å^{-1}.*

For a positive t_2 the band bottom is deepest at the zone boundary, see Fig. 6.13(b). A negative sign for t_2 causes for a phase shift of π in the cosine according to $\cos(k_y b + \pi) = -\cos(k_y b)$. Here the deepest band bottom is found at the middle of the SBZ, as depicted in Fig. 6.13(c). The geometry can be simplified by assuming the next nearest neighbors in k_y direction to be orthogonal as sketched in Fig. 6.14(a). The corresponding dispersion equation accounts to:

$$E(\mathbf{k}) = E_0 + 2t_1 \cos(k_x 2a) \pm 2t_2 \cos(k_y b). \tag{6.10}$$

Here the phase shift has no influence on the band bottom as a function of k_y with its maximum always being located at the middle of the SBZ, see Fig. 6.14(b). Trying to

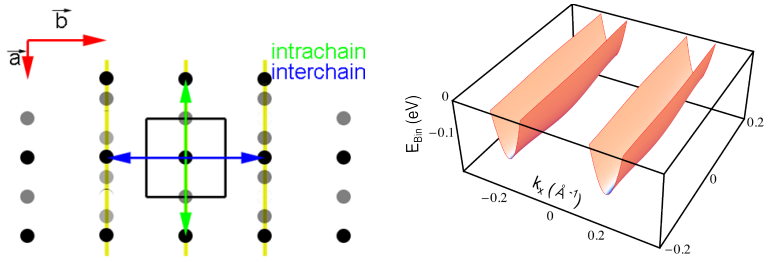

(a) *Modified geometry.*

(b) *TB band structure.*

Figure 6.14.: *(a) Modified geometry for next nearest neighbors assuming a quadratic unit cell with next nearest neighbors at 2a and b. (b) TB band structure yielding a V-shaped band bottom with its minimum at $k_y = 0$ Å^{-1}.*

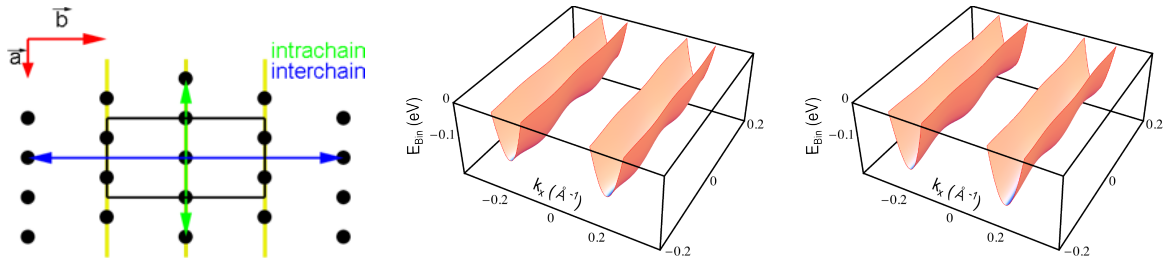

(a) *Geometry for second nearest neighbors.*

(b) *Band structure for positive t_2.*

(c) *Band structure for negative t_2.*

Figure 6.15.: *(a) Tight-binding model for second nearest neighbors at 2a and 2b. (b) Corresponding TB band structure for positive t_2. The band bottom is deepest half way towards the zone boundary, i.e. at $k_x = 0.1$ Å^{-1}. (c) For negative sign of t_2 the band bottom has its minimum at $k_x = 0$ Å^{-1} and at the zone boundary at $k_x = 0.2$ Å^{-1}.*

incorporate the c(8×2) symmetry in the tight-binding concept, one can use the second nearest neighbors along k_y as depicted in Fig. 6.15(a). The dispersion relation reads:

$$E(\mathbf{k}) = E_0 + 2t_1 \cos(k_x 2a) \pm 2t_2 \cos(k_y 2b). \tag{6.11}$$

Here a W-shape applies for the band bottom for positive t_2 in Fig. 6.15(b), while the negative sign of t_2 results in a M-shape for the band bottom, which has its minimum at $k_y = 0$ Å^{-1} and $k_y = 0.2$ Å^{-1}, see 6.15(c).

Since no real indication of any warping within the Fermi surface of the 1D pocket was found in the MDC analysis, the models shown above shall only give a hint how to model the band structure in an oversimplified way. What they do allow indeed is a determination of the transverse hopping matrix element t_2, which in all cases was approximated to be $t_2 = 0.006$ eV which is a consequence of an Δk uncertainty of 0.01 Å^{-1} from the MDC analysis in Fig. 6.12. The ratio of $\frac{t_1}{t_2} = \frac{0.13}{0.006} \sim 22$ at best will be used as an indicator within the comparison of Au/Ge(001) with related nanowire systems in the following section.

6.5. Fermi surfaces of related nanowire systems

Gold on silicon

The obvious example to compare Au/Ge(001) with, is gold on silicon. Here the most prominent examples are the stepped substrates of (553)- and (557)-orientation. For Si(557) an electron-like surface state is reported [150] which is split due to the Rashba effect [151]. The band bottom appears close to the zone boundary, while the Fermi crossings are almost half way to the zone boundary [150]. Thus, these metallic states approximately carry a charge of half an electron each. The corresponding Fermi surface is of nearly 1D character [152, 153], see Fig. 6.16(a). Tight-binding modeling leads to an anisotropy as deduced from the ratio $t_1/t_2 > 70$ comparing the next nearest neighbor interaction along t_1 and perpendicular t_2 to the chain direction [152].

This ratio becomes a little smaller, i.e. $\frac{t_1}{t_2} \sim 40$, going to Au/Si(553) where also a Rashba-split pair of almost half filled bands exists [152]. In addition, there is a third

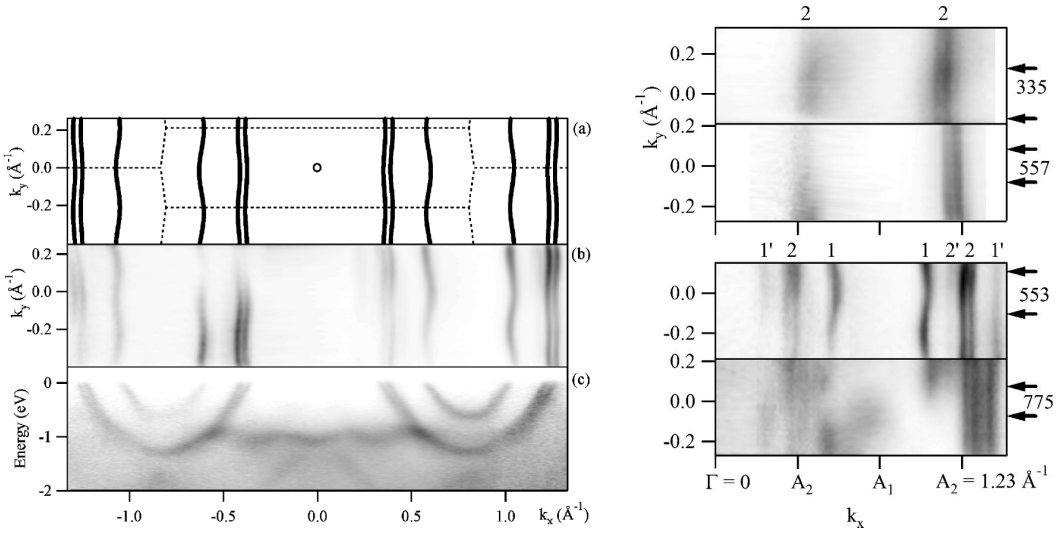

(a) *Fermi surface of Au/Si(553).* **(b)** *Dito for stepped substrates.*

Figure 6.16.: *Electronic band structure of Au/Si(553) and related high index silicon substrates. (a) Fermi surface and underlying band structure of Au/Si(553). Good agreement is found for tight-binding modeling using next nearest neighbors. Figure reprinted with permission from J.N. Crain, A. Kirakosian, K.N. Altmann, C. Bromberger, S. C. Erwin, J.L. McChesney, J.-L. Lin and F.J. Himpsel, Phys. Rev. Lett., Vol. 90, page 176805, 2003, http://link.aps.org/doi/10.1103/PhysRevLett.90.176805 [152]. (b) Fermi surfaces for Au on various stepped silicon substrates. For higher index surfaces the undulations of the Fermi surface are more and more suppressed due to the increasing wire distance. Figure reprinted with permission from J.N. Crain, J.L. McChesney, F. Zheng, M.C. Gallagher, P.C. Snijders, M. Bissen, C. Gundelach, S.C. Erwin and F.J. Himpsel, Phys. Rev. B, Vol. 69, page 125401, 2004, http://link.aps.org/doi/10.1103/PhysRevB.69.125401 [153]. Copyright (2012) by the American Physical Society.*

band of $\sim \frac{1}{3}$ filling which exhibits a stronger undulation ($\frac{t_1}{t_2} \sim 12$) in the direction perpendicular to the wires [152]. The increased lateral coupling can be understood from the decreased wire distance of $d_{553} = 1.48$ nm compared to $d_{557} = 1.92$ nm [153]. The different Fermi surfaces as a function of the substrate index are displayed in Fig. 6.16(b). For higher indices the wire distance increases, vice versa the undulations of Fermi surface. The electronic confinement is surprisingly good if one recalls the atomic arrangement of the gold chains. Structural analyses report one chain of gold atoms embedded in a silicon terrace for Au/Si(557) and two gold chains for Au/Si(553) [42]. The performed DFT calculations prove the bands to result from these gold chains [42].

Indium on silicon

Like Au/Si indium on Si(111) develops three electron-like surface states m_1, m_2 and m_3 [32, 154]. The fillings are $m_3 = 0.5$, $m_2 = 0.38$ and $m_1 = 0.11$ [34], see Fig. 6.17(a) and (b). The lower filled bands m_1 and m_2 are both affected by a cosinoidal undulation

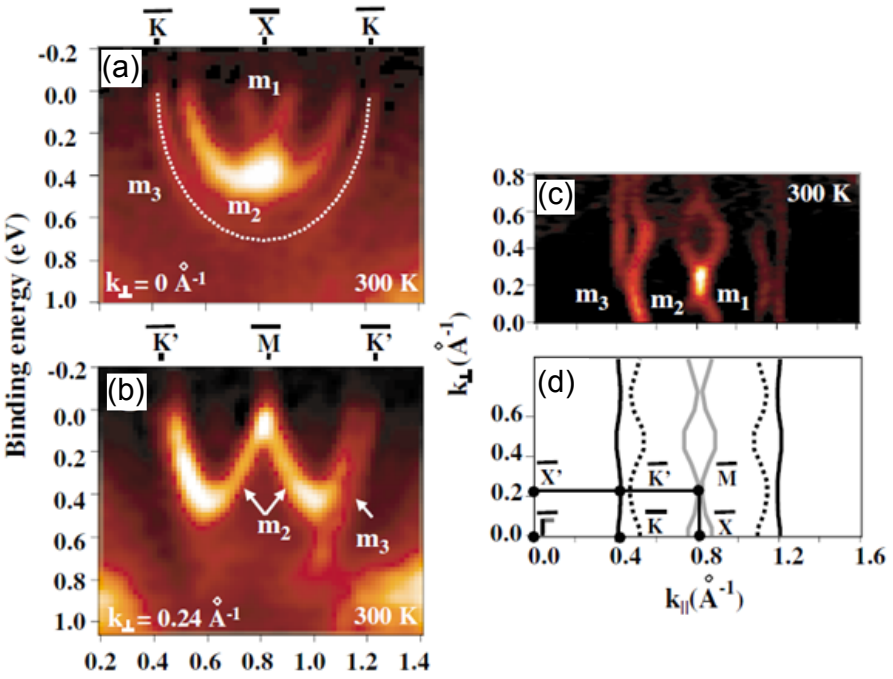

Figure 6.17.: *(a) Band structure of In/Si(111) along the $\bar{K} - \bar{X} - \bar{K}$ and (b) along the $\bar{K}' - \bar{M} - K'$ line. Three surface states (m_1, m_2 and m_3) of parabolic shape are visible. (c) Underlying Fermi surface. (d) Sketch of the experimental Fermi surface showing distinct undulations in the direction perpendicular to the wire direction. Figure reprinted with permission from J.R. Ahn, J.H. Byun, H. Koh, E. Rotenberg, S.D. Kevan and H.W. Yeom, Phys. Rev. Lett., Vol. 93, page 106401, 2004, http://link.aps.org/doi/10.1103/PhysRevLett.93.106401 [34]. Copyright (2012) by the American Physical Society.*

of the Fermi surface perpendicular to the wire direction in Fig. 6.17(c) and (d), which indicates a certain degree of lateral coupling. A detailed tight-binding modeling yields $t_1/t_2 = 72$ for m_3 being the closest 1D band, while t_1/t_2 account to 8 for m_1 and m_2 [34]. On average In/Si(111) can be rather classified quasi-1D instead of real 1D. This is supported from its real space appearance, where the indium chains are found to consist of four atoms in width [32, 35, 155].

Lead on silicon

As an example of a two-dimensional shape, the Fermi surface of Pb on Si(557) [156] is presented in Fig. 6.18. Here six different bands (m_1 to m_6) can be found, which cause a complex interference of oval and circular shapes forming the Fermi surface. For the closest 1D bands (m_2, m_3 and m_4) a tight-binding anisotropy of 3 to 7 is reported [156]. The Fermi surface contour can be understood from 2D electronic states formed by the lead atoms on the silicon terraces which are then modulated by the 1D potential caused by the regular steps [157].

The main attributes which are equal or different for the four related systems Au/Si(55x), In/Si(111), Pb/Si(557) and Au/Ge(001) are given in Tab. 6.1. Notably, all major nanowire systems have electron-like dispersing bands. The two gold induced nanowires on Si(553) and (557) share most of the attributes of Au/Ge(001). The small anisotropy ratio (t_1/t_2) for Au/Ge(001) is mainly caused by the small band filling, which mainly

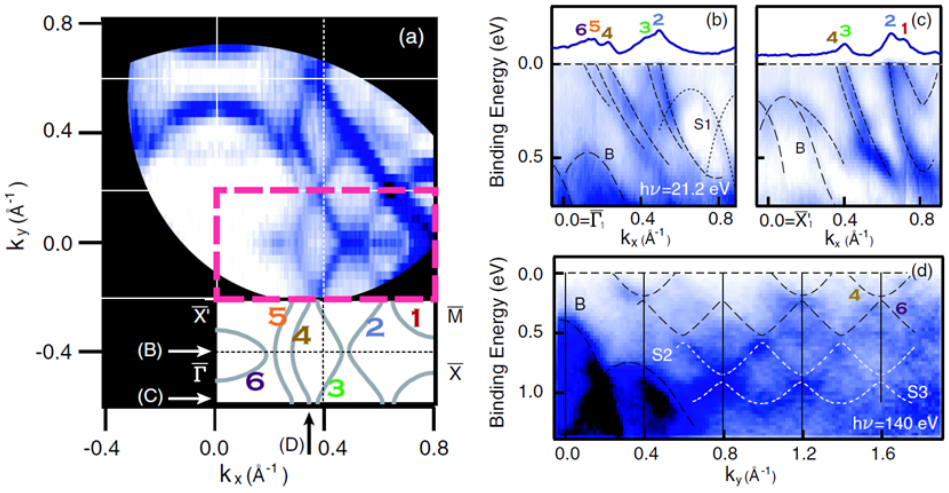

Figure 6.18.: *(a) Fermi surface of Pb/Si(557). Several two-dimensional oval shapes result from the six surface states $m_1 - m_6$. Three different band map cuts (B,C and D) are chosen to illustrate the dispersing behavior of these surface states. (b)-(d) Band maps of the three different directions as depicted in (a). Figure reprinted with permission from K.S. Kim, H. Morikawa, W.H. Choi and H.W. Yeom, Phys. Rev. Lett., Vol. 99, page 196804, 2007, http://link.aps.org/doi/10.1103/PhysRevLett.99.196804 [156]. Copyright (2012) by the American Physical Society.*

determines t_1. However, the high-index substrates show a way how the coupling to the second dimension, i.e. between the nanowires, can be lowered in terms of tight-binding by simply increasing the wire distance using higher substrate miscut angles. As will be shown in chapter 7, the anisotropy concluded from tight-binding is not as significant for the electronic ground state of Au/Ge(001).

attribute	Au/Ge	Au/Si(55 7/3)	In/Si(111)	Pb/Si(557)
on plane substrate	yes	no	yes	no
electron-like dispersion	yes	yes	yes	yes
1D Fermi surface	yes	yes	quasi	no
number of surface states	2	2/3	3	6
band filling	0.25	0.3-0.5	0.5	?
highest t_1/t_2	22	70	72	3-7

Table 6.1.: *Similarities of some representative nanowire systems compared to Au/Ge(001). All nanowire systems have at least two reconstruction-induced bands which exhibit an electron-like dispersion.*

6.6. Debate over dispersion direction

Results by the Komori group

The Au/Ge(001) system has been also studied by the group of Prof. Komori, Tokyo university. The reported ARPES measurements were performed with a Helium lamp at $h\nu = 21.2$ eV and synchrotron radiation at 33 eV [128]. Their data as shown in Fig. 6.19 also contain the electron-like surface state at $k_x = 0.2/0.59/0.98$ Å^{-1} but no sign of the additional 2D state at $k_x = 0.4/0.8$ Å^{-1}. Note that all data of Ref.[128] are second derivative only. The electron surface state is interpreted in terms of a parabola with a band bottom at $E_B = -0.14$ eV close to the results presented in this thesis. From the EDC stack in Fig. 6.19(b) metallic behavior is concluded, although a detailed line shape analysis is lacking. The dispersion direction however is assigned perpendicular to the wire direction as indicated by the surface Brillouin zone of vertical hexagonal shape in Fig. 6.19(c).

The corresponding Fermi surface displayed in Fig. 6.20 is interpreted as an anisotropic two-dimensional oval shape. The reason for the different appearance might be the comparablly low energy resolution of 60 meV and the low statistics of the data. Subsequent studies by the Komori group were performed on vicinal substrates with a four degree miscut along the [110] direction [158]. The miscut angle in combination with slightly increased growth temperatures (740 K instead of 690 K) leads to the preferred appearance of double-height steps. From the LEED pattern provided in Ref. [158] one can identify a certain imbalance of both domains of wires, parallel and perpendicular to the step

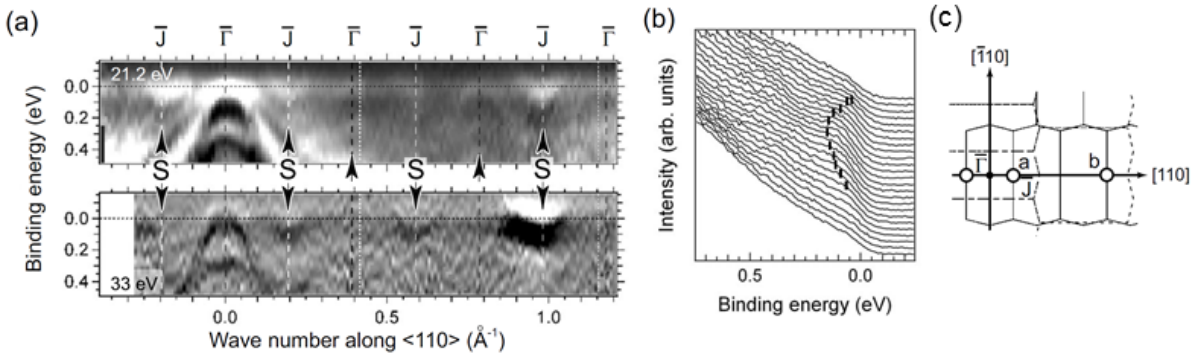

Figure 6.19.: *(a) Band map of Au/Ge(001) from Komori group including normal emission recorded at $h\nu$=21.2 eV and 33 eV. The electron-like surface state is present at $k_x = 0.2/0.59/0.98$ Å^{-1}. (b) The band bottom is located at $E_B = -0.14$ eV. A crossing of the Fermi energy is also reported. (c) Sketch of the surface Brillouin zone. The dispersion is assigned to the direction perpendicular to the nanowires as in scenario (b) of Fig. 6.4. Figure reprinted with permission from K. Nakatsuji, R. Niikura, Y. Shibata, M. Yamada, T. Iimori and F. Komori, Phys. Rev. B, Vol. 80, page 081406, 2009, http://link.aps.org/doi/10.1103/PhysRevB.80.081406 [128]. Copyright (2012) by the American Physical Society.*

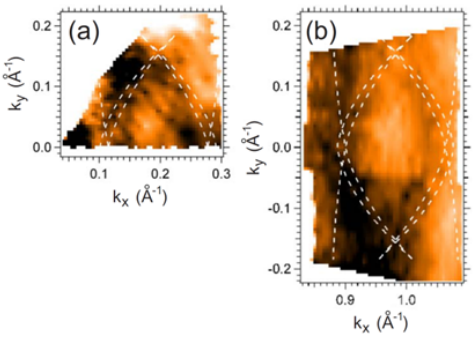

Figure 6.20.: *(a) Fermi surface obtained in the first SBZ of Au/Ge(001) by the Komori group. (b) Counter part in the third SBZ. Both data sets are interpreted in terms of an oval shape suggesting a two-dimensional character of the conducting states. Figure reprinted with permission from K. Nakatsuji, R. Niikura, Y. Shibata, M. Yamada, T. Iimori and F. Komori, Phys. Rev. B, Vol. 80, page 081406, 2009, http://link.aps.org/doi/10.1103/PhysRevB.80.081406 [128]. Copyright (2012) by the American Physical Society.*

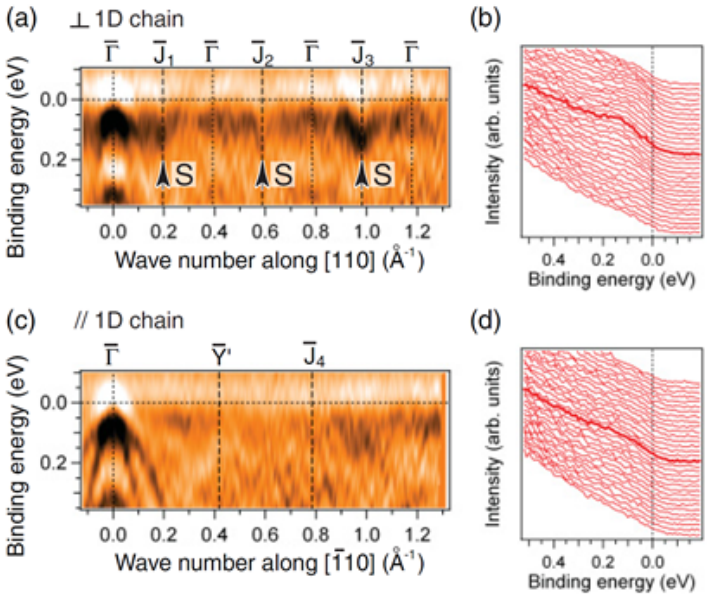

Figure 6.21.: *Band structure of an intended single-domain Au/Ge(001) surface by Komori group. (a) Band map perpendicular to the wire direction. (b) Corresponding EDC stack of the electron pocket. (c) and (d) are supposed to show the direction along the wires with less intensity. Thus, the conclusion is drawn of a main dispersion perpendicular to the wire direction. Figure reprinted with permission from K. Nakatsuji, Y. Motomura, R. Niikura and F. Komori, Phys. Rev. B, Vol. 84, page 115411, 2011, http://link.aps.org/doi/10.1103/PhysRevB.84.115411 [158]. Copyright (2012) by the American Physical Society.*

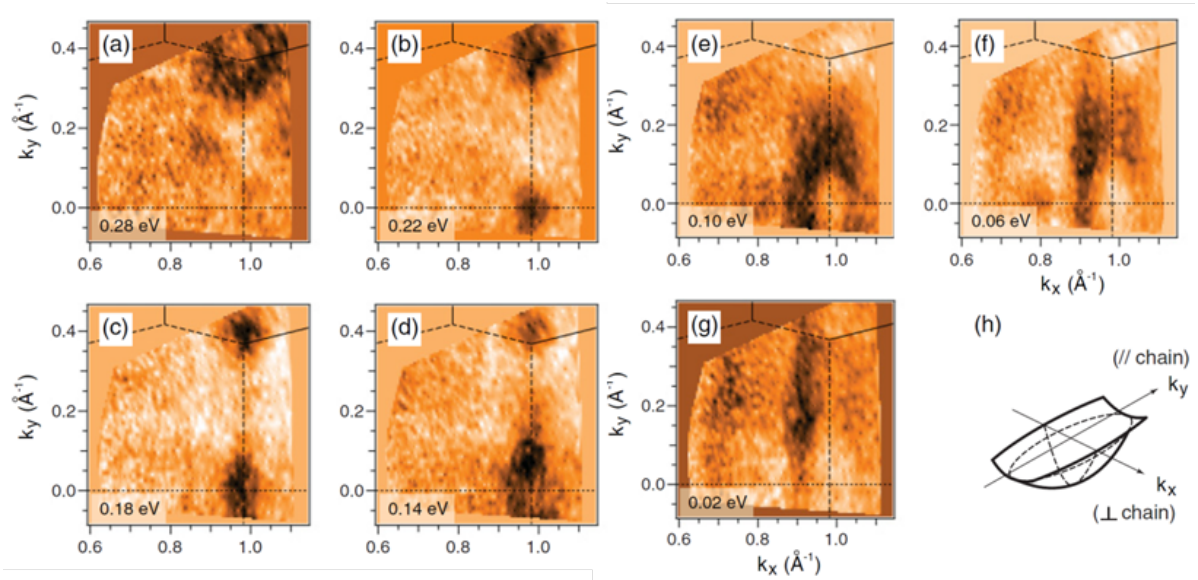

Figure 6.22.: *Constant energy surfaces for an Au/Ge(001) sample with a domain imbalance obtained with He I excitation by Komori group. Going from higher binding energies (a) towards the Fermi level (g) a more or less one-dimensional shape is revealed matching the results shown in this thesis at $h\nu = 100$ eV. Figure reprinted with permission from K. Nakatsuji, Y. Motomura, R. Niikura and F. Komori, Phys. Rev. B, Vol. 84, page 115411, 2011, http://link.aps.org/doi/10.1103/PhysRevB.84.115411 [158]. Copyright (2012) by the American Physical Society.*

edges. However, the second domain is not fully suppressed and thus still contributes to the ARPES signal. By again using $h\nu = 21.22$ eV they conclude a much more pronounced dispersion perpendicular to the wires compared to the parallel direction, see Fig. 6.21.

The resulting constant energy surfaces of the miscut sample are displayed in Fig. 6.22. Decreasing the binding energy from $E_B = 0.28$ eV towards E_F reveals a circular anisotropic shape around $E_B = 0.1$ eV while a clearly 1D shape is visible close to E_F. The three dimensional band shape is thus concluded by the authors to have a boat-like shape as drawn in Fig. 6.22(h).
Although the Komori group does provide the very same k-values for the position of the 1D band, they surprisingly do not observe the second hole-like state in other surface Brillouin zones then the first one. Their argumentation is somehow limited to the interpretation of observed shapes or symmetries, but they refrain from detailed analysis in terms of fitting routines or integrated line shape. Both, the weak signal in their data as well as the lack of some dispersing features presented in this thesis must be related to the low energy resolution of 60 meV and also a reduced sample quality. Although their interpretation of a main dispersion perpendicular to the chain direction remains speculative on the basis of their vicinal samples, the idea of using miscut substrate to reveal the true dispersion direction is smart.

First steps towards mono domain Au/Ge(001) on vicinal substrates

As a contribution to the ongoing debate how to relate the band dispersion to a real space direction, nanowires were grown on vicinal Ge substrates with miscut angles of two and three degrees. The vicinal substrates were prepared according to the planar ones by ex situ chemical etching and oxidation. After oxide removal the same (2×1) dual-domain LEED pattern was visible as for the planar substrates. Thus, the energetics of the bare Ge doe not favor one domain over the other even in the presence of a miscut angle.

The situation changes after deposition of gold. The deposition temperature was slightly increased compared to the growth on planar substrates (approx. 690 K instead of 650 K, as measured by an infrared pyrometer). The electron diffraction pattern is now dominated by the domain, where all wires align parallel to the step edges, see horizontal lines of reflexes being enhanced over its vertical counter part in Fig. 6.23(a). As judged from the absolute LEED intensities of the individual domains in Fig. 6.23(b), the ratio between wires perpendicular to the step edges (A) and parallel to them (B) can be judged to be between 2:1 and 3:1, which corresponds to a ratio of 75%:25% at best.

This result is substantiated by STM, where the parallel alignment dominates on the scale of 100 nm × 100 nm in Fig. 6.24(a). Line scans across the terraces are composed of even multiples of single-height steps, see Fig. 6.24(b). This explains the new stacking sequence of B-B-B with the wires parallel to the step edges. These results nicely match previous published data by Melnik/Gallagher [159] and Nakatsuji *et al.* [158], who both reported a preferential growth of wires parallel to the step edges using one and four degree miscut samples.

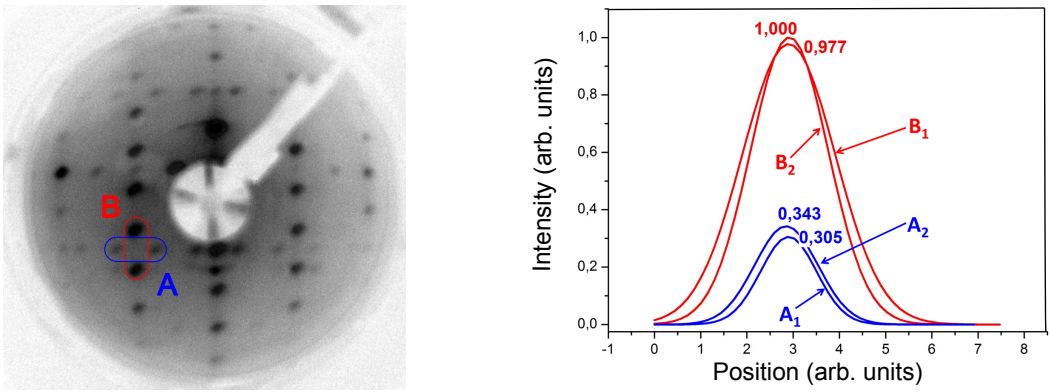

(a) *LEED pattern.* **(b)** *Intensity profiles.*

Figure 6.23.: *LEED pattern at 29 eV recorded for Au/Ge(001) using a vicinal Ge substrate with a miscut angle of three degrees. (b) Extracted relative intensities for the two domains perpendicular (A) and parallel (B) to the step edges. Normalizing the intensity to domain B yields a three times smaller intensity value for orientation A. Thus, the ratio A:B corresponds roughly to 1:3.*

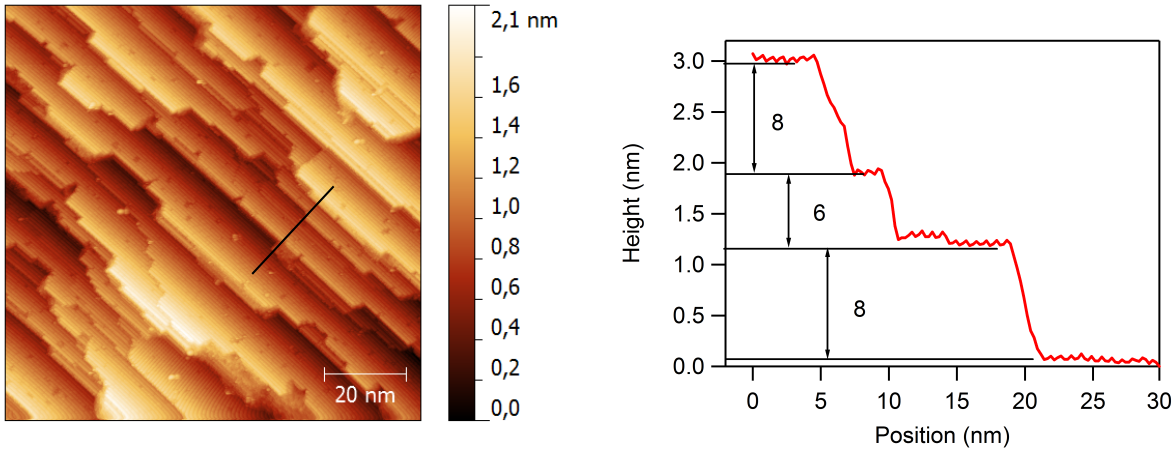

(a) *Unoccupied states 100×100 nm^2.* **(b)** *Line profile.*

Figure 6.24.: *(a) Unoccupied states (U = 1 V, I = 100 pA) from STM showing a distinct domain imbalance with a preferential alignment of the wires parallel to the step edges. (b) Line profile taken along the black line in (a). The height difference between the terraces accounts to an even multiple (6 or 8) of a single height step (1.4 Å) as expected from the parallel wire alignment.*

The miscut substrate in principle provides all requirements for future Fermi surface mapping of an almost single-domain sample.

Spatial record of the density of states by STS

Scanning tunneling spectroscopy can be used to simultaneously probe the topography and the local density of states. The latter is recorded by the signal of the lock-in amplifier. This method does not suffer from the dual-domain problem of ARPES since one probes only a single domain. The measurements were conducted at liquid nitrogen (77 K) at an energy of ±20 meV around E_F where the band structure is dominated by the electron pockets. As demonstrated in Fig. 6.25(a) and (c) the conduction path follows the direction of the topography, which is plotted in Fig. 6.25(b) and (d). These conducting filaments in the dI/dV maps are continuous, very narrow and well separated from each other. The underlying inhomogeneous intensity modulations must be attributed to sub-surface defect atoms [160]. The seamless conduction path along the wire direction clearly contradicts the statement of a rotated conduction path by the Komori group [128, 158] presented in the previous sections.

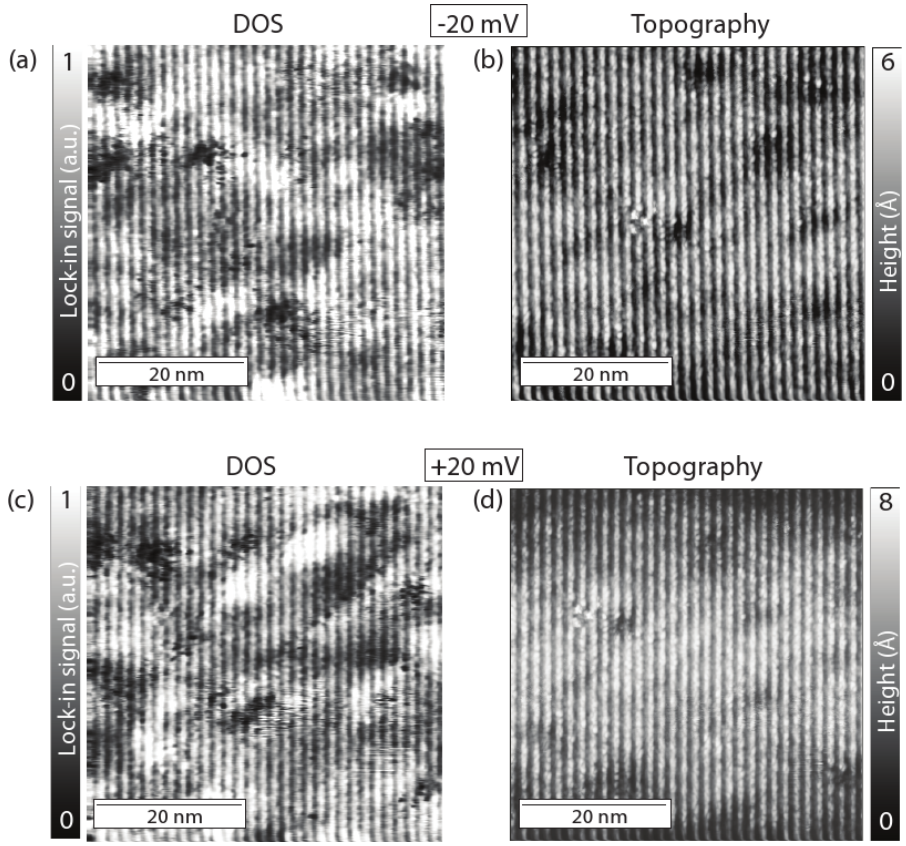

Figure 6.25.: *Density of states map of the Au/Ge(001) surface acquired with a lock-in amplifier (I = 0.4 nA, U_{eff} = 7 mV): (a) occupied states at -20 mV and (c) unoccupied states +20 mV. The bright conducting filaments run from top to bottom, likewise the topography in (b) and (d). This clearly shows that the conduction path at the surface follows the direction of the 1D architecture. Thus, the 1D electrons propagate along the chains [12].*

Summary of the electronic states

The band structure of the gold-induced nanowires on Ge(001) have been analyzed by angle-resolved photoemission:

- An electron-like dispersion of small band depth is found right below the Fermi energy which is of one-dimensional character as judged from the Fermi surface analysis.
- A second, hole-like interface state exists, which resembles the Ge heavy-hole, light-hole and split-off band.
- Both states share the same repeating scheme and do not shift in $k_\perp$ as a function of the photon energy.
- A fully occupied "garland-band" is observed at higher binding energies at the c(8×2) zone boundary.
- The general appearance of the electron pocket can be modeled by a simple tight-binding approach. The extracted anisotropy, i.e. the hopping ratio along and perpendicular to the chain direction (t_1/t_2), is smaller compared to the related Au/Si(55X) systems.
- The dispersion direction as well as the shape of Fermi surface have been questioned by experimental data from the Komori group. They claim the strongest dispersion perpendicular to the chain direction from vicinal samples with a domain imbalance.
- Own STM data of Au/Ge(001) using three degree miscut substrates have confirmed the preferential growth of wires aligned parallel to the step edges.
- The conduction path probed by spatial dI/dV maps follows the chain direction thereby supporting the ARPES scenario of a main dispersion *along* the chain direction.

7. Electronic ground state of Au/Ge(001)

7.1. Possible ground state scenario

The shape of the Fermi surface with the lack of 2D dispersion is well suited for hosting a charge density wave by nesting within the Fermi surface. Various nesting conditions are possible as sketched in Fig. 7.1: $\mathbf{q}_1 = 0.12$ Å$^{-1} = 0.15$ **G**, with **G** being the reciprocal lattice vector in the 1D direction $\frac{\pi}{3.99} = 0.79$ Å^{-1}, $\mathbf{q}_2 = 0.28$ Å$^{-1} = 0.35$ **G** and $\mathbf{q}_3 = 0.52$ Å$^{-1} = 0.65$ **G**. Notably, none of them is commensurate with the lattice, i.e. $q_{1,2,3} \neq 2\pi/(n \cdot a_0)$ with n$\in \mathbb{N}$.

In case of a CDW ground state, an additional superstructure in real space should occur which can be probed with low-energy electron diffraction as a function of temperature. The pattern recorded at room temperature is given in Fig. 7.2(a). Beside the basic c(8×2) reconstruction the additional p(4×1) superstructure is also visible. Note that the superstructure is incompatible with the nesting vectors. Going to much lower temperatures, i.e. $T = 10$ K, still yields the same pattern in Fig. 7.2(b). The slight twist is only caused by the lens voltages. The lack of a phase transition upon cooling is the first experimental evidence *against* the presence of a charge density wave.

The second key feature of a CDW is the opening of a band gap and a band backfolding. This is analyzed in detail in the energy distribution curve (EDC) stack of the ARPES band map for one electron pocket in Fig. 7.3(a) where only one single hump is present in each individual EDC. Going from the band bottom towards the Fermi vectors no sign of a gap or backfolding can be identified. Thus, a detailed inspection of the line shape is performed in Fig. 7.3(b).

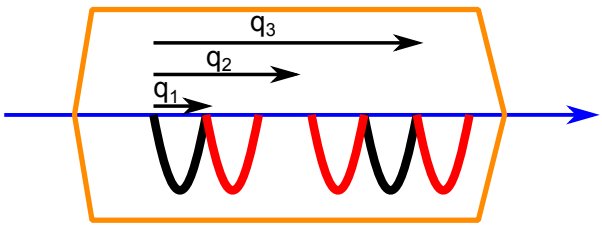

Figure 7.1.: *Nesting conditions for the band structure of Au/Ge(001). Three different nesting conditions may be fulfilled with* $\mathbf{q}_1 = 0.12$ *Å*$^{-1}$, $\mathbf{q}_2 = 0.28$ *Å*$^{-1}$ *and* $\mathbf{q}_3 = 0.52$ *Å*$^{-1}$. *None of them is commensurate with the lattice.*

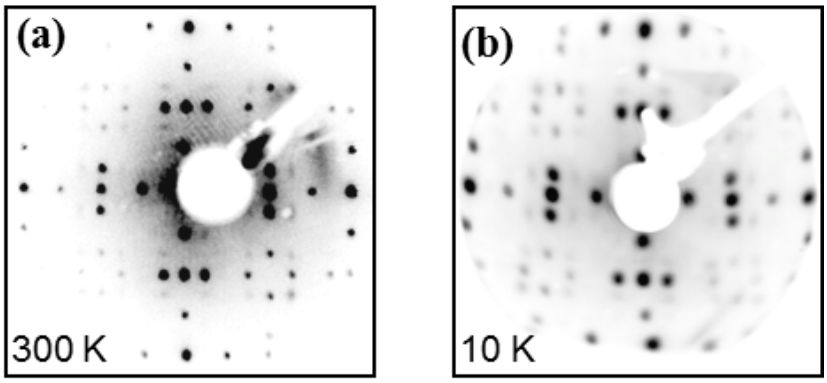

Figure 7.2.: *(a) LEED pattern at 21 eV recorded at RT showing the c(8×2) and the p(4×1) reconstruction. (b) No change is observed at $T = 10$ K suggesting a lack of a Peierls transition. From [5].*

As a reference for a metal exhibiting a clear Fermi statistics, the EDC of a polycrystalline Ta foil in contact with the sample is plotted in black dots. The red solid overlay of the Fermi distribution fit directly reflects the combined resolution from the experimental setup (30 meV) and the applied temperature ($4k_BT \sim 5$ meV). The Ta Fermi edge is closely resembled by the angle-integrated spectrum of the 2D band plotted below (yellow dots). Here, one has to account for a sloping background to fit a Fermi edge (blue solid line). Nevertheless, the fit result reflects the metallic character of the 2D band at $T = 15$ K. This observation is useful to have an intrinsic reference for the chem-

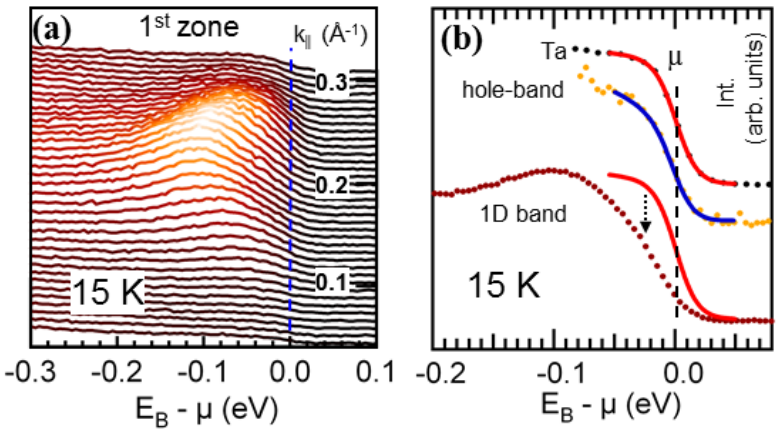

Figure 7.3.: *(a) EDC stack of one electron pocket at $T = 15$ K. Beside the low spectral weight at μ no energy gap or backfolding is visible. (b) Spectral function of a polycrystalline Ta foil resembling a Fermi edge. The angle-integrated spectrum of the hole-like state exhibits the same step-like shape (orange dots) although one has to account for a sloping background (fit solid blue line). In contrast, the spectral weight of the 1D band is remarkably suppressed at μ which is indicative of a non-Fermi liquid behavior. From [5].*

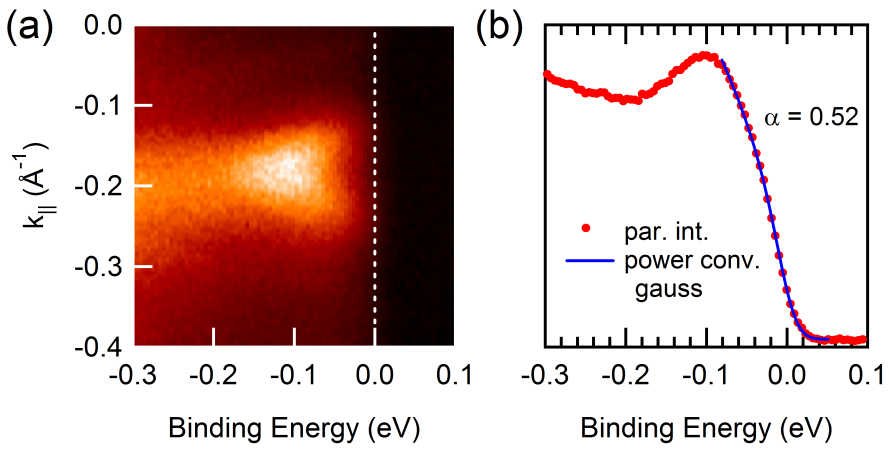

Figure 7.4.: *(a) Band map of one single electron pocket. The intensity fades from approximately $E_B = -100$ meV towards E_F. (b) Band integrated EDC (red marker) fitted with a power-law containing a Gaussian broadening of 16 meV (solid blue line). From the fitting routine a TLL exponent of $\alpha = 0.52$ can be extracted, which may serve as a first indicator for the size of α with respect to the limited energy resolution of ∼30 meV.*

ical potential, which rules out any possible influence from charging, i.e. surface photo voltage [161, 162]. In contrast to the 2D band, the angle-integrated spectrum of the 1D electron pockets does not exhibit a step-like function as expected in a metallic Fermi scenario. A suppression of spectral weight is observed close to the chemical potential, see lowest curve in Fig. 7.3(b) with additional overlay of the Ta reference.

To explain this spectral line shape one may argue with finite size segments of wires getting positively charged by the irradiation of the sample with UV light. The finite length of the segments or size limiting defects along the wire act as barriers for any continuous conduction path [163]. This scenario seems unlikely because the substrate is sufficiently doped to prevent charging as judged from the 2D band exhibiting the same Fermi edge as the Ta foil of the sample holder. Thus, in the absence of a CDW the line shape should in principle resemble the undistorted 1D metal, i.e. a *Tomonaga-Luttinger liquid*.

A precise TLL evaluation with respect to the limited energy resolution of the beamline is given in Fig. 7.4, where (a) shows the close-up of one electron pocket with a suppression of spectral weight towards E_F. The band-integrated EDC in (b) is now fitted with a convoluted function of both a power-law for a Tomonaga-Luttinger model and a Gaussian distribution to account for the limited energy resolution. Using a Gaussian standard deviation of 16 meV yields an TLL exponent α of 0.52 on an energy scale up to $E_B = -85$ meV, which can serve as a first hint for the size of α. A detailed line shape analysis will be given for the data collected at the HRPES beamline of the Swiss Light Source for photon energies below 100 eV with an improved resolution below 15 meV.

7.2. Line shape analysis

With the improved energy resolution the band integrated spectra for both surface states are again analyzed using band maps taken at $h\nu = 35$ eV, see Fig. 7.5(a), where both surface states are present and well resolved. The integrated spectra are straight forward analyzed by using simplified equations like eq. 2.22 neglecting the temperature. The more complex model functions including temperature (eq. 2.23) or momentum resolution (eq. 2.18) exceed the scope of this thesis. The integration windows for both the 1D and 2D band are presented in Fig. 7.5(b) and (c), with the latter showing the heavy p-doping of the 2D hole parabola which is clearly cut below its top by the Fermi energy.

The angle integrated line shape of the 2D band is displayed in Fig. 7.6(a) as a function of temperature. The intensity of each spectrum is normalized to a constant background at high kinetic energies. All spectra have a step-like shape which coincides over a wide energy range. The only difference appears around E_F, where the thermal broadening sets in. They can be fitted with a Fermi distribution with two linear background slopes above and below the Fermi level.

A detailed example is given for $T = 10$ K in Fig. 7.6(b) where the fit yields a Fermi energy of 30.551 eV with $kT = 3.5$ meV. From the extracted width of the Fermi fit

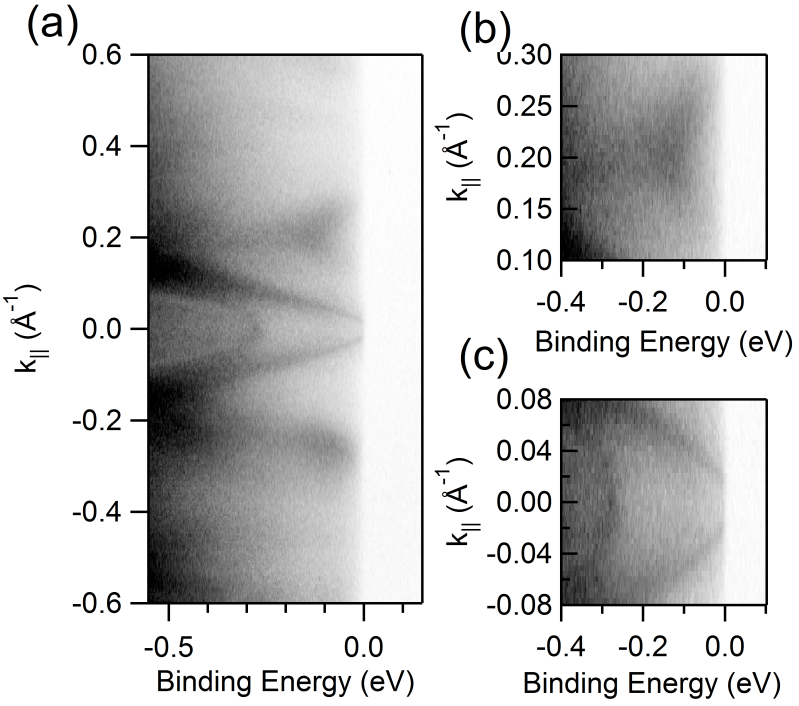

Figure 7.5.: *(a) Band map at $h\nu$=35 eV $\bar{\Gamma}$-$\bar{K}$ at $T = 10$ K. (b) Section for integration over 1D band. (c) Dito for 2D band. The hole-like parabola is cut below its top by E_F like in a heavy p-doping scenario.*

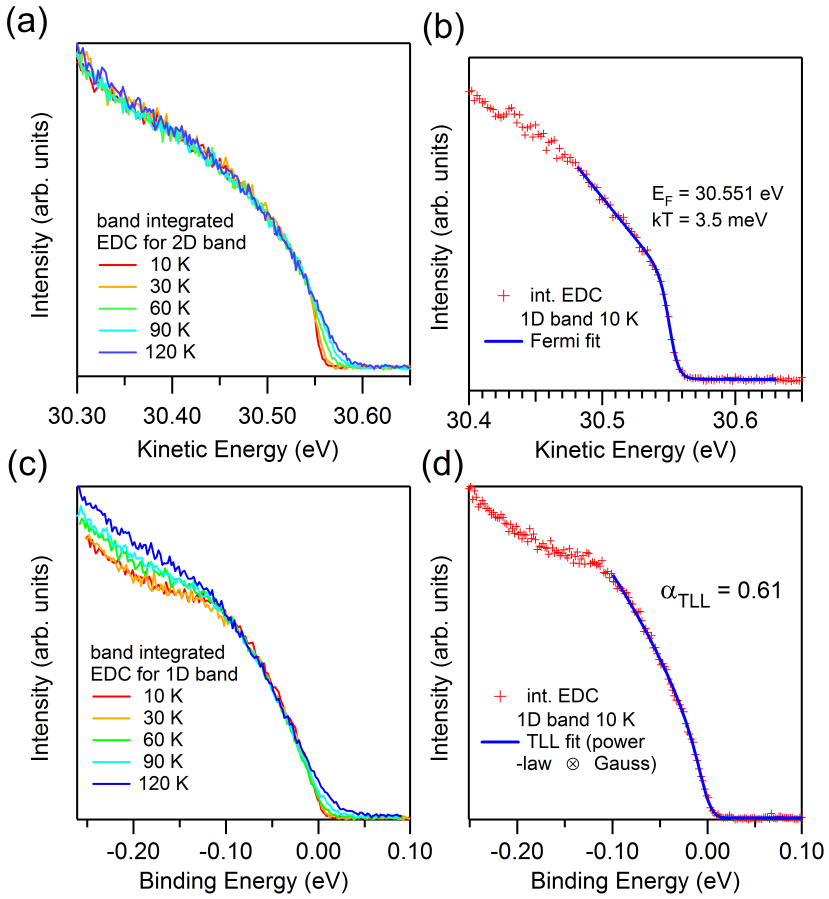

Figure 7.6.: *(a) Band integrated EDC for the 2D surface state as a function of temperature. (b) Close-up of the energy cut off of (a). (c) Fermi fit of band integrated EDC for the 2D surface state at $T = 10$ K. (d) Position of the Fermi energy as a function of temperature. (e) Band integrated spectra for 1D band. (f) Power-law fit for 1D band at $T = 10$ K with convoluted Gauss function.*

$(=4k_BT_{eff})$ one can deduce the combined energy resolution of the spectrometer at HRPES endstation (beamline optic and electron analyzer) according to:

$$(4k_BT_{eff})^2 = (4k_BT_{Temp})^2 + (4k_BT_{Res})^2\,, \tag{7.1}$$

$$\sqrt{(4 * 3.5meV)^2 - (4 * 0.86meV)^2} = 4k_BT_{Res}, \tag{7.2}$$

$$4k_BT_{Res} = 13.6meV, \tag{7.3}$$

which is compatible with the beamline settings.

The band integrated spectra for the 1D band in Fig. 7.6(c) do not exhibit a step-like shape but decrease in a more continuous way towards E_F. Their intensity again is normalized to the background value right above E_F. The curve of Fig. 7.6(d) recorded

at $T = 10$ K exhibits the smallest width with a clear lack of a step-like shape. Applying a power-law fit convolved with a Gaussian distribution yields a TLL exponent $\alpha = 0.61$, which is slightly increased compared to the results based on the ALS data. The used fit routine accounts for a power-law of the form $A \cdot E^{\alpha} \otimes Gauss(\sigma)$ using a certain slope A and a constant offset.

To eliminate the uncertainty caused by the slope and the Gaussian broadening, it seems more appropriate to plot the data in a double logarithmic (log-log) scale. Here, the bare linear range applies for the TLL power-law. The corresponding temperature series is depicted in Fig. 7.7(a)-(e). A linear slope is apparent on the scale from $E_B = -100$ meV to $E_B = -10$ meV towards E_F. Data points within $E_B \in [E_F$ -10 meV, $E_F]$ start

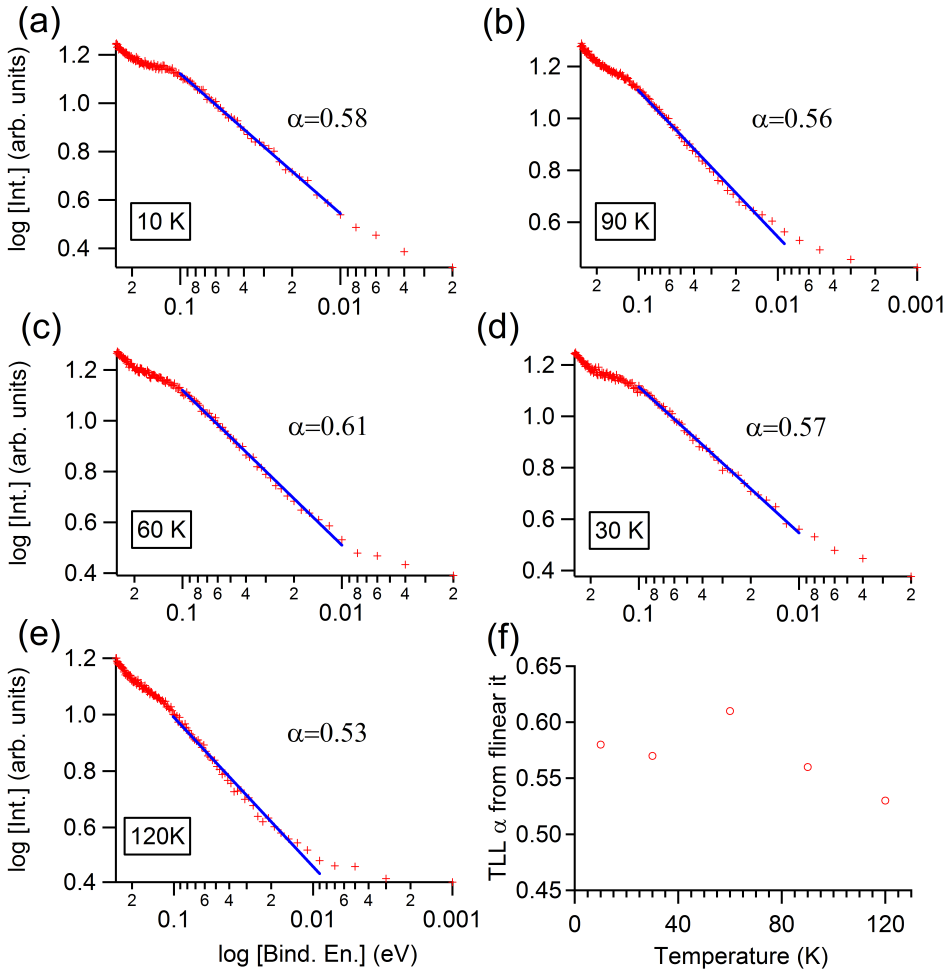

Figure 7.7.: *Log-log plot of band integrated EDCs for the 1D band as a function of temperature. The linear fit on the range of [100 meV, 10 meV] yields the TLL exponent α. (a) $T = 10$ K; (b) $T = 30$ K; (c) $T = 60$ K; (d) $T = 90$ K; (e) $T = 120$ K; (f) TLL exponent α plotted vs. temperature.*

to deviate from the linear slope which is due to the thermal broadening. The hump observed at higher binding energies, i.e. $E_B > -100$ meV, results from the inset of the band bottom. Using the energy range from $E_B = -100$ meV to $E_B = -10$ meV for the linear fitting yields a TLL exponent $\alpha = 0.58$ for $T = 10$ K which is only little less than from the convolved power-law fit. Within the applied temperature regime no significant change on the TLL exponent is observed. The temperature averaged value accounts to 0.57. Since $\alpha = 0.57$ exceeds 0.5 the spinon does not exhibit a clear peak in the band structure [56]. This explains the single hump structure of the 1D band, see Fig. 7.3(a), where a clear two-peak signature (spin-charge separation) is *suppressed*.

7.3. Alternative explanations for a power-law line shape

To substantiate the interpretation of the power-law line shape in terms of TLL physics one must exclude any other possible origins. One influence on the line shape could be for instance a poorly conducting substrate. Robert Joynt has shown on theoretical grounds that in this case the conventional view in photoemission, that the extracted photoelectron does not suffer any additional losses after penetration out of the solid, fails [164]. He revealed that inelastic processes indeed can influence the low-energy excitation spectrum around the chemical potential in a way to mimic a Pseudo gap in the presence of a true metal. Despite the debate on the validity of the assumptions used by Joynt (see Refs. [165–167]), this scenario would require a distinct change of the line shape as a function of temperature and thereby of the charge carrier density, which is definitely not observed in the experiment, e.g. in the log-log-plots, and can be ruled out.

Thinking of a poorly conducting substrate makes the discussion even more complex when charging of the sample is involved (surface photo voltage, SPV). In this case the corresponding spectra should be shifted towards higher binding energy due to the positive charged substrate [162]. This effect could not be observed for Au/Ge(001), neither for valence band or core-levels nor as a function of photon flux adjusted by the beamline entrance slits. In a more detailed picture Starowicz and co-workers have applied a refined model on the basis of isolated, charged clusters, i.e. sodium on gold-induced chains on Si(335) [163]. For this specific case they can adjust the parameters in a way to yield similar results compared with the experimental line shape, where no Fermi edge but a more power-law like shape is found [163]. This phenomenon would result in size-dependent Coulomb gaps in the meV range, something which is not compatible with the experiment presented here.

For a related nanowire system, i.e. Au/Si(557), spin-charge separation was reported based on two dispersing features in ARPES [168]. This interpretation was refined in a subsequent ARPES study with improved resolution [150], where the two dispersing peaks could explicitly be related to a Rashba-type splitted pair of bands. Thus, to finally

countercheck the interpretation of the ARPES results in the framework of TLL physics, a second experimental probe will be presented in the following based on scanning tunneling spectroscopy. STS offers the advantage of an increased energy resolution, which is mainly limited by the width of the tip's Fermi distribution (approx. $5-6$ meV). Furthermore, the scanning technique allows local spectroscopy, e.g. at chain ends thereby providing access to the end exponent α_{end} (see eq. 2.21).

TLL analysis on Au/Ge(001) from STS

The DOS extracted from the derivative of the tunneling current yields a TLL exponent $\alpha = 0.53$ when averaged over several wires segments in the middle of a terrace without defects [8], see Fig. 7.8(a). The same exponent can be found for the temperature dependent scaling at $E = 0$ eV in Fig. 7.8(b), as expected for a TLL. Both power-laws, in energy and temperature, prove the universal scaling behavior, i.e. all spectra recorded for different temperatures collapse on one single curve when plotted over energy divided by temperature [8].

In case of STS a poor conducting substrate can cause an "intrinsic" or an "extrinsic" Coulomb blockade. The former case accounts for Coulomb-like interactions between electrons when one electron is removed from the wire. A corresponding model curve for the "intrinsic" Coulomb blockade according to Ref. [169] is plotted as a solid grey line in Fig. 7.8 in comparison to the energy dependent DOS. The mismatch is obvious, especially for the low-energy range around the chemical potential. For the "'dynamical" Coulomb

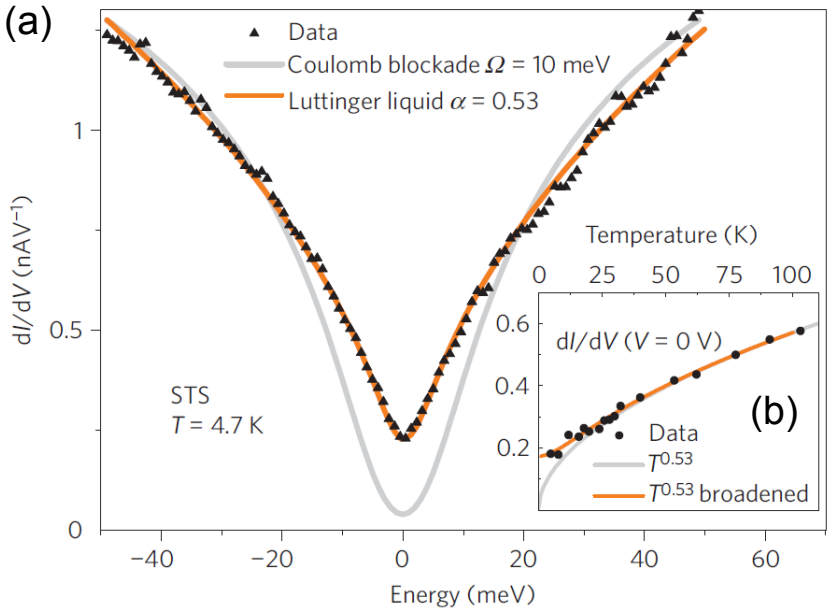

Figure 7.8.: *Scanning tunneling spectroscopy on Au/Ge(001). (a) The DOS scales as a power-law in energy and (b) temperature with the very same exponent $\alpha = 0.53$. From [8].*

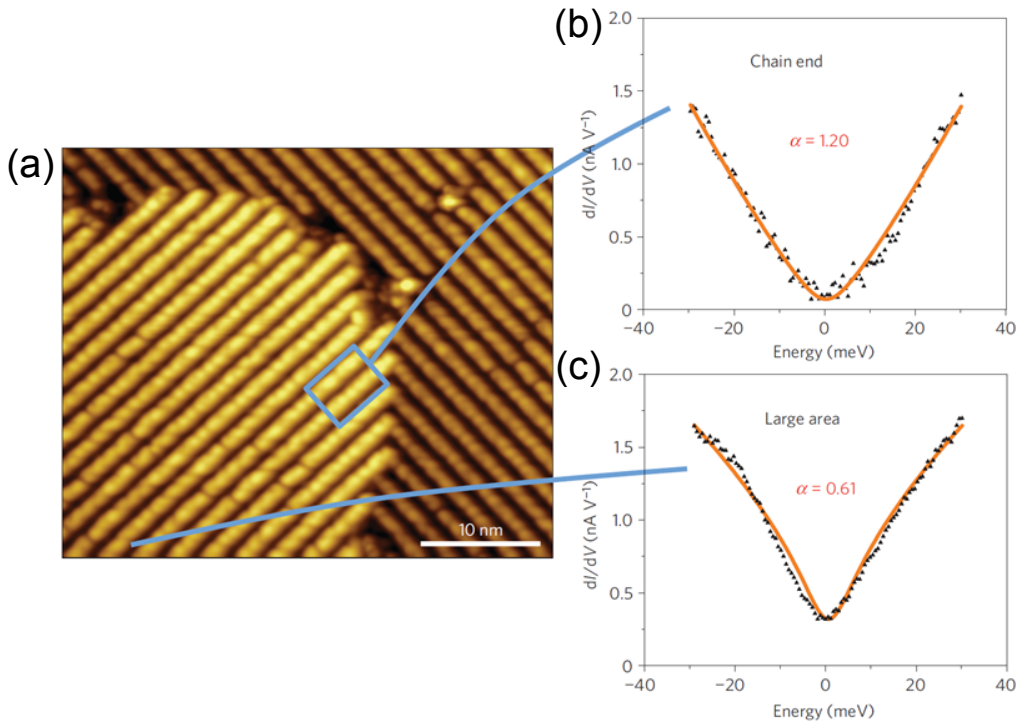

Figure 7.9.: *Scanning tunneling spectroscopy close to chain ends. (a) Topography used for STS measurements. (b) Averaged STS spectrum at chain ends showing an increase of the TLL exponent from 0.53 towards 1.2. From [8].*

blockade two main aspects apply, which can be disproved in case of Au/Ge(001): first, for the relevant impedance regime the external resistance R must exceed the quantum resistance $R_Q = h/2e = 25.8$ kΩ. This is not the case for the highly doped substrates which cause a total impedance of about 50 Ω. Second, the power-law exponent should resemble the ratio of external and quantum impedance, i.e. $\alpha = 2R/R_Q = 0.004$, which is also in contradiction to the experimental finding. Thus, the interpretation of the power-law in terms of TLL physics can be held substantiated from both ARPES and STS, independently.

Moreover, the TLL concept and its match to the experiment can be further tested by local spectroscopy data recorded at chain ends, which represent a natural boundary for the conduction electrons. Here, again a close match between theoretical expectations and experiment can be found, see Fig. 7.9. Calculating the stiffness coefficient K_ρ from the bulk exponent of $\alpha_{bulk} = 0.53$ yields $K_\rho = 0.26$ and an expectation value for the boundary of $\alpha_B = 1.43$ using eq. 2.21, which is close to the experimental value of $\alpha_{end} = 1.2$ in Fig. 7.9(b).

This fact explains the difference in the TLL exponent between STS and ARPES. The latter always has to average over several terraces and therefore chain ends. Thus, the slightly increased value of $\alpha_{ARPES} = 0.57$ compared to $\alpha_{STS} = 0.53$ is well supported

by this picture.
The match between theory and the STS-experiment for the boundary exponent can be even improved by applying a more refined theoretical approach to the data. The common TLL concept accounts only for one band with two Fermi crossings. Considering now two electron pockets as observed in ARPES, i.e. four Fermi crossings, even and odd pairs of charge and spin appear in bosonization [57]. As a consequence, eq. 2.21 has to be refined according to:

$$\alpha_B = \frac{1}{4}(K_\rho^{-1} - 1). \tag{7.4}$$

Again using the stiffness constant $K_\sigma = 0.26$ yields a theoretical boundary (end) exponent of $\alpha_B = 1.27$ which represents a better match to $\alpha_{end} = 1.2$ than the simple one band case.

7.4. Classification of the TLL behavior of Au/Ge(001) within the literature

There exists a small number of materials which have been discussed in terms of TLL physics from various experimental and theoretical points of view. Examples comprise layered compounds similar to high-temperature superconductors, i.e. $SrCuO_2$, where spin-charge separation was unambiguously shown by ARPES [170]. Another class are organic materials like TTF-TCNQ [19, 20] or $(DMe\text{-}DCNQI)_2Cu$ [171]. In the following, three other examples will be elucidated, which have raised some interest very recently.

Lithium purple bronze

The most prominent and probably most extensively studied TLL system, at least by ARPES, is lithium purple bronze $Li_{0.9}Mo_6O_{17}$. It is a quasi-onedimensional metal, which exhibits a phase transition of unclear origin at about $T = 24$ K before it turns superconducting at $T = 1.8$ K ([174] and references therein). The k-resolved ARPES spectra did not show spin-charge separation in terms of two distinct dispersing feature but were affected by one dispersing peak and and a leading edge close E_F. These spectra were interpreted using TLL exponent $\alpha = 0.9$ within the assumption of spin independent repulsive interaction [174].

The raised question on the influence of the growth method (temperature gradient flux or electrolyte reduction) was answered subsequently to have no effect on the TLL line shape [175]. By using comparatively high photon energy of $h\nu = 500$ eV, the TLL power-law could be still observed with the same exponent as for using $h\nu = 30$ eV [176] (note that α was corrected to better fit 0.65 instead of 0.9). Thus, the TLL behavior was concluded to be a bulk property and to originate from the anisotropic chain-like structure below the cleavage plane. The exponent α of ~ 0.6 was later on verified by

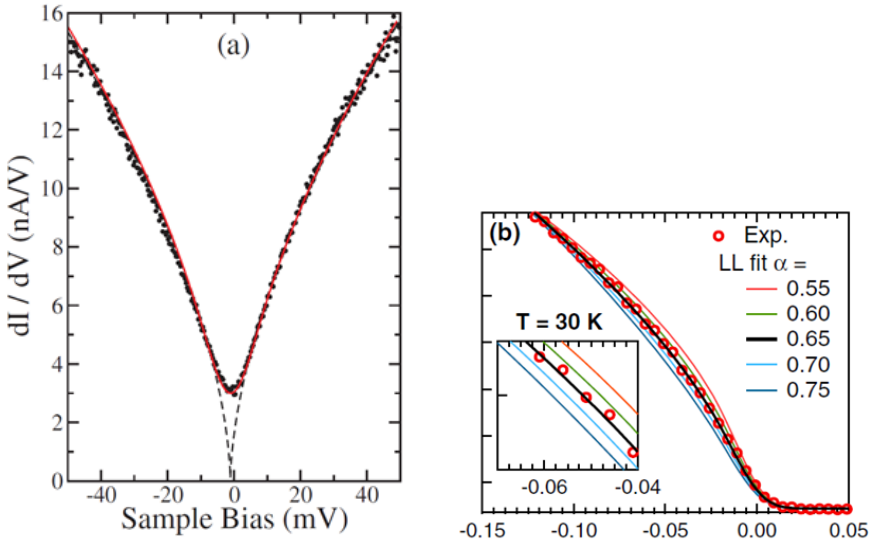

(a) *STS spectrum of* $Li_{0.9}Mo_6O_{17}$. **(b)** *ARPES line shape of* $Li_{0.9}Mo_6O_{17}$.

Figure 7.10.: *TLL physics in* $Li_{0.9}Mo_6O_{17}$. *(a) Density of states measured by STS showing a power-law with exponent* $\alpha = 0.6$. *Figure reprinted with permission from J. Hager, R. Matzdorf, J. He, R. Jin, D. Mandrus, M. A. Cazalilla and E. W. Plummer, Phys. Rev. Lett., Vol. 95, page 186402, 2005, http://link.aps.org/doi/10.1103/PhysRevLett.95.186402 [172]. (b) Band integrated line shape from ARPES revealing a power-law as well. The exponent agrees well with the previous STS experiment. Figurer reprinted with permission from F. Wang, J. V. Alvarez, S.-K. Mo, J. W. Allen, G.-H. Gweon, J. He, R. Jin, D. Mandrus and H. Höchst, Phys. Rev. Lett., Vol. 96, page 196403, 2006, http://link.aps.org/doi/10.1103/PhysRevLett.96.196403 [173]. Copyright by the American Physical Society.*

STS measurements [172], see Fig. 7.10 which also shows the complementary ARPES results from ref. [173]. Latest ARPES results could also prove the universal scaling of the temperature dependent TLL line shape [177].

Quantum wires of GaAs/AlGaAs

One-dimensional conductors can be realized by double quantum well heterostructures made of GaAs/AlGaAs [179]. Both quantum wells are separated by a thin AlGaAs barrier. Subsequent over-growth of the quantum wells yields two artificial quantum wires along the edge of the sample. A certain gating configuration now allows to measure the tunneling current through a single tunnel junction thereby revealing the dispersion relations of the elementary excitations of these wires. The conductance is suppressed if the bias between source and drain (V_{sd}) is zero but apart from that shows two distinct dispersion curves which can be related to spinon and holon dispersion, i.e. spin-charge separation. Both features are interpreted as TLL physics [179]. Detailed analyses re-

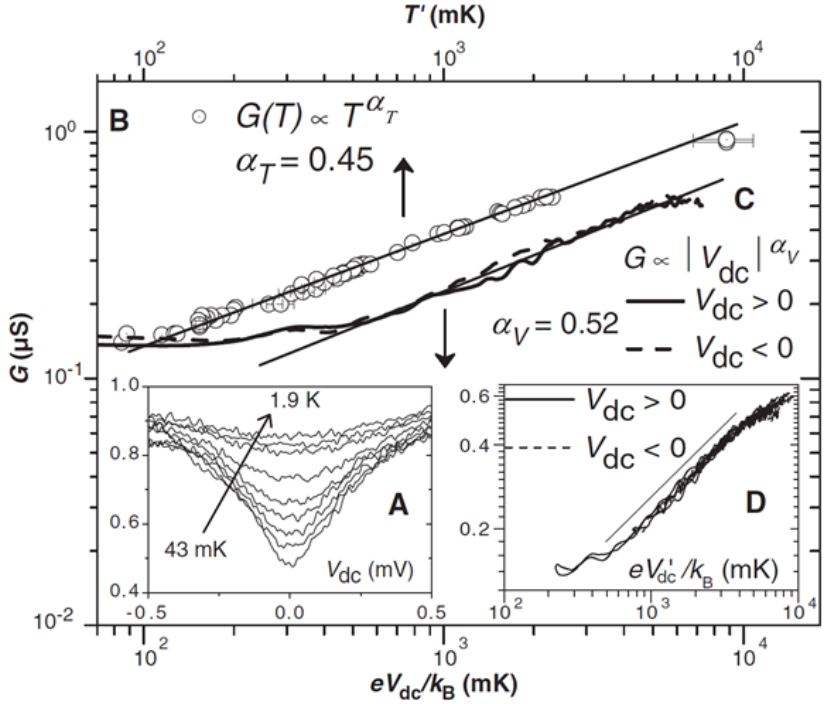

Figure 7.11.: *TLL physics observed in the conductance G of gated GaAs/AlGaAs quantum wires as a function of (a) bias (V_{dc}) and (b) temperature T. Both exhibit a power-law shape. For details concerning (c) and (d) see Ref. [178]. From [178]. Reprinted with permission from AAAS, Copyright (2013).*

ported two spin channels and one charge channel with a second one being suppressed in the experiment [180]. A precise determination of the TLL exponent as a function of V_{sd} and temperature T leads to $\alpha_{sd} = 0.52$ and $\alpha_T = 0.45$ [178] displayed in Fig. 7.11.

Single-walled carbon nanotubes

A close realization of a one-dimensional conductor is given by single-walled carbon nanotubes (SWNTs). These rolled tubes made of graphene can be either metallic or semiconducting depending on their chirality. Investigations of the conductance of metallic SWNTs by Bockrath and co-workers revealed a power-law $G(T) \propto T^{\alpha}$ as a function of temperature [58]. Moreover, the differential conductance measured as a function of the applied bias voltages follows a power-law as well [58], see Fig. 7.12(a). Using an expression close to eq. 2.20 leads to a bulk exponent of $\alpha_{bulk} = 0.3$ and $\alpha_{end} = 0.6$ close to the end of the tubes. Subsequent ARPES studies observed a suppression of spectral weight close to E_F which again can be explained by a TLL power-law of the density of states [181], data are shown in Fig. 7.12(b). Further ARPES experiments could prove the decrease of the TLL exponent when putting low concentrations of potassium on top

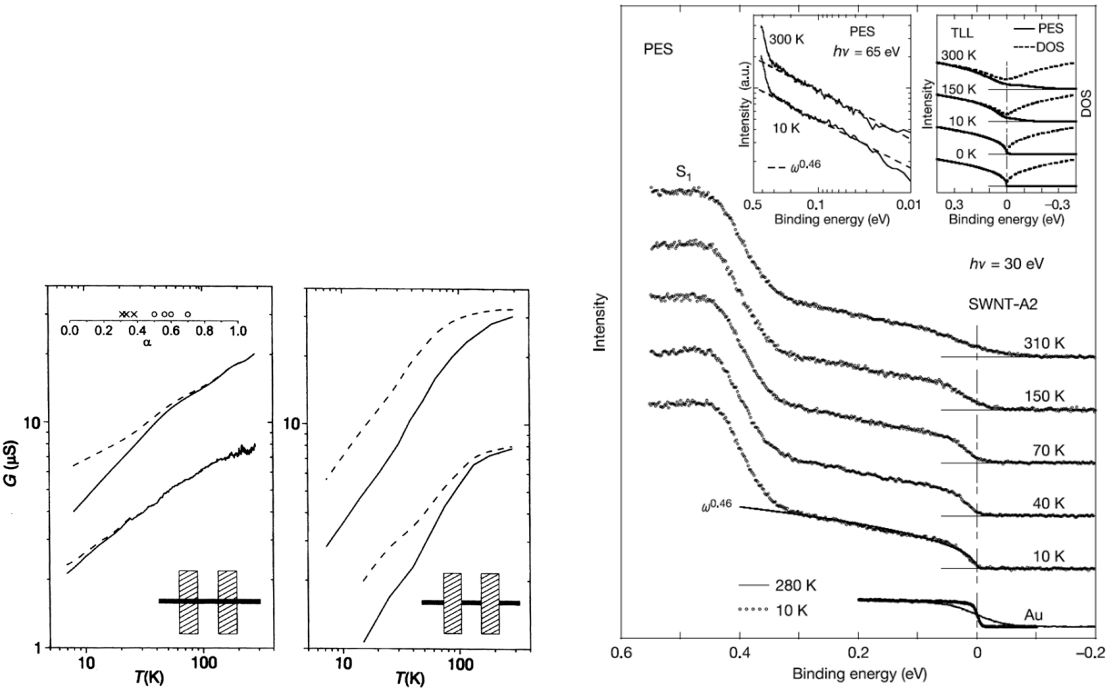

(a) *Conductance.* **(b)** *ARPES.*

Figure 7.12.: *TLL physics found in single-walled carbon nanotubes. A power-law is observed for the differential conductance as a function of temperature depending on the growth mode [58]. The left inset displays the variety of exponents found for different samples. Reprinted by permission from Macmillan Publishers Ltd: Nature, [58], Copyright (2013). (b) Temperature dependent line shape analysis from ARPES revealing the very same power-law behavior found in the conductance measurements. Reprinted by permission from Macmillan Publishers Ltd: Nature, [181], Copyright (2013).*

of the carbon nanotubes [182], where finally a transition from the TLL regime to a Fermi liquid was reported for highest possible doping concentration.

In conclusion, the TLL exponent α and accordingly K_ρ of Au/Ge(001) is of the same order as for the previously reported TLL systems $Li_{0.9}Mo_6O_{17}$, single-walled carbon

material	α	K_ρ	technique	reference
Au/Ge(001)	0.57/0.53	(0.25)/0.26	ARPES/STM	[8]
$Li_{0.9}Mo_6O_{17}$	0.65/0.6	0.24	ARPES/STM	[172, 173]
GaAs/AlGaAs	0.52	0.37	conductance	[178]
SWNT	0.3/0.46	0.35/0.28	conductance/ARPES	[58, 181]

Table 7.1.: *Table of TLL exponent and stiffness coefficient for lithium purple bronze, single-walled carbon nanotubes, gated semiconductor quantum chains and gold-induced nanowires on Ge(001).*

nanotubes or gated semiconductors based on AlGaAs/GaAs, see tab. 7.1. Both, angle-resolved photoemission and scanning tunneling spectroscopy, are well established and complementary methods to extract the TLL parameters, as e.g. shown independently for $Li_{0.9}Mo_6O_{17}$.

8. The surface as atomic playground - influence of alkali adsorption

The observed TLL behavior in the surface system of Au/Ge(001) provokes the question whether or not the system is susceptible to additional ad-atoms which might have two possible influences: (i) bridging of neighboring chains, thereby increasing the interchain coupling which should in principle lead to a cross-over from a TLL back to a Fermi liquid. (ii) doping of the system. By choosing an appropriate dopant atom or molecule, the band filling can be increased and for the present case of undoped Au/Ge(001) with less than half-filling a triggered charge density wave at half-filling might be possible. Successful doping of nanowire systems from the literature is known for Au/Si(111) using a substrate miscut of 2°, where additional silicon atoms migrate from the bulk to the surface and form regular arrays on the gold induced chains thereby driving the former metallic system insulating [26]. For In/Si(111) some reports exist for electron doping by sodium adsorption [27–29].

Excess gold on Au/Ge(001)

Subsequent studies on surplus Au (deposition at T=15 K during live ARPES measurement at beamline 7.0.1 ALS) on the Au/Ge(001) surface did not yield any change in the band filling as observed by ARPES. Reaching a critical amount only leads to a vanishing band structure signal indicating a beginning metalization in terms of a polycrystalline closed film. This finding is in good agreement with potentiometry measurements performed in the group of Prof. Rolf Möller at the university of Duisburg-Essen [183]. They deposited an excess amount of gold as electrodes for two of three STM tips onto Au/Ge(001) while the third one was used to record the topography and the electrochemical potential. Their data indicate a lack of coupling between the Au islands and the nanowires, which is consistent with the present ARPES finding.

8.1. Electron doping by potassium adsorption

Alternatively, a small amount, estimated to be less than a monolayer of potassium was evaporated at room temperature on the Au/Ge(001) surface yielding spot-like decorations along the wire direction as observed in unoccupied states at U=+1.5 V, see Fig. 8.1(a). The decoration already looses (electronic) contrast at +1.2 V in Fig. 8.1(b),

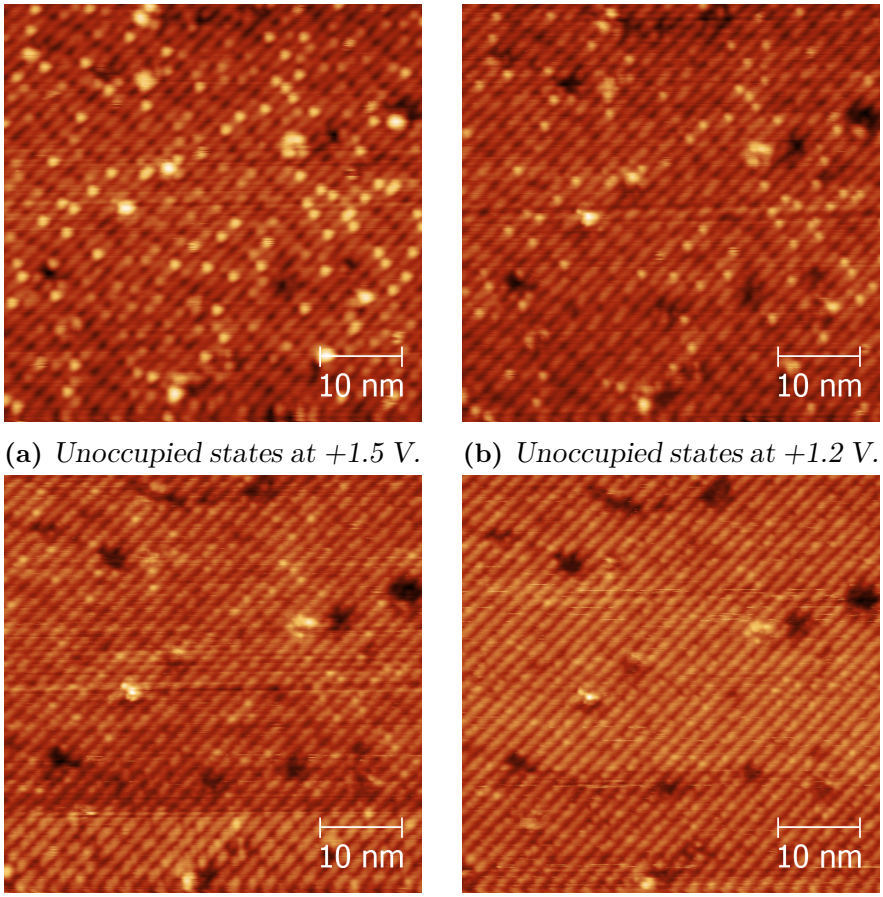

(a) *Unoccupied states at +1.5 V.* **(b)** *Unoccupied states at +1.2 V.*

(c) *Unoccupied states at +0.9 V.* **(d)** *Unoccupied states at +0.6 V.*

Figure 8.1.: *Bias series for unoccupied states of slightly potassium doped Au/Ge(001): (a) STM image at $U = +1.5$ shows few bright protrusions on the original nanowires. (b) At $U = +1.2$ V the contrast of the protrusions already decreases. (c)-(d) For lower bias, e.g. +0.9 and +0.6 V, the protrusions vanish. STM data by M. Moressi and C. Blumenstein.*

while it vanishes for lower bias voltages towards E_F like at +0.9 V and +0.6 V as shown in Fig. 8.1(c) and (d).

To study the influence on the band filling, ARPES measurements were conducted again at the ALS. Samples were kept at low-temperature down to 30 K during potassium evaporation from a commercial SAES getter source. Samples were aligned in normal emission to cut the $\bar{\Gamma}$-point of the surface Brillouin zone. The corresponding band structure yielding the two small electron pockets around $\bar{\Gamma}$ is depicted in Fig. 8.2(a). Potassium was evaporated during live ARPES measurements. The first potassium evaporation yields already an increased band width of 200 meV and a change in k_F by roughly 0.01-0.02 $Å^{-1}$. The band filling can be further increased as displayed after three evaporation cycles in Fig. 8.2(c), but at the cost of a reduced spectra quality which must be attributed to the disorder induced by the randomly adsorbed potassium atoms.

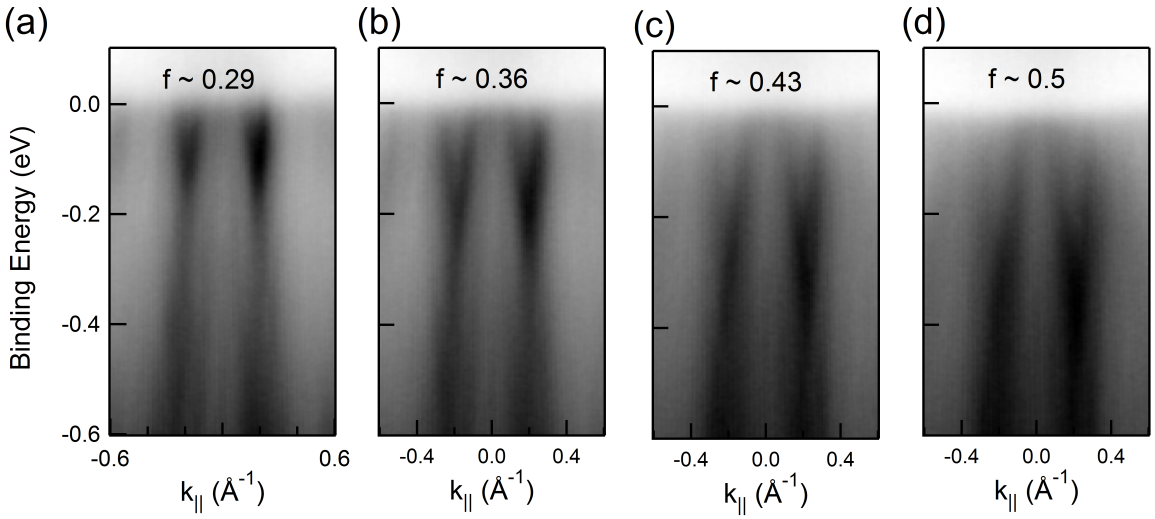

Figure 8.2.: *Band maps along $\bar{\Gamma}-\bar{K}$ for different potassium concentrations. (a) The bare Au/Ge(001) band structure with the small electron pockets around the $\bar{\Gamma}$-point. (b) Band situation after first potassium evaporation. Notably, the increased band filling ($f = 0.36$) causes an increase of the band depth and new k_F-values. (c) Further increase of potassium shifts the parabola downwards at the cost of spectra quality. (d) Roughly at half filling no indication of an energy gap nor a band backfolding is observed.*

The stepwise adsorption of potassium leads to a linear increase in the band filling as monitored by the band depth and k_F-values for the inner branches of both parabolas as plotted in Fig. 8.3(a) and (b). The highest achieved band depth is about 510 meV and a $k_{F1} = 0.04$ Å^{-1}. Compared to the initial values of 0.14 Å^{-1} the band filling can be

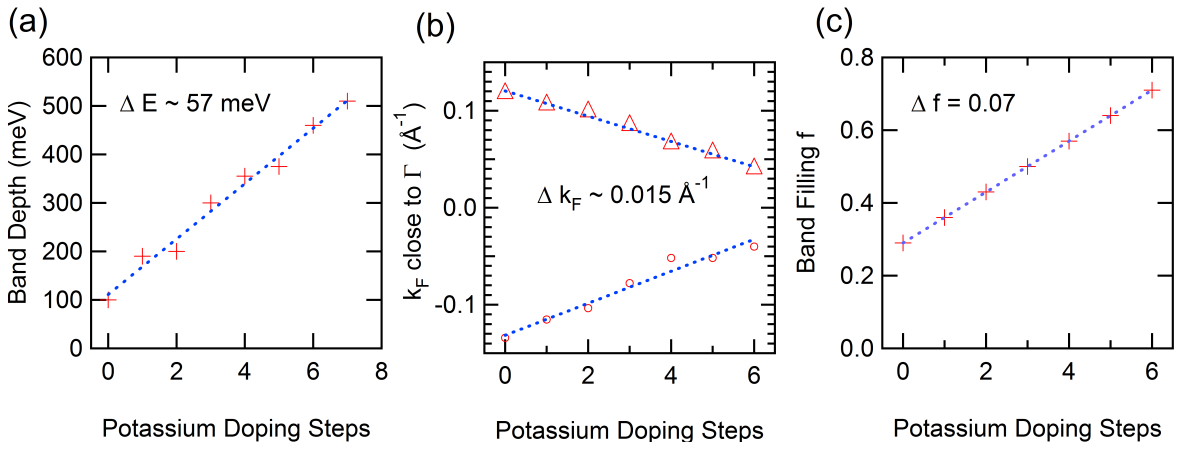

Figure 8.3.: *(a) Band depth from EDC at the band bottom ($k_x = 0.2$ Å^{-1}, (b) corresponding k_F vectors from the MDC close to E_F and (c) band filling f calculated from the ratio of occupied k-space and surface Brillouin zone size. All three parameter show a linear scaling as a function of potassium cycles with $\Delta E = 57$ meV, $\Delta k_F \sim 0.015$ and $\Delta f = 0.07$.*

increased to $\Delta k_F = 0.32$ Å^{-1} for one pocket which accounts to a total band filling of roughly 0.75 for both bands related to the size of the Brillouin zone. Thus, the critical values of half filling for a Peierls instability could be passed without any sign of a band backfolding or opening of an energy gap, at least at the applied low temperatures (∼30 K) and energy resolution (∼30 meV).

The disorder induced by the potassium atoms should in principle give rise to the TLL exponent α, as the potassium atoms should act as new boundaries within the chains. Unfortunately, the disorder simultaneously blurs the ARPES spectra that much, that a meaningful line shape analysis seems to be impossible. One possibility to overcome the disorder effect on the spectral function would be local tunneling spectroscopy.

8.2. New potassium induced (4×3) reconstruction

The sub monolayer coverage by potassium can increase the band filling of Au/Ge(001) just by randomly adsorbing along the wire. Notably, a new reconstruction can be induced for increased amounts of K on fully covered Au/Ge(001) adsorbed at room-temperature followed by an annealing step at 450-500 K. The new symmetry as judged by LEED is of p(4×3)-type, see experimental data in Fig. 8.4(a) compared to a reconstructed LEED image for a dual domain sample of (4×3) type in Fig. 8.4(b) .

The appearance in STM is similar to the former images of the doped Au/Ge(001) nanowires. They do not exhibit a certain wiggling in the overview images in Fig. 8.5 but

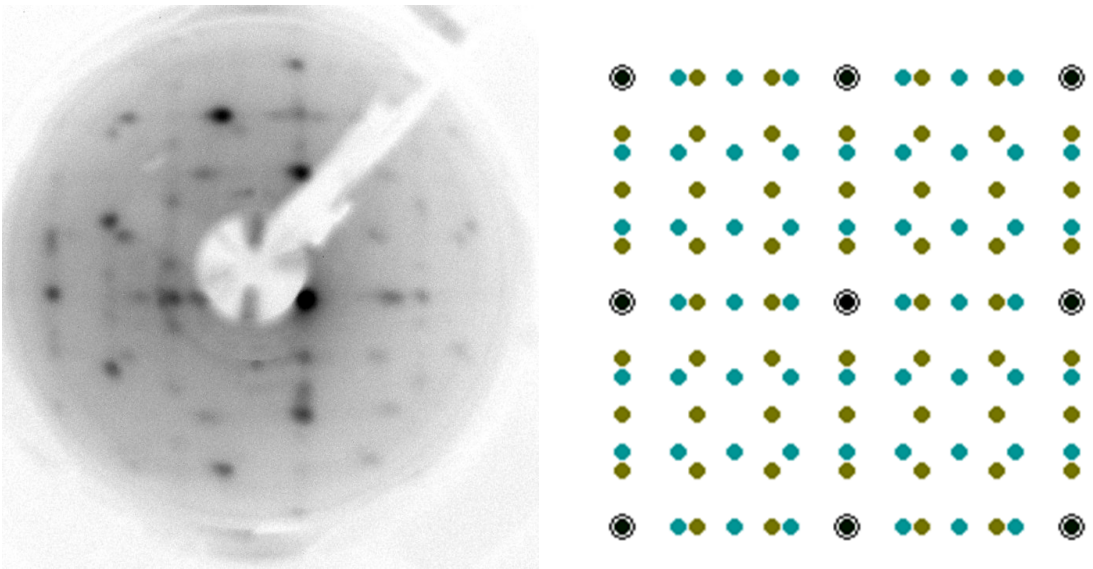

(a) *Experiment at 28 eV.* **(b)** *Constructed (4×3) pattern.*

Figure 8.4.: *LEED pattern of: (a) The new potassium induced reconstruction on Au/Ge(001) recorded at 28 eV. (b) Constructed LEED pattern for a dual-domain sample of p(4×3) symmetry.*

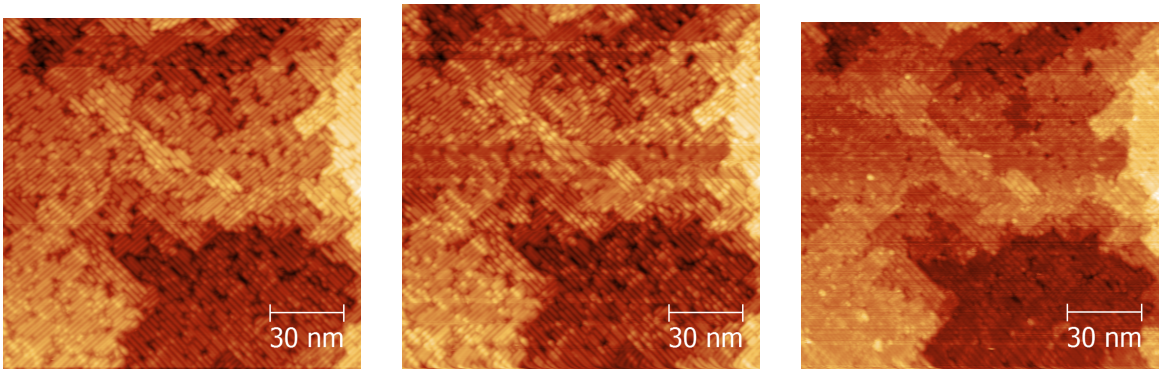

(a) *Unoccupied states at +1.5 V.*

(b) *Unoccupied states at +1.2 V.*

(c) *Unoccupied states at +0.6 V.*

Figure 8.5.: *Bias series for unoccupied states of slightly potassium doped Au/Ge(001): (a) STM image at $U = 1.5$ shows few bright protrusions on the original nanowires. (b) At $U = 1.2$ V the contrast of the protrusions reaches its maximum. (c) For lower bias, e.g. +0.6 V, the protrusions vanish.*

do show random decorations along the wire direction, see for instance Fig. 8.5(b). These decorations again vanish for lower bias voltages, so one may speculate about potassium atoms as the origin of these decorations. The size distribution of the potassium reconstruction is characterized by a shorter wire length compared to the initial Au/Ge(001) reconstruction.

The detailed shape of the potassium reconstruction is revealed in Fig. 8.5(a), which can be best described as pearls on a rope aligned in parallel with few pearls being brighter and more expanded. These segments seem to be decorated by additional K

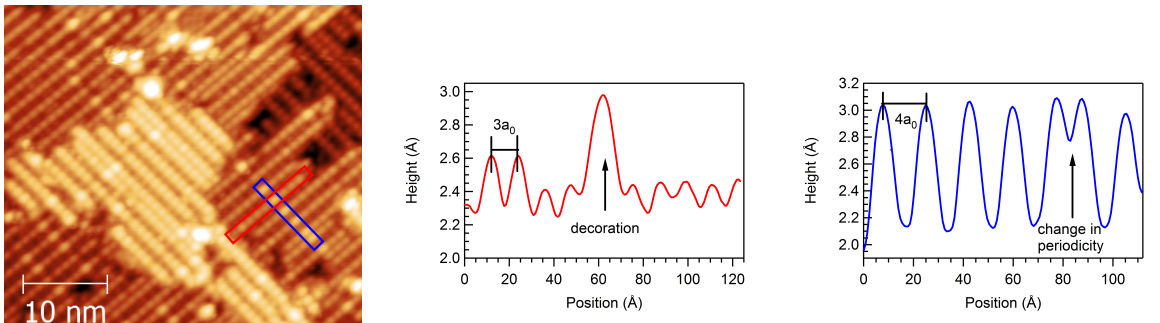

(a) *Occupied states at -1 V.*

(b) *Line-profile along the ropes.*

(c) *Line-profile perpendicular to ropes.*

Figure 8.6.: *(a) Occupied states at -1 V showing ropes of charge again forming wires. (b) Line-profile perpendicular to the ropes revealing a ×4 periodicity. (c) Dito along the ropes yielding a symmetry of ×3. Both results are in perfect agreement with the diffraction pattern of Fig. 8.4.*

ad-atoms. Line-profiles along (Fig. 8.6b) and perpendicular (Fig. 8.6c) to these chains reveal a repeating scheme of ×3 along the ropes and ×4 perpendicular to it.

Alkali on Ge(001) surface from the literature

The p(3×4) reconstruction is best compared with reports in the literature of alkali metals on the bare Ge(001), which are mostly based on sodium instead of potassium. Here Ernst and co-workers developed a detailed phase diagram, see Fig. 8.7, revealing two chain-like reconstructions for room temperature deposition [184, 185]: a (2×1) reconstruction at a coverage $\theta = \frac{1}{2}$ ML and a (4×1) at $\theta = \frac{1}{4}$ ML. Further annealing of these structures lead to partial desorption of sodium exhibiting first an incommensurate (3×2) at around $T = 520$ K ($\theta = \frac{1}{6}$ ML), which turns commensurate at $T = 620$ K.

For higher temperatures ($T = 660$ K) again a (4×1) reconstruction at $\theta = 0.085$ ML is found, which turns into a (6×1) at even lower coverage of $\theta = 0.055$ ML at $T = 680$ K. The high integer index thereby always indicates the periodicity perpendicular to the wire direction. Both the high-temperature (4×1) and the (6×1) reconstruction are characterized by ×3 streaks in LEED, see Fig. 8.8, which indicate a lateral distance of $3a_o$ along the chains, but weak correlation between the wires [185].

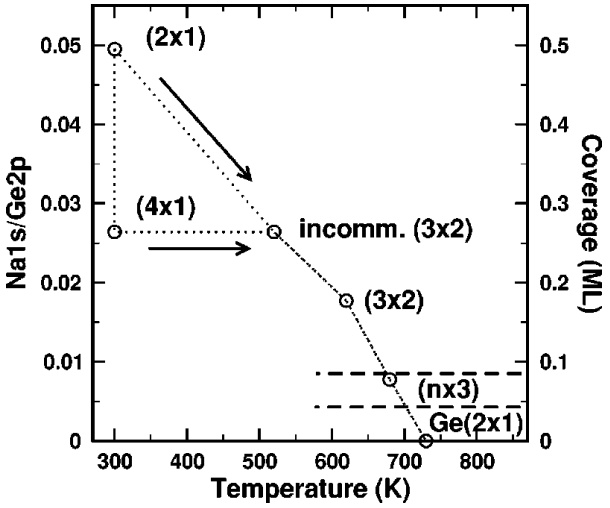

Figure 8.7.: *Phase diagram of sodium on Ge(001). At room temperature two reconstructions are found depending on the sodium coverage θ: a (2×1) reconstruction at θ = 0.5 ML and a (4×1) at θ = 0.25 ML. Further annealing yields an incommensurate (3×2) after desorption of sodium at T = 520 K, which turns commensurate at T = 620 K. Higher annealing temperatures, i.e. less sodium, results in (n×3) phases for n = 4, 6, 8. Figure reprinted with permission from W. Ernst, K.-L. Jonas, V. von Oeynhausen, C. Tegenkamp and H. Pfnür, Phys. Rev. B, Vol. 68, page 205303, 2003, http://link.aps.org/doi/10.1103/PhysRevB.68.205303. [185]. Copyright (2012) by the American Physicalk Society.*

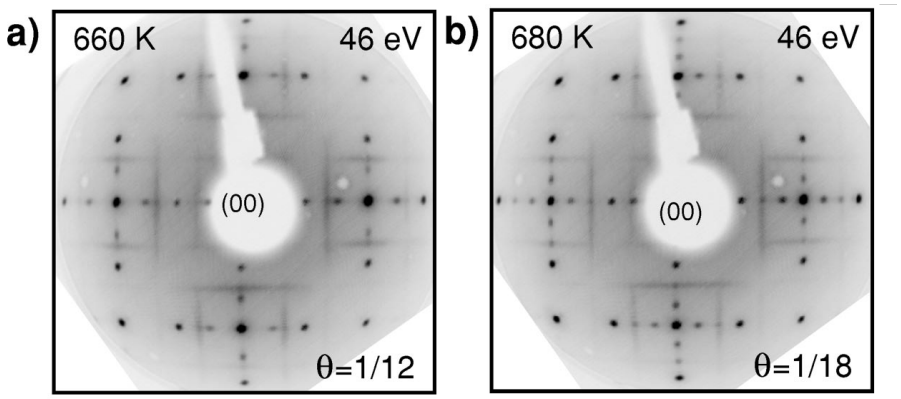

Figure 8.8.: *LEED pattern of Na/Ge(001) for : (a) the (4×1) reconstruction at T = 660 K and θ = 0.085 ML. (b) The (6×1) symmetry is found at θ = 0.065 ML and T = 680 K. Figure reprinted with permission from W. Ernst, K.-L. Jonas, V. von Oeynhausen, C. Tegenkamp and H. Pfnür, Phys. Rev. B, Vol. 68, page 205303, 2003, http://link.aps.org/doi/10.1103/PhysRevB.68.205303. [185]. Copyright (2012) by the American Physical Society.*

Structural analysis of the Na/Ge(001) surface by scanning tunneling microscopy verified the growth of the sodium chains parallel to the original Ge dimers. The growth mode is discussed by Ernst *et al.* to result from exchange between germanium dimers and sodium as concluded from the STM line-profiles, where the final sodium chains differ only little from the former Ge-dimers. This substitutional growth mode can also explain the relatively high temperatures (T = 660/680 K) which are required to build these reconstructions. Theoretical investigations of the alkali metal adsorption on the Ge(001)-p(2×1) reconstruction by Czech *et al.* indicate that sodium and potassium only differ little concerning their preferred adsorption site and appearance in calculated STM images [186].
Transferring the growth mode and the symmetries of Na/Ge(001) to the inspection of potassium on Au/Ge(001), a good match is found for the (4×1/3) reconstruction, which in case of K/Au/Ge(001) develops long-range order along the chain direction with neighboring chains being correlated such that a clear ×3 diffraction pattern can be observed. The slightly lower growth temperature of 450-500 K for K/Au/Ge(001) might be related to the gold atoms involved in the initial reconstruction which might lower the growth potential for the potassium chains. Further analysis is required to reveal the electronic ground state (ARPES) and the chemical configuration (XPS).

9. Conclusion

The gold-induced nanowires formed on Ge(001) are a prime candidate to study the electronic states of an undisturbed one-dimensional system. As concluded from STM, Au/Ge(001) is a close approach towards chains of single atom width. The substrate mediated growth leads to excellent long-range order and a very low defect density. In this context a cleaning procedure was introduced based on wet-chemical etching and subsequent thermal dry oxidation. The oxide is very thin, but homogeneous and acts as a passivating layer as judged from x-ray electron spectroscopy and AFM. The desorption of the oxide in UHV yields a high quality reconstructed Ge(001) surface as visible from XPS, STM and LEED. This cleaning procedure is simple, effective and, what is most critical, reproduceable to adopt the sample preparation to the various synchrotron facilities used within this thesis.
Structural insight in Au/Ge(001) was achieved from surface x-ray diffraction. Here, the challenging experimental requirements including an UHV set-up were all provided by the Material Science beamline at the Swiss Light Source, Villligen CH. Using 15 keV x-rays and a surface component l close to zero allowed to record a large set of in-plane reflexes which could be used to derive the autocorrelation function, i.e. the Patterson map. This map provides the in-plane distances between the strongest scattering atoms within the unit cell. Therefore, based on the most reliable reported gold coverage an allocation of the Patterson map peaks to Au-Au and Au-Ge distances was carried out. On the basis of a so-called "minimal structural model" two building blocks were identified: Au-Au homo-dimers forming the trenches and Au-Ge hetero-dimers within the wire embankment. Since the surface truncation rods from SXRD did not allow for a reliable vertical refinement, DFT calculations were performed in collaboration with Prof. Bechstedt and Simeon Sauer from Jena university. The total free energy compared to the bare Ge(001) surface is lowered by 0.7 eV during the relaxation process rendering the model stable. The relaxation itself leaves the Au homo-dimer unaffected while the former flat Au-Ge hetero-dimer gets buckled with the Ge atom slightly above the Au atom. Calculated STM images based on this "minimal structural model" already provide a good qualitative match with the experiment, although some discrepancies like the wire height or sideward buckling amplitude remain. Remarkably, the outstanding charge clouds observed in STM originate from Ge in the calculations, pointing out the important role of Ge in electronic/topographic contrast of the wire embankment as observed in STM. An alternative cross-check for the "minimal structural model" is provided by calculating the Patterson map for both the non-relaxed and the relaxed configuration. The non-relaxed configuration yields a reasonable agreement for the locations of all Au-Au maxima of

the experiment, albeit with a different intensity distribution. Within the relaxed version the maxima corresponding to the buckled dimer split leading to deviations from the experiment. Thus, a more refined structural approach based on more extensive SXRD data is desirable.
The electronic states of Au/Ge(001) are analyzed by ARPES. Two states are found for the gold-induced reconstruction. A hole-like state with the dispersion of a downward parabola is observed at the center of the Brillouin zone. It seems to resemble the well known valence band of bulk Ge with light/heavy-hole and split off branches, although within a heavy p-doping scenario and with a new surface periodicity. The corresponding Fermi surface is clearly of two-dimensional shape and the angle-integrated line shape follows a Fermi distribution proving the metallic character of this state.
The second surface state with an electron-like dispersion is of small band depth ($\sim$130 meV) and exhibits suppression of spectral weight towards the chemical potential. The constant energy surface at the chemical potential proves the 1D character of this state. Although there exists some debate on how to assign the dispersion direction to the real space architecture, only the chosen assignment along the wire direction seems plausible. This is supported by STM where only continuous conducting filaments are observed along the wire direction for all applied voltages. The tight-binding modeling of the dispersion for this electron pocket suggests a smaller anisotropy compared to gold on stepped silicon surfaces. Nevertheless, this degree of confinement does not hinder the Tomonaga-Luttinger regime. It is revealed as a power-law of the band integrated spectral function. The temperature dependent line shapes can be described by the Tomonaga-Luttinger liquid model with an exponent α of about 0.57 averaged for temperature between 10 K and 120 K. The exponent is slightly enhanced compared to tunneling spectroscopy data by Blumenstein [8]. This can be understood from the averaging effect in ARPES, where the photon spot covers several terraces including various chain ends. These are found to increase the TLL exponent as concluded from local STS.
In conclusion, the nanowires of Au/Ge(001) are an outstanding example of a combined spatially and electronically confined system exhibiting the rarely observed Tomonaga-Luttinger phase. The spectroscopic access by ARPES is well suited to study the band structure and the one-particle spectral function as the finger print for the present correlation effects. Necessarily, this method requires a wide range of photon energies to completely reveal the symmetry of the involved surface states. The extracted TLL exponent α agrees well with complementary results obtained by STS. Additional adsorption of potassium on the surface leads to an increased band filling. Simultaneously, disorder is introduced to the surface which causes a smearing out of dispersing features in ARPES, thereby preventing a quantitative analysis of the TLL exponent. However, no cross-over from the TLL state to a charge-density wave phase can be observed within the band structure in terms of energy gaps or band backfolding, even not in the presence of half-filling. This might be a first proof of a possible robustness of the TLL state against lateral coupling between the wires.

Further prospects

Improvement of structural model

To accomplish a final structural model additional SXRD experiments are required. These should include the surface truncations rods as a function of the surface normal component l for the basic c(8×2) as well as the additional p(4×1) reconstruction. Another source for structural informations can be Raman spectroscopy which was used in case of indium chains on silicon (111) [187, 188] to verify the complex hexagon model proposed by SXRD [155]. First promising results were already obtained for the bare Ge(001) surface [11].

Electronic structure

Concerning the electronic structure of Au/Ge(001) a more refined analysis on the temperature dependency of the TLL exponent in ARPES including more temperature steps and an increased energy resolution could be promising. Alternative approaches to study the TLL behavior might be provided by four-point-probe conductance measurements [189], spectroscopic ellipsometry yielding the optical conductance [190] or high energy electron loss spectroscopy (HREELS) [191].

Manipulation of the electronic states

The surface character of Au/Ge(001) allows the adsorption of doping materials, as exemplified in this thesis for potassium. Here, a stepwise increase of the band filling of the 1D band was monitored. No sign of a cross-over to a Fermi liquid was observed. Possible approaches would be:

- Local spectroscopy by STS to circumvent the disorder and reveal the influence of potassium on the TLL exponent.
- Use of molecules instead of alkali atoms to enhance the lateral overlap between the nanowires due to the larger extent of the molecules. Maybe also p-type doping would be possible.
- Substitution of gold by other elements to allow bonded doping atoms, which would minimize the disorder of the system.
- Intentional increase of defects or chain ends by ad-atoms or insufficient gold coverage to adjust the chain length. Defects act as boundaries for conduction electrons.
- Use Au/Ge(001) as a template for additional nanostructures or -wires. The rare examples of metals again forming atomic chains on other nanowires comprise indium on Au/Si(553) [194, 195] and lead on Au/Si(557) [196].

Appendix

A. Beamlines

Beamline 7.0.1 Advanced Light Source

Photoelectron spectroscopy always requires UHV conditions. The setup at the electron structure factory (ESF) at beamline 7.0.1. of the Advanced Light Source, Berkeley USA, is depicted in Fig. A.1. It consists of so called fast entry load-lock, which allows a sample introduction into the chamber within 20 minutes. From there one can transfer to the separated preparation chamber through the storage room, called roundhouse. The base pressure is typically in the mid 10^{-11} torr range. In the preparation chamber samples are degassed at about 350C° until the base pressure is reached again (takes usually 0.5-2h). A quick flash desorps the artificially grown oxide and the bare substrate quality can be checked with LEED. The chamber design allows afterwards the simultaneous evaporation on the heated substrate and the measurement of the Au amount with a quartz crystal. The typical Au rate was set to 0.2 Å per second and the total amount to 24 Å. The final c(8×2) reconstruction with the p(4×1) superstructure was again checked with LEED.

The sample could be held in the six-axis goniometer of the analysis chamber at temperature down to T=15 K, but also heating was possible albeit via contact with a wobble stick which could not be performed during a measurement. What is unique to the ARPES setup is the direct location of both an Au and K source directly below the lens cone of the Scienta analyzer, which allowed live view with the beam during doping experiment or cycles of doping and spectra recording. The analyzer is a standard Scienta R4000 hemispherical electron analyze with an acceptance angle of ± 15°. Due to the limited optical resolution the curved slits were always chosen to yield a total (combined) resolution of ≤ 25-30 meV. The beamline has three grating providing a nominal energy range of 80-1200 eV (schematic in Fig. A.2), but only values around 100 eV were used due to cross-sections and resolution issues. The polarization is fixed and lies in the horizontal plane. Since the wire direction is always aligned with the analyzer slit, the polarization direction typically corresponds to the this nanowire domain whereas is orthogonal in-plane to the second one. The beam spot size is $\sim 50\mu$m and thus exceeds the typical terrace size of one domain as judged by STM.

The ring current of 500 mA is operated at 1.9 GeV in the top-up mode (frequent injection of electrons) with a circumference of 196,8 m.

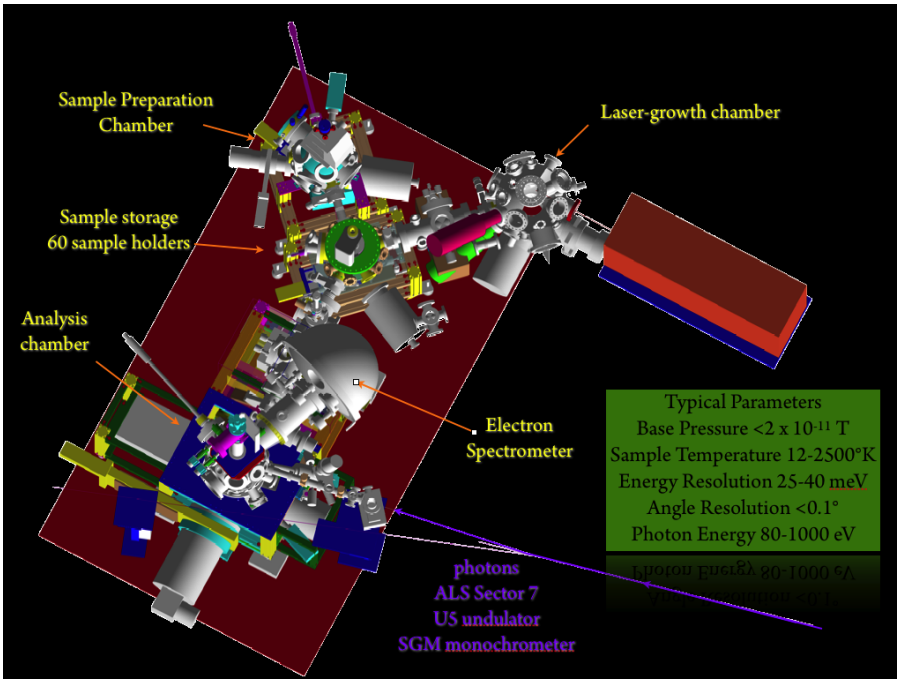

Figure A.1.: *Schematic drawing of the electronic structure factory (ESF) at beamline 7.0.1. Advanced Light Source Berkeley, USA. The setup contains a separate preparation chamber equipped with a LEED optics, electron beam evaporators and a direct heating stage. Freshly prepared samples can be stored in the round house before being directly transferred to the analysis chamber. The corresponding specifications of the beamline are displayed in the green frame.*

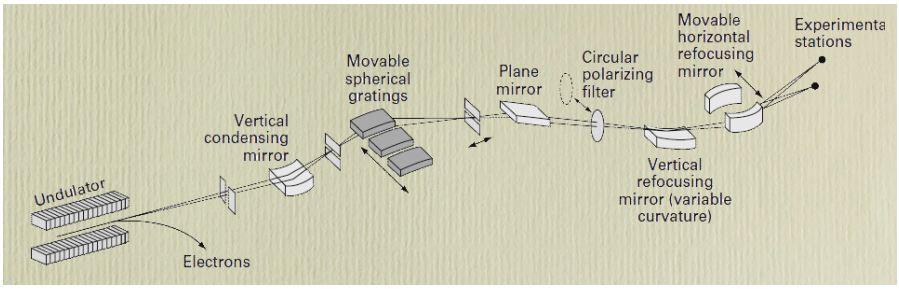

Figure A.2.: *Schematic drawing of optics for beamline 7.0.1. with the main parts being the undulator, mirror grating and focusing mirrors.*

HRPES Beamline Swiss Light Source

The Swiss Light Source, Villigen CH, is like the Advanced Light Source a third generation synchrotron. The electron ring is operated at 2.4 GeV (circumference 288 m) in the top-up mode (400 mA), and in case of the SIS high-resolution photoemission spectroscopy (HRPES) endstation the undulator XA09L provides linear horizontal ($h\nu$=10-800 eV), linear vertical (100-800 eV) and circular (50-800 eV) polarization. The spot size is slightly

bigger 50×100 μm compared to the 50 μm^2 at the ALS. The energy can be adjusted between 17 eV and 100 eV in the low voltage mode of the Scienta, which is also the favorable range for the band structure investigations of Au/Ge(001) with a reasonable energy resolution. The UHV chamber is equipped with a six-axis goniometer giving access to the complete k-space. The cooling capabilities allow a minimum temperature of about 10 K as well as a counter heater for temperature dependent measurements which are used for the line shape analysis.

The setup at the HRPES endstation of Surface and Interface Spectroscopy (SIS) beamline undulator XA09L at the Swiss Light Source is very similar to the setup of the ALS. Again, the chamber is composed of a load lock, an analysis and a preparation chamber, albeit without quartz crystal, but with Au ebeam and direct heating facility. The sample preparation is again monitored by LEED, a series of typical LEED pattern of the bare Ge(001) surface (a)/(b) and after growth (c) of Au/Ge(001) is presented in Fig. A.3.

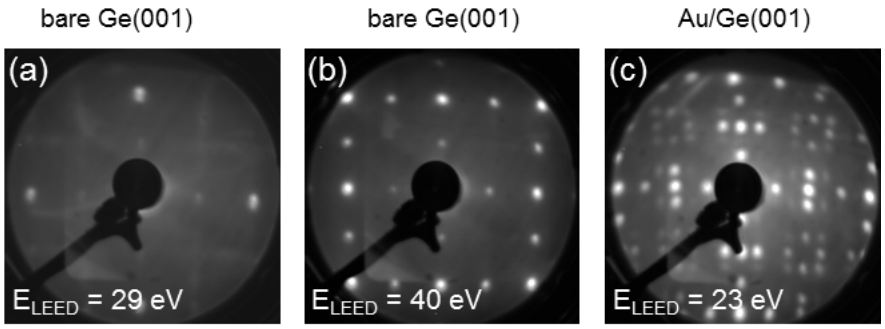

Figure A.3.: *(a) Bare Ge(001) surface at 29 eV showing the (2×1) spots and the c(4×2) streaks, which are absent at 40 eV shown in (b). (c) LEED pattern of the reconstructed Au/Ge(001) with the c(8×2) and additional (4×1) superspots.*

The goniometer in the analysis chamber is also of six-axis type, but provides a little better cooling due to the improved contact of sample holder and cryogenic parts of the manipulator, see image in Fig. A.4, which allows temperatures down to 10 K instead of 15 K and a reduced LHe consumption.

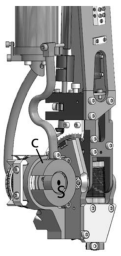

Figure A.4.: *Six-axis goniometer. Due to the improved and massive cryo-contact attached to the whole sample holder a minimal temperature of T=10 K is achieved.*

Connection to ALS sample and spectra quality

Switching from one experimental setup at a synchrotron to another always requires the adjustment of the growth parameters due to the different sample holders (thermal contact, contact area of the sample etc.) and evaporation source (distance, crucible size, fabricate etc.). In case of the HRPES endstation the sample is only marginally fixed with clamps on both sides which cause a decrease in the heat dissipation as compared to the ALS where the sample was fixed to a large extent on both sides with Ta-foil. To compensate this effect, the heating current had to be reduced to ensure the correct temperature of about 650 K. Gold was evaporated by an electron beam evaporator without any rate meter like a quartz micro crystal. The correct Au amount and the required thermal energy were checked with low-energy electron diffraction, which had to show the well known c(8×2) reconstruction and the p(4×1) superstructure. A typical series LEED images can be found in the Fig. A.3.

To compare the achieved sample quality with the results obtained at the ALS, a band map was taken at $h\nu$=100 eV at T=10 K, shown in Fig. A.5. The cut along the $\bar{\Gamma}$-K line shows exactly the same two electronic states: an electron pocket located at $k_{||}$=0.2Å^{-1} and a hole-like parabola at the $\bar{\Gamma}$-point. The interplay of an (possibly) increased sample quality and the lower temperature allows the thoroughly observation of the repetition scheme for both electronic states in the next surface Brillouin zone with $\Delta k=\pi/2a_0$. This nicely matches the results of the Advanced Light Source with an overall improved quality.

Material Science Beamline Swiss Light Source

The sample preparation for the SXRD experiments was again conducted at the SIS endstation. For the measurements the sample had to be transferred into a mobile chamber (called “baby chamber” due to the small and compact size) which is equipped with a

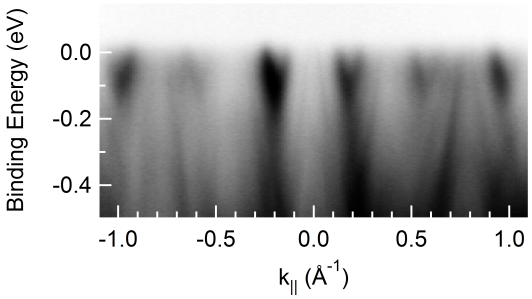

Figure A.5.: *Band structure measurement at T=10 K along the $\bar{\Gamma}$-$\bar{K}$ taken with $h\nu$=100 eV. The two well established reconstruction-induced states are present. An improvement of the spectra quality is noticed allowing the observation of the band repetition outside the first SBZ. This must be ascribed to the lower temperature and/or improved sample quality.*

sample storage within a beryllium dome allowing for the x-ray scattering, see Fig. A.6(a). The chamber is pumped with a iongetter pump at a base pressure of p=$1{\cdot}10^{-9}$ mbar. The chamber is mounted on a hexapod with an angular precision of 0.0012° as depicted in Fig. A.6(b), while the angular precision of the movable detector Pilatus 100k detector account to 0.0025° [192]. The Pilatus 100k detector is custom built and designed by the SLS staff. It consists of an array of 366×157 pixel with an active area of 7.9×3.4 cm^2 in total. This special detector allows fast data acquisition and does not suffer from electronic noise which makes it superior to conventional CCD array [88]. The thickness of the silicon sensor is 300 μm and provides a x-ray adsorption $<$ 95% below 8 keV, 74% at 12 keV and 25% at 20 keV with the beamline ranging from 5 keV to 40 keV [88]. Further details on the beamline specifications are given in Ref.[193].

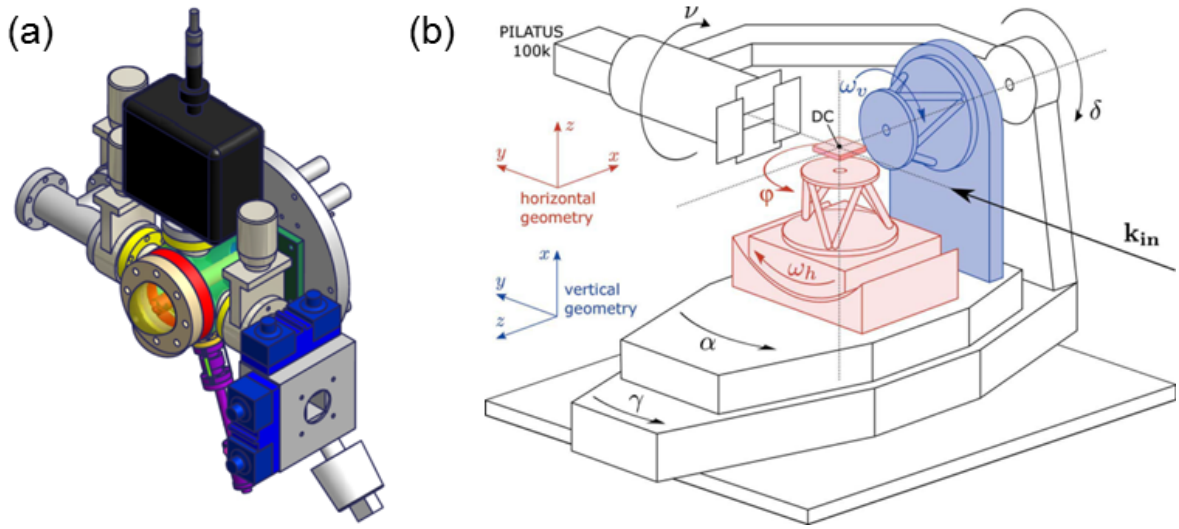

Figure A.6.: *(a) Mobile transport UHV chamber for SXRD experiments. The beryllium dome is visible at the front side with the sample location underneath. The base pressure is ∼$1{\cdot}10^{-9}$ mbar achieved with an ion getter pump (black). The chamber is attached to the hexapod of the endstation in (b) in the same geometry as the drawing (vertical geometry).*

B. Alternative structural models

On the basis of the Patterson map obtained from SXRD and the coverage of 0.75 of ML of Au from Gallagher *et al.* [43] some other basic structure proposals can be made by attaching the Au atoms onto the reconstructed Ge(001) surface. The first alternative model [1(a/b] consists of the well known Au homo-dimers in the trenches (TR) while the nanowires (NW) are composed of single atoms in a ladder configuration 1(a) which can be modified by dimerization along the nanowire yielding configuration 1(b). From the side view in Fig. B.7(a) the artificial height of the nanowire embankment becomes apparent which was introduced to account for the pronounced height contrast observed in STM [1, 124].

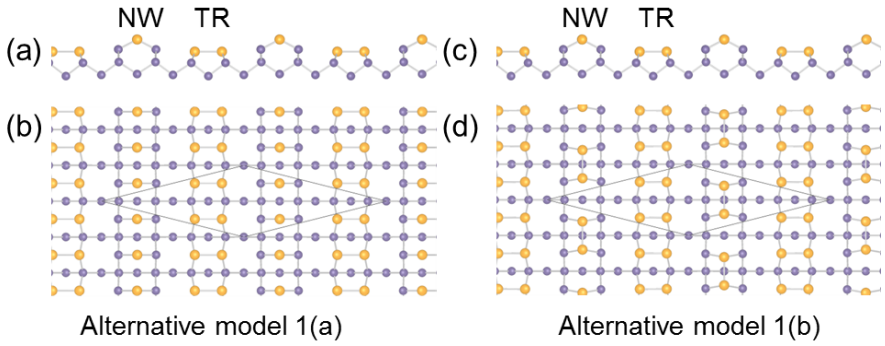

Figure B.7.: *Alternative model 1: (a) and (c) side view showing a hexagon of five Ge atoms and a Au atom on top as the building block of the nanowires (NW). The trenches (TR) consist of a flat Au homo-dimer. (b) and (d) top view of configuration 1(a) and 1(b) which differ by the dimerization of the single Au atoms in the latter case. The c(8×2) unit cell is implemented by the flat lying diamond proving the right coverage of six Au atoms on eight Ge atoms underneath (0.75 ML).*

The relaxation of both models within the GGA results in positive values for the free energy $\Delta\Omega_{1a/b}$=+0.40(7/8) eV (a/b) rendering both configuration energetically unfavorable. A second quick cross-check is given by the DFT derived STM images of Fig. B.8. Here a strong deviation from the experiment is observed in terms of interrupted segments along the wire direction instead of continuous conduction paths for almost all bias values and independent of the leading sign of the polarity.

In a slightly modified version of alternative model 1, the artificial wire embankment is omitted resulting in a flat single atom which is located below the line of the Au homo-dimer of the trenches, see Fig. B.9(a) and (b). The total free energy $\Delta\Omega_2$=+0.354 eV is slightly decreased compared to the alternative model 1, but still far above zero. The corresponding STM images derived from this model exhibit a more pronounced height for the trenches than for the wires which clearly contradicts the experimental data. Thus, both building blocks containing a single atom along the chain with (1) and without (2) an additional embankment of Ge atoms beneath the top wire atom of Au

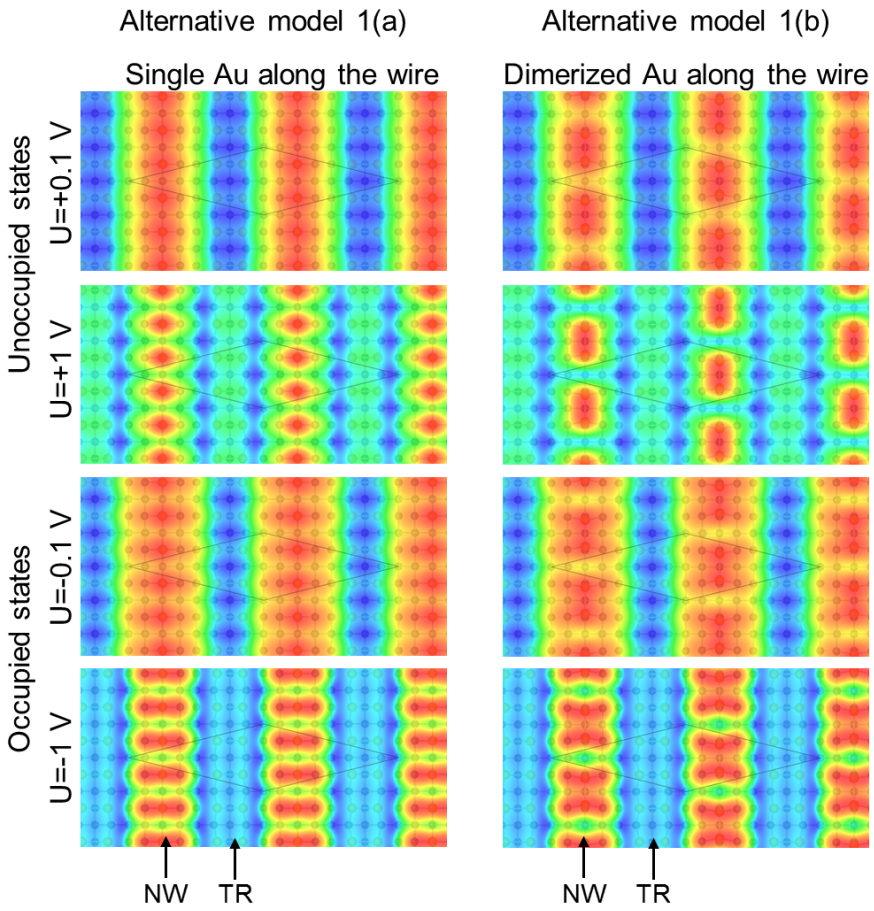

Figure B.8.: *Calculated STM images on the basis of both alternative models 1(a) and (b) from DFT. Only the unoccupied states show a continuous conduction path compatible with the experiment whereas all other experimental conditions yield discrete segments along the wire direction contradicting the experimental findings.*

do not result in plausible structures compatible with actual experimental findings. Due to the eminent discrepancies from the total free energy and the derived STM images a further analysis in terms of calculated Patterson maps based on the relaxed model coordinates is omitted.

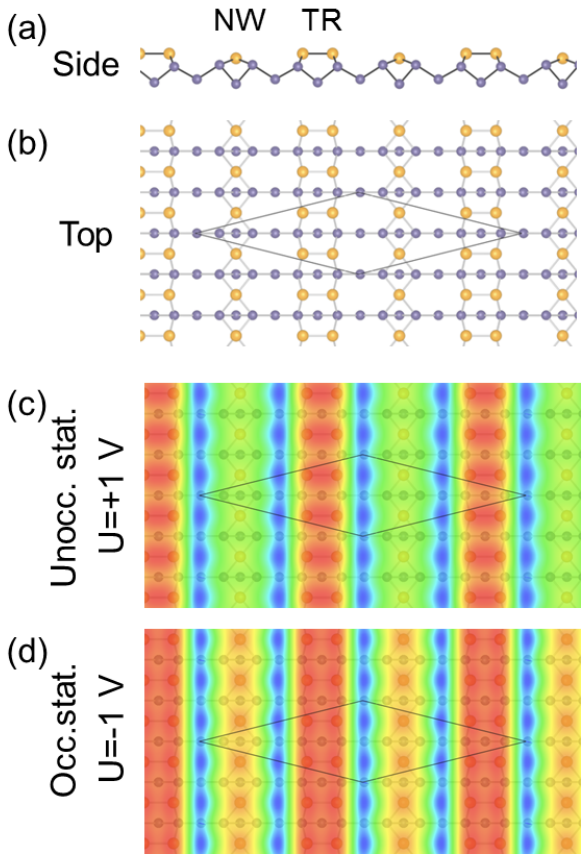

Figure B.9.: *(a) Top and (b) side view of alternative model 2. The supposed wire ridge is made of single Au atoms tetravalent bound to Ge atoms. It is located slightly below the well known Au homo-dimer building the trenches. The calculated STM images are comprised of a pronounced linear charge originating from the supposed trenches instead of the wires which clearly contradicts the experimental STM data.*

Bibliography

List of own publications

[1] J. Schäfer, C. Blumenstein, S. Meyer, M. Wisniewski and R. Claessen, *New Model System for a One-Dimensional Electron Liquid: Self-Organized Atomic Gold Chains on Ge(001)*, Phys. Rev. Lett. **101**, 236802 (2008).

[2] A. Hofmann, X. Y. Cui, J. Schäfer, S. Meyer, P. Höpfner, C. Blumenstein, M. Paul, L. Patthey, E. Rotenberg, J. Bünemann, F. Gebhard, T. Ohm, W. Weber and R. Claessen, *Renormalization of Bulk Magnetic Electron States at High Binding Energies*, Phys. Rev. Lett. **102**, 187204 (2009).

[3] J. Schäfer, S. Meyer, C. Blumenstein, K. Roensch, R. Claessen, S. Mietke, M. Klinke, T. Podlich, R. Matzdorf, A. A. Stekolnikov, S. Sauer and F. Bechstedt, *Self-organized atomic nanowires of noble metals on Ge(001): atomic structure and electronic properties*, New. J. Phys. **11**, 125011 (2009).

[4] J. Schäfer, C. Blumenstein, S. Meyer, M. Wisniewski and R. Claessen, *Reply to Comment on "New Model System for a One-Dimensional Electron Liquid: Self-Organized Atomic Gold Chains on Ge(001)"*, Phys. Rev. Lett. **103**, 209702 (2009).

[5] S. Meyer, J. Schäfer, C. Blumenstein, P. Höpfner, A. Bostwick, J. L. McChesney, E. Rotenberg and R. Claessen, *Strictly one-dimensional electron system in Au chains on Ge(001) revealed by photoelectron k-space mapping*, Phys. Rev. B **83**, 121411 (2011).

[6] P. Höpfner, J. Schäfer, A. Fleszar, S. Meyer, C. Blumenstein, T. Schramm, M. Heßmann, X. Cui, L. Patthey, W. Hanke and R. Claessen, *Electronic band structure of the two-dimensional metallic electron system Au/Ge(111)*, Phys. Rev. B **83**, 235435 (2011).

[7] C. Blumenstein, S. Meyer, A. Ruff, B. Schmid, J. Schäfer and R. Claessen, *High purity chemical etching and thermal passivation process for Ge(001) as nanostructure template*, J. Chem. Phys. **135**, 064201 (2011).

[8] C. Blumenstein, J. Schäfer, S. Mietke, S. Meyer, A. Dollinger, M. Lochner, X. Y. Cui, L. Patthey, R. Matzdorf and R. Claessen, *Atomically controlled quantum chains hosting a Tomonaga-Luttinger liquid*, Nat. Phys. **7**, 776 (2011).

[9] C. Blumenstein, J. Schäfer, S. Mietke, S. Meyer, A. Dollinger,M. Lochner, X.Y. Cui, L. Patthey, R. Matzdorf, R. Claessen, *Debate over dispersion direction in a Tomonaga-Luttinger-liquid system Reply*, Nat. Phys. **8**, 174 (2012).

[10] S. Meyer, T. E. Umbach, C. Blumenstein, J. Schäfer, R. Claessen, S. Sauer, S. J. Leake, P. R. Willmott, M. Fiedler and F. Bechstedt, *Structural examination of Au/Ge(001) by surface x-ray diffraction and scanning tunneling microscopy*, Phys. Rev. B **85**, 235439 (2012).

[11] J. Räthel, E. Speiser, N. Esser, U. Bass, S. Meyer, J. Schäfer, J. Geurts, *Surface phonons of Ge(001) and their correlation with the p(2×1) and c(4×2) reconstruction as shown by Raman spectroscopy*, Phys. Rev. B **86**, 035312 (2012).

[12] C. Blumenstein, S. Meyer, S. Mietke, J. Schäfer, A. Bostwick, E. Rotenberg, R. Matzdorf, R. Claessen, *Au-induced quantum chains on Ge(001) - symmetries, long-range order, and conduction path*, J. Phys. Cond. Mat. **25**, 014015 (2013).

[13] G. Li, P. Höpfner, J. Schäfer, C. Blumenstein, S. Meyer, A. Bostwick, E. Rotenberg, R. Claessen and W. Hanke, *Magnetic order in a frustrated two-dimensional atom lattice at a semiconductor surface*, Nat. Commun. **4**, 1620 (2013).

[14] S. Meyer, J. Schäfer, C. Blumenstein, L. Dudy, P. Höpfner, T.E. Umbach, A. Dollinger, X.Y. Cui, L. Patthey, R. Claessen, *Photon energy and temperature dependent analysis of the Tomonaga-Luttinger system Au/Ge(001) by angle-resolved photoemission*, manuscript (2012).

References

[15] E. Dagotto, *Correlated electrons in high-temperature superconductors*, Rev. Mod. Phys. **66**, 763 (1994).

[16] M. Imada, A. Fujimori and Y. Tokura, *Metal-insulator transitions*, Rev. Mod. Phys. **70**, 1039 (1998).

[17] G. Grüner, *The dynamics of charge-density waves*, Rev. Mod. Phys. **60**, 1129 (1988).

[18] V. Vescoli, L. Degiorgi, W. Henderson, G. Grüner, K. P. Starkey and L. K. Montgomery, *Dimensionality-Driven Insulator-to-Metal Transition in the Bechgaard Salts*, Science **281**, 1181 (1998).

[19] F. Zwick, S. Brown, G. Margaritondo, C. Merlic, M. Onellion, J. Voit and M. Grioni, *Absence of Quasiparticles in the Photoemission Spectra of Quasi-one-dimensional Bechgaard Salts*, Phys. Rev. Lett. **81**, 2974 (1997).

[20] R. Claessen, M. Sing, U. Schwingenschlögl, P. Blaha, M. Dressel and C. S. Jacobsen, *Spectroscopic Signatures of Spin-Charge Separation in the Quasi-One-Dimensional Organic Conductor TTF-TCNQ*, Phys. Rev. Lett. **88**, 096402 (2002).

[21] R. Plass and L. D. Marks, *Submonolayer Au on Si(111) phase diagram*, Surf. Sci. **380**, 497 (1997).

[22] I. Barke, F. Zheng, S. Bockenhauer, K. Sell, V. v. Oeynhausen, K. H. Meiwes-Broer, S. C. Erwin and F. J. Himpsel, *Coverage-dependent faceting of Au chains on Si(557)*, Phys. Rev. B **79**, 155301 (2009).

[23] J. Kraft, M. G. Ramsey and F. P. Netzer, *Surface reconstructions of In on Si(111)*, Phys. Rev. B **55**, 5384 (1997).

[24] P. C. Snijders and H. H. Weitering, *Colloquium : Electronic instabilities in self-assembled atom wires*, Rev. Mod. Phys. **82**, 307 (2010).

[25] G. V. Nazin, X. H. Qiu and W. Ho, *Visualization and Spectroscopy of a Metal-Molecule-Metal Bridge*, Science **302**, 77 (2003).

[26] W. H. Choi, P. G. Kang, K. D. Ryang and H. W. Yeom, *Band-Structure Engineering of Gold Atomic Wires on Silicon by Controlled Doping*, Phys. Rev. Lett. **100**, 126801 (2008).

[27] H. Morikawa, C. C. Hwang and H. W. Yeom, *Controlled electron doping into metallic atomic wires: Si*(111)4×1-*In*, Phys. Rev. B **81**, 075401 (2010).

[28] S. V. Ryjkov, T. Nagao, V. G. Lifshits and S. Hasegawa, *Phase transition and stability of Si(111)-(8×'2')-In surface phase at low temperatures*, Surf. Sci. **488**, 15 (2001).

[29] H. Shim, S.-Y. Yu, W. Lee, J.-Y. Koo and G. Lee, *Control of phase transition in quasi-one-dimensional atomic wires by electron doping*, Appl. Phys. Lett. **94**, 231901 (2009).

[30] R. Peierls, *Quantum Theory of Solids*, Clarendon Press, Oxford (1964).

[31] K. Rossnagel, *On the origin of charge-density waves in select layered transition-metal dichalcogenides*, J. Phys. Condens. Matter **23**, 213001 (2011).

[32] H. W. Yeom, S. Takeda, E. Rotenberg, I. Matsuda, K. Horikoshi, J. Schaefer, C. M. Lee, S. D. Kevan, T. Ohta, T. Nagao and S. Hasegawa, *Instability and Charge Density Wave of Metallic Quantum Chains on a Silicon Surface*, Phys. Rev. Lett. **82**, 4898 (1999).

[33] P. C. Snijders, S. Rogge and H. H. Weitering, *Competing Periodicities in Fractionally Filled One-Dimensional Bands*, Phys. Rev. Lett. **96**, 076801 (2006).

[34] J. R. Ahn, J. H. Byun, H. Koh, E. Rotenberg, S. D. Kevan and H. W. Yeom, *Mechanism of Gap Opening in a Triple-Band Peierls System: In Atomic Wires on Si*, Phys. Rev. Lett. **93**, 106401 (2004).

[35] A. A. Stekolnikov, K. Seino, F. Bechstedt, S. Wippermann, W. G. Schmidt, A. Calzolari and M. B. Nardelli, *Hexagon versus Trimer Formation in In Nanowires on Si(111): Energetics and Quantum Conductance*, Phys. Rev. Lett. **98**, 026105 (2007).

[36] S. Wippermann and W. G. Schmidt, *Entropy Explains Metal-Insulator Transition of the Si(111)-In Nanowire Array*, Phys. Rev. Lett. **105**, 126102 (2010).

[37] S. itiro Tomonaga, *Remarks on Bloch's Method of Sound Waves applied to Many-Fermion Problems*, Progress of Theoretical Physics **5**, 544 (1950).

[38] J. M. Luttinger, *An exactly soluble model of a many-fermion system*, Journal of Mathematical Physics **4**, 1154 (1963).

[39] F. D. M. Haldane, *'Luttinger liquid theory' of one-dimensional quantum fluids. I. Properties of the Luttinger model and their extension to the general 1D interacting spinless Fermi gas*, J. Phys. C: Solid State Physics **14**, 2585 (1981).

[40] R. Winkler, *Spin−Orbit Coupling Effects in Two-Dimensional Electron and Hole Systems*, Springer, Berlin (2003).

[41] I. Barke, F. Zheng, T. K. Rügheimer and F. J. Himpsel, *Experimental Evidence for Spin-Split Bands in a One-Dimensional Chain Structure*, Phys. Rev. Lett. **97**, 226405 (2006).

[42] S. C. Erwin and F. J. Himpsel, *Intrinsic magnetism at silicon surfaces*, Nat. Comm. **1**, 58 (2010).

[43] M. C. Gallagher, S. Melnik and D. Mahler, *Temperature- and exposure-dependent study of the Ge(001)c*(8×2)*-Au surface*, Phys. Rev. B **83**, 033302 (2011).

[44] J. Wang, M. Li and E. I. Altman, *Scanning tunneling microscopy study of self-organized Au atomic chain growth on Ge(001)*, Phys. Rev. B **70**, 233312 (2004).

[45] J. Wang, M. Li and E. Altman, *Scanning tunneling microscopy study of Au growth on Ge(001): Bulk migration, self-organization, and clustering*, Surf. Sci. **596**, 126 (2005).

[46] J. R. Ahn, P. G. Kang, K. D. Ryang and H. W. Yeom, *Coexistence of Two Different Peierls Distortions within an Atomic Scale Wire: Si(553)-Au*, Phys. Rev. Lett. **95**, 196402 (2005).

[47] Y. J. Sun, S. Agario, S. Souma, K. Sugawara, Y. Tago, T. Sato and T. Takahashi, *Cooperative structural and Peierls transition of indium chains on Si(111)*, Phys. Rev. B **77**, 125115 (2008).

[48] J. Voit, *One-dimensional Fermi liquids*, Rep. Prog. Phys. **58**, 977 (1995).

[49] K. Schönhammer, *Interacting fermions in one dimension: The Tomonaga-Luttinger model*, eprint arXiv:cond-mat/9710330 (1997).

[50] A. Damascelli, Z. Hussain and Z.-X. Shen, *Angle-resolved photoemission studies of the cuprate superconductors*, Rev. Mod. Phys. **75**, 473 (2003).

[51] H. L. Störmer, D. C. Tsui and A. C. Gossard, *The fractional quantum Hall effect*, Rev. Mod. Phys. **71**, S298 (1999).

[52] N. W. Ashcroft and D. N. Mermin, *Solid state physics*, Brooks/Cole, 1 edn. (1976).

[53] V. Meden and K. Schönhammer, *Spectral functions for the Tomonaga-Luttinger model*, Phys. Rev. B **46**, 15753 (1992).

[54] J. Voit, *Charge-spin separation and the spectral properties of Luttinger liquids*, Phys. Rev. B **47**, 6740 (1993).

[55] A. Schofield, *Non-Fermi liquids*, Contemporary Physics **40**, 95 (1999).

[56] J. Voit, *Spectral properties of nearly free and strongly correlated one-dimensional electrons*, J. Electron Spec. Rel. Phenom. **117-118**, 469 (2001).

[57] D. Schuricht, S. Andergassen and V. Meden, *Local spectral properties of Luttinger liquids: scaling versus nonuniversal energy scales*, ArXiv e-prints (2011).

[58] M. Bockrath, D. Cobden, J. Lu, A. Rinzler, R. Smalley, L. Balents and P. McEuen, *Luttinger-liquid behaviour in carbon nanotubes*, Nature **397**, 598 (1999).

[59] K. Schönhammer and V. Meden, *Correlation effects in photoemission from low dimensional metals*, J. Electron Spec. Rel. Phenom. **62**, 225 (1993).

[60] H. J. Schulz, *Correlation exponents and the metal-insulator transition in the one-dimensional Hubbard model*, Phys. Rev. Lett. **64**, 2831 (1990).

[61] J. Solyom, *The Fermi gas model of one-dimensional conductors*, Advances in Physics **28**, 201 (1979).

[62] F. D. M. Haldane, *General Relation of Correlation Exponents and Spectral Properties of One-Dimensional Fermi Systems: Application to the Anisotropic $S = \frac{1}{2}$ Heisenberg Chain*, Phys. Rev. Lett. **45**, 1358 (1980).

[63] K. Schönhammer, *Luttinger Liquids: The Basic Concepts*, arXiv:cond-mat/0305035 (2003).

[64] A. Luther and V. J. Emery, *Backward Scattering in the One-Dimensional Electron Gas*, Phys. Rev. Lett. **33**, 589 (1974).

[65] R. G. Pereira, S. R. White and I. Affleck, *Spectral function of spinless fermions on a one-dimensional lattice*, Phys. Rev. B **79**, 165113 (2009).

[66] M. Khodas, M. Pustilnik, A. Kamenev and L. I. Glazman, *Fermi-Luttinger liquid: Spectral function of interacting one-dimensional fermions*, Phys. Rev. B **76**, 155402 (2007).

[67] A. Imambekov and L. I. Glazman, *Universal Theory of Nonlinear Luttinger Liquids*, Science **323**, 228 (2009).

[68] R. Egger and A. O. Gogolin, *Effective Low-Energy Theory for Correlated Carbon Nanotubes*, Phys. Rev. Lett. **79**, 5082 (1997).

[69] C. Kane, L. Balents and M. P. A. Fisher, *Coulomb Interactions and Mesoscopic Effects in Carbon Nanotubes*, Phys. Rev. Lett. **79**, 5086 (1997).

[70] A. Schulz, A. De Martino, P. Ingenhoven and R. Egger, *Low-energy theory and RKKY interaction for interacting quantum wires with Rashba spin-orbit coupling*, Phys. Rev. B **79**, 205432 (2009).

[71] J. Voit and H. J. Schulz, *Electron-phonon interaction and phonon dynamics in one-dimensional conductors*, Phys. Rev. B **37**, 10068 (1988).

[72] R. Peierls, *Quantum Theory of Solids*, Oxford University (1955).

[73] H. Fröhlich, *On the Theory of Superconductivity: The One-Dimensional Case*, Proceedings of the Royal Society of London. Series A. Mathematical and Physical Sciences **223**, 296 (1954).

[74] D. Allender, J. W. Bray and J. Bardeen, *Theory of fluctuation superconductivity from electron-phonon interactions in pseudo-one-dimensional systems*, Phys. Rev. B **9**, 119 (1974).

[75] S. K. Chan and V. Heine, *Spin density wave and soft phonon mode from nesting Fermi surfaces*, J. Phys. F: Metal Physics **3**, 795 (1973).

[76] S. Hüfner, *Photoelectron Spectroscopy*, Springer, Berlin, 3 edn. (2003).

[77] M. P. Seah and W. A. Dench, *Quantitative electron spectroscopy of surfaces: A standard data base for electron inelastic mean free paths in solids*, Surf. Interf. Ana. **1**, 2 (1979).

[78] S. Tanuma, C. J. Powell and D. R. Penn, *Calculations of electron inelastic mean free path data for 14 organic-compounds over the 50-2000 eV range*, Surf. Interf. Ana. **21**, 165 (1994).

[79] F. Himpsel, *Experimental-determination of bulk energy-band dispersions*, Appl. Opt. **19**, 3964 (1980).

[80] C.S. and Fadley, *X-ray photoelectron spectroscopy: Progress and perspectives*, J. Electron Spec. Rel. Phenom. **178-179**, 2 (2010).

[81] N. V. Smith, P. Thiry and Y. Petroff, *Photoemission linewidths and quasiparticle lifetimes*, Phys. Rev. B **47**, 15476 (1993).

[82] O. Fischer, M. Kugler, I. Maggio-Aprile, C. Berthod and C. Renner, *Scanning tunneling spectroscopy of high-temperature superconductors*, Rev. Mod. Phys. **79**, 353 (2007).

[83] F. J. Giessibl, *Atomic resolution on Si(111)-(7 x 7) by noncontact atomic force microscopy with a force sensor based on a quartz tuning fork*, Appl. Phys. Lett. **76**, 1470 (2000).

[84] F. Jona, J. Strozier and W. Yang, *Low-energy electron diffraction for surface structure analysis*, Rep. Prog. Phys. **45**, 527 (1982).

[85] R. Feidenhans'l, *Surface structure determination by X-ray diffraction*, Surf. Sci. Rep. **10**, 105 (1989).

[86] I. K. Robinson and D. J. Tweet, *Surface X-ray diffraction*, Rep. Prog. Phys. **55**, 599 (1992).

[87] M. M. Woolfson, *Direct methods in crystallography*, Rep. Prog. Phys. **34**, no. 2, 369 (1971).

[88] C. M. Schlepütz, R. Herger, P. R. Willmott, B. D. Patterson, O. Bunk, C. Brönnimann, B. Henrich, G. Hülsen and E. F. Eikenberry, *Improved data acquisition in grazing-incidence X-ray scattering experiments using a pixel detector*, Act. Cryst. Sec. A **61** (2005).

[89] P. Willmott, *An Introduction to Synchrotron Radiation - Techniques and Applications*, Wiley, Chichester, West Sussex, United Kingdom, 1 edn. (2011).

[90] S. Ferrer, X. Torrelles, V. H. Etgens, H. A. van der Vegt and P. Fajardo, *Atomic Structure of the c(4 × 2) Surface Reconstruction of Ge(001) as Determined by X-Ray Diffraction*, Phys. Rev. Lett. **75**, 1771 (1995).

[91] M. W. Radny, G. A. Shah, S. R. Schofield, P. V. Smith and N. J. Curson, *Valence Surface Electronic States on Ge(001)*, Phys. Rev. Lett. **100**, 246807 (2008).

[92] D. J. Paul, *Si/SiGe heterostructures: from material and physics to devices and circuits*, Semicond. Sci. Technol. **19**, R75 (2004).

[93] Y. Kamata, *High-k/Ge MOSFETs for future nanoelectronics*, Materials Today **11**, 30 (2008).

[94] F. Bechstedt, *Principles of Surface Physics*, Springer, Berlin, 1 edn. (2003).

[95] B. Stankiewicz and L. Jurczyszyn, *The influence of thermal fluctuations on electronic and structural properties of Ge(001) surface*, Surf. Sci. **601**, 1981 (2007).

[96] P. Krüger and J. Pollmann, *Dimer Reconstruction of Diamond, Si, and Ge (001) Surfaces*, Phys. Rev. Lett. **74**, 1155 (1995).

[97] H. Zandvliet, *The Ge(001) surface*, Physics Reports **388**, 1 (2003).

[98] H. J. Zandvliet, R. van Gastel, O. Gurlu and B. Poelsema, *Coexistence of (2×1) and c(4×2) phases on Ge(001)*, Phys. Lett. A **326**, 457 (2004).

[99] A. Molle, M. N. K. Bhuiyan, G. Tallarida and M. Fanciulli, *In situ chemical and structural investigations of the oxidation of Ge(001) substrates by atomic oxygen*, Appl. Phys. Lett. **89**, 083504 (2006).

[100] L. H. Chan, E. I. Altman and Y. Liang, *Development of procedures for obtaining clean, low-defect-density Ge(100) surfaces*, J. Vac. Sci. Technol. A **19**, 976 (2001).

[101] S. Gan, L. Li, T. Nguyen, H. Qi, R. F. Hicks and M. Yang, *Scanning tunneling microscopy of chemically cleaned germanium (100) surfaces*, Surf. Sci. **395**, 69 (1998).

[102] J. E. Van Nostrand, S. J. Chey, M. A. Hasan, D. G. Cahill and J. E. Greene, *Surface Morphology during Multilayer Epitaxial Growth of Ge(001)*, Phys. Rev. Lett. **74**, 1127 (1995).

[103] H. Okumura, T. Akane and S. Matsumoto, *Carbon contamination free Ge(100) surface cleaning for MBE*, Appl. Surf. Sci. **125**, 125 (1998).

[104] K. Prabhakarana, T. Ogino, R. Hull, J. C. Bean and L. J. Peticolas, *An efficient method for cleaning the Ge(001) surface*, Surf. Sci. **316**, L1031 (1994).

[105] J. S. Hovis, R. J. Hamers and C. M. Greenlief, *Preparation of clean and atomically flat germanium(001) surfaces*, Surf. Sci. **440**, L815 (1999).

[106] K. Prabhakaran and T. Ogino, *Oxidation of Ge(100) and Ge(111) surfaces: an UPS and XPS study*, Surf. Sci. **325** (1995).

[107] K. Williams and R. Muller, *Etch rates for micromachining processing*, Journal of Microelectromechanical Systems **5**, 256 (1996).

[108] K. Williams, K. Gupta and M. Wasilik, *Etch rates for micromachining processing-Part II*, Journal of Microelectromechanical Systems **12**, 761 (2003).

[109] S. M. Sze, *Semiconductor devices, physics and technology*, Wiley, New York (1985).

[110] A. Delabie, F. Bellenger, M. Houssa, T. Conard, S. V. Elshocht, M. Caymax, M. Heyns and M. Meuris, *Effective electrical passivation of Ge(100) for high-k gate dielectric layers using germanium oxide*, Appl. Phys. Lett. **91**, 082904 (2007).

[111] S. Saito, T. Hosoi, H. Watanabe and T. Ono, *First-principles study to obtain evidence of low interface defect density at Ge/GeO2 interfaces*, Appl. Phys. Lett. **95**, 011908 (2009).

[112] M. Houssa, G. Pourtois, M. Caymax, M. Meuris, M. M. Heyns, V. V. Afanas'ev and A. Stesmans, *Ge dangling bonds at the (100)Ge/GeO2 interface and the viscoelastic properties of GeO2*, Appl. Phys. Lett. **93**, 161909 (2008).

[113] Z. Liu, Y. Sun, F. Machuca, P. Pianetta, W. E. Spicer and R. F. W. Pease, *Preparation of clean GaAs(100) studied by synchrotron radiation photoemission*, J. Vac. Sci. Technol. A **21**, 212 (2003).

[114] T. Deegan and G. Hughes, *An X-ray photoelectron spectroscopy study of the HF etching of native oxides on Ge(111) and Ge(100) surfaces*, Appl. Surf. Sci. **123**, 66 (1998).

[115] J. F. Moulder, W. F. Strickle, P. E. Sobol and K. D. Bomben, *Handbook of X-ray Photoelectron Spectroscopy*, Perkin-Elmer Corporation, Minnesota (1992).

[116] O. Gurlu, H. J. W. Zandvliet and B. Poelsema, *Electronic Properties of* (2×1) *and* $c(4 \times 2)$ *Domains on Ge(001) Studied by Scanning Tunneling Spectroscopy*, Phys. Rev. Lett. **93**, 066101 (2004).

[117] N. Oncel, A. van Houselt, J. Huijben, A.-S. Hallbäck, O. Gurlu, H. J. W. Zandvliet and B. Poelsema, *Quantum Confinement between Self-Organized Pt Nanowires on Ge(001)*, Phys. Rev. Lett. **95**, 116801 (2005).

[118] J. Kubby and J. Boland, *Scanning tunneling microscopy of semiconductor surfaces*, Surf. Sci. Rep. **26**, 61 (1996).

[119] A. Bettac, J. Koeble, K. Winkler, B. Uder, M. Maier and A. Feltz, *QPlus: atomic force microscopy on single-crystal insulators with small oscillation amplitudes at 5 K*, Nanotechnology **20**, 264009 (2009).

[120] A. Sweetman, S. Gangopadhyay, R. Danza, N. Berdunov and P. Moriarty, *qPlus atomic force microscopy of the Si(100) surface: Buckled, split-off, and added dimers*, Appl. Phys. Lett. **95**, 063112 (2009).

[121] O. Gurlu, O. Adam, H. Zandvliet and B. Poelsema, *Self-organized, one-dimensional Pt nanowires on Ge(001)*, Appl. Phys. Lett. **83**, 4610 (2003).

[122] M. Kulawik, N. Nilius and H.-J. Freund, *Influence of the Metal Substrate on the Adsorption Properties of Thin Oxide Layers: Au Atoms on a Thin Alumina Film on NiAl(110)*, Phys. Rev. Lett. **96**, 036103 (2006).

[123] C. Blumenstein, J. Schäfer, M. Morresi, S. Mietke, R. Matzdorf and R. Claessen, *Symmetry-Breaking Phase Transition without a Peierls Instability in Conducting Monoatomic Chains*, Phys. Rev. Lett. **107**, 165702 (2011).

[124] A. van Houselt, M. Fischer, B. Poelsema and H. J. W. Zandvliet, *Giant missing row reconstruction of Au on Ge(001)*, Phys. Rev. B **78**, 233410 (2008).

[125] D. Kockmann, T. F. Mocking, A. v. Houselt, B. Poelsema and H. J. W. Zandvliet, *Structural and Electronic Properties of Au Induced Nanowires on Ge(001)*, J. Phys. Chem. C **113**, 17156 (2009).

[126] T. F. Mocking, D. Stam, B. Poelsema and H. J. Zandvliet, *Dynamics of Au-induced nanowires on Ge(001)*, Surf. Sci. **604**, 2021 (2010).

[127] R. Niikura, K. Nakatsuji and F. Komori, *Local atomic and electronic structure of Au-adsorbed Ge(001) surfaces: Scanning tunneling microscopy and x-ray photoemission spectroscopy*, Phys. Rev. B **83**, 035311 (2011).

[128] K. Nakatsuji, R. Niikura, Y. Shibata, M. Yamada, T. Iimori and F. Komori, *Anisotropic two-dimensional metallic state of* $Ge(001)c(8 \times 2) - Au$ *surfaces: An angle-resolved photoelectron spectroscopy*, Phys. Rev. B **80**, 081406 (2009).

[129] S. Sauer, F. Fuchs, F. Bechstedt, C. Blumenstein and J. Schäfer, *First-principles studies of Au-induced nanowires on Ge(001)*, Phys. Rev. B **81**, no. 7, 075412 (2010).

[130] H. W. Yeom, K. Horikoshi, H. M. Zhang, K. Ono and R. I. G. Uhrberg, *Nature of the broken-symmetry phase of the one-dimensional metallic In/Si(111) surface*, Phys. Rev. B **65**, 241307 (2002).

[131] J. R. Ahn, W. H. Choi, Y. K. Kim, H. S. Lee and H. W. Yeom, *High-resolution photoemission spectroscopy study of clean and Au-nanowire-decorated Si(5 5 12) surfaces*, Phys. Rev. B **68**, 165314 (2003).

[132] K. S. Kim, W. H. Choi and H. W. Yeom, *Photoemission study of the anisotropic phase formation of Pb on Si(557)*, Phys. Rev. B **75**, 195324 (2007).

[133] P. E. J. Eriksson and R. I. G. Uhrberg, *Surface core-level shifts on clean Si(001) and Ge(001) studied with photoelectron spectroscopy and density functional theory calculations*, Phys. Rev. B **81**, 125443 (2010).

[134] A. Goldoni, S. Modesti, V. R. Dhanak, M. Sancrotti and A. Santoni, *Evidence for three surface components in the 3d core-level photoemission spectra of Ge(100)-(2×1) surface*, Phys. Rev. B **54**, 11340 (1996).

[135] T.-W. Pi, J.-F. Wen, C.-P. Ouyang and R.-T. Wu, *Surface core-level shifts of Ge(100)-2×1*, Phys. Rev. B **63**, 153310 (2001).

[136] P. H. Citrin, G. K. Wertheim and Y. Baer, *Core-Level Binding Energy and Density of States from the Surface Atoms of Gold*, Phys. Rev. Lett. **41**, 1425 (1978).

[137] G. D. Mahan, *Excitons in Metals: Infinite Hole Mass*, Phys. Rev. **163**, 612 (1967).

[138] S. Doniach and M. Sunjic, *Many-electron singularity in X-ray photoemission and X-ray line spectra from metals*, J. Phys. C: Sol. St. Phys. **3**, 285 (1970).

[139] S. Hüfner and G. K. Wertheim, *Core-line asymmetries in the x-ray-photoemission spectra of metals*, Phys. Rev. B **11**, 678 (1975).

[140] S. D. Kevan and N. G. Stoffel, *Metal-Insulator Transition on the Ge(001) Surface*, Phys. Rev. Lett. **53**, 702 (1984).

[141] S. D. Kevan, *Surface states and reconstruction on Ge(001)*, Phys. Rev. B **32**, 2344 (1985).

[142] K. Nakatsuji, Y. Takagi, F. Komori, H. Kusuhara and A. Ishii, *Electronic states of the clean Ge(001) surface near Fermi energy*, Phys. Rev. B **72**, 241308 (2005).

[143] C. Jeon, C. C. Hwang, T.-H. Kang, K.-J. Kim, B. Kim, Y. Chung and C. Y. Park, *Evidence from ARPES that the Ge(001) surface is semiconducting at room temperature*, Phys. Rev. B **74**, 125407 (2006).

[144] P. E. J. Eriksson, M. Adell, K. Sakamoto and R. I. G. Uhrberg, *Origin of a surface state above the Fermi level on Ge(001) and Si(001) studied by temperature-dependent ARPES and LEED*, Phys. Rev. B **77**, 085406 (2008).

[145] J. Tauc, R. Grigorovici and A. Vancu, *Optical Properties and Electronic Structure of Amorphous Germanium*, Phys Stat. Sol. (b) **15**, 627 (1966).

[146] R. N. Dexter, H. J. Zeiger and B. Lax, *Cyclotron Resonance Experiments in Silicon and Germanium*, Phys. Rev. **104**, 637 (1956).

[147] T. B. Boykin, G. Klimeck and F. Oyafuso, *Valence band effective-mass expressions in the $sp^3d^5s^*$ empirical tight-binding model applied to a Si and Ge parametrization*, Phys. Rev. B **69**, 115201 (2004).

[148] S.-J. Tang, T.-R. Chang, C.-C. Huang, C.-Y. Lee, C.-M. Cheng, K.-D. Tsuei, H.-T. Jeng and C.-Y. Mou, *Dispersive resonance bands within the space-charge layer of a metal-semiconductor junction*, Phys. Rev. B **81**, 245406 (2010).

[149] Y. Ohtsubo, S. Hatta, K. Yaji, H. Okuyama, K. Miyamoto, T. Okuda, A. Kimura, H. Namatame, M. Taniguchi and T. Aruga, *Spin-polarized semiconductor surface states localized in subsurface layers*, Phys. Rev. B **82**, 201307 (2010).

[150] R. Losio, K. N. Altmann, A. Kirakosian, J.-L. Lin, D. Y. Petrovykh and F. J. Himpsel, *Band Splitting for Si(557)-Au: Is It Spin-Charge Separation?*, Phys. Rev. Lett. **86**, 4632 (2001).

[151] T. Okuda, K. Miyamaoto, Y. Takeichi, H. Miyahara, M. Ogawa, A. Harasawa, A. Kimura, I. Matsuda, A. Kakizaki, T. Shishidou and T. Oguchi, *Large out-of-plane spin polarization in a spin-splitting one-dimensional metallic surface state on Si(557)-Au*, Phys. Rev. B **82**, 161410 (2010).

[152] J. N. Crain, A. Kirakosian, K. N. Altmann, C. Bromberger, S. C. Erwin, J. L. McChesney, J.-L. Lin and F. J. Himpsel, *Fractional Band Filling in an Atomic Chain Structure*, Phys. Rev. Lett. **90**, 176805 (2003).

[153] J. N. Crain, J. L. McChesney, F. Zheng, M. C. Gallagher, P. C. Snijders, M. Bissen, C. Gundelach, S. C. Erwin and F. J. Himpsel, *Chains of gold atoms with tailored electronic states*, Phys. Rev. B **69**, 125401 (2004).

[154] T. Abukawa, M. Sasaki, F. Hisamatsu, T. Goto, T. Kinoshita, A. Kakizaki and S. Kono, *Surface electronic structure of a single-domain Si(111)4x1-In surface: a synchrotron radiation photoemission study*, Surf. Sci. **325**, 33 (1995).

[155] C. Kumpf, O. Bunk, J. H. Zeysing, Y. Su, M. Nielsen, R. L. Johnson, R. Feidenhans'l and K. Bechgaard, *Low-Temperature Structure of Indium Quantum Chains on Silicon*, Phys. Rev. Lett. **85**, 4916 (2000).

[156] K. S. Kim, H. Morikawa, W. H. Choi and H. W. Yeom, *Strong Lateral Electron Coupling of Pb Nanowires on Stepped Si(111): Angle-Resolved Photoemission Studies*, Phys. Rev. Lett. **99**, 196804 (2007).

[157] C. Tegenkamp, T. Ohta, J. L. McChesney, H. Dil, E. Rotenberg, H. Pfnür and K. Horn, *Coupled Pb Chains on Si(557): Origin of One-Dimensional Conductance*, Phys. Rev. Lett. **100**, 076802 (2008).

[158] K. Nakatsuji, Y. Motomura, R. Niikura and F. Komori, *Shape of metallic band at single-domain Au-adsorbed Ge(001) surface studied by angle-resolved photoemission spectroscopy*, Phys. Rev. B **84**, 115411 (2011).

[159] S. Melnik and M. Gallagher, *Growth of the Au-induced c(8×2) structure on vicinal Ge(001)*, Surf. Sci. **606**, L10 (2012).

[160] G. W. Brown, H. Grube and M. E. Hawley, *Observation of buried phosphorus dopants near clean* Si(100)-(2 × 1) *surfaces with scanning tunneling microscopy*, Phys. Rev. B **70**, 121301 (2004).

[161] J. E. Demuth, W. J. Thompson, N. J. DiNardo and R. Imbihl, *Photoemission-Based Photovoltage Probe of Semiconductor Surface and Interface Electronic Structure*, Phys. Rev. Lett. **56**, 1408 (1986).

[162] M. Alonso, R. Cimino and K. Horn, *Surface photovoltage effects in photoemission from metal-GaP(110) interfaces: Importance for band bending evaluation*, Phys. Rev. Lett. **64**, 1947 (1990).

[163] P. Starowicz, O. Gallus, T. Pillo and Y. Baer, *Size Effects in Photoemission of One-Dimensional Metals*, Phys. Rev. Lett. **89**, 256402 (2002).

[164] R. Joynt, *Pseudogaps and Extrinsic Losses in Photoemission Experiments on Poorly Conducting Solids*, Science **284**, 777 (1999).

[165] D. L. Mills, *Final-state interactions in photoemission: Energy loss by the exiting electron*, Phys. Rev. B **62**, 11197 (2000).

[166] R. Joynt, *Comment on "Final-state interactions in photoemission: Energy loss by the exiting electron"*, Phys. Rev. B **65**, 077403 (2002).

[167] D. L. Mills, *Reply to "Comment on 'Final-state interactions in photoemission: Energy loss by the exiting electron' "*, Phys. Rev. B **65**, 077404 (2002).

[168] P. Segovia, D. Purdie, M. Hengsberger and Y. Baer, *Observation of spin and charge collective modes in one-dimensional metallic chains*, Nature **402**, 504 (1999).

[169] L. Bartosch and P. Kopietz, *Zero bias anomaly in the density of states of low-dimensional metals*, Euro. Phys. J. B **28**, no. 1, 29 (2002).

[170] B. Kim, H. Koh, E. Rotenberg, S. Oh, H. Eisaki, N. Motoyama, S. Uchida, T. Tohyama, S. Maekawa, Z. Shen and C. Kim, *Distinct spinon and holon dispersions in photoemission spectral functions from one-dimensional SrCuO2*, Nat. Phys. **2**, 397 (2006).

[171] A. Sekiyama, A. Fujimori, S. Aonuma, H. Sawa and R. Kato, *Fermi-liquid versus Luttinger-liquid behavior and metal-insulator transition in N,N'-dicyanoquinonediimine-Cu salt studied by photoemission*, Phys. Rev. B **51**, 13899 (1995).

[172] J. Hager, R. Matzdorf, J. He, R. Jin, D. Mandrus, M. A. Cazalilla and E. W. Plummer, *Non-Fermi-Liquid Behavior in Quasi-One-Dimensional* $Li_{0.9}Mo_6O_{17}$, Phys. Rev. Lett. **95**, 186402 (2005).

[173] F. Wang, J. V. Alvarez, S.-K. Mo, J. W. Allen, G.-H. Gweon, J. He, R. Jin, D. Mandrus and H. Höchst, *New Luttinger-Liquid Physics from Photoemission on* $Li_{0.9}Mo_6O_{17}$, Phys. Rev. Lett. **96**, 196403 (2006).

[174] J. D. Denlinger, G.-H. Gweon, J. W. Allen, C. G. Olson, J. Marcus, C. Schlenker and L.-S. Hsu, *Non-fermi-liquid single particle line shape of the quasi-one-dimensional non-cdw metal* $li_{0.9}mo_6O_{17}$*: Comparison to the luttinger liquid*, Phys. Rev. Lett. **82**, 2540 (1999).

[175] G.-H. Gweon, S.-K. Mo, J. W. Allen, J. He, R. Jin, D. Mandrus and H. Höchst, *Luttinger liquid angle-resolved photoemission line shapes from samples of* $Li_{0.9}Mo_6O_{17}$ *grown by the temperature-gradient-flux technique*, Phys. Rev. B **70**, 153103 (2004).

[176] F. Wang, S.-K. Mo, J. W. Allen, H.-D. Kim, J. He, R. Jin, D. Mandrus, A. Sekiyama, M. Tsunekawa and S. Suga, *Case for bulk nature of spectroscopic Luttinger liquid signatures observed in angle-resolved photoemission spectra of* $Li_{0.9}Mo_6O_{17}$, Phys. Rev. B **74**, 113107 (2006).

[177] F. Wang, J. V. Alvarez, J. W. Allen, S.-K. Mo, J. He, R. Jin, D. Mandrus and H. Höchst, *Quantum Critical Scaling in the Single-Particle Spectrum of a Novel Anisotropic Metal*, Phys. Rev. Lett. **103**, 136401 (2009).

[178] Y. Jompol, C. J. B. Ford, J. P. Griffiths, I. Farrer, G. A. C. Jones, D. Anderson, D. A. Ritchie, T. W. Silk and A. J. Schofield, *Probing Spin-Charge Separation in a Tomonaga-Luttinger Liquid*, Science **325**, 597 (2009).

[179] O. M. Auslaender, A. Yacoby, R. de Picciotto, K. W. Baldwin, L. N. Pfeiffer and K. W. West, *Tunneling Spectroscopy of the Elementary Excitations in a One-Dimensional Wire*, Science **295**, 825 (2002).

[180] O. M. Auslaender, H. Steinberg, A. Yacoby, Y. Tserkovnyak, B. I. Halperin, K. W. Baldwin, L. N. Pfeiffer and K. W. West, *Spin-Charge Separation and Localization in One Dimension*, Science **308**, 88 (2005).

[181] H. Ishii, H. Kataura, H. Shiozawa, H. Yoshioka, H. Otsubo, Y. Takayama, T. Miyahara, S. Suzuki, Y. Achiba, M. Nakatake, T. Narimura, M. Higashiguchi, K. Shimada, H. Namatame and M. Taniguchi, *Direct observation of Tomonaga-Luttinger-liquid state in carbon nanotubes at low temperatures*, Nature **426**, 540 (2003).

[182] H. Rauf, T. Pichler, M. Knupfer, J. Fink and H. Kataura, *Transition from a Tomonaga-Luttinger Liquid to a Fermi Liquid in Potassium-Intercalated Bundles of Single-Wall Carbon Nanotubes*, Phys. Rev. Lett. **93**, 096805 (2004).

[183] C. A. Bobisch, M. R. Kaspers, A. M. Bernhart, M. Wojtaszek, F. Krok, M. Szymonski and R. Möller, *Scanning tunneling potentiometry on the Au/Ge(001) surface*, March meeting of the German Physical Society (DPG) Berlin **O**, 79.1 (2012).

[184] W. Ernst, C. Tegenkamp, H. Pfnür, K.-L. Jonas, V. von Oeynhausen and K. Meiwes-Broer, *The structure of Na adsorbed on Ge(100) and its influence on substrate morphology*, Surf. Sci. **540**, 303 (2003).

[185] W. Ernst, K.-L. Jonas, V. von Oeynhausen, C. Tegenkamp and H. Pfnür, *Restructuring of the Ge(100) surface by Na chains*, Phys. Rev. B **68**, 205303 (2003).

[186] B. Czech, P. Mikolajczyk and B. Stankiewicz, *Low-coverage alkali metal adsorption on the Ge(001)-p(1×2) surface*, Appl. Surf. Sci. **256**, 4784 (2010).

[187] K. Fleischer, S. Chandola, N. Esser, W. Richter and J. F. McGilp, *Surface phonons of the* Si(111) : In-(4×1) *and* (8×2) *phases*, Phys. Rev. B **76**, 205406 (2007).

[188] S. Chandola, K. Hinrichs, M. Gensch, N. Esser, S. Wippermann, W. G. Schmidt, F. Bechstedt, K. Fleischer and J. F. McGilp, *Structure of Si(111)-In Nanowires Determined from the Midinfrared Optical Response*, Phys. Rev. Lett. **102**, 226805 (2009).

[189] T. Tanikawa, I. Matsuda, T. Kanagawa and S. Hasegawa, *Surface-State Electrical Conductivity at a Metal-Insulator Transition On Silicon*, Phys. Rev. Lett. **93**, 016801 (2004).

[190] P. W. Anderson, *Infrared conductivity of cuprate metals: Detailed fit using Luttinger-liquid theory*, Phys. Rev. B **55**, 11785 (1997).

[191] C. G. Hwang, N. D. Kim, S. Y. Shin and J. W. Chung, *Possible evidence of non-Fermi liquid behaviour from Quasi-one-dimensional indium nanowires*, New J. Phys. **9**, 249 (2007).

[192] C. M. Schlepütz, S. O. Mariager, S. A. Pauli, R. Feidenhans'l and P. R. Willmott, *Angle calculations for a (2+3)-type diffractometer: focus on area detectors*, J. Appl. Cryst. **44**, 73 (2011).

[193] B. Patterson, R. Abela, H. Auderset, Q. Chen, F. Fauth, F. Gozzo, G. Ingold, H. Kühne, M. Lange, D. Maden, D. Meister, P. Pattison, T. Schmidt, B. Schmitt, C. Schulze-Briese, M. Shi, M. Stampanoni and P. Willmott, *The materials science beamline at the Swiss Light Source: design and realization*, Nuclear Instruments and Methods in Physics Research Section A: Accelerators, Spectrometers, Detectors and Associated Equipment **540**, 42 (2005).

[194] J.R. Ahn, P.G. and Kang, J.H. Byun, and H.W. Yeom, *Adsorbate-induced reconstruction of an array of atomic wires: Indium on the Si(553)-Au surface*, Phys. Rev. B **77**, 035401 (2008).

[195] P.G. Kang, H. Jeong, and H.W. Yeom, *Microscopic mechanism of templated self-assembly: Indium metallic atomic wires on Si(553)-Au*, Phys. Rev. B **79**, 113403 (2009).

[196] P. Nita, G. Zawadzki, M. Krawiec, and M. Jałochowski, *Structural and electronic properties of double Pb chains on the Si(553)-Au surface*, Phys. Rev. B **84**, 085453 (2011).

Acknowledgment

This thesis could not have been finished without the help of many people. It is, therefore, my obligation to especially thank the following persons:

- Prof. Dr. Ralph Claessen, for offering the opportunity to perform my work at his chair Experimentelle Physik 4, sharing his wisdom of condensed matter physics and supporting the various synchrotron travels.
- Special thanks to Priv.-Doz. Dr. Jörg Schäfer, for his continuous motivation and the supervision of this work. He not only wrote the synchrotron proposals but also provided the appropriate visions of what to measure and of what to expect.
- Prof. Dr. Jean Geurts, for the enlightening collaboration in the field of optics and for agreeing to act as the second reviewer of this thesis.
- Prof. Dr. Friedhelm Bechstedt and Simeon Sauer for the fruitful collaboration in the field of density functional theory modeling.
- I gratefully acknowledge support by a great number of excellent scientists at the various synchrotron facilities. First to mention Eli Rotenberg and Aaron Bostwick at the ALS; Xiaoyu Cui, Ming Shi and Luc Patthey at the SLS HRPES endstation; Bartosz Slomski, Gabriel Landolt and Hugo Dil at the SLS Cophee endstation; as well as Prof. Phil Willmott and Steven Leake at the MS beamline, SLS.
- Synchrotron work is always the work of many. So I am highly indebted to my colleagues Christian Blumenstein and Philipp Höpfner, not only for being the best colleagues one can ask for, but also for continuously supporting my with the various beamtimes.
- I also had the pleasure to meet a lot of motivated Diploma-(Bachelor-)students, who all contributed to the results presented in this thesis by keeping the lab running or sharing the beamtime with me. In order of appearance: Andreas Dollinger, Thorsten Umbach, Christoph Loho and Stefan Glass.
- My PhD colleagues and all other EP4 members for the comfortable atmosphere, as well as sharing frustrating times with me.
- Moni, heart and soul of EP4.

Furthermore, I would like to thank my family and friends, who constantly pushed me to the finish line:

- My parents, always being a guide for life.
- My sisters, for pushing both thumbs.
- My friends outside the lab, offering me distraction and teaching me real life.
- I am deeply grateful to my girlfriend Jana: for moving to Würzburg, sharing her life with me and continuously believing that there will be an end. I love you!

Erklärung

Hiermit erkläre ich an Eides statt, dass ich die Dissertation eigenhändig, d.h. insbesondere selbstständig und ohne Hilfe einer kommerziellen Promotionsberatung angefertigt und keine anderen als die angegeben Quellen und Hilfsmittel benutzt habe.

Würzburg den 5.5.2013 Sebastian Meyer

Hiermit erkläre ich an Eides statt, dass ich die Gelegenheit zum Promotionsvorhaben nicht kommerziell vermittelt bekommen habe und insbesondere nicht eine Person oder Organisation eingeschaltet habe, die gegen Entgelt Betreuer bzw. Betreuerinnen für die Anfertigung von Dissertationen sucht.

Würzburg den 5.5.2013 Sebastian Meyer

Hiermit erkläre ich, dass ich die Regeln der Universität Würzburg über gute wissenschaftliche Praxis eingehalten habe.

Würzburg den 5.5.2013 Sebastian Meyer

Hiermit erkläre ich, dass die vorliegende Dissertation nicht in gleicher oder anderer Form bereits in einem anderen Prüfungsfach vorgelegt habe.

Würzburg den 5.5.2013 Sebastian Meyer